

COMPUTATIONAL FLUID DYNAMICS OF
DISPERSED TWO-PHASE FLOWS AT
HIGH PHASE FRACTIONS

HENRIK RUSCHE

Thesis submitted for the degree of
Doctor of Philosophy of the University of London
and
Diploma of Imperial College

Imperial College of Science, Technology & Medicine
Department of Mechanical Engineering
Exhibition Road, London SW7 2BX

December 2002

Abstract

This study describes the development and validation of Computational Fluid Dynamics (CFD) methodology for the simulation of dispersed two-phase flows.

A two-fluid (Euler-Euler) methodology previously developed at Imperial College is adapted to high phase fractions. It employs averaged mass and momentum conservation equations to describe the time-dependent motion of both phases and, due to the averaging process, requires additional models for the inter-phase momentum transfer and turbulence for closure. The continuous phase turbulence is represented using a two-equation $k - \varepsilon$ -turbulence model which contains additional terms to account for the effects of the dispersed on the continuous phase turbulence. The Reynolds stresses of the dispersed phase are calculated by relating them to those of the continuous phase through a turbulence response function.

The inter-phase momentum transfer is determined from the instantaneous forces acting on the dispersed phase, comprising drag, lift and virtual mass. These forces are phase fraction dependent and in this work revised modelling is put forward in order to capture the phase fraction dependency of drag and lift. Furthermore, a correlation for the effect of the phase fraction on the turbulence response function is proposed. The revised modelling is based on an extensive survey of the existing literature.

The conservation equations are discretised using the finite-volume method and solved in a solution procedure, which is loosely based on the PISO algorithm, adapted to the solution of the two-fluid model. Special techniques are employed to ensure the stability of the procedure when the phase fraction is high or changing rapidly.

Finally, assessment of the methodology is made with reference to experimental data for gas-liquid bubbly flow in a sudden enlargement of a circular pipe and in a plane mixing layer.

Additionally, Direct Numerical Simulations (DNS) are performed using an interface-capturing methodology in order to gain insight into the dynamics of free rising bubbles, with a view towards use in the longer term as an aid in the development of inter-phase momentum transfer models for the two-fluid methodology. The direct numerical simulation employs the mass and momentum conservation equations in their unaveraged form and the topology of the interface between the two phases is determined as part of the solution. A novel solution procedure, similar to that used for the two-fluid model, is used for the interface-capturing methodology, which allows calculation of air bubbles in water. Two situations are investigated: bubbles rising in a stagnant liquid and in a shear flow. Again, experimental data are used to verify the computational results.

Acknowledgements

I wish to express my gratitude to my supervisors, Professor David Gosman and Dr. Raad Issa, for their continued support, guidance and constructive criticism. Very special thanks are also due to my “unofficial” supervisor Mr. Henry Weller for his vital support, invaluable insights and the use of the FOAM software library.

I am also indebted to Dr. Hrvoje Jasak and Dr. Čedo Kralj for their support and encouragement, especially during the preparation of this thesis. It benefited from their numerous, valuable comments and the helpful discussions.

Furthermore, I would like to acknowledge the collaboration and companionship of my colleagues Dr. Gavin Tabor and Dr. Alireza Behzadi who worked with me on the BRITE project. I also miss the many fruitful discussions with members and visitors of Professor Gosman’s CFD group as well as other members of the Thermofluids Section who are too numerous to mention here.

My thanks also go to Mrs. Nicky Scott-Knight and Mrs. Susan Clegg for the arrangement of many administrative matters.

Finally, the financial support provided by Computational Dynamics Ltd., Imperial Chemical Industries p.l.c., TotalElfFina, Unilever Research Laboratory and the Commission of the European Communities in the framework of the BRITE-EURAM III programme, which made this study possible, is gratefully acknowledged.

Henrik Rusche

December 2002

Contents

Abstract	3
Acknowledgements	5
Contents	7
List of Figures	11
List of Tables	15
List of Animations	17
Nomenclature	19
1 Introduction	25
1.1 Background	25
1.2 CFD Methodologies for Two-Phase Flow	28
1.2.1 Direct Numerical Simulation	29
1.2.2 Discrete DPE Model	30
1.2.3 Two-Fluid Model	33
1.3 Objectives of this Work	35
1.4 Present Contributions	36
1.5 Previous and Related Studies	38
1.5.1 Solution Procedures for the DNS of Two-Phase Flow	38
1.5.2 Solution Procedures for the Two-Fluid Model	41
1.5.3 Modelling Drag	42
1.5.4 Modelling Drag at High Phase Fractions	50
1.5.5 Modelling Lift	55
1.5.6 Two-Phase Turbulence Modelling	64
1.5.7 Validation Test Cases for the Two-Fluid Methodology	67
1.6 Thesis Outline	72
2 Finite Volume Discretisation	75
2.1 Discretisation of the Solution Domain	75
2.2 Arrangement and Storage of Variables	78
2.3 Equation Discretisation	79
2.3.1 Face Interpolation	80
2.3.2 Gradient	82

2.3.3	Time Derivative	83
2.3.4	Convection Term	83
2.3.5	Diffusion Term	83
2.3.6	Source Term	84
2.3.7	Curl	84
2.3.8	Average	85
2.4	Boundary Conditions	85
2.5	Temporal Discretisation	88
2.6	Solution Techniques for Systems of Linear Algebraic Equations	89
2.6.1	Analysis of Matrix Structure	91
2.6.2	Under-Relaxation	94
2.7	Finite Volume Notation	95
2.8	Closure	97
3	Two-Fluid Methodology	99
3.1	Governing Equations	99
3.1.1	Averaged Phase Momentum and Continuity Equations	99
3.1.2	Inter-phase Momentum Transfer	100
3.1.3	Turbulence Model by Gosman et al. [121]	105
3.2	Solution Procedure	107
3.2.1	Phase-Intensive Momentum Equation	108
3.2.2	Discretisation of the Phase Momentum Equations	109
3.2.3	Phase Momentum Correction Equations	111
3.2.4	Pressure Equation	112
3.2.5	Practices for the Inter-phase Momentum Transfer Term	113
3.2.6	Solution of the Phase Continuity Equations	115
3.2.7	Solution of the $k - \varepsilon$ -Turbulence Model	120
3.2.8	Boundary Conditions	120
3.2.9	Sequence of Solution	123
3.2.10	Solution Procedure of Weller	125
3.3	Basic Tests of the Solution Procedure	128
3.3.1	Test Case: Sudden Enlargement in a Circular Pipe	128
3.3.2	Test Case: Phase Separation in a Tank	133
3.3.3	Test Case: Bubble Plume	137
3.4	Closure	146
4	Interface-Capturing Methodology	147
4.1	Governing Equations	147
4.1.1	Momentum and Continuity Equations	148
4.1.2	Indicator Function	149
4.1.3	Non-Inertial Frame of Reference	150
4.2	Solution Procedure	152
4.2.1	Indicator Equation with Bounded Compression	152
4.2.2	Calculation of Surface Tension	154
4.2.3	Final Form of the Momentum Equation	155
4.2.4	Pressure-Velocity Solution Procedure	156
4.2.5	Boundary Conditions	158

4.2.6	Motion of the Moving Reference Frame	159
4.2.7	Time Step Control	160
4.2.8	Sequence of Solution	161
4.3	Test of Numerical Methodology	162
4.3.1	Free Rising Bubbles	162
4.3.2	Free Rising Bubbles in Linear Shear	171
4.4	Closure	177
5	Turbulence Response Coefficient Modelling	179
5.1	Turbulence Response Coefficient at High Phase Fractions	180
5.2	Two-Fluid Methodology: Sudden Enlargement of a Circular Pipe	181
5.3	Two-Fluid Methodology: Plane Mixing Layer	186
5.4	Closure	193
6	Drag Modelling	197
6.1	Definitions	198
6.2	Models for Single DPEs	200
6.2.1	Analytical Results	201
6.2.2	Empirical Correlations for Particles	202
6.2.3	Empirical Correlations for Droplets	204
6.2.4	Empirical Correlations for Bubbles in Clean Water	205
6.2.5	Empirical Correlations for Bubbles in Contaminated Water	207
6.2.6	Other Empirical Correlations for Bubbles	209
6.3	Influence of Phase Fraction on the Drag Coefficient	211
6.3.1	Empirical Correlations for Particles	212
6.3.2	Empirical Correlations for Droplets	216
6.3.3	Empirical Correlations for Bubbles	219
6.3.4	New Correlations	221
6.4	Model Selection and Testing	224
6.4.1	Bubbles at Low Phase Fraction	226
6.4.2	Droplets at Low Phase Fraction	228
6.4.3	Particles at High Phase Fraction	228
6.4.4	Droplets at High Phase Fraction	235
6.4.5	Bubbles at High Phase Fraction	242
6.5	Calculations Using the Two-Fluid Methodology	249
6.6	Closure	257
7	Lift Modelling	259
7.1	Definitions	260
7.2	Models for Single DPEs	261
7.2.1	Analytical Results	261
7.2.2	Computational Results for Particles	264
7.2.3	Empirical Correlations for Particles	265
7.2.4	Computational Results for Bubbles	269
7.2.5	Empirical Correlations for Bubbles	271
7.3	The Influence of Phase Fraction on the Lift Coefficient	276
7.4	Calculations Using the Two-Fluid Methodology	278

7.5	Interface Capturing Methodology: Rising Bubble in Shear Flow	285
7.6	Closure	297
8	Closure	299
8.1	Conclusions	299
8.2	Suggestions for Future Work	303
A	Determination of the Projected Diameter from Interface-Capturing Calculations	307
B	Determination of the Lift Coefficient from Interface-Capturing Calculations	311
	Bibliography	315

List of Figures

1.1	Averaged modelling approaches for two-phase flow.	31
1.2	Free-surface methodologies.	39
1.3	Drag coefficient as a function of the Reynolds number for solid spheres.	43
1.4	Shape regimes of fluid particles in unhindered gravitational motion through liquids (from [56]).	45
1.5	Terminal velocity as a function of diameter for air bubbles in water (from [56]).	48
1.6	Shear-induced lift on a spherical particle (from [261]).	57
1.7	Sketch of the flow field around a DPE in linear shear. The shedding of non-symmetric vortices could produce an average lateral lift force towards the lower velocity side.	58
1.8	Sketch of an undeformed and distorted DPE.	59
1.9	Lift coefficient for a clean spherical bubble in a linear shear flow as a function of the Reynolds number.	61
2.1	Discretisation of the solution domain (from [255]).	76
2.2	Parameters in finite volume discretisation (from [255]).	77
2.3	Two types of variable storage arrangements: a) volume field: values are stored at the cell centres; b) face field: values are stored at the face centres (from [255]).	78
2.4	Parameters in finite volume discretisation for cells with a boundary face.	86
3.1	Modifier function f_a as a function of the phase fraction α for different values A and B	104
3.2	Sketch of the setup for the sudden enlargement test case.	129
3.3	Results for the sudden enlargement test case: a) lower section of the computational mesh; b) mean liquid velocity \bar{U}_b ; c) gas phase fraction α_a ; d) turbulent viscosity ν^t	131
3.4	Residuals in the dispersed phase continuity equation for the coarse mesh.	132
3.5	Cell values of the dispersed phase fraction at the outlet of the sudden enlargement.	133
3.6	Residual in the dispersed phase continuity equation for the fine mesh. .	134
3.7	Time sequence of the phase fraction and the velocity fields for the complete separation test case using the Weller [423] solution procedure. $\rho_b/\rho_a = 20$	136
3.8	Time sequence of the phase fraction and the velocity fields for the phase separation test case using the standard solution procedure. $\rho_b/\rho_a = 20$.	137

3.9	Time sequence of the phase fraction and the velocity fields for the phase separation test case using the Weller [423] solution procedure. $\rho_b/\rho_a = 1000$	138
3.10	Sketch of the setup for the bubble plume test case.	139
3.11	Time sequence of the phase fraction and the gas velocity field for the bubble plume test case. The air flow rate is 48 l/h.	141
3.12	Time sequence of the phase fraction and the liquid velocity field for the bubble plume test case. The air flow rate is 48 l/h.	142
3.13	Time averaged phase fraction and the velocity fields for the bubble plume test case. The air flow rate is 48 l/h.	143
3.14	Liquid velocity in the vertical direction at three locations.	144
3.15	Fourier transform of the liquid velocity in the vertical direction at two locations and different air flow rates.	145
3.16	Variation of period of the vertical liquid velocity with the air flow rate.	145
4.1	Sketch of the space domain and its non-inertial frame of reference ($\hat{x} - \hat{y}$) relative to the inertial frame ($x - y$).	151
4.2	Sketch of the setup for free rising bubbles in a quiescent liquid.	163
4.3	Rise velocity as a function of time for bubbles with nominal diameters between 1 and 5 mm.	164
4.4	Characteristic velocity fields around free rising bubbles, $\log(\mathcal{M}_0) = -11$	165
4.5	Bubble trajectories in the horizontal $x - z$ plane for bubbles with nominal diameters between 1 to 5 mm.	166
4.6	Bubble trajectories in the vertical $x - y$ plane for bubbles with nominal diameters between 1 to 5 mm.	166
4.7	Calculated and measured bubble $\mathcal{R}e$ as a function of \mathcal{E}_o	167
4.8	Time sequence of the velocity fields around a free rising bubble, $d = 2.5$ mm, $\log(\mathcal{M}_0) = -11$	168
4.9	Rise velocity of bubble with a nominal diameter of 2.5 mm as a function of time.	170
4.10	Lateral velocities of bubble with a nominal diameter of 2.5 mm as a function of time.	170
4.11	Fourier transform of the rise and lateral velocity of a bubble with a nominal diameter of 2.5 mm.	170
4.12	Sketch of the setup for free rising bubble in linear shear.	172
4.13	Velocity field around sheared free rising bubbles, $\log(\mathcal{M}_0) = -5.3$, $\omega = -3.8$ 1/s.	173
4.14	Streak-lines coloured by velocity magnitude around sheared free rising bubbles, $\log(\mathcal{M}_0) = -5.3$, $\omega = -3.8$ 1/s.	173
4.15	Calculated and measured Reynolds number $\mathcal{R}e$ as a function of Eötvös number \mathcal{E}_o , $\log(\mathcal{M}_0) = -5.3$, $\omega = -3.8$ 1/s.	174
4.16	Bubble trajectories in the vertical $x - y$ plane for bubbles with nominal diameters between 2.84 and 5.54 mm, $\log(\mathcal{M}_0) = -5.3$, $\omega = -3.8$ 1/s.	175
4.17	Lift coefficient C_l as a function of time for bubbles with nominal diameters between 2.84 and 5.54 mm, $\log(\mathcal{M}_0) = -5.3$, $\omega = -3.8$ 1/s.	176
4.18	Calculated and measured lift coefficient C_l as a function of the Eötvös number \mathcal{E}_{oh}	177

5.1	Turbulence response function as a function of the phase fraction.	180
5.2	Results for the sudden enlargement test case: predicted profiles of the mean axial liquid velocity compared with experimental data.	182
5.3	Results for the sudden enlargement test case: predicted phase fraction profiles compared with experimental data.	184
5.4	Results for the sudden enlargement test case: predicted profiles of the turbulent kinetic energy of the continuous phase compared with experimental data.	185
5.5	Sketch of the setup for the plane mixing layer test case.	187
5.6	Results for the mixing layer test case: a) gas phase fraction α_a ; b) mean liquid velocity \bar{U}_b ; c) turbulent viscosity ν^t ; d) computational mesh. . .	190
5.7	Results for the mixing layer test case: predicted phase fraction profiles compared with experimental data.	191
5.8	Results for the mixing layer test case: predicted profiles of the mean liquid velocity in x -direction compared with experimental data.	192
5.9	Results for the mixing layer test case: predicted profiles of the turbulent kinetic energy of the liquid compared with experimental data.	194
6.1	Experimental values of the ratio C_d/C_{d0} and best fits to equation (6.80). a) Particles; b) Droplets; c) Bubbles.	222
6.2	Plot of $C_{d0} - Re_0$ and $U_{r0} - d$ from various drag correlations for bubbles in clean and contaminated water.	225
6.3	Comparison of the predictions of various drag correlations for particles with data set P1 ($Ar < 1$).	230
6.4	Comparison of the predictions of various drag correlations for particles with data set P2 ($Ar = 8.3 \times 10^2$).	231
6.5	Comparison of the predictions of various drag models for particles with data set P3 ($Ar \approx 1.6 \times 10^5$).	233
6.6	Comparison of the predictions of various drag correlations for particles with data set P4 ($Ar = 1.9 \times 10^6$).	234
6.7	Comparison of the predictions of various drag correlations for droplets with data set D1 ($30 < Ar < 91$).	237
6.8	Comparison of the predictions of various drag correlations for droplets with data set D2 ($1.1 \times 10^3 < Ar < 4.2 \times 10^3$).	239
6.9	Comparison of the predictions of various drag correlations for droplets with data set D3 ($3.5 \times 10^3 < Ar < 1.3 \times 10^4$).	240
6.10	Comparison of the predictions of various drag correlations for droplets with data set D4 ($8.6 \times 10^4 < Ar < 3.0 \times 10^5$).	241
6.11	Comparison of the predictions of various drag correlations for droplets with data set D5 ($3.4 \times 10^5 < Ar < 1.0 \times 10^6$).	242
6.12	Comparison of the predictions of various drag correlations for bubbles with data set B1 ($2.7 \times 10^5 < Ar < 7.8 \times 10^5$).	244
6.13	Plot of the normalised bubble velocity against turbulence intensity. . .	245
6.14	Comparison of the predictions of various drag correlations for bubbles with data set B2 ($2.7 \times 10^5 < Ar < 7.8 \times 10^5$).	246
6.15	Comparison of the predictions of various drag correlations for bubbles with data set B3 ($2.7 \times 10^5 < Ar < 7.8 \times 10^5$).	247

6.16 Comparison of the predictions of various drag correlations for bubbles with data set B4 ($2.7 \times 10^5 < Ar < 7.8 \times 10^5$)	248
6.17 Results for the mixing layer test case: predicted phase fraction profiles compared with experimental data.	251
6.18 Results for the mixing layer test case: predicted profiles of the mean liquid velocity in x -direction compared with experimental data.	252
6.19 Results for the sudden enlargement test case: predicted profiles of the mean axial liquid velocity compared with experimental data.	254
6.20 Results for the sudden enlargement test case: predicted phase fraction profiles compared with experimental data.	255
6.21 Relative difference in α calculated from equation (6.82) as a function of the liquid velocity $U_{b,x}$	256
7.1 Lift coefficient C_{lp} for a sphere in a linear shear flow as a function of the Reynolds number Re (from [212]).	265
7.2 Lift coefficient $C_{l\omega}$ calculated from equation (7.13) for a solid sphere in a linear shear flow as a function of the Reynolds number Re and the dimensionless shear rate Sr	268
7.3 Bubble trajectories in linear shear flows (from [388]).	271
7.4 a) Sketch of the experimental apparatus; b) Lift coefficient as a function of the bubble diameter (from [389]).	272
7.5 Trajectories and characteristic shapes of bubbles of five size classes in three glycerol-water solutions.	274
7.6 Lift coefficient as a function of the phase fraction. Original correlation by Beyerlein et al. [31] and the model developed in the present work. .	277
7.7 Contour plot of the dimensionless shear rate Sr	279
7.8 Contour plots of the lift coefficient for the sudden enlargement test case.	281
7.9 Results for the sudden enlargement test case: predicted phase fraction profiles compared with experimental data.	282
7.10 Results for the sudden enlargement test case: predicted profiles of the mean axial liquid velocity compared with experimental data.	284
7.11 Contour plots of the lift coefficient for the mixing layer test case.	285
7.12 Results for the mixing layer test case: predicted phase fraction profiles compared with experimental data.	286
7.13 Results for the mixing layer test case: predicted profiles of the mean liquid velocity in x -direction compared with experimental data.	287
7.14 Time sequence of the velocity fields around free rising air-water bubbles ($\log(Mo) = -11$) in linear shear flows with two different shear rates ($\omega = -10$ and -100 1/s).	290
7.15 Bubble trajectories in a horizontal $x - z$ plane and vertical $x - y$ plane ($\log(Mo) = -11$).	292
7.16 Magnitude of the relative velocity $-U_r$ and lift coefficient as functions of time ($\log(Mo) = -11$).	294
A.1 Sketch of an ellipsoid.	308
B.1 Forces on a dispersed phase element in a simple shear flow.	312

List of Tables

1.1	Relationship between the relative distance between the DPEs and the phase fraction.	51
1.2	Modelling approaches for drag at high phase fraction.	54
1.3	Overview of gas-liquid validation test cases.	68
1.4	Overview of liquid-liquid validation test cases.	69
2.1	Finite volume notation.	96
3.1	Multiplier terms in inter-phase momentum transfer term.	105
3.2	Coefficients in the two-phase $k - \varepsilon$ -model.	105
3.3	Boundary conditions applied to each equation for each boundary type. .	123
3.4	Two-phase numerical solution procedure.	124
3.5	Two-phase numerical solution procedure of Weller [423].	127
3.6	Under-relaxation factors λ used for the sudden enlargement test case. .	130
4.1	Interface-capturing numerical solution procedure.	162
4.2	Comparison of calculated and measured bubble rise velocities.	167
4.3	Comparison of calculated and measured velocity periods and amplitudes for a bubble with a nominal diameter of 2.5 mm.	171
6.1	Magnitudes of various terms in the model of Ishii and Zuber [168] . .	216
6.2	Coefficients in new correlations.	224
6.3	Data sets chosen for comparison with drag correlations for particles at high phase fraction.	229
6.4	Data sets chosen for comparison with drag correlations for droplets at high phase fraction.	236
6.5	Data sets chosen for comparison with drag correlations for bubbles at high phase fraction.	243
7.1	Experimental results obtained by Ford and Loth [104].	276
7.2	Parameters of the calculations and time-averaged results for the relative velocity and lift coefficient.	288

List of Animations

The CD-ROM accompanying this thesis contains the following animations:

1. Two-fluid methodology: phase fraction (iso-lines) and liquid velocity field (vectors) for the bubble plume test case. The air flow rate is 48 l/h.
2. Interface capturing methodology: velocity field (vectors) and iso-surface of the indicator function ($\gamma = 0.5$) for a free rising air bubble in water, $d = 2.5$ mm.
3. Interface capturing methodology: velocity field (vectors) and iso-surface of the indicator function ($\gamma = 0.5$) for a free rising air bubble in a linear shear flow, $d = 2.5$ mm, $\omega = 10$ 1/s.
4. Interface capturing methodology: velocity field (vectors) and iso-surface of the indicator function ($\gamma = 0.5$) for a free rising air bubble in a linear shear flow, $d = 2.5$ mm, $\omega = 100$ 1/s.

Nomenclature

Normal symbols represent scalar quantities and boldface symbols represent vector and tensor quantities. Generally, boldface Roman symbols represent vector and boldface Greek symbols represent tensor quantities, but this rule is not adhered too religiously. Dimensions and units are given in terms of the full SI set, *i.e.* mass (M) in kg, length (L) in meters (m), time (t) in seconds (s) *etc..*

Roman Symbols

Symbol	Description	Dimensions	Units
a	Cube edge length or matrix coefficient	L	m
a, b, c	half axes of the ellipsoid or bubble	L	m
A	Multiplier term in an inter-phase momentum transfer term or Area or amplitude	L^2	m^2
$[A]$	Square matrix of the coefficients		
\mathcal{A}	system of linear equations		
C	Dimensionless coefficient (<i>e.g.</i> for drag model)	—	1
C_f	Friction coefficient	$M/(L^3 t^3)$	$kg/(m^3 s^3)$
d	Diameter	L	m
\mathbf{d}	Vector between two cells centres	L	m
D	Tube diameter	L	m
$[D]$	Square matrix of the diagonal coefficients		
f	Function (<i>e.g.</i> Drag modifier)	—	1
\mathbf{f}	Acceleration vector due to body forces	L/t^2	m/s^2
F	Flux		
\mathbf{F}	Force vector (<i>e.g.</i> for drag force)	ML/t^2	N
\mathbf{g}	Acceleration vector due to gravity	L/t^2	m/s^2
$H(\mathbf{x}, t)$	step (Heaviside) function	—	1
\mathbf{I}	Identity tensor	—	1

Symbol	Description	Dimensions	Units
j	Drift flux	L/t	m/s
$J(\varepsilon)$	Function in lift model	—	1
k	Turbulent kinetic energy	L^2/t^2	J/kg
\mathbf{k}	Vector in the non-orthogonality treatment	L	m
K	Dimensionless coefficient	—	1
l, m	half axes of the ellipsoid or bubble	L	m
L	Turbulent length scale	L	m
\mathbf{M}	Interfacial momentum transfer rate vector	$M/(L^2t^2)$	kg/(m ² s ²)
\mathcal{M}	Discretised terms due to inter-phase momentum transport		
n	Dimensionless coefficient (<i>e.g.</i> for Drift flux model)	—	1
\mathbf{n}	Unit normal vector	—	1
$[N]$	square matrix of the off-diagonal coefficients		
p	Pressure	M/Lt^2	Pa
P	Production of turbulent kinetic energy	L^2/t^3	m ² /s ³
q	Turtuosity factor	—	1
R	Source		
\mathbf{R}	Reynolds stress (kinematic) tensor	L^2/t^2	m ² /s ²
$[R]$	Source vector		
S	Source term		
\mathbf{S}	Surface area vector	L^2	m ²
t	Time	t	s
T	Period	t	s
\mathcal{T}	Discretised terms due to transport		
\mathbf{U}	Velocity in a inertial frame of reference	L/t	m/s
U^*	Normalised velocity magnitude	—	1
V	Volume	L^3	m ³
\mathbf{V}	Velocity in a non-inertial frame of reference	L/t	m/s
w	width	L	m
\mathbf{x}	Spatial position vector	L	m
z	Cross-section factor	—	1

Greek Symbols

Symbol	Description	Dimensions	Units
α	Volume fraction	—	1
α^*	Phase fraction at close packing	—	1

Symbol	Description	Dimensions	Units
	or recombined value	—	1
β	Dimensionless coefficient (<i>e.g.</i> for C_t -model)	—	1
δ	Delta function or very small scalar value		
Δ	Difference		
Δ	Vector in the non-orthogonality treatment	L	m
η	Turbulent phase fraction diffusivity	L^2/t	m^2/s
ε	Turbulent kinetic energy dissipation rate	L^2/t^3	$J/kg s$
γ	Indicator function or blending factor	—	1
Γ	Diffusivity		
κ	Viscosity ratio or curvature of the interface	— $1/L$	1 $1/m$
λ	Under-relaxation factor	—	1
μ	Dynamic viscosity	M/Lt	Ns/m^2
ν	Kinematic viscosity	M^2/t	m^2/s
ω	Shear rate	$1/L$	$1/m$
ρ	Density	M/L^3	kg/m^3
ϱ	Density ratio	—	1
ϕ	tensorial quantity		
$[\phi]$	Column vector of dependent variable		
σ	Surface tension or Schmidt number	M/t^2 —	N/m 1
τ	Stress tensor	M/Lt^2	Pa
Θ	Moment of inertia	ML^4	kgm^4

Dimensionless Numbers

Symbol	Description	Definition
Ar	Archimedes number	$\frac{d^3 g \rho_c \Delta \rho }{\mu_c^2} = \sqrt{\frac{\mathcal{E}o^3}{\mathcal{M}o}}$
C_d	Drag coefficient	$\frac{F_d}{\frac{1}{2} \rho_c A U_r^2}$
\mathcal{C}_o	Courant number	$\mathcal{C}_o = \frac{\mathbf{U}_f \cdot \mathbf{S}}{\mathbf{d} \cdot \mathbf{S}} \Delta t$
$C_{l\nabla}$	Lift coefficient defined by Auton [10, 9]	$\frac{F_l}{\rho_c V \mathbf{U}_r \cdot (\nabla \mathbf{U}_c) }$

Symbol	Description	Definition
$C_{l\omega}$	Lift coefficient defined by Magnaudet [260]	$\frac{F_l}{\rho_c V \mathbf{U}_r \times (\nabla \times \mathbf{U}_c) }$
C_{lp}	Lift coefficient	$\frac{F_l}{\frac{1}{2} \rho_c A U_r^2}$
\mathcal{E}_o	Eötvös number	$\frac{g_{\text{eff}} \Delta \rho d^2}{\sigma}$
$\mathcal{D}\epsilon$	Deformation factor	$\frac{a - b}{a + b}$
\mathcal{G}	Morton number (original formulation)	$\frac{g_{\text{eff}} \mu_c^4}{\rho_c \sigma^3} = \frac{\rho_c}{ \Delta \rho } \mathcal{M}\mathcal{o}$
\mathcal{H}	Dimensionless group in drag model	
\mathcal{J}	Dimensionless group in drag model	
$\mathcal{L}a$	Laplace number	$\frac{\rho_c \sigma d}{\mu_c^2}$
$\mathcal{M}\mathcal{o}$	Morton number	$\frac{g_{\text{eff}} \mu_c^4 \Delta \rho }{\rho_c^2 \sigma^3}$
$\mathcal{R}e$	Reynolds number	$\frac{\rho_c U_r d}{\mu_c}$
$\mathcal{R}e_\nabla$	Shear Reynolds number	$\frac{\rho_c \nabla \mathbf{U}_c d^2}{\mu_c} = \mathcal{R}e \mathcal{S}r$
$\mathcal{S}r$	Dimensionless shear rate	$\frac{ \nabla \mathbf{U}_c d}{U_r}$
$\mathcal{S}t$	Stokes number	$\frac{\rho_d d^2 U_r}{18 \rho_c \nu_c L}$
$\mathcal{W}e$	Weber number	$\frac{\rho_c d U_r^2}{\sigma}$

Subscripts

Symbol	Description
\mathbf{Q}_a	\mathbf{Q} in phase a
\mathbf{Q}_α	Phase fraction
\mathbf{Q}_b	\mathbf{Q} in phase b or Basset
\mathbf{Q}_B	\mathbf{Q} at the boundary
\mathbf{Q}_c	\mathbf{Q} in the continuous phase or centre or compression

Symbol	Description
\mathbf{Q}_{cube}	\mathbf{Q} for a cube
\mathbf{Q}_d	\mathbf{Q} in dispersed phase or Drag
\mathbf{Q}_{DPE}	\mathbf{Q} for a dispersed phase element
\mathbf{Q}_E	Explicitly treated part
\mathbf{Q}_e	Eddy
\mathbf{Q}_{eff}	Effective \mathbf{Q}
\mathbf{Q}_f	\mathbf{Q} at face f or face interpolation
\mathbf{Q}_F	\mathbf{Q} of the moving frame of reference
\mathbf{Q}_h	Projected
\mathbf{Q}_{hyd}	Hydraulic
\mathbf{Q}_I	Implicitly treated part
\mathbf{Q}_l	Lift or left
\mathbf{Q}_{lat}	Lateral
\mathbf{Q}_m	Mixture or mixing
\mathbf{Q}_N	Value of \mathbf{Q} of neighbouring cell N
\mathbf{Q}_o	Other
\mathbf{Q}_P	\mathbf{Q} of cell P
\mathbf{Q}_φ	\mathbf{Q} in phase φ
\mathbf{Q}_ϕ	\mathbf{Q} of property ϕ
\mathbf{Q}_r	Relative \mathbf{Q} between two phases or right
\mathbf{Q}_{rise}	rise
\mathbf{Q}_s	Value of \mathbf{Q} for the spurious current
\mathbf{Q}_t	Turbulent
\mathbf{Q}_{vm}	Virtual Mass
\mathbf{Q}_w	Water or width
\mathbf{Q}_0	Single dispersed phase element

Superscripts

Symbol	Description
\mathbf{Q}^C	Calculated value
\mathbf{Q}^E	Value for an ellipsoid
\mathbf{Q}^C	Convective component
\mathbf{Q}^D	Diffusive component
$\mathbf{Q}^{E\&R}$	Data of Ellingsen-Risso
\mathbf{Q}^f	at the first time step
$\mathbf{Q}^{H\&R}$	Correlation of Hadamard-Rybczynski
\mathbf{Q}^{highRe}	high Reynolds number
\mathbf{Q}^{lowRe}	low Reynolds number
\mathbf{Q}^{Me}	Model of Mendelson
\mathbf{Q}^n	at the next time step
\mathbf{Q}^o	at the previous time step
\mathbf{Q}^{Sa}	Model of Saffman
\mathbf{Q}^{St}	Model of Stokes
\mathbf{Q}^t	Turbulent
\mathbf{Q}^{To}	Correlation of Tomiyama
\mathbf{Q}^T	Total convective component
\mathbf{Q}^*	Predicted \mathbf{Q} or modified \mathbf{Q} or smoothed \mathbf{Q}
\mathbf{Q}^\sharp	Corrected \mathbf{Q}

Oversymbols

Symbol	Description
$\overline{\mathbf{Q}}$	Ensemble average
\mathbf{Q}'	Fluctuations or value at the interface
$\hat{\mathbf{Q}}$	Value relative to the moving frame of reference

Chapter 1

Introduction

1.1 Background

In many diverse industries, including process, power, aerospace and transport, flows with two or even more phases are common practice and often such flows are the rule rather than the exception. Multi-phase flows are encountered in very different types of equipment such as transportation lines, stirred vessels, furnaces, distillation and bubble columns as well as engine injection and coolant systems. In most cases, the proper functioning of the equipment crucially depends on the existence of two-phase flow. In other cases, they are unwanted, but may simply not be possible or economically feasible to avoid. Therefore, the analysis and understanding of two-phase flows is of paramount importance if processes involving two-phase flows are to be optimally and safely designed and controlled.

The term “two-phase flow” covers an extremely wide range of flow patterns and regimes. It is useful to subdivide these into a small number of classes, to give a first impression of the physical processes involved. Two-phase flows are often broadly categorised by the physical states of the constituent components and by the topology of the interfaces. Thus, a two-phase flow can be classified as gas-solid, gas-liquid, solid-liquid, or in the case of two immiscible liquids, liquid-liquid. Similarly, a flow can be broadly classified topologically as separated, dispersed or transitional [29, 144, 165]. This variety of combinations makes the design of industrial equipment for two-phase flow applications a very difficult task.

In the process and associated industries it is usually difficult to obtain experimental data from existing industrial processes since they are often carried out at elevated temperatures and pressures or might employ hazardous substances. In addition, the disruption caused by the installation of the measuring devices is often intolerable. Hence, the design process traditionally relies on experimental pilot scale studies and empirical correlations [29, 139]. Pilot scale studies are carried out on a smaller scale and often at ambient temperature and pressure, as well as employing convenient modelling fluids. These experiments are usually expensive and time consuming. Furthermore, the use of pilot scale studies requires the use of scaling laws to the full-size plant, which may not be well established [29]. For two-phase flow applications, these difficulties are more pronounced because of the increased number of fluid properties as well as the variety of flow patterns and regimes. On the other hand, empirical correlations suffer from the disadvantage that the experimental information is encoded in an overall/global parametric form, which effectively conceals detailed localised information. The latter might be crucial for a successful design process.

From the above considerations, it is clear that the development of a methodology that predicts in considerable detail and with sufficient accuracy the entire flow field of a flow and, in particular, two-phase flow is highly desirable. Such a methodology exist in form of computational fluid dynamics (CFD). CFD is the analysis of engineering systems involving fluid flow, heat transfer and associated phenomena, such as two-phase flow, by means of computer-based simulation.

The development of CFD is part of a general trend in the move away from experimental studies and empirical correlations to more generally applicable and accurate mathematical models of engineering systems. Examples include computational solid mechanics [201, 107] and molecular dynamics simulations [198]. Such methodologies can be used with increasing confidence in areas outside those studied experimentally. Moreover, a far broader in-depth insight into the process can be gained. Overviews of application of CFD in the process and associated industries are given in [119, 46, 392, 207, 156, 198]. It should be noted that CFD and other numerical methods are still under development in many ways and will continue to be so for the foreseeable future. However, at their present state they go a long way towards meeting

some of the requirements posed upon them. In addition, experimental and empirical methods are still being developed further. All of these methods are complimentary and benefit each other.

Up to now, the development of CFD methodologies for dispersed two-phase flows has been focused on relatively low volume fractions (< 10%) of the dispersed phase. However, a number of important industrial processes are carried out at higher volume fractions. For example, bubble columns, mixer vessels and the production of liquid-liquid emulsions like margarine which operate at volume fractions of up to 90%.

The prediction of these processes poses additional problems: firstly, the physical processes such as inter-phase momentum, heat and mass transfer as well as turbulence effects are not well understood; and secondly, the flow regime might change when the volume fraction of the dispersed phase is very high. The results of this transition might be an inversion or a complete separation of the phases. Phase inversion and separation occur either by design or by accident in many industrial processes.

Phase separation processes are common in the chemical industry. Such processes are often employed to isolate products from unwanted by-products, *e.g.* in gravity settlers, bubble and distillation columns. These processes are relatively well researched and understood due to their widespread use. However, there are secondary effects which require further clarification. For example, the prediction of the entrainment of drops into the gas streams of bubble and distillation columns.

On the other hand, phase inversion is usually unwanted and occurs, for example, when a liquid/liquid process is operated at very high volume fraction of the dispersed phase. The addition of very little amounts of dispersed phase or changes in the operating conditions result in a rapid inversion of the phases, *i.e.* the dispersed phase suddenly becomes continuous and vice-versa. Examples can be found in the food industry and include the manufacture of many low-fat spreads and margarine. The understanding of phase inversion is limited as the detailed physics is not well understood and this is why the design of industrial devices has to rely on trial and error in dealing with phase inversion.

In both, phase inversion and separating flows, regions where the originally dispersed phase becomes the continuous phase and vice versa exist simultaneously. Be-

tween such regions thin transition regions exist, which are referred to as free-surfaces in this study. At free-surfaces, rapid changes in the flow properties occur. The representation of such singularities in a numerical method is often troublesome and many numerical techniques have been devised for this purpose. However, they usually increase the complexity of the numerical solution procedure.

The remainder of this Chapter is structured as follows: In the following section, three well-known CFD methodologies for the prediction of the dynamics of two-phase flows are introduced, two of which are extensively used and developed further in this study. Then, the objectives of this work are stated in Section 1.4. The objectives are followed by a list of the specific contributions made to the field. Next, Section 1.5 reviews previous and related studies and, finally, an outline of the contents of Chapters 2 to 7 is given in Section 1.6.

1.2 CFD Methodologies for Two-Phase Flow

Any numerical methodology consists of a model and a solution procedure. A model is a mathematical representation, *i.e.* a set of equations, of the physical and/or chemical process to be predicted or simulated. Models usually neglect some less important or less influential phenomena. The solution procedure specifies the details about how to obtain an approximate solution to the model equations numerically.

The dynamics of many two-phase flows encountered in engineering applications are adequately modelled by the Navier-Stokes equations augmented by a Newtonian law of viscosity and an equation of state. Heat and mass transfer as well as chemical reactions and phase changes are not considered in this study. The description is general in the sense that it is not restricted to a particular flow regime, *e.g.* laminar/turbulent or dispersed/separated. In principle, it is possible to obtain a numerical solution based on this model by direct numerical simulation. However, further simplifications might be needed in order to reduce the complexity of the final mathematical model.

1.2.1 Direct Numerical Simulation

In a Direct Numerical Simulation (DNS) of a two-phase flow, the Navier-Stokes equations are employed without further manipulation and the topology of the interface between the two-phases is determined as part of the solution. No additional modelling assumptions are introduced.

DNS requires very high resolution in order to resolve a broad range of temporal and spatial scales. These scales are associated with the topology of the interface, *e.g.* the size of the Dispersed Phase Element¹ (DPE), or with the fluid motion, *e.g.* the eddies encountered in the turbulent motion. Resolving these scales is computationally expensive both in terms of computer memory size execution time. Therefore, DNS is restricted to low Reynolds numbers and a few DPEs due to its high computational cost.

Special numerical techniques are needed to keep track of the position of the interface between the phases. These techniques are often referred to as free surface solution procedures. Many of these have been devised and they are classified and explained in more detail in Section 1.5.1.

DNS of two-phase flow has been employed mainly by the research community because of the in-depth insight which can be gained from its results. The applications often involve only single DPEs [333, 71, 385, 53, 76, 49] because of the restrictions mentioned above. However, many applications are focused on the simulation of complex phenomena such as primary break-up of liquid jets [375, 438], secondary break-up of drops [132], variable surface tension effects due to temperature gradients or presence of surfactants [290, 180, 181], deformation of fluid particles in shear flow [388, 281, 91, 373, 253, 371] as well as phase change [390, 22, 48, 192, 193]. The interaction of many DPEs has been investigated by [92, 93, 94, 42, 188, 157, 158].

The applications mentioned above deal with laminar flows. However, virtually all flows of practical interest are turbulent, mainly caused by the large scale of the equipment. Unfortunately, DNS of turbulent flows is not feasible as part of the engineering design process due to the fact that turbulent flows exhibit an enormous range

¹In this study we use the term “Dispersed Phase Element” for bubbles, droplets and particles and the term “fluid particle” for bubbles and droplets

of spatial (and temporal) scales. These scales range from the Kolmogorov length scale to the size of the equipment under consideration and it is not feasible to resolve all these scales in a numerical simulation due to limited computer resources.

Therefore, it is doubtful that DNS will become widespread in industrial applications in the near future. However, its utility lies in the investigation of complex phenomena as well as the validation and development of models for the interaction of DPEs with the surrounding fluid. It is the latter application for which DNS is adopted in this study.

Fortunately, the level of detail provided by DNS is not necessary in many engineering applications. For most purposes of equipment or process design, macroscopic information about the flow field is sufficient. Practical simulations of turbulent flows are therefore carried out using conservation equations which describe the mean properties of the flow. Of course, turbulent fluctuations and the details of the two-phase flow need to be accounted for to the extent that they affect the mean flow properties. In this way, the computational effort needed to obtain a solution can be greatly reduced and a solution can be obtained in a reasonable time span.

In mathematical terms, a macroscopic description is obtained by taking suitable averages of the microscopic conservation equations. Due to the loss of information associated with the averaging process, additional terms appear in the averaged equations which require closure, *i.e.* have to be expressed in terms of known, mean variables. For example, averaging the Navier-Stokes equations yields the Reynolds stresses, which have to be expressed through a turbulence model.

Several models have been devised to describe two-phase systems on a macroscopic level. Two well-known models are outlined next.

1.2.2 Discrete DPE Model

The dispersed DPE model assumes that the topology of the two-phase flow is dispersed. The two phases are therefore referred to as the continuous and the dispersed phase. A macroscopic description of the dispersed phase is obtained by replacing the microscopic conservation equations with a discrete formulation. In this discrete formulation, the dispersed phase is represented by individual DPEs, which are tracked through the

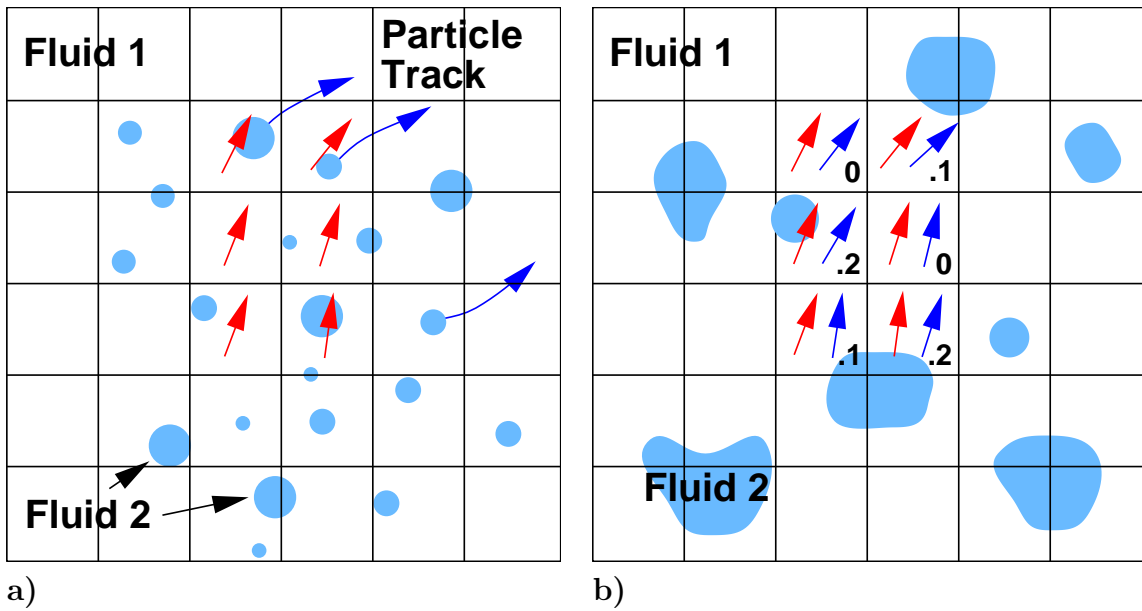


Figure 1.1: Averaged modelling approaches for two-phase flow: **a)** discrete DPE (Euler-Lagrange) model and **b)** two-fluid (Euler-Euler) model.

flow domain by solving an appropriate equation of motion. The equation of motion is the conservation equation of momentum expressed in the Lagrangian formulation, in which the dependent variables are the properties of material particles that are followed in their motion. On the other hand, the conservation equations for the continuous phase are expressed in the Eulerian frame, where the fluid properties are considered as functions of space and time in an absolute (or inertial) frame of reference. Because of this mixed treatment of the two phases, the discrete DPE model is also referred to as the Euler-Lagrange model.

The model is depicted in Figure 1.1a. As mentioned earlier, an Eulerian description is used for the continuous phase (here Fluid 1). This is denoted by the velocity vectors (red), which are located at the cell-centres of the computational mesh used for the CFD solution. The trajectories of the DPEs (here Fluid 2) are shown in blue.

In most applications of practical interest, the wide range of temporal and spatial scales encountered in turbulent flows precludes DNS of the microscopic conservation equations for the continuous fluid. Hence, the averaged Navier-Stokes equations accompanied by a suitable turbulence model are employed. The averaging removes small scale fluctuations from the model. However, the effect of these fluctuations on the dispersed phase have to be taken into account if, for example, the dispersion of small particles

is to be predicted accurately. They are re-introduced through stochastic models which add local fluctuations on top of the mean values, *e.g.* [120, 81, 298, 440, 30, 122].

For sufficiently dilute suspensions, where the particle size is small, the influence of the dispersed phase on the motion of the continuous phase can be neglected. The coupling between the phases is then said to be one-way. However, the matter is somewhat complicated if the motions of the continuous and the dispersed phase are closely coupled, *i.e.* the continuous phase influences the motion of the DPEs and vice versa. This two-way coupling can be taken into account in the discrete DPE model with relative ease and is done by accounting for the influence of the dispersed phase in the momentum equation and the turbulence model of the continuous phase [65, 205].

An important advantage of the discrete DPE model lies in the possibility to store properties of the dispersed phase, *e.g.* size, shape or rotational speed, separately for each DPE. The effects of these properties on the DPE's motion are accounted for in the equation of motion, which is solved separately for each DPE. Of course, other physical and/or chemical processes such as heat and mass transfer can be included accordingly. In this way the distribution of properties in the ensemble as well as the cross-correlations between properties can be modelled accurately. Therefore, the discrete DPE model is well suited for cases where an accurate predictions of property distributions and cross-correlations is essential, *e.g.* evaporating droplets or combusting coal particles.

However, problems arise when the phase fraction of the dispersed phase is high. The first problem is that the computational effort required for the dispersed phase is proportional to the number of DPEs because each DPE requires the solution of its equations of motion. The problem can be circumvented by calculating the motion of a finite number of computational parcels, each containing DPEs possessing the same characteristics such as size, velocity, shape *etc..* However, the number of DPEs in a parcel may have a marked effect on some of the obtained statistics, as shown by [86, 205]. Secondly, for moderate to high phase fractions, the increased coupling between the DPEs and the continuous phase can introduce numerical stability problems [205], which are difficult to handle in a mixed Euler/Lagrange framework.

The discrete DPE model has been successfully applied to low volume fraction gas-

solid dispersed flows such as particle laden jets (*e.g.* [63, 81, 355, 65]), fuel injection systems (*e.g.* [80, 169, 205]) and bubble columns (*e.g.* [420, 285, 224, 223, 256, 77, 218]).

1.2.3 Two-Fluid Model

In the two-fluid model, both phases are described using Eulerian conservation equations. Hence, the model is also referred to as the Euler-Euler model. Each phase is treated as a continuum, each inter-penetrating each other, and is represented by averaged conservation equations. The averaging process introduces the phase fraction α into the equation set, which is defined as the probability that a certain phase is present at a certain point in space and time [147].

Figure 1.1b shows a sketch of the two-fluid model. The velocity of each phase is represented by one set of velocity vectors, which are shown in red and blue for fluid 1 and 2, respectively. The phase fraction of the dispersed phase is shown by small numbers in the lower right corners of the cells.

Due to the loss of information associated with the averaging process, additional terms appear in the averaged momentum equation for each phase, which require closure. In addition to the Reynolds stresses, which enter into the averaged single-phase flow equations, an extra term that accounts for the transfer of momentum between the phases appears. This term is known as the averaged inter-phase momentum transfer term and accounts for the average effect of the forces acting at the interface between continuous phase and the DPEs.

The two-fluid methodology is applicable to all flow regimes, including separated, dispersed or intermediate regimes, since the topology of the flow is not prescribed. However, the formulation of the inter-phase momentum transfer term and the two-phase turbulence model is the crux of the two-fluid methodology because it depends on the exact nature of the flow. Consequently, the resulting predictive capabilities relies heavily on them.

The derivation of the average inter-phase momentum transfer term starts from instantaneous momentum transfer term. The main components of this term are due to the drag, lift and virtual mass forces acting at the interface between the two phases. The relationships for drag and lift are the subject of this study and a review of the

physical phenomena and modelling approaches are given in Sections 1.5.3 and 1.5.5.

It has been noted, that the dispersed DPE model allows quite naturally to represent additional dispersed phase properties, *e.g.* size, shape and temperature, as well as their effect on the continuous phase. This is more difficult in the two-fluid model because the conservation equations, *e.g.* for the dispersed phase enthalpy, are employed in averaged form and extra terms, similar to those encountered in the averaged phase momentum equations, appear during their derivation, which require closure. Additional problems arise if the distribution of a property is to be represented, *e.g.* size distributions. Two approaches can be employed in an Eulerian framework to represent the Probability Density Function (PDF) of a property: firstly, the PDF can be discretised into a discrete number of classes (population balance). In this case, a transport equation for the probability of each class is solved. Secondly, the form of the PDF can be presumed beforehand and a transport equation for each parameter of the presumed distribution is solved. In both cases, the effects of the property distribution on the average inter-phase transfer term have to be account for.

In the process and associated industries, the size distribution of the DPEs is often very important for two reasons: firstly, it might be part of the specification of the final product and, hence, the quality of the product depends on it; and secondly, all inter-phase transport phenomena are governed by the mean area concentration, which is determined by the size distribution. Over the last ten years, several approaches of varying complexity have been proposed to account for size distributions of DPEs within the two-fluid model [238, 250, 126, 259, 147].

However, it should be noted that the two-fluid model, by definition, incorporates two-way coupling and, despite the other complexities, is the preferred method for engineering applications, especially when the phase fraction is high. For these reasons the two-fluid model is adopted in this study.

1.3 Objectives of this Work

The research presented in this study formed part of a larger research project² carried out under the auspices of the EEC BRITE/EuRam programme. This project involved three companies in the chemical and food industry, a commercial CFD software company and three academic institutions.

In a precursor BRITE project³, research was focused on dispersed two-phase flow at relatively low phase fractions (< 10%) of the dispersed phase. As mentioned in Section 1.1, many important industrial processes are carried out at higher phase fractions. Therefore, the overall aim of the present BRITE project was to produce validated predictive methods applicable to two-phase flow at high phase fractions, eventually to be embodied in a commercial CFD code for the design of two-phase chemical processes. Since the industrial partners are mostly interested in dispersed gas-liquid and liquid-liquid flows, the project concentrated on these systems.

There were many aspects to the projects mentioned above, including theoretical studies into local physical effects and experimental studies to provide suitable data for validation purposes. These investigations culminated in the formulation of suitable mathematical models, which were then integrated into a commercial multi-purpose CFD code.

The principle objectives of the study described in this thesis are as follows:

- Development of an improved numerical solution technique for the two-fluid model applicable to the full range of phase fraction. The new solution technique should combine numerical stability and computational efficiency, especially in situations where phase inversion or complete separation occur;
- Determination of suitable physical models to close the two-fluid model, again over the full range of phase fraction. Such models include those describing drag, lift and turbulence effects for liquid-liquid and gas-liquid systems. Correlations for solid-liquid systems are included in this study because the examination of these

²Project number BE 4322 – Development of a Computational Code for the Design of Multi-Phase Processes at High Phase Fractions.

³Project number BE 4098 – The Development of Validated Predictive Models for the Optimal Design of Multi-Phase Chemical Processes.

systems has been found very useful in order to understand the more complex physics associated with systems of fluid particles (see footnote (1) on page 29);

- Critical evaluation of the methodology with reference to the experimental data provided by the project partners and additional data obtained from the literature.

1.4 Present Contributions

This study is concerned with the simulation of dispersed two-phase flow at high phase fractions, excluding heat and mass transfer as well as phase change. It presents the author's contribution, which is a continuation of the efforts made by the author's predecessors and colleagues at Imperial College during the past decade, *e.g.* Politis [310], Oliveira [294], Hill [147], Ubbink [403], Weller [426, 424], Brennan [39]. Their contributions are related to the modelling of solid-liquid [310, 39], liquid-liquid [147] and gas-liquid [294, 147] dispersed flows mostly at low phase fractions as well as the development and validation of improved solution procedures [310, 294, 147, 403, 426, 424, 39].

The following specific contributions have been made in this study:

- A review and analysis of the literature with respect to:
 - Modelling of phenomena encountered in dispersed two-phase flow at high phase fractions, especially drag and lift;
 - Numerical methodologies for the solution of the two-fluid model;
 - Numerical methodologies for the DNS of two-phase flow;
 - Test cases suitable for the validation.
- Research related to the DNS of two-phase flow:
 - Implementation and testing of a novel interface-capturing methodology;
 - Validation against experimental data: calculation of a free rising air bubble in water. Results for different bubble diameters are obtained;
 - Validation against experimental data: calculation of a free rising air bubble in linear shear flow. Here, the viscosity of the surrounding fluids is much

larger than that of water and the effects of different liquid viscosities and bubble sizes are shown.

- Research related to the modelling of drag at high phase fractions:
 - Formulation of a new drag model applicable to high values of the phase fraction;
 - Validation of the new drag model against experimental data for sudden enlargement and plane mixing layer flows using the two-fluid methodology.
- Research related to the modelling of lift:
 - Performance of DNS of a free rising air-water bubble in linear shear flow to gain insight into the lateral motion of bubbles in this type of flow. Different shear rates and bubble diameters are investigated;
 - Validation of existing and improved lift models against experimental data for sudden enlargement and plane mixing layer flows using the two-fluid methodology.
- Research related to the modelling of two-phase turbulence at high phase fractions:
 - Formulation of an improved model for the turbulence response function C_t applicable to high values of the phase fraction;
 - Validation of the new C_t -model against experimental data for sudden enlargement and plane mixing layer flows using the two-fluid methodology.
- Research related to the two-fluid methodology:
 - Implementation and testing of an improved numerical algorithm for the two-fluid methodology which improves stability and convergence in situations where the phase fraction is high;
 - Assembly and implementation of improved models for the inter-phase momentum transfer term suitable for higher phase fractions;
 - Validation against experimental data: calculation of sudden enlargement, plane mixing layer, separation tank and bubble column flows.

1.5 Previous and Related Studies

An overview of the literature relevant to this study is presented next. In the first two Sections, the solution procedures for the two-fluid model and for the direct numerical simulation of two-phase flow are reviewed. Then, the physics and modelling approaches related to the drag and lift forces on DPEs in dispersed two-phase flow as well as turbulence are presented. However, it should be noted that detailed reviews of the individual drag and lift models are presented later in Chapters 6 and 7. Finally, validation test cases for the two-fluid methodology are reviewed in Section 1.5.7.

1.5.1 Solution Procedures for the DNS of Two-Phase Flow

Free-surface methodologies are numerical solution techniques for the prediction of two-phase flows where the topologies of the interfaces are also outcomes of the solution. Extensive reviews of such methods can be found in [349, 347, 99, 395, 339, 321, 102, 266]. Free-surface methodologies can be classified into surface tracking, moving mesh and volume tracking methods [266]:

Surface Tracking Methods define a sharp interface whose motion is followed. The interface is marked and tracked, either with a height function [292, 99, 96] or a set of marker particles/segments (see Figure 1.2a) [115, 114, 406, 311].

Moving Mesh Methods associate the interface with a set of nodal points of the computational mesh. In this way, a sharp interface is maintained. The mesh might be adjusted to fit the interface (interface-fitted mesh methods, see Figure 1.2b) [333, 374, 243, 378, 433, 53, 99] or following the fluid (Lagrangian methods) [106, 108, 188].

Volume Tracking Methods do not define the interface as a sharp boundary. Rather, the different fluids are marked either by massless particles [137, 136, 68, 69, 204] or by an indicator function, which may be a volume fraction (see Figure 1.2c) [155, 404, 49], a level set [300, 367] or a phase-field [176, 288].

Moving mesh and surface tracking methods maintain the exact position of the interface, which simplifies the analysis near the interface. On the other hand, the

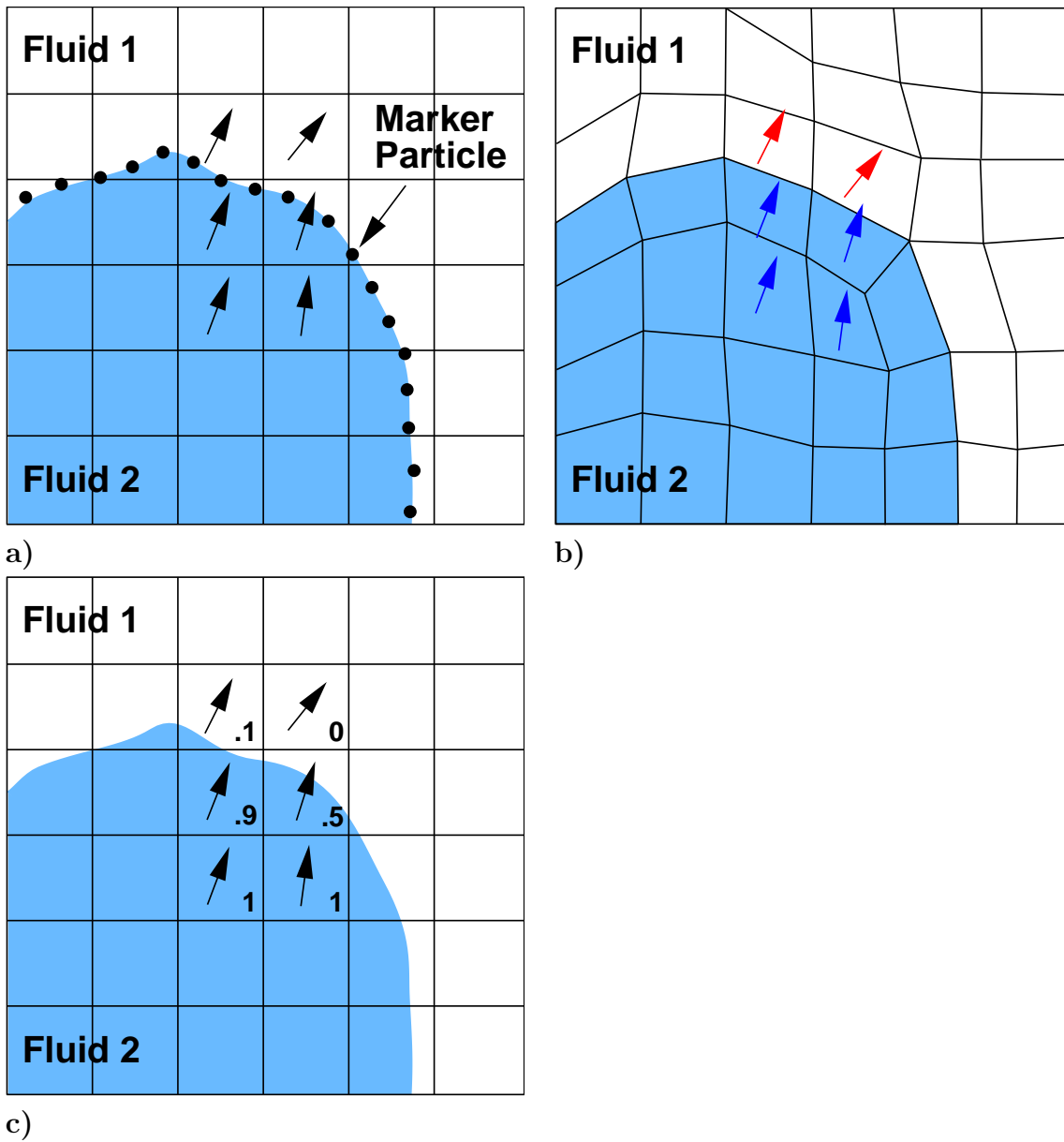


Figure 1.2: Free-surface methodologies: **a)** surface tracking method with marker particles on the interface (Front-tracking method); **b)** moving mesh method (Interface-fitted mesh method); **c)** volume tracking method where the fluids are marked by the volume fraction field.

mesh/marker particles/segments have to be relocated and eventually re-meshed, when the interface undergoes large deformations, which adds additional complexity. Another drawback of these methods is that they require intervention to handle topological changes, *e.g.* the merging of two interfaces [394, 395].

Surface tracking methods have the advantage that the representation of the surface is independent of the representation of the flow field. Hence, the resolution of the surface and that of the flow field may be chosen independently. Of course, the level of

detail should be comparable in order to resolve the fluid motion properly. However, this freedom is helpful, for example, in order to improve the accuracy of the evaluation of the surface tension force by increasing the resolution of the interface. However, surface tracking methods have the disadvantage that they do not strictly conserve the volume of each fluid [395], whereas conservation can be enforced in some volume methods (when a volume fraction is used) and in some moving mesh methods.

In volume methods, an indicator function (volume fraction, level set or phase-field) is used to represent the interface and one is confronted with the question how to convect the interface without diffusing, dispersing or wrinkling it. This is particularly troublesome, when the volume fraction is chosen as an indicator function because the convection scheme has to guarantee that the volume fraction stays bounded, *i.e.* remains within its physical bounds of 0 and 1. This problem has been addressed by a number of authors and two distinct methodologies to convect the volume fraction have emerged: volume-of-fluid (VOF) methods utilise convection schemes which reconstruct the interface from the volume fraction distribution before advecting it [155, 437, 6, 321, 331, 49]. On the other hand, interface-capturing techniques use high-order convection schemes [403, 404, 57, 432, 74].

The surface tension term in the Navier-Stokes equation creates additional difficulties because it is a singular term. These difficulties manifest themselves in numerical instabilities and/or numerical noise as well as poor representation of capillary effects. In surface tracking and moving mesh methods, the surface tension force can be evaluated directly from the discrete representation of the interface.

On the other hand, in volume methods, the exact position of the interface is unknown and the location of the interface is often represented by an indicator function. Here, the Continuum Surface Force (CSF) formulation by Brackbill et al. [37] is used to calculate the surface tension force from the distribution of the indicator function.

An often reported problem is the existence of the so-called spurious “currents” in the flow field of the numerical simulations [214, 311, 431, 403]. These currents are vortices which appear in the neighbourhood of interfaces despite the absence of any external forces. Lafaurie et al. [214] (see [339]) showed that the Reynolds number based on magnitude of the largest spurious currents $\mathcal{R}e_s$ around a bubble/drop is proportional

to the Laplace number $\mathcal{L}a$:

$$K\mathcal{R}e_s = \mathcal{L}a \quad (1.1)$$

where the Laplace and Reynolds numbers are defined as:

$$\mathcal{L}a = \frac{\sigma \rho d}{\mu^2} \quad (1.2)$$

$$\mathcal{R}e_s = \frac{U_s \rho d}{\mu} \quad (1.3)$$

Here, μ , ρ and σ are the dynamic viscosity, density and surface tension, respectively. d and U_s stand for the bubble/drop diameter and the velocity magnitude of the largest spurious current.

They gave $K = 100$ for their algorithm and computations became difficult when $\mathcal{L}a$ exceeds 10^6 , which occurs, for example, for a 14 mm air-water bubble or drop. Scardovelli and Zaleski [339] also reported that the problem is less pronounced in the marker method of Tryggvason and coworkers where K appears to be around 10^5 .

1.5.2 Solution Procedures for the Two-Fluid Model

Various solution procedures have been proposed to solve the set of coupled differential equations arising in the two-fluid models. Most of them use segregated approaches, in which the set of equations is solved sequentially. Some authors have proposed other solution techniques which utilise Riemann [360] or partial block solution [229, 228] techniques to handle the coupling between the equations in a more implicit manner. These techniques have not been investigated in this study, since they are often very demanding in terms of computational time, memory requirements and code complexity.

Focusing on segregated approaches for two-phase flows, a number of different methodologies can be identified in the literature, *e.g.* IPSA [357], BRITE [310, 147], ASTRID [376], two-phase ICE [196] and two-phase SOLA [152]. Among these there is little agreement concerning either the form of the equations to be solved or the solution procedure. However, certain similarities exist, for example, the use of the continuity equation in order to derive an equation for the pressure. The pressure change is then utilised to correct the velocities.

In this study, we adopt the modifications of Weller [426] to the BRITE solution procedure. In addition, further improvements are proposed to make the solution procedure more stable. This is discussed in detail in Section 3.2.

1.5.3 Modelling Drag

One of Newton’s important studies was on the laws governing the free-fall of particles in air. He measured the terminal velocity of particles with different diameters dropped from St. Paul’s Cathedral in London [291]. He then derived a relationship for the particle drag as a function of the particle diameter and terminal velocity and found that the drag force on the particle is proportional to the square of the terminal velocity. This relationship was later extended to include the effects of different densities of the particle and the fluid as well as different fluid viscosities, *e.g.* [2, 340, 225].

Theoretical work on this subject started with the analytical work of Stokes [363]. He neglected the non-linear convection term in the Navier-Stokes equations and found that the drag force is proportional to the terminal velocity. The solution is only valid when the influence of convection can be neglected with respect to diffusion, *i.e.* for the creeping flow. His work was later extended by including the convection terms in linearised form, *e.g.* Oseen [299] (see [56]). Since then, progress to obtain an analytical solution has stalled due to the complexity of the flow surrounding a sphere in all but the simplest flow regimes.

However, numerical methods provide means to obtain approximate solutions to the Navier-Stokes equations, *e.g.* [325, 164, 105]. These direct numerical simulations provide valuable information about the drag on a sphere at intermediate flow speeds, but become increasingly expensive for turbulent flows for the reasons given in Section 1.2.1. Hence, most of the knowledge about the effect of free stream turbulence on the drag force of a spherical particle has been obtained experimentally, *e.g.* [55, 1].

The results of all of these studies are usually presented in non-dimensional form as the “standard drag curve” depicted in Figure 1.3. In this representation, the drag coefficient C_d is plotted as a function of the Reynolds number $\mathcal{R}e$, where the former is defined for a single DPE in an infinite medium as the drag force on the DPE divided

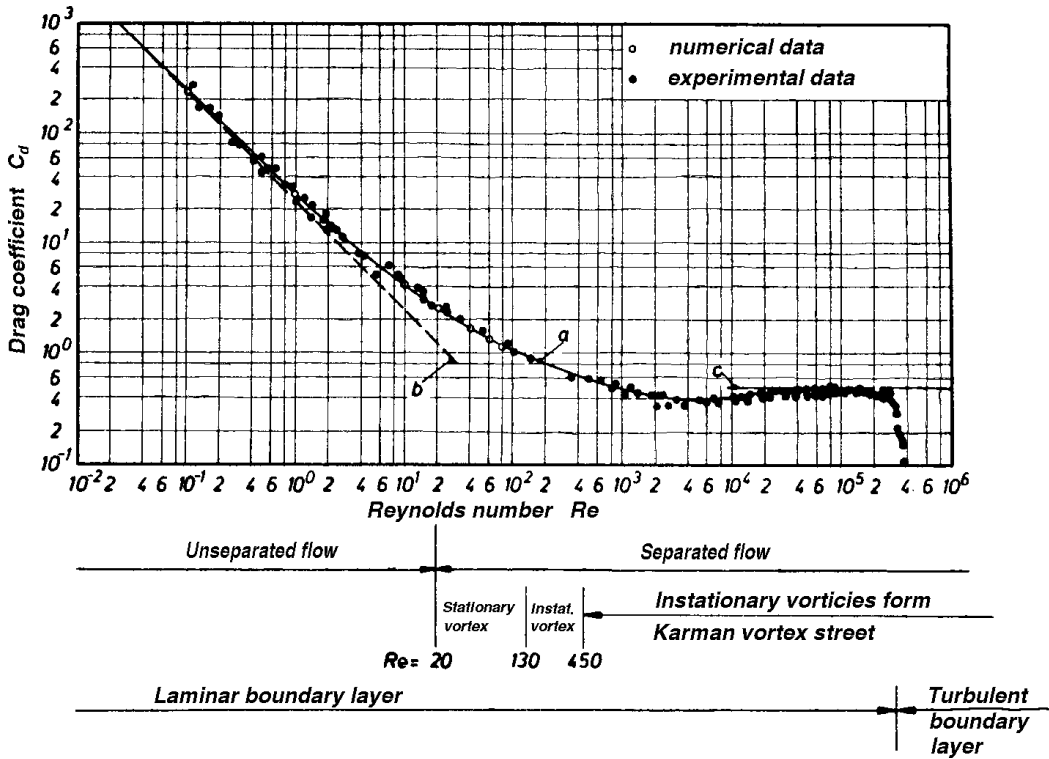


Figure 1.3: Drag coefficient as a function of the Reynolds number for solid spheres: **a)** Brauer [38]; **b)** Stokes' law [363] $C_d = \frac{24}{Re}$; **c)** Newton's law $C_d = 0.44$ (from [273]).

by the dynamic pressure force, thus:

$$C_d = \frac{F_d}{\frac{1}{2}\rho_c A U_r^2} = \frac{\text{Drag force}}{\text{Dynamic pressure force}} \quad (1.4)$$

and Re is given as:

$$Re = \frac{\rho_c U_r d}{\mu_c} = \frac{\text{Inertia}}{\text{Viscous}} \quad (1.5)$$

Here, μ_c and ρ_c are the dynamic viscosity and density of the continuous phase, respectively. F_d and U_r are the magnitudes of the drag force \mathbf{F}_d and the relative velocity between the phases \mathbf{U}_r , where the latter is defined as $\mathbf{U}_r = \mathbf{U}_c - \mathbf{U}_d$. A stands for the projected area of the DPE normal to \mathbf{U}_r . For fluid particles, but also irregular shaped particles, it can be difficult to determine A . Therefore, A is often calculated from $A = \pi \frac{d^2}{4}$, where d is the nominal diameter, *i.e.* diameter of a sphere having the same volume V as the DPE. Hence, the influences of the shape, deformation or orientation of the DPE on the projected area are neglected.

The laws of Stokes and Newton are also plotted in Figure 1.3. The drag coefficient is inversely proportional to the Reynolds number for low Reynolds numbers (Stokes'

law), whereas for high Reynolds numbers it is independent of it (Newton's law). Also shown are experimental and numerical data points from various sources as well as the drag curve due to Brauer [38].

Visualisation experiments and numerical simulations provide valuable insight into the flow structure around spheres. In the lower part of Figure 1.3, several well-known flow regimes are listed. They can be characterised as follows:

- $\mathcal{R}e < 20$: unseparated flow; laminar boundary layer
- $20 < \mathcal{R}e < 130$: separated flow; steady, laminar wake; laminar boundary layer
- $130 < \mathcal{R}e < 450$: separated flow; unsteady, laminar wake; Kármán vortex street; laminar boundary layer
- $450 < \mathcal{R}e < 3 \times 10^5$: high sub-critical flow; laminar boundary layer
- $\mathcal{R}e > 3 \times 10^5$: critical transition and supercritical flow; turbulent boundary layer

It should be mentioned that a similar sequence of regimes occurs in the flow around most bodies.

The physics of the flow around fluid particles¹ differs in two ways from that around particles. Firstly, the momentum transfer from the continuous fluid results in circulation inside the fluid particle (internal circulation); and secondly, their shape is not fixed.

For solid particles, the drag coefficient depends only on the characteristics of the flow surrounding the particle and is primarily a function of the particle Reynolds number and the turbulence intensity of the continuous phase. In the case of fluid particles the drag coefficient is also dependent on the other fluid properties characterised by the Eötvös $\mathcal{E}o$ and Morton $\mathcal{M}o$ numbers as well as the ratios of the fluid densities ϱ and viscosities κ . These dimensionless groups are defined as:

$$\mathcal{E}o = \frac{g_{\text{eff}} |\Delta\rho| d^2}{\sigma} = \frac{\text{Gravity}}{\text{Surface Tension}} \quad (1.6)$$

$$\mathcal{M}o = \frac{g_{\text{eff}} \mu_c^4 |\Delta\rho|}{\rho_c^2 \sigma^3} = \text{Material Group} \quad (1.7)$$

$$\varrho = \frac{\rho_d}{\rho_c} \quad (1.8)$$

$$\kappa = \frac{\mu_d}{\mu_c} \quad (1.9)$$

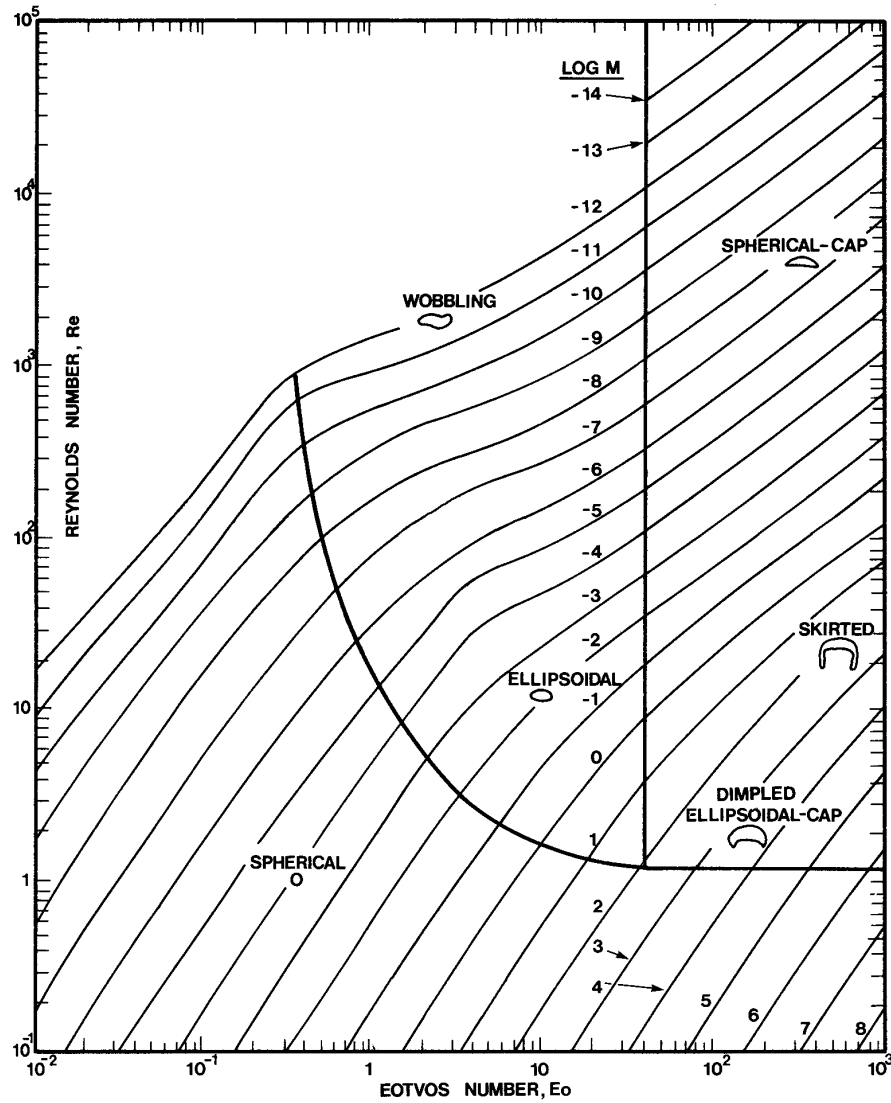


Figure 1.4: Shape regimes of fluid particles in unhindered gravitational motion through liquids (from [56]).

where σ is the surface tension and $\Delta\rho$ is the density difference between the continuous and dispersed phases, *i.e.* $\Delta\rho = \rho_d - \rho_c$. g_{eff} is the magnitude of the effective acceleration given by $g_{\text{eff}} = |\mathbf{g}_{\text{eff}}| = |\mathbf{g} - \frac{D_c \mathbf{U}_c}{Dt}|$ where $\frac{D_\varphi}{Dt}$ stands for the substantive derivative, *i.e.* $\frac{D_\varphi}{Dt} = \frac{\partial}{\partial t} + \mathbf{U}_\varphi \cdot \nabla$. The effective acceleration takes into account the acceleration of the continuous fluid which can be appreciable, *e.g.* in vicinity of the mixer blades of a stirred tank. Note that the Morton number \mathcal{M}_o is only a function of the fluid properties for fluid particles in quiescent liquids. It is a strong function of the viscosity of the continuous phase, which enters with a power of four. Its value ranges from 9.4×10^4 to 3.1×10^{-12} for air bubbles in corn syrup and hot tap water, respectively.

Figure 1.4 shows the characteristic shapes of fluid particles rising in a quiescent

fluid as a function of the Eötvös and Morton numbers. The diagram also gives the Reynolds number based on the terminal velocity as a function of the same parameters. It is apparent that for low \mathcal{E}_o , *e.g.* for small fluid particles, a spherical shape is retained, whereas for high \mathcal{E}_o the bubble takes an ellipsoidal or largely deformed shape. This effect is more pronounced for low \mathcal{M}_o , *e.g.* when the continuous phase has a low viscosity. For very low \mathcal{M}_o and \mathcal{E}_o around 3, *e.g.* millimeter-size bubbles in fluids with a low viscosity, an unstable or “wobbling” motion is encountered. This can be explained as follows: as a fluid particle rises through a continuous phase, work is done on the continuous phase by the fluid particle at a rate equal to the rise velocity times the buoyancy force acting on the fluid particle. In a very viscous fluid, this energy can be dissipated completely through laminar viscous dissipation, but in a low viscosity fluid some of it is also released through wake shedding. The onset of vortex shedding coincides with the appearance of path oscillations known as secondary motion [83, 396, 95] and it has been concluded that the path oscillations are caused by the vortex shedding.

The unstable secondary motion of bubbles is very complex and has received considerable attention, *e.g.* [130, 334, 12, 399, 257, 258, 87, 88, 387]. It can be thought of as a superposition of two types of motion: firstly, oscillations in the bubble trajectory (defined as the path of the bubble centroid) combined with changes of the orientation of the bubble; and secondly, bubble shape oscillations.

Regarding the first type of oscillations, instabilities of the bubble trajectory occur in the intermediate range of the bubble sizes. This regime is denoted “wobbling” in Figure 1.4. Small, nearly spherical, *e.g.* [334, 12], and large, spherical-cap bubbles, *e.g.* [421], do not exhibit this type of oscillations and usually rise rectilinearly. Once the bubble becomes more deformed into an oblate spheroid, instabilities set in and result in a zigzag or helical (or spiral) trajectory. The zigzag trajectory is characterised by side-to-side movement in a vertical plane and the orientation of the plane has been observed both to remain constant, *e.g.* [334], or to change randomly as the bubble rises, *e.g.* [398]. The helical trajectory of a bubble assumes either clockwise or counter-clockwise direction, depending on the conditions where the bubble is generated [130]. The motion of a bubble may be first zigzag and then change into a helical one, but the reverse transition has never been reported [334, 12, 257, 258]. Furthermore, it should

be noted that the rise velocity of zigzagging bubbles is usually smaller than that of those exhibiting a helical motion.

There is no unanimous agreement on the conditions that decide whether the trajectory of a bubble is zigzag or helical. The type of oscillation seems to be controlled by two factors: the physical properties of the surrounding phase, especially the presence of surfactants, *e.g.* [398]; and the way the bubble is generated/released and thus the initial perturbations, *e.g.* [334]. Recently, it has been suggested by [87, 88, 387] that the dynamics of bubbles involves two natural modes of oscillations. The primary mode develops first, leading to a zigzag trajectory. Then, under certain circumstances, the secondary mode grows, causing the trajectory to progressively change into a circular helix. This conjecture helps to explain the effects of both initial perturbations and surfactants.

Recently, Lunde and Perkins [258] performed experiments with expanded polystyrene spheroids and observed marked zigzag motion with angular displacements from the vertical of as much as 50° . This result is significant because it shows that path instabilities do not require shape variations or a shear-free boundary condition. Consequently, it can be concluded that the motion is controlled by the mode in which the bubble/polystyrene spheroid sheds its vorticity.

Figure 1.5 depicts the terminal rise velocity of air bubbles in water as a function of the bubble diameter. Three regimes can be identified: spherical, “wobbling” (here denoted ellipsoidal) and spherical-cap. In the shaded area, the bubble rise velocity is not simply a function of the bubble diameter and large variations of the rise velocity for a given nominal bubble diameter are found. For example, for a bubble with a diameter of 2 mm, the rise velocity varies by a factor of three. On the other hand, outside the shaded area, *i.e.* in the spherical-cap and most of spherical regime, the rise velocity is primarily a function of the bubble size. Unfortunately, many industrial applications operate in the “wobbling” regime and it follows that the quality of predictions hinges on its accurate description.

Traditionally, the variation of the rise velocity for a fixed bubble diameter has been explained by the presence of surface-active agents (surfactants) [56, 95]. Surface tension is reduced when surfactants accumulate at the interface. However, it is not

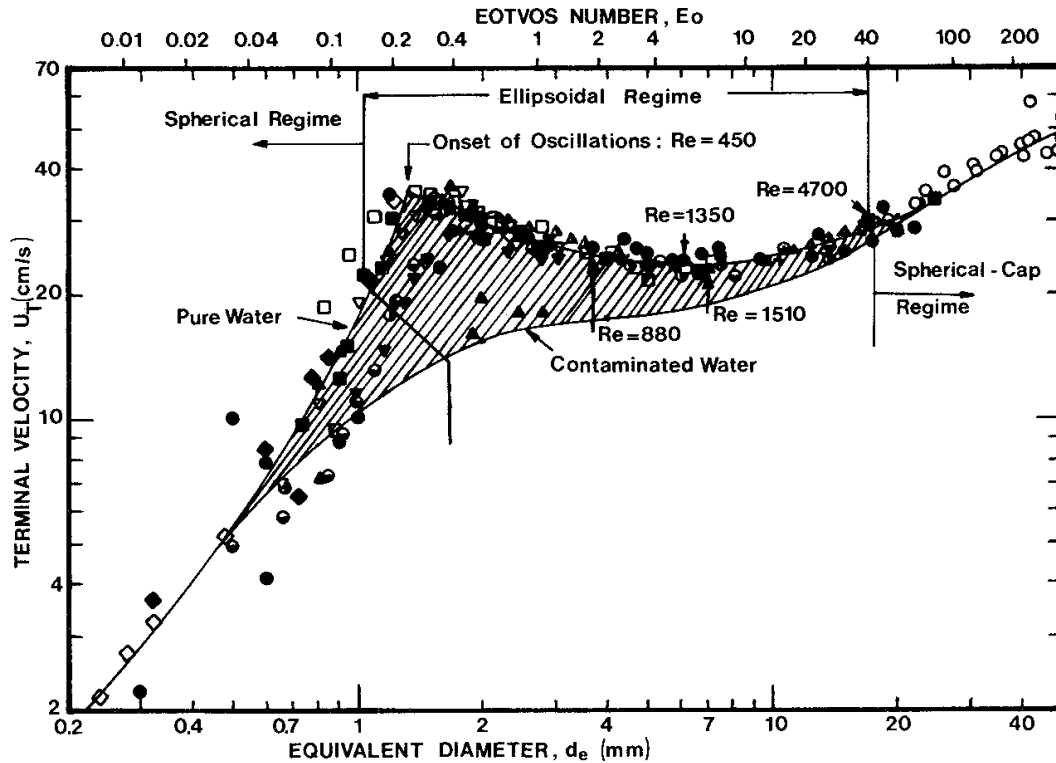


Figure 1.5: Terminal velocity as a function of diameter for air bubbles in water (from [56]).

the uniform reduction of the surface tension which is important, but the effect of a gradually varying distribution of the inter-facial surfactant concentration. The mechanism can be described by the “surface tension gradient model” proposed by [241, 84]: a gradually varying distribution of the inter-facial surfactant concentration produces a surface tension gradient, which in turn generates a tangential force acting against the flow causing the accumulation. For example, when a fluid particle moves through a continuous phase, the surrounding fluid tends to sweep the adsorbed surfactant to the rear and the resultant concentration gradient gives rise to a tangential force acting in the opposite flow direction. In this situation, the boundary condition is not a free-shear condition and the interface is said to be immobilised.

The immobilisation of the interface has several effects on the fluid particle: firstly, it tends to damp out the internal circulation and thereby increases the drag on the fluid particle [33, 128]. This increase of drag is only substantial for small fluid particles ($d < 1 \text{ mm}$) where the flow around the fluid particle is dominated by viscous forces. Provided the creeping flow approximation holds, the drag on the fluid particle can be approximated by the Hadamard-Rybczynski theory [131, 332] for pure systems and

the Stokes' law for contaminated systems [56]. Secondly, more vorticity is generated at an immobilised interface than at a clean interface. This promotes early separation and increases the size of the wakes behind the bubble. This, in turn, reduces the pressure drop across the bubble and thus diminishes the bubble deformation, although the surface tension force is effectively reduced by the presence of surfactants, as noted earlier. The reduction of deformations has been shown experimentally by [397, 56] and confirmed numerically by [67, 180, 181]. The larger wakes also indicate that the form drag increases, in addition to the increase in viscous drag mentioned earlier [180, 181].

In order to attempt to take these effects into account, most drag models for bubbles available in the literature are derived with reference to a particular level of contamination, *e.g.* clean, slightly contaminated or fully contaminated. The available experimental evidence seemed to suggest that the rise velocity is highly sensitive to the presence of surfactants. Since it is nearly impossible to remove all surfactants from a system, even under laboratory conditions, most systems encountered in engineering applications are believed to be contaminated [56]. Consequently, in the case of an air-water system, tap water is regarded as a contaminated or slightly contaminated system. “Pure” water is only obtained by carefully distilling the water twice or more.

Recently, Tomiyama et al. [387] challenged the view that the variation of the rise velocity for a fixed bubble diameter can be explained by the presence of surfactants alone. His group conducted experiments with air bubbles in clean, tap and contaminated water and found that multiple stable states exist. For each of these states, the bubble assumes a particular shape and posses a characteristic rise velocity falling into the shaded area of Figure 1.5. They explained this as being due to non-linearities in the Navier-Stokes equations as well as the inter-facial conditions. They also found that the level of deformation, quantified by the bubble aspect ratio, correlated well with the rise velocity. In their experiments, the shape and the rise velocity of the bubbles was strongly affected by the initial perturbations exerted on the bubbles during generation/release. For small initial perturbations, they showed that air bubbles in clean water rise with velocities that have been previously only reported for air bubbles in contaminated water. Under these conditions, the bubble trajectory is zigzag. On the other hand, for air bubbles in contaminated water, only a single state existed and the

rise velocity was independent of the initial perturbations. This was attributed to rapid damping of perturbations in the presence of surfactants. They concluded that the large scattering of the rise velocity is not primarily caused by the presence of surfactants, but variations in the initial perturbations.

Finally, their results for bubbles in tap water were very similar to the results for bubbles in clean water. This showed that tap water should actually be considered as a clean system and that the variation of the rise velocity for a given bubble diameter should be explained with reference to the initial perturbations exerted on the bubble. They obtained a correlation for the bubble rise velocity as a function of the aspect ratio of the bubble, which is given by equation (6.42), but the latter quantity is itself a dependent variable and seems to depend on the history of the bubble. However, it should be pointed out that the existing correlations for clean and contaminated systems provide the limiting cases for air bubbles in clean as well as tap water. On the other hand, air bubbles in contaminated water are described well by the existing models.

1.5.4 Modelling Drag at High Phase Fractions

Many two-phase processes operate at high phase fractions, as outlined in Section 1.1. Their prediction relies on the accurate description of the effects that are caused by the presence of other DPEs in the vicinity of an individual DPE. Obviously, these effects are governed by the average distance between the DPEs, which depends on the phase fraction and the distribution of the DPEs in space. As an illustration, consider a regular lattice of spherical DPEs of diameter d located at the corners of a cube with an edge length of a . In this situation, a is also the closest distance between two DPEs and the phase fraction α is given by:

$$\alpha = \frac{V_{DPE}}{V_{cube}} = \frac{\pi}{6} \left(\frac{d}{a} \right)^3 \quad (1.10)$$

where V_{DPE} and V_{cube} stand for the volume of the cube and a DPE, respectively.

In Table 1.1, α is tabulated for several values of the normalised distance between the DPEs a/d . The phase fraction peaks at 53.5% for the smallest possible distance ($a/d = 1$) and decreases rapidly for increasing values of a/d . It is less than 1% for $a/d = 4$, but it is likely even then that two DPEs will have an appreciable influence on

$a/d [-]$	1	2	4	6	8	10
$\alpha [-] \%$	52.3	6.54	0.818	0.242	0.102	0.0523

Table 1.1: Relationship between the relative distance between the DPEs and the phase fraction.

each other if they are located behind each other because of wake effects. Hence, some influence must be anticipated even at this relatively low α .

The possible interactions between the DPEs are numerous. For solid particles settling in a vessel filled with a lighter fluid, Barnea and Mizrahi [15] identified the following effects:

Pseudo-hydrostatic effect: The average hydrostatic pressure gradient in the suspension is greater than that in the fluid alone. Consequently, the buoyancy force acting on a particle in a suspension is also larger because it is the integral of the vertical component of the hydrostatic pressure normal to the particle surface. It follows that the mixture density must be used in the expression for the buoyancy force instead of that for the fluid [208, 15, 441].

Momentum transfer effect: The presence of other particles affects the momentum transfer between each particle and the fluid through distortions of the streamlines and wakes. Furthermore, the fluid flow around the particles is hindered by the other particles in the suspension. This effect is related, although not strictly equivalent, to the increase of the “apparent” bulk viscosity of the suspension which becomes evident when the latter is sheared.

“Wall hindrance effect”: Significant effects are detectable even when a single particle is settling in a closed vessel whose size is not sufficiently larger than that of the particle. The settling particle causes, via displacement, an opposite motion of the fluid, which causes additional friction between the fluid and the walls. In addition, the flow field around the particle is disturbed by the presence of the wall. Analogously, the following effects are felt by an individual particle in a suspension: firstly, additional drag is induced by the motion of the displaced fluid; and secondly, its flow field is restricted by the presence of the surrounding particles.

Segregation effects: Suspensions often contain particles of various shapes and sizes, which respond differently to the motion of the fluid. Hence, local inhomogeneities can develop, which are counteracted by dispersive effects. Suspensions at high phase fractions and those with narrow size distributions tend to exhibit weaker segregation effects [139]. In this study, segregation effects are neglected because we assume uniform size distributions.

Other effects: Some interactions between the particles in a suspension are not through hydrodynamic effects. Examples include flocculation and aggregation. However, these effects are beyond the scope of this study.

The effects outlined above usually increase the exchange of momentum between the particle and the fluid in a dense suspension. Hence, a particle in a suspension sinks slower than the same particle in an infinite fluid. However, it is well known that the drag on a particle is reduced if another particle is placed in front of it. This slip streaming effect can substantially increase the terminal velocity of a particles moving together in a cluster, *e.g.* Koglin [202] measured a maximum increase of the terminal velocity by a factor of three at an average phase fraction of 2%. However, it should be noted that the segregation of particles into clusters is less likely in a dense suspension and, therefore, this effect is not effective when the α is high [197].

The problem is complicated further if fluid particles are considered: firstly, these are deformable, which complicates their dynamics substantially, as outlined in the previous Section. Secondly, systems of fluid particles are inherently unstable due to the possibility of coalescence and, therefore, often need to be prepared shortly before their behaviour is studied experimentally. In this respect, liquid-liquid flows are often easier to handle because they can be stabilised with surfactants and α can then be pushed up to 70% while the flow is still dispersed.

In gas-liquid flows, coalescence cannot be controlled as effectively and the bubbles quickly form gas pockets. The flow is now said to be in the slug or churn turbulent regime. It should be noted that the models presented in this study are derived for dispersed flows and cease to be valid in other flow regimes. Unfortunately, the exact conditions for the transition depend on the apparatus and the flow rates *etc..* However, it is interesting to note that Liu and Bankoff [249] were able to operate a vertical pipe

flow in the dispersed flow regime at average and maximum local phase fractions of 41% and 52%, respectively. On the other hand, Serizawa et al. [346] found that they were not able to stabilise a bubbly flow in the same type of device beyond an average and maximum local phase fraction of 20% and 30%, respectively.

Over the years several models have been proposed to determine the drag on DPEs at elevated phase fractions. They can be categorised into different modelling approaches, which are summarised in Table 1.2. A short description of the main features of each category is given below:

Friction Factor: Some authors [341] prefer to use a friction coefficient C_f instead of a drag coefficient to express the inter-phase momentum transfer due to drag \mathbf{M}_a^d , thus:

$$\mathbf{M}_a^d = C_f \mathbf{U}_r \quad (1.11)$$

where \mathbf{M}_a^d is the inter-phase momentum transfer due to drag per unit volume.

Note that C_f is not dimensionless.

Drift flux: Drift flux models have been widely used to express the influence of the phase fraction on drag. See Wallis [414] for a general introduction. In general, drift flux models take the following form:

$$\frac{j}{U_{r0}} = \alpha(1 - \alpha)^n \quad (1.12)$$

where j stands for the drift flux defined as:

$$j = \alpha(1 - \alpha)U_r \quad (1.13)$$

The empirical coefficient n depends on the phase fraction and $\mathcal{R}e$. Correlations for n are derived by fitting measurements.

Drag Coefficient Ratio: In this approach, the measured ratio of the drag coefficient to its single-particle value is fitted to a function of the phase fraction [208, 429], such that:

$$\frac{C_d}{C_{d0}} = f(\alpha) \quad (1.14)$$

Modelling Approach					
Friction Factor	Drift Flux	$\frac{C_d}{C_{d0}} = f(\alpha)$	Theoretical Model	Mixture Viscosity	Ergun Type Correlation
Particles	—	Wallis [414] Richardson and Zaki [319]	— new correlation	Tabor [369] Ishii and Zuber [168]	Barnea and Mizrahi [15] Andersson [5]
Droplets	—	Wallis [414] Hartland [208]	new correlation	— Ishii and Zuber [168]	Barnea and Mizrahi [16] Kumar et al. [209] Pilhofer [307]
Bubbles	Schwarz and Turner [341]	Wallis [414] Wen and Yu [429]	new correlation	Johansen and Boysan [187] Ishii and Zuber [168]	— —

Table 1.2: Modelling approaches for drag at high phase fraction.

Theoretical Model: The effect of the phase fraction on the drag is derived theoretically, for example, by considering the pairwise interactions between two particles [369, 187].

Mixture Viscosity: The presence of other DPEs is taken into account by considering their effect via a mixture viscosity. This mixture viscosity is then used to define the Reynolds number appearing in a suitable drag correlation [15, 168, 208].

Ergun type correlation: The correlation by Ergun [90] provides the pressure drop across a closely packed bed of particles as a function of $\mathcal{R}e$. It has been extended to cover fluidised beds of particles and swarms of droplets by introducing additional, empirical parameters [5, 307].

1.5.5 Modelling Lift

The interest in the transverse lift acting on a particle can be traced to the time of Poiseuille [309], who reported that blood cells keep away from the walls of capillaries. It was not clear what causes this phenomena for a long time until the remarkable observations by Segré and Silberberg [342, 343] that small neutrally buoyant spheres of various sizes suspended in a Poiseuille flow in a tube migrated slowly to a position about 0.5 to 0.7 tube radii from the tube axis. This experiment demonstrated convincingly the existence of a lateral force on spherical particles. At the same time, Oliver [297] investigated buoyant particles in the same type of flow. He found that downward settling particles in downward flowing liquids move towards the wall, whereas upwards moving particles moved towards the axis. Since then, considerable work on inertial lift of particles in suspension has been conducted, mostly for flows in tubes and channels, *e.g.* [116, 62, 400].

Most experimental work to quantify the lateral forces on DPEs has been carried out using the following types of experiment:

Levitation experiment: the DPE is maneuvered into an equilibrium position within a shear flow. The shear flow might be produced by an inclined circular pipe [85] or a rotating cylinder [287]. The lateral forces due to the shear are then inferred

from the equilibrium position and the other forces of known magnitude, *e.g.* drag, buoyancy and virtual mass.

Pendant experiment: the DPE is suspended into a vertical shear flow using a rod [434, 435] or a thread [280]. The pendant assumes a stable position slightly off the vertical axis due to the lateral forces acting upon the DPE. This type of experiment has been carried out for particles in air and the shear flow was produced by a grid of parallel rods, which were not equally spaced.

The lateral forces on the sphere can be calculated from the equilibrium position or the surface pressure distribution. In the former method, the lateral forces are inferred for the equilibrium position from the inclination angle and the other forces of known magnitude [434, 435, 280]. In the latter method, the surface pressure distribution is measured by pressure transducers embedded into the sphere and the lift coefficient is calculated by numerical integration over the surface [434, 435].

Tracking experiment: the trajectory of the DPE is recorded using Particle Image Velocimetry (PIV) [359, 104], (high speed) video camera [389, 212, 51] or stroboscope photography [195]. Usually, the experiment is designed such that the flow field of the continuous fluid is known a-priori, *e.g.* by using an apparatus similar to the one shown in Figure 7.4a. However, the flow field of the continuous fluid can be determined simultaneously, for example, if PIV is used to trace the DPE [359, 104].

The analysis of the experiments mentioned above is further complicated if the flow becomes unsteady, *e.g.* because of boundary layer separation or oscillations in the trajectory. Therefore, most of the work has focused on low $\mathcal{R}e$ flows to avoid these additional complications.

Another problem is that of repeatability if free-moving DPEs are considered. The trajectories are often random due to turbulence and/or the manner of introduction into the flow. Indeed, in the case of bubbles, the phenomenon of helical and zigzag trajectories has been attributed to varying injection arrangements and conditions in the experimental setups of the different researchers, as outlined in Section 1.5.3. Therefore,

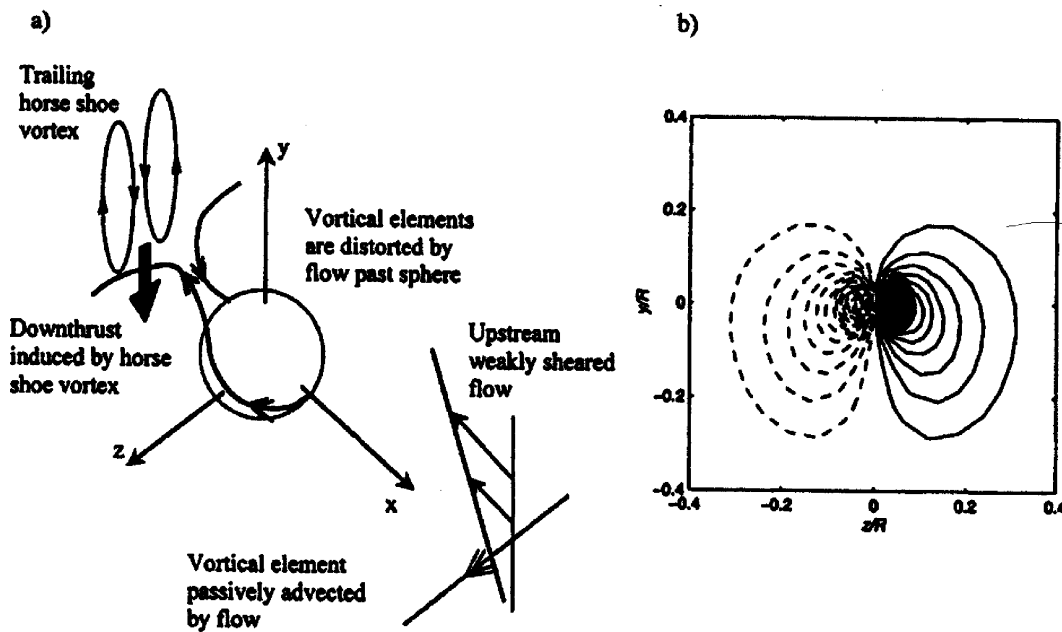


Figure 1.6: Shear-induced lift on a spherical particle: **a)** A schematic diagram shows how incident vortical elements are tilted and stretched (double arrow indicate the direction of the vorticity ω). **b)** Shows a numerical solution of the high Reynolds number flow ($\mathcal{R}e = 500$) Legendre and Magnaudet [235] illustrating the horseshoe vortex. The iso-contours correspond to constant values of the stream-wise vorticity ω_y one diameter downstream of the bubble centre (from [261]).

a large number of trajectories have to be recorded to obtain reliable averages, which often surpasses the acquisition, storage and processing capabilities of most commercially available video equipment [280]. However, this problem can be avoided (at least for particles) if tethered rather than free-moving DPEs are used.

There are several causes for lateral lift forces on a DPE:

Shear of the Fluid: a lateral force can be induced by shear in the surrounding continuous phase itself. This effect is named after Saffman [335], who derived an expression for it for very low $\mathcal{R}e$.

In contrast to two-dimensional flows past rigid bodies, where an initially uniform vorticity field remains uniform because vortical elements are not stretched, three-dimensional bodies moving in a uniform shear field permanently alter the vorticity field by stretching and tilting vortical elements that move with the fluid. This is described by the Cauchy-Helmholtz-Kelvin result [19]. An essential feature of sheared flow past a rigid body is the generation of vorticity parallel to the direction of motion, which manifests itself as an attached horseshoe vortex. As

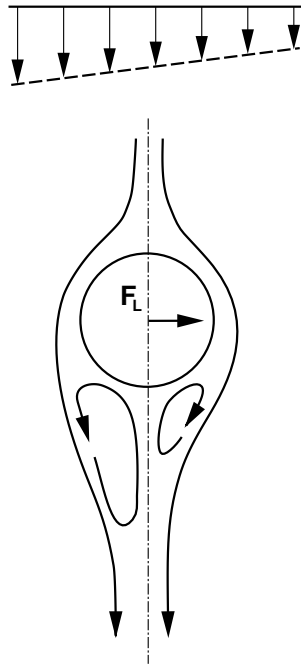


Figure 1.7: Sketch of the flow field around a DPE in linear shear. The shedding of non-symmetric vortices could produce an average lateral lift force towards the lower velocity side.

illustrated in Figure 1.6, the horseshoe vortex induces a down-thrust on the fluid and the body feels a corresponding lift force. This kind of lateral force acts to move the body towards the higher velocity side, as depicted in Figure 1.6.

Wake Phenomena: even for uniformly approaching flows it is well known that wake forces are of major concern to offshore civil structures [338, 246, 247]. Moreover, Jordan and Fromm [191] showed that a cylinder in a weak shear flow experiences an instantaneous lateral force due to vortex shedding, which is approximately 16 times larger than the average lateral force produced by shear. In view of this evidence, it is surprising how little attention has been given to vortex shedding and wake effects on lateral forces.

When a vortex is shed, the space it occupied behind the body is replaced by liquid moving more slowly than the rotational velocity of the vortex. A significant velocity reduction occurs due to the sharp turn that the incoming fluid has to make to occupy the volume immediately after the body. The Bernoulli equation predicts that this decrease in the velocity of the fluid will generate an increase in pressure. Therefore, when a vortex is shed, a transient lateral force on the body will arise. After averaging over an appropriate period of time, this effect will

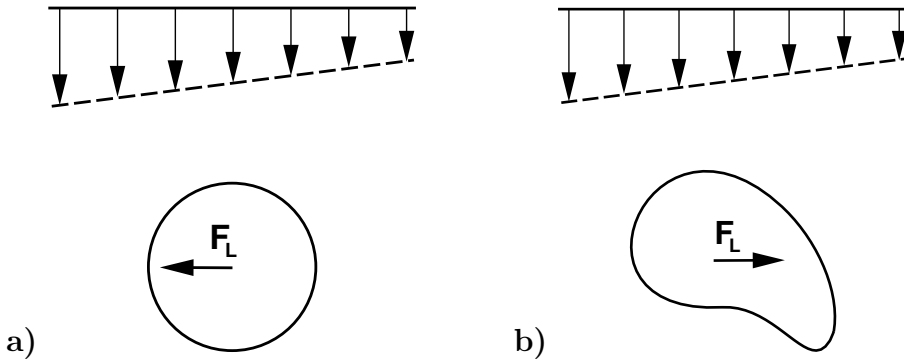


Figure 1.8: Sketch of an **a)** undeformed and **b)** distorted DPE. Note that the distorted bubble may experience a lift force acting towards the lower velocity side.

generate a non-zero lateral force if the wakes on either side of the centreline are not symmetric as depicted in Figure 1.7. This necessarily always happens in a shear flow and the flow visualisation of [337] as well as the numerical simulations of [191, 17] show very clearly how this mechanism may produce a non-zero average lateral force. Interestingly, this net force acts in opposite direction to that induced by the shear of the fluid, *i.e.* towards the lower velocity side. Wake phenomena become crucial when the density ratio is large, *e.g.* in bubbly flows, because, in this case, the liquid-phase vortices shed by the bubble deliver considerable momentum to it.

It should be noted, however, that the flow around a fixed body differs considerably from the flow around a freely moving one. This alters the forces on the body and, hence, the above argument can only provide an idea for the mechanisms that govern the lift force acting on a moving DPE.

Deformation: the phenomena discussed are altered for non-spherical DPEs, but the exact mechanisms are not very well understood. Furthermore, fluid particles deform substantially when the shear of the fluid is strong enough and this feeds back on the hydrodynamic forces. This coupling between shear and deformation manifests itself in a spectacular way in the lateral migration of non-spherical bubbles. Kariyasaki [195] and Tomiyama et al. [389] reported measurements that show that strongly deformed bubbles rising in a vertical linear shear flow migrate in the direction opposite to that followed by spherical bubbles. Several authors [373, 386, 91, 253] have performed direct numerical simulations showing

the same tendency. A possible reason for this effect is illustrated in Figure 1.8. The fluid particle may be deformed such that it assumes an airfoil-like shape and could experience a lateral force towards the lower velocity side.

Rotation: rotation of a solid particle moving in a fluid results in different local relative velocities and causes a lateral force. This effect is named after Magnus [262]. The rotation may be caused by collisions with a wall, inter-particle collisions or simply because of the shear of the fluid. It must be pointed out that it is difficult to measure the rotational speed of a particle accurately and it is impossible to calculate it without detailed knowledge of the mechanics of inter-particle and wall collisions. The Magnus effect described above is caused by solid body rotation and, hence, does not apply to bubbles and droplets, which do not rotate in the same way.

Surfactants: the presence of surfactants on the surface of small fluid particles is known to produce inter-facial shear stresses and therefore to increase the drag as discussed in Section 1.5.3. It is likely that surfactants also have a considerable influence on the lateral force because the amount of inter-facial vorticity may be several orders of magnitude larger than for a clean interface [236]. However, to the author's knowledge no studies have been carried out to quantify this effect.

We shall now discuss some results for the lift force acting on a clean spherical bubble, *i.e.* a sphere under a shear-free boundary condition instead of a no-slip one. One can of course argue that in most practical situations bubbles are neither clean nor spherical. However, the study of the lift force on a clean spherical bubble is interesting in order to identify the influential dimensionless groups in this limiting case.

Auton [10, 9] showed that the lift force \mathbf{F}_l on a clean spherical bubble in steady inviscid flow is proportional to the cross product of the vorticity of the continuous phase $\nabla \times \mathbf{U}_c$ and the relative velocity \mathbf{U}_r between the two phases. Hence, he proposed the following definition for the dimensionless lift coefficient C_l for a single DPE in an infinite medium:

$$C_l = \frac{F_l}{\rho_c V |\mathbf{U}_r \times (\nabla \times \mathbf{U}_c)|} \quad (1.15)$$

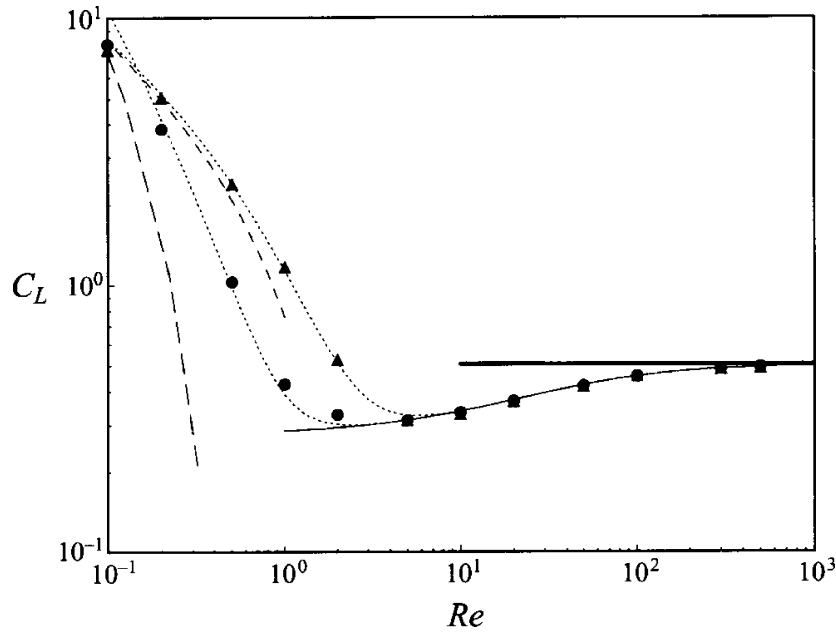


Figure 1.9: Lift coefficient for a clean spherical bubble in a linear shear flow as a function of the Reynolds number. Solid line: analytical solution for inviscid flow; dotted lines: curve fit for the numerical results for $\mathcal{Sr} = 0.02$ (\bullet) and $\mathcal{Sr} = 0.2$ (\blacktriangle); dashed lines: analytical solution for creeping flow for $\mathcal{Sr} = 0.02$ and $\mathcal{Sr} = 0.2$ (from [235]).

With this definition, the lift coefficient is a constant ($C_l = 0.5$) for the case of a spherical bubble in weakly sheared inviscid flow.

In the limit of creeping flow, the theoretical result of Saffman [335] for particles has been extended by [267, 236] to the case of clean spherical bubbles. In this case, C_l depends on the characteristics of the surrounding flow and is primarily a function of \mathcal{Re} and the dimensionless shear rate \mathcal{Sr} , defined as:

$$\mathcal{Sr} = \frac{|\nabla \mathbf{U}_c| d}{U_r} \quad (1.16)$$

In another study, Legendre and Magnaudet [235] used direct numerical simulation to study the lift force on a clean spherical bubble in a linear shear flow in the range $0.01 < \mathcal{Re} < 500$ and $0.01 < \mathcal{Sr} < 1$. Their work is interesting because it enables the determination of the range of validity of the analytical solutions very low \mathcal{Re} and inviscid flow.

All of the results mentioned above are plotted in Figure 1.9. It is evident that C_l approaches a constant value of 0.5 for high Reynolds numbers. On the other hand, for low Reynolds numbers, the lift coefficient is a function of the Reynolds number and the shear rate. For low shear rates ($\mathcal{Sr} = 0.02$), it is evident that \mathcal{Re} has to be less than 0.1

to match the analytical result of Legendre and Magnaudet [236]. However, at higher $Sr = 0.2$, the their result works up to a Reynolds number of unity. It is interesting to note that the shear rate has no influence on the lift coefficient at moderate to high Reynolds numbers ($Re > 5$). The analytical result for inviscid flow by [10, 9] is recovered for Reynolds numbers larger than 100.

A Reynolds number of 100 corresponds to an air-water bubble with a diameter of approximately 0.7 mm and a terminal velocity of 0.13 m/s, as evident from Figure 1.5. A bubble of this size is almost spherical and, therefore, the analytical result for inviscid flow should apply provided surface contamination is kept to a minimum. Unfortunately, these assumptions do not hold in most practical situations. Firstly, the bubbles in practical equipment are often larger and deformed; secondly, the flow is usually turbulent; and finally, the effects of neighbouring bubbles when the phase fraction is high is not taken into account.

Given the large number of influencing factors listed above and the limited understanding of the physical processes involved, it not surprising that no model exists that predicts the lateral force on DPEs with satisfactory accuracy. This is also evident from the varying values used for the lift coefficient in different CFD calculations using the two-fluid model. A short overview of these is presented next.

Lahey et al. [216] compared the modelling used in several studies of bubbly flows by the groups at the Renslaer Polytechnic Institute (RPI) and the École Centrale de Lyon (ECL). For small bubbles, they proposed constant lift coefficients of 0.1 (RPI) and 0.25 (ECL). Subsequently, the latter value has been confirmed for a plane mixing layer by Hill et al. [148, 147] and a lower value of 0.1 was successfully utilised for bubble plumes by Sheng and Irons [351, 348]. Despite these successes, several authors showed that in order to fit the experimental data of bubbly flow in a sudden enlargement of a vertical circular pipe, the lift force would have to act in the opposite direction to that implied by a positive lift coefficient, *i.e.* “negative” lift occurs [25, 228, 416]. This was also observed in the measurements of Rinne and Loth [326, 327]. Furthermore, Aloui and Souhar [3, 4] found a qualitatively different void fraction distribution for horizontal air/water bubbly flow in a symmetric duct of rectangular cross-section undergoing a sudden enlargement. Grosssetete [129] applied the two-fluid model to developing bubbly

flow in a vertical pipe and found that for some injection conditions the lift coefficient would have to be negative in order to fit the experimental data. A similar result has been found for bubble columns [391, 368, 177, 127, 149, 32]. Here, a negative lift coefficient is needed to predict the increase of the phase fraction towards the centreline of the column.

The importance of the lift force in the prediction of the phase fraction distribution of bubbly flows in vertical pipes has been stressed by many researchers. Numerous experimental studies have been undertaken in order to elucidate the flow patterns in such flows, *e.g.* [346, 141, 443, 444, 410, 345, 248, 249, 129, 289, 59]. Utilising these data sets, several researchers have then proposed lift models to predict the phase fraction distribution, *e.g.* [31, 419, 215, 216, 220, 443]. By simplifying the two-fluid momentum equations and introducing an appropriate turbulence model they obtained an equation for the phase distribution across the pipe for fully developed flow. They were then able to infer the value of the lift coefficient by comparing the model predictions and the experimental data.

Wang et al. [419, 215] correlated the data for a number of cases and found that C_l is a function of the local phase fraction, bubble $\mathcal{R}e$, $\mathcal{S}r$, the ratio of the bubble and pipe diameters as well as the ratio of the mean gas and terminal bubble velocities. The lift coefficient diminished exponentially with the local phase fraction and ranged between 0.01 and 0.1, which is far from the “classical” value of 0.5 for high $\mathcal{R}e$. Beyerlein et al. [31] utilised a similar approach to derive a correlation for the lift coefficient. Their correlation is simply a function of the phase fraction and decreases rapidly with the mean phase fraction.

On the other hand, it has been clarified through a number of recent experimental studies [345, 444, 248, 129] that the lateral migration of bubbles in co-current pipe flow also depends strongly on the bubble size. Smaller bubbles with diameters up to 5 mm tend to migrate towards the pipe wall. This leads to a saddle-shaped phase fraction distribution with a pronounced maximum close to the wall, which is referred to as a “wall peak” distribution. On the other hand, larger bubbles accumulate in the centre of the pipe (“core peak” distribution). Tomiyama et al. [389] attributed this marked change to the increased deformation of the bubbles subjected to a shear flow because,

as shown earlier, their deformation can change the direction of the lift.

Despite these enormous efforts, the prediction of the phase fraction profile for a bubbly flow in a circular pipe remains a difficult task because of the coupled effects of shear, wake phenomena and deformation on the lift force as well as the turbulence of the continuous phase. Hence, to the author's knowledge no model exists that takes into account all these factors to predict the distribution of bubbles with satisfactory accuracy.

Another route to obtain insight into the motion of DPEs is provided by direct numerical simulation. Such research has been undertaken by several authors, their main areas of interest being the shape of single rising bubbles [333, 53, 385, 49] or drops [71, 36], bubbles [388, 373, 91] or drops [281] in shear flow as well as bubble-bubble interactions [92, 93, 94, 42, 188, 157, 158].

Nearly all of the above research work has been conducted for bubbles in fluids with high liquid viscosities, *i.e.* at high Morton numbers, in order to keep the Reynolds number small and to save computational resources. Furthermore, numerical difficulties arise when the surface tension force is high, as mentioned in Section 1.5.1. Hence, none of the above studies are concerned with air bubbles in water. This is extremely unsatisfactory since low Morton number fluids are typical of many industrial applications. It should be mentioned that although interesting conclusions can be drawn from the existing results, extrapolation to air-water systems, with extremely low Morton numbers, is of dubious validity.

In this study, an interface-capturing technique is used to calculate the dynamics of single air-water bubbles. The motivation for this work stems from the fact that, as noted above, very little is known about the lift force on bubbles, especially when the Morton number is low. A new interface-capturing methodology due to Weller [424] will be outlined in Chapter 4. This methodology is then used to investigate two situations: the rise of single bubbles in a quiescent liquid and in a linear shear flow.

1.5.6 Two-Phase Turbulence Modelling

As outlined in Section 1.2.3, the two-fluid model requires closure relations for the Reynolds stresses, which arise in the momentum equations as a result of the averaging

process. These unknown stresses represent the effects of turbulence on the average phase momentum and need to be expressed in terms of known quantities.

Before we discuss the different approaches to two-phase turbulence modelling, it should be mentioned that velocity fluctuations in the continuous phase arise from a number of sources. The first source may be identified as that of “ordinary” single-phase turbulent fluctuations, *i.e.* fluctuations resulting from the existence of an energy cascade fed by mean velocity gradients, which will be referred to as shear-induced turbulence. Other sources are associated with the presence and relative motion of the DPEs, as follows [219, 228]:

1. One contribution comes from the random stirring of the continuous phase induced by the relative motion between the phases. These perturbations have a magnitude comparable to the magnitude of the relative velocity and a length scale of the order of 3-4 DPE diameters. These fluctuations do not constitute turbulent motion in the usual sense and after Lance and Bataille [219], this source of fluctuations is often referred to as “pseudo-turbulence” in order to distinguish it from “true turbulence”;
2. A second contribution stems from the existence of wakes behind the DPEs. If the wakes are turbulent, bubble-induced “true turbulence” with length scales smaller than the DPE diameter is generated. However, the fluctuations produced by laminar wakes should be considered as another source of pseudo-turbulence;
3. A third contribution originates from the deformation of the interfaces of fluid particles due to acceleration, presence of shear or interaction with turbulent eddies. Again, this mechanism does not constitute “true turbulence”.

Turbulence modelling for two-phase flows has been reviewed recently by several authors [147, 228, 231, 417]. They tend to focus on the specific turbulence effects, in which the individual author is interested, and the equations derived can vary significantly due to the simplifying assumptions introduced in the derivation.

As in single-phase flow turbulence modelling, second-order closure models, which solve transport equations for each component of the Reynolds Stress, constitute the highest level of closure currently feasible for practical applications. So far, only two

authors [252, 221] developed two-phase Reynolds stress turbulence models, whereas the majority of authors invoke the Boussinesq hypothesis [35] and model the turbulent stress-strain relation analogous to the constitutive relation of a viscous fluid, *e.g.* [251, 233, 121, 376, 27, 350, 370]. The turbulent viscosity is then related to the fluid's turbulent kinetic energy k and its dissipation rate ε , which are governed by their own transport equations. These two-equation models represent the minimum level of closure that allows an internal length scale to be calculated and the additional computational effort required to solve the equations is moderate. Two-equation models have been applied successfully to numerous single- and two-phase flows and, hence, their strengths and weaknesses are well known. Due to these facts, two-equation models are frequently employed in practical calculations.

Most two-phase turbulence models of dispersed flows are based on a single-phase turbulence model for the continuous phase. The presence of the dispersed phase is accounted for by additional terms, *e.g.* [251, 233, 121, 376, 27, 350, 370]. Recently, Tabor [370] outlined a more elaborate, four-equation model where separate $k-\varepsilon$ systems are assembled for each phase. This model requires additional closure and more effort is needed to finalise the coupling terms.

In this study, the two-phase two-equation turbulence model by Gosman et al. [121] is adopted. It consists of the standard $k-\varepsilon$ -model [230] with additional source terms to incorporate the effects of the dispersed phase on the turbulence. The dispersed phase turbulence is related to that of the continuous phase through a turbulence response coefficient C_t , which is defined as the ratio of the r.m.s. velocity fluctuations of the dispersed phase U'_a to those of the continuous phase U'_b :

$$C_t = \frac{U'_a}{U'_b} \quad (1.17)$$

This approach is more attractive than other practices because of its simplicity. However, its implications have to be carefully considered [147]. In particular, a scalar relationship for C_t implies that the velocity fluctuations in each direction are related by the same coefficient. This is not necessarily the case for all flows, as shown by [89], and more elaborate models have been derived, which treat C_t as a vector, albeit with limited success.

At low phase fractions, C_t is governed by the density ratio ρ_b/ρ_a , the size of the

DPE compared to that of the turbulence eddies d/L as well as the ratio of the response time of the DPE and a characteristic turbulence time scale, *i.e.* Stokes number \mathcal{St} , defined as:

$$\mathcal{St} = \frac{\rho_d d^2 U_r}{18 \rho_c \nu_c L} \quad (1.18)$$

where μ_c , ρ_c and ρ_d are the dynamic viscosity and density of the continuous and dispersed phase, respectively. L denotes a characteristic length scale for the turbulence eddies, *e.g.* the Lagrangian integral length scale [151]. d and U_r stand for the nominal diameter of the DPE and the magnitude of the relative velocity vector \mathbf{U}_r , respectively.

For $d/L < 1$, C_t takes values close to unity if the response time is small compared to the turbulence time scale, *i.e.* $\mathcal{St} \ll 1$ [66]. This is the case for small particles or bubbles which follow the continuous flow exactly. On the other hand, for large Stokes' numbers, the value of C_t depends on the density ratio. Thus, C_t is smaller than unity for large density ratios, *i.e.* heavy particles, because they are unaffected by the surrounding turbulence field. However, it is larger than unity for gas-liquid flows [328, 89]. Expressions for C_t have been put forward by various authors [121, 310, 171, 174, 52] by considering simplified equations of motion for single DPEs encountering a turbulence eddy within the continuous phase under the assumption that L is much larger than d .

Recent experimental data [109, 227, 7] suggest that both phases fluctuate in unison as one entity when the phase fraction is high. Consequently, C_t approaches a constant value close to unity as the phase fraction increases. This effect is not taken into account in the current C_t -models and a modified expression will be proposed and tested in Chapter 5.

1.5.7 Validation Test Cases for the Two-Fluid Methodology

The accuracy of two-phase flow models and the accuracy and robustness the solution procedure have to be assessed against well-defined validation test cases, so that deficiencies can be localised and further improvements can be made. An ideal test case should have a well-characterised geometry and boundary conditions. Also local measurements of the phase fraction, phase velocities and turbulence quantities should be available.

Test Case	Source(s)	low α	high α	steady	Modelling req.
Vertical Pipe Flow	<i>e.g.</i> [346, 419, 249, 129]	✓	✓	✓	Lift & Wall Forces, Near Wall Turbulence
Sudden Enlargement	[25, 26, 28, 222]		✓	✓	Lift Force, Turbulence
Venturi	[377]		✓	✓	
T-Junction	[312, 142, 34]	✓		✓	
Bluff Body	[160, 436, 190]		✓		Lift Force
Bubble Plume	[82, 20, 21, 118, 306, 317]	✓			Turbulence
Bubble Jet	[366, 365, 163, 162]		✓	(✓)	Lift Force, Turbulence
Bubble Column	<i>e.g.</i> [322, 150, 271, 126]	✓	✓		Coalescence (het. regime), Lift Force
Mixer Vessel	[41, 100, 13, 282]	✓	cavities	MRF	Lift Force, Break-Up, Coalescence
Homogenous Turbulence	[219, 89, 227]	✓	✓	✓	Turbulence
Homogenous Shear Flow	[221, 222]	✓		✓	Turbulence
Plane Mixing Layer	[329, 328, 222, 227]	✓	✓	(✓)	
Boundary Layer	[283, 222]	✓		✓	Lift Force
Rotating Pipe	[277]	✓	cavities	✓	
Centrifugal Pump	[276]			✓	

Table 1.3: Overview of gas-liquid validation test cases.

Tables 1.3 and 1.4 give an overview of test cases, which have been identified in the present study as suitable for validation purposes. It is striking that there are far more test cases available for gas-liquid systems than for liquid-liquid ones. This reflects the relative ease of measuring events in gas-liquid systems as well as the enormous importance of gas-liquid reactors and heat and mass transfer equipment in the process and associated industries.

The present research is concerned with dispersed flows at high phase fractions.

Test Case	Source(s)	low α	high α	steady	Modelling req.
Vertical Pipe Flow	[97]		✓	✓	Lift & Wall Forces, Near Wall Turbulence
Plane Mixing Layer	[8, 7]	✓	✓	(✓)	Lift Force
Homogenous Turbulence	[7]	✓	✓	✓	Turbulence
Pipe Mixer	[380, 199, 182, 183, 184]	✓		✓	Break-Up
Pin Stirrer	[407]		✓		Break-Up, Coalescence
Model Extraction Column	[206]		✓		Break-Up, Coalescence

Table 1.4: Overview of liquid-liquid validation test cases.

Therefore, the dispersed phase fraction should be relatively high ($\alpha > 10\%$). Of the test cases which reach into the high phase fraction regime, the most suitable in the context of this work are:

Plane Mixing Layer (g-l): The hydrodynamics of a gas-liquid mixing layer at low phase fractions has been investigated first by [329, 328]. Here, it was found that the lateral expansion in bubbly flow is more pronounced than in single-phase flow. Furthermore the velocity fluctuations in the liquid phase are strongly modified from their single-phase values, but could be approximated by the superposition of shear-induced and bubble-induced contributions.

The measurements have been extended to higher phase fractions by Larue de Tournemine et al. [227]. The behaviour of these flows exhibits a high sensitivity to small volume fraction differences between the two inlet flows. In the range of investigated flow parameters, the local volume fraction seems to strongly affect the flow pattern. In the case of mixing layers with an initial imposed gradient of the volume fraction, buoyancy effects control the development of the flow leading to a highly non-stationary behaviour.

Bubble Plume and Jet (g-l): In this type of flow, the gas or gas-liquid mixture is injected locally into a column filled with pure liquid. For small gas flow rates, the

gas forms a bubble plume, which oscillates periodically from side to side. The flow turns into a turbulent jet if the gas flow rate is increased sufficiently and the local phase fraction can then reach value up to 80% close to the injector.

Several authors, *e.g.* [82, 265, 348, 284, 439], performed calculations and compared them with the experimental data. They found that an accurate prediction of this type of flow depends strongly on the turbulence and lift models.

Sudden Enlargement (g-l): Gas-liquid flow in a sudden enlargement of a circular, vertical pipe is an important building-block flow and has been investigated experimentally by Bel F'dhila [25]. Several validation studies [27, 25, 228, 418, 416, 103, 393] have been performed utilising his data and it has proven to be challenging for the modelling as well as the numerical aspects. In particular, the inclusion of lift effects, using current practices, leads to unacceptable results, *e.g.* [228, p. 139].

Bubble Column (g-l): Gas-liquid reactors in the form of bubble columns and mixer vessels have an enormous importance in the process and associated industries. Hence, they received considerable attention, both in terms of experimental and theoretical efforts.

For bubble columns, a number of data sets are available from the literature, which contain local measurements of velocities, phase fraction, bubble size and often turbulence quantities. Some of these extend to very high phase fractions ($> 40\%$). These have been utilised by a number of authors [126, 210, 179, 177, 314, 156] as test cases in their numerical studies.

Mixer Vessel (g-l): This type of two-phase reactor has been investigated thoroughly and some important experimental studies, which are suitable for validation purposes are given in Table 1.3. It should be noted that the mean phase fraction is usually less than 5% in the mixer vessels mentioned in the table. However, even at these relatively low phase fractions, the gas tends to accumulate in the low-pressure region behind the impeller blades. These gas cavities significantly alter the trailing vortices behind the impeller blades and thus have a marked effect on the impeller performance and mixing characteristics [411]. Unfortunately,

detailed measurements in the proximity of the gas cavities are very difficult to obtain.

Several CFD studies have been carried out to investigate the flow of gas-liquid mixtures in mixer vessels, *e.g.* [121, 13, 78, 156, 75]. The problem of gas cavities behind the impeller blades has been addressed recently by several authors [316, 324, 323, 315] using numerical calculations to investigate their formation and break-up.

Bluff Body (g-l): An alternative to the study of cavities behind impeller blades is to examine flows around bluff bodies. Interestingly, it appears that the experimental results around bluff bodies show a different behaviour in that the phase fraction increases in front of the body and decreases in its wake. Two-phase flows around bluff bodies have been investigated numerically by [405, 364, 393]. The authors obtained reasonable results for the flow around a circular cylinder and were able to predict the decrease in the phase fraction profile downstream of the cylinder, but failed to predict the increase in front.

Plane Mixing Layer (l-l): As mentioned earlier, data sets suitable for validation of liquid-liquid systems are extremely rare. Recently, a liquid-liquid mixing layer has been investigated by Augier et al. [8]. This study includes local measurements of phase fraction, phase velocities and turbulence intensities.

In the mixing layer flow investigation, two distinct configurations were studied. The first was a volume fraction induced mixing layer where the dispersed phase is injected only on one side of the separating plate. In this case, the flow structure is non-stationary and is governed by the difference of apparent densities between the layers. Large scale, low frequency fluctuations develop in the flow, which are essentially described by the unsteady mean momentum balance equation. The behaviour is essentially analogous to the gas-liquid mixing layer investigated by Larue de Tournemine et al. [227].

The second type of mixing layer flow studied was induced by a velocity gradient of the continuous phase on each side of the dividing plate, with no significant volume fraction gradient. The results show that the mixing layer diffuses more

rapidly when the phase fraction is increased. This enhancement in diffusion could not be explained by the increase in the tangential component of the Reynolds stress as is the case in single-phase flow.

In this thesis, three flows are calculated using the two-fluid methodology to assess the numerical solution procedure as well as the models for the inter-phase momentum transfer (drag and lift) and turbulence, which are either identified in the literature or derived in the present study. The test cases are: a plane mixing layer (g-l) [328, 222], a sudden enlargement (g-l) [25, 222] and a bubble plume (g-l) [118, 306]. Liquid-liquid flows are not computed in this study because these often require additional modelling, *e.g.* for break-up and coalescence, as shown in Table 1.4. Hence, the validation work conducted concentrates on gas-liquid flows.

1.6 Thesis Outline

The remainder of this thesis is organised as follows. Chapter 2 describes the fundamentals of the finite volume discretisation. No reference to a specific set of governing equations is made at this point. The discussion covers spatial, temporal as well as equation discretisation along with the numerical boundary condition treatment. Next, the structure of the resulting systems of linear algebraic equations is discussed with respect to boundedness and convergence. Finally, a finite volume notation is put forward, which is then utilised in the following Chapters to describe the solution procedures for the two-fluid and interface-capturing methodology in concise and unambiguous manner.

The next two Chapters present the two CFD methodologies used in this study, namely the two-fluid and interface-capturing methodology. Each of the Chapters starts by stating the governing equations. Then, the solution procedure is discussed by presenting the discretised equations together with the overall solution procedure. Finally, both methodologies are validated against suitable test cases.

In Chapter 5, a revised model for the turbulence response function at high phase fractions is put forward, which is based on recent experimental data. The new correlation is incorporated into the two-fluid methodology and assessed against experimental

data for two test cases.

Next, the modelling of drag in dispersed two-phase systems is discussed in Chapter 6. The subject has a long history and previous modelling efforts are summarised in a comprehensive literature survey. The review focuses on gas-liquid and liquid-liquid systems. However, for completeness, correlations derived for solid-liquid systems are also included. Additionally, a new correlation for all systems is proposed. Finally, several models are compared with data from the literature in order to assess their validity.

The objective of Chapter 7 is to contribute to the development of correlations for the lift force in dispersed two-phase systems. First, the literature related to the modelling of the lift force in dispersed gas-liquid and liquid-liquid systems is reviewed. For completeness, correlations derived for solid-liquid systems are also included in this study. The performance of several models is assessed against experimental data for two test cases. Finally, novel results for a free-rising air-water bubble in linear shear are presented. These results are used to explain some of the modelling deficiencies that are evident in the two-fluid simulations.

Finally, in Chapter 8, the main findings and conclusions are summarised. Various outstanding issues are identified and suggestions for future research are given.

Chapter 2

Finite Volume Discretisation

The term discretisation means approximation of a continuum problem into discrete quantities. The finite volume method and others, such as the finite element method, all discretise the problem as follows:

Spatial discretisation Splitting the space domain into a set of cells that fill and bound it when connected;

Temporal discretisation For transient problems, dividing the time domain into a finite number of time intervals, or time steps;

Equation discretisation Generating a system of algebraic equations in terms of discrete quantities defined at specific locations in the domain, from the governing equations that characterise the problem.

This Chapter describes the fundamentals of the finite volume discretisation. The technique has been described by many authors [301, 99, 413, 153, 255] and is used extensively in this study. No reference to the specific set of governing equations is made at this point. They will be presented in the following Chapters.

2.1 Discretisation of the Solution Domain

Discretisation of the solution domain is shown in Figure 2.1. The solution domain consists of a space and a time domain. The space domain is subdivided by a computational mesh on which the governing equations are subsequently discretised. Discretisation of

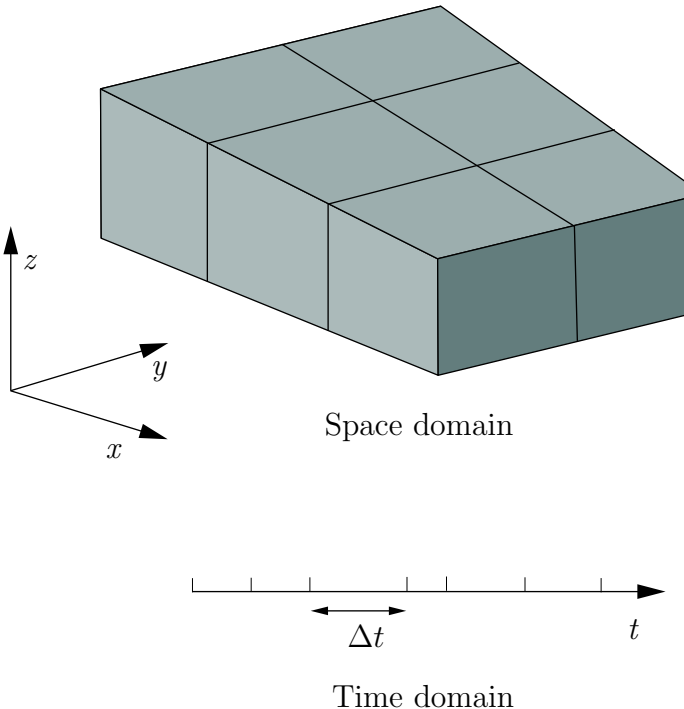


Figure 2.1: Discretisation of the solution domain (from [255]).

time, if required, is simple: it is broken into a set of time steps Δt . The time step may change during a numerical simulation, either pre-specified or depending on some condition calculated during the simulation.

Discretisation of space requires the subdivision of the domain into a number of cells, or control volumes. The cells are contiguous, *i.e.* they do not overlap with one another, and completely fill the domain. It follows naturally that the boundary of the space domain is decomposed into faces connected to the cell next to it.

Two typical cells are shown in Figure 2.2. A cell is bounded by a set of faces, given the generic label f . The cell faces are divided into two groups – internal faces (between two cells) and boundary faces, which coincide with the boundaries of the space domain. The position vector of the centre of a flat¹ face \mathbf{x}_f is defined, such that:

$$\int_S (\mathbf{x} - \mathbf{x}_f) dS = 0 \quad (2.1)$$

In this study, all faces are flat. However, the treatment of non-flat faces is explained in [255].

Dependent variables and other properties are stored at the centre P of the cell.

¹For a flat face, all vertices lie in one plane.

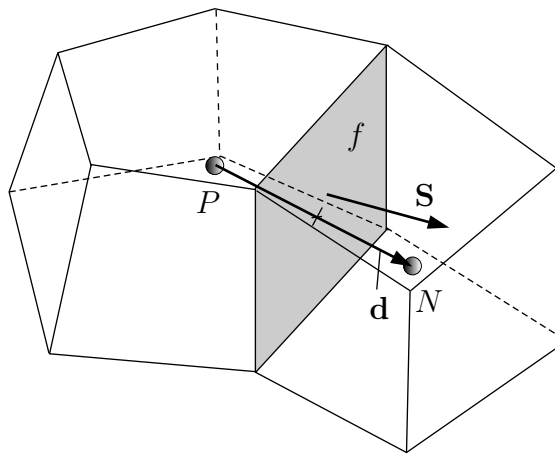


Figure 2.2: Parameters in finite volume discretisation (from [255]).

The position vector of the cell centre \mathbf{x}_P is defined, such that:

$$\int_{V_P} (\mathbf{x} - \mathbf{x}_P) dV = 0 \quad (2.2)$$

The face area vector \mathbf{S} is normal to the face and its magnitude is equal to the area of the face. It points out of the cell of interest P into the neighbouring cell N . The unit vector \mathbf{n} normal to the face is defined as $\mathbf{n} = \frac{\mathbf{S}}{|\mathbf{S}|}$ and \mathbf{d} denotes the vector between the centre of the cell of interest P and the centre of a neighbouring cell N , *i.e.* $\mathbf{d} = \mathbf{x}_N - \mathbf{x}_P$. A computational mesh is orthogonal when \mathbf{d} is orthogonal to the face plane, *i.e.* parallel to \mathbf{S} , for each face in the mesh.

The software library used in this study [255, 427] does not impose a limitation on the number of faces bounding each cell. The only requirement is that each cell must be convex. This kind of mesh is often referred to as “unstructured” [99, 153] and offers great freedom in mesh generation and manipulation, in particular when the geometry of the space domain is complex or changes in time.

It should be noted, however, that in this study only static meshes are employed. The geometry of a static mesh does not change in time with respect to the local frame of reference. However, the local frame of reference might be moving relative to an inertial frame of reference. In this case, the acceleration of this moving frame of reference has to be accounted for in the governing equations. This is the case for the simulation of single bubbles using the interface-capturing methodology and will be explained in detail in Section 4.1.3.

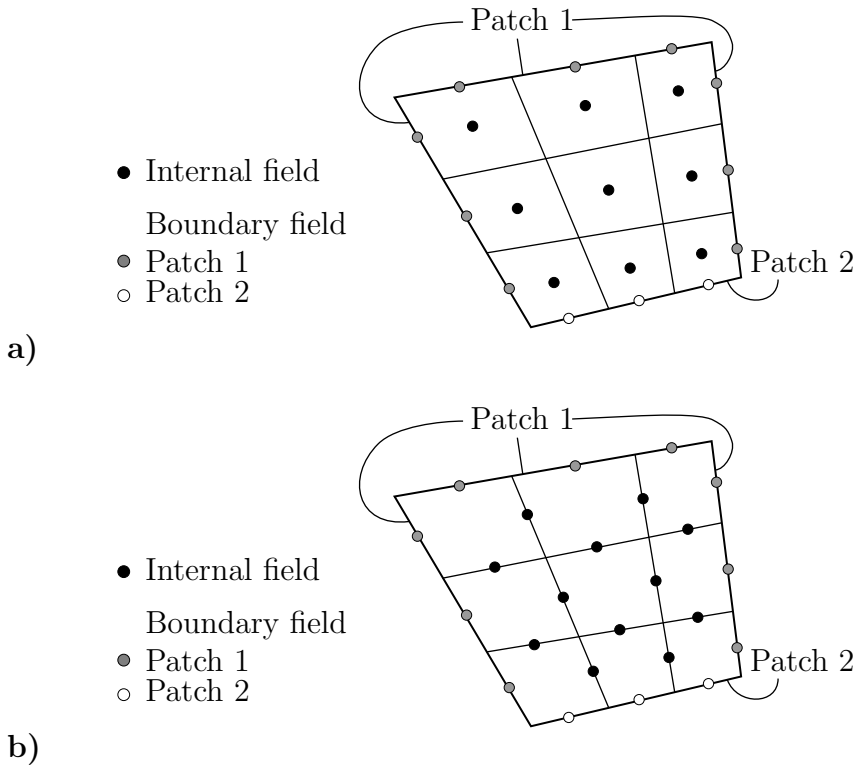


Figure 2.3: Two types of variable storage arrangements: **a)** volume field: values are stored at the cell centres; **b)** face field: values are stored at the face centres (from [255]).

2.2 Arrangement and Storage of Variables

The first issue when discretising the governing equations is to select the locations in the domain at which the values of the dependent² and other variables are to be stored. There are several alternatives and two which are typical for the finite volume method are depicted in Figure 2.3: In the first, the variables are stored at the centre of each cell of the space domain and at the face centres of the boundary faces. This storage arrangement will be referred to as a “volume field” in the remainder of this study. The second storage arrangement is termed “face field” and the variables are stored at the centre of each face.

The obvious choice is to store all dependent variables at the cell centres (*i.e.* in volume fields) and to use the same control volumes for all variables; this is called the “collocated” arrangement. In the “staggered” arrangement [137, 154, 301] the velocities are stored at the cell faces (in a face field) or vertices, separate from other variables.

²Dependent variables are determined by solving a governing equation for them.

The collocated arrangement, however, has significant advantages: firstly, the number of coefficients that must be calculated is minimised because each of the governing equations is discretised using the same control volume. Secondly, it has significant advantages in complex solution domains, especially when the boundaries have slope discontinuities or the boundary conditions are discontinuous [99].

However, the collocated arrangement was not used for a long time because of difficulties with pressure-velocity coupling and the occurrence of oscillations (checkerboarding) in the pressure field [301, 99, 413, 305, 304]. A simple cure for this problem was proposed by Rhie and Chow [318] and since then the collocated arrangement has been adopted by most CFD codes, including commercial ones.

In this study, the collocated variable arrangement is adopted, although it has been found that a revised solution procedure is sometimes necessary to handle sharp density gradients frequently encountered in the solution of the two-fluid and interface-capturing models. The revised solution procedure mimics the operation of a solution procedure devised for a staggered variable arrangement, but keeping the collocated variable arrangement. Details of this procedure will be given in Sections 3.2 and 4.2.

2.3 Equation Discretisation

The purpose of equation discretisation is to transform one or more governing equations into a corresponding system of algebraic equations. The solution of this system approximates the solution to the original equations at some pre-determined locations in space and time. Consider the generic form of the standard transport equation for any tensorial quantity ϕ :

$$\underbrace{\frac{\partial \rho\phi}{\partial t}}_{\text{time derivative}} + \underbrace{\nabla \cdot (\rho \mathbf{U} \phi)}_{\text{convection term}} = \underbrace{\nabla \cdot (\Gamma \nabla \phi)}_{\text{diffusion term}} + \underbrace{S_\phi(\phi)}_{\text{source term}} \quad (2.3)$$

where ρ is the density, \mathbf{U} is the velocity, Γ is the diffusivity and $S_\phi(\phi)$ represents a source term. The terms in the standard transport equation represent the rate of change per unit volume (time derivative), the efflux by convection per unit volume (convection term), the rate of transport due to diffusion (diffusion term) and the rate of production/destruction per unit volume (source term).

In the following Sections, the standard transport equation is used as an example to explain equation and temporal discretisation. However, more complex transport equations are frequently encountered in multi-phase flow and other complex physics applications. The finite volume method is, of course, not limited to the discretisation of governing equations similar to the standard transport equation and the discretisation of additional terms which are encountered in the applications of this study are discussed along with the discretisation of the terms in the standard transport equation.

A finite volume discretisation of equation (2.3) is formulated by integrating over the control volume V_P and time:

$$\begin{aligned} & \int_t^{t+\Delta t} \left[\int_{V_P} \frac{\partial \rho \phi}{\partial t} dV + \int_{V_P} \nabla \cdot (\rho \mathbf{U} \phi) dV \right] dt \\ &= \int_t^{t+\Delta t} \left[\int_{V_P} \nabla \cdot (\Gamma \nabla \phi) dV + \int_{V_P} S_\phi(\phi) dV \right] dt \end{aligned} \quad (2.4)$$

Most spatial derivative terms are converted to integrals over the surface S bounding the volume using the generalised form of the Gauss's theorem:

$$\int_V \nabla \otimes \phi \, dV = \int_S d\mathbf{S} \otimes \phi \quad (2.5)$$

where $d\mathbf{S}$ is the outward pointing differential of the surface area vector. The symbol \otimes is used to represent any tensor product, *i.e.* inner, outer or cross, and the respective derivatives: divergence $\nabla \cdot \phi$, gradient $\nabla \phi$ and curl $\nabla \times \phi$ when the particular derivative is defined. The volume and surface integrals are then approximated using appropriate schemes.

In the remainder of this Section, details of the discretisation practices utilised to approximate the volume integrals of equation (2.4) are discussed. The discussion is not carried out on a strict term-by-term basis in order to be able to introduce some notation for face interpolation (Section 2.3.1) and face gradients (Section 2.3.2). This notation is then utilised in the discretisation of the convection (Section 2.3.4) and diffusion (Section 2.3.5) term. The discretisation of the time integrals of equation (2.4) is considered in Section 2.5.

2.3.1 Face Interpolation

Interpolation of the cell-centred values to the face centres is fundamental to the finite volume method. It is utilised by many discretisation practises discussed in this Section

and is therefore outlined next.

Many face interpolation schemes have been devised and reviews can be found in [99, 301, 185, 286, 304]. The face value $\phi_{f(F,S,\gamma)}$ can be evaluated from the values in the neighbouring cells using a variety of schemes, denoted by S, which may require a flux F through face f and in some cases one or more parameters γ .

The exact definition of the flux depends on the governing equations and the numerical solution procedure. The flux field (a face field) is usually a result of the numerical solution procedure and satisfies continuity constraints. Its calculation will be discussed in Sections 3.2 and 4.2. For the discussion in this Section, the mass flux through face f might serve as an example. It is defined as $F = \mathbf{S} \cdot (\rho \mathbf{U})_f$. This choice is consistent with the flux used in the discretisation of the convection term of equation (2.3) presented in Section 2.3.4.

The face interpolation schemes used in this study are discussed next:

Central differencing (CD) is second-order accurate [99], but the solution can be unbounded³ [301, 99, 301]:

$$\phi_{f(CD)} = f_x \phi_P + (1 - f_x) \phi_N \quad (2.6)$$

$$\text{where } f_x \equiv \frac{|\mathbf{x}_f - \mathbf{x}_N|}{|\mathbf{x}_f - \mathbf{x}_N| + |\mathbf{x}_f - \mathbf{x}_P|}.$$

Note that ϕ_f stands for $\phi_{f(CD)}$ for brevity.

Upwind differencing (UD) determines ϕ_f according to the direction of the flow [60, 112, 14]. The scheme is given by:

$$\phi_{f(F,UD)} = \begin{cases} \phi_P & \text{for } F \geq 0 \\ \phi_N & \text{for } F < 0 \end{cases} \quad (2.7)$$

UD guarantees boundedness of the solution, but it is only first order accurate. It can be shown that the leading truncation error of UD resembles a diffusive flux, *e.g.* [99, p. 72]. This effect is termed numerical diffusion and can severely distort the solution on coarse meshes. The boundedness of the solution is effectively ensured at the expense of accuracy.

³The physically realistic value of a property (like density, phase fraction or turbulent kinetic energy) lies within proper bounds. These should be guaranteed by the numerical scheme.

Blended differencing (BD) schemes combine UD and CD in an attempt to preserve boundedness with reasonable accuracy. They are linear combinations of UD and CD:

$$\phi_{f(F, \text{BD}, \gamma)} = (1 - \gamma) \phi_{f(F, \text{UD})} + \gamma \phi_{f(\text{CD})} \quad (2.8)$$

The blending factor $0 \leq \gamma \leq 1$ determines how much numerical diffusion will be introduced. Several expressions have been proposed to select the blending coefficient γ and state of the art is reviewed by [99, 185, 286, 304]. In this study, the Gamma differencing scheme (GD) introduced by Jasak et al. [186, 185] is utilised.

2.3.2 Gradient

The gradient term, $\nabla\phi$, can be evaluated in a variety of ways. In this study, the following two methods are utilised:

Gauss integration This operation yields the cell-centred gradient of ϕ . The discretisation is performed using the standard method of applying the Gauss's theorem to the volume integral:

$$\int_V \nabla\phi \, dV = \int_S d\mathbf{S} \phi \approx \sum_f \mathbf{S}\phi_f \quad (2.9)$$

where the value ϕ_f on face f can be evaluated in the variety of ways described in Section 2.3.1. However, in this study, CD is used exclusively.

Face normal gradient is the inner product of the face gradient $\nabla_f\phi$ and unit normal to the face \mathbf{n} , *i.e.* $\nabla_f^\perp\phi = \mathbf{n} \cdot \nabla_f\phi$. Here, $\nabla_f\phi$ denotes the gradient at the face. It does not, however, imply a specific discretisation technique. The face normal gradient can be approximated using the scheme:

$$\nabla_f^\perp\phi = \frac{\phi_N - \phi_P}{|\mathbf{d}|} \quad (2.10)$$

This approximation is second order accurate when the vector \mathbf{d} between the centre of the cell of interest P and the centre of a neighbouring cell N is orthogonal to the face plane, *i.e.* parallel to \mathbf{S} . In the case of non-orthogonal meshes, a correction term could be introduced which is evaluated by interpolating cell-centred gradients obtained from Gauss integration (see above).

2.3.3 Time Derivative

Discretisation of the time derivative such as $\frac{\partial \rho\phi}{\partial t}$ of equation (2.3) is performed by integrating it over a control volume. In this study, the Euler implicit time differencing scheme is used exclusively. It is unconditionally stable, but only first order accurate in time. For the static meshes employed in this study, assuming linear variation of ϕ within a time step gives:

$$\int_V \frac{\partial \rho\phi}{\partial t} dV \approx \frac{\rho_P^n \phi_P^n - \rho_P^o \phi_P^o}{\Delta t} V_P \quad (2.11)$$

where $\phi^n \equiv \phi(t + \Delta t)$ stands for the new value at the time step we are solving for and $\phi^o \equiv \phi(t)$ denotes old values from the previous time step.

2.3.4 Convection Term

Discretisation of convection terms such as $\nabla \cdot (\rho \mathbf{U} \phi)$ of equation (2.3) is performed by integrating over a control volume and transforming the volume integral into a surface integral using the Gauss's theorem as follows:

$$\int_V \nabla \cdot (\rho \mathbf{U} \phi) dV = \int_S d\mathbf{S} \cdot (\rho \mathbf{U} \phi) \approx \sum_f \mathbf{S} \cdot (\rho \mathbf{U})_f \phi_{f(F,S)} = \sum_f F \phi_{f(F,S)} \quad (2.12)$$

where F is the mass flux through the face f defined as $F = \mathbf{S} \cdot (\rho \mathbf{U})_f$. Again, the value ϕ_f on face f can be evaluated in the variety of ways described in Section 2.3.1.

2.3.5 Diffusion Term

Discretisation of diffusion terms such as $\nabla \cdot (\Gamma \nabla \phi)$ of equation (2.3) is done in a similar way to the convection term. After integration over the control volume, the term is converted into a surface integral:

$$\int_V \nabla \cdot (\Gamma \nabla \phi) dV = \int_S d\mathbf{S} \cdot (\Gamma \nabla \phi) \approx \sum_f \Gamma_f (\mathbf{S} \cdot \nabla_f \phi) \quad (2.13)$$

Note that the above approximation is only valid if Γ is a scalar.

On orthogonal meshes, the face normal gradient $\nabla_f \phi$ defined in Section 2.3.2 is a second order accurate approximation for the face gradient used in the approximation.

However, on non-orthogonal meshes, an additional correction term is introduced in order to preserve second order accuracy. Thus the full gradient approximation reads:

$$\mathbf{S} \cdot \nabla_f \phi = \underbrace{|\Delta| \nabla_f^\perp \phi}_{\text{orthogonal contribution}} + \underbrace{\mathbf{k} \cdot (\nabla \phi)_f}_{\text{non-orthogonal correction}} \quad (2.14)$$

where Δ and \mathbf{k} are vectors to be determined by the non-orthogonality treatment. Non-orthogonality treatments have been subject to intensive research [99, 286]. In this study the over-relaxed approach by Jasak [185] is utilised.

2.3.6 Source Term

Source terms, such as $S_\phi(\phi)$ of equation (2.3), can be a general function of ϕ . Before discretisation, the term is linearised:

$$S_\phi(\phi) = \phi S_I + S_E \quad (2.15)$$

where S_E and S_I may depend on ϕ . The term is then integrated over a control volume as follows:

$$\int_V S_\phi(\phi) dV = S_I V_P \phi_P + S_E V_P \quad (2.16)$$

The importance of linearisation becomes more clear after the discussion of temporal discretisation in Section 2.5. There is some freedom on exactly how a particular source term is linearised. When deciding on the form of discretisation, its interaction with other terms in the equation and its influence on boundedness and accuracy should be examined. This is discussed in detail in Section 2.6.1.

2.3.7 Curl

The curl, $\nabla \times \phi$, is only defined for vectors. It could be determined by invoking the Gauss's theorem. However, it computationally less expensive to calculate it from the cell-centred gradient described in Section 2.3.2 using the following relationship:

$$\nabla \times \phi = 2 * (\text{skew } \nabla \phi)$$

where the antisymmetric part of the second rank tensor \mathbf{T} is defined as $\text{skew}(\mathbf{T}) = \frac{1}{2} (\mathbf{T} - \mathbf{T}^T)$ and the Hodge dual of \mathbf{T} is a vector whose components are given by

${}^*\mathbf{T} = (T_{23}, -T_{13}, T_{12})$. Note that both operations are only defined for second rank tensors.

2.3.8 Average

Under some circumstances it is necessary to create an average over some region of space *e.g.* for smoothing or for numerical stability. Such averaging procedures are denoted $\langle \phi \rangle_{\square}$, *e.g.* $\langle \phi \rangle_{\nabla}$ is the average of ϕ over the computational molecule of ∇ operator. The average is defined as:

$$\langle \phi \rangle_{\square} = \frac{1}{N} \sum_{P=\square} \phi_P \quad (2.17)$$

where \square is a set of cells over which the average is taken and N is the number of cells in \square .

One group of particularly problematic terms have the form $\frac{\nabla \phi}{\phi}$, which cannot be evaluated numerically in the limit of $\phi \rightarrow 0$ even if the gradient also approaches zero. Consider the case that the cell centre value of ϕ is zero but a neighbour cell value is not. In this situation it is not possible to divide by the cell-centre value. This problem can be avoided if the denominator is averaged over the computational molecule of the ∇ operator, *i.e.* $\frac{\nabla \phi}{\langle \phi \rangle_{\nabla} \pm \delta}$ where δ denotes a small stabilising factor added to the denominator when $\langle \phi \rangle_{\nabla}$ is positive (or subtracted when $\langle \phi \rangle_{\nabla}$ is negative).

2.4 Boundary Conditions

A continuum problem is not complete without boundary and initial conditions. The latter are only necessary for transient problems and will be specified together with the particular problems in the relevant Chapters of this study. Boundary conditions can take many forms, but most of them can be divided into two types:

Dirichlet prescribes the value of the dependent variable on the boundary and is therefore termed “fixed value”;

von Neumann prescribes the gradient of the variable normal to the boundary and is therefore termed “fixed gradient”.

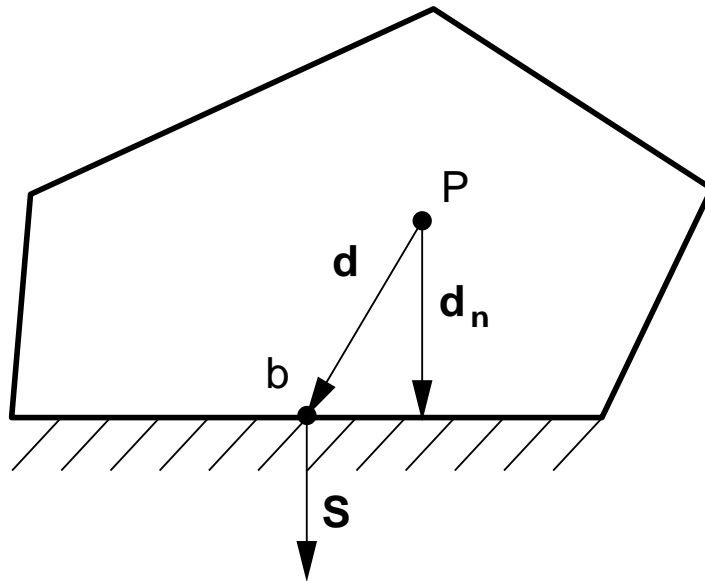


Figure 2.4: Parameters in finite volume discretisation for cells with a boundary face.

Some of the discretisation practises discussed in the previous Section involve the sum over faces \sum_f of the face interpolate ϕ_f or the face gradient $\nabla_f \phi$. The numerical boundary condition treatment is invoked when the sum over faces \sum_f includes boundary faces. Therefore, a numerical boundary condition must be specified on every boundary face and for each dependent variable.

A few additional parameters are required for the following discussion. Figure 2.4 shows a control volume P . One of its faces coincides with the boundary of the space domain. This face is labelled b . The vector between cell centre P and the centre of the boundary face is denoted by \mathbf{d} and its component normal to the boundary face by \mathbf{d}_n . In the following, it is assumed that the boundary condition specified is valid for the whole face. The numerical implementation of fixed value and fixed gradient boundary conditions is described next:

Fixed Value A fixed value is specified at the boundary ϕ_B , hence:

- It is substituted in cases when the discretisation requires the value on a boundary face, *i.e.* $\phi_f = \phi_B$, for example, in the convection term discussed in Section 2.3.4.
- In terms where the face gradient $\nabla_f \phi$ is required, *e.g.* diffusion term (Section 2.3.5), it is calculated using the boundary face value and cell centre

value:

$$\mathbf{S} \cdot \nabla_f \phi = |\mathbf{S}| \frac{\phi_b - \phi_P}{|\mathbf{d}_n|} \quad (2.18)$$

This practise is second order accurate if ϕ_B is constant along the face. It is only first order accurate when ϕ_B varies along the face and the mesh is non-orthogonal. However, a correction term could be introduced similar to the one discussed in Section 2.3.5 in order to improve accuracy.

Fixed Gradient The fixed gradient boundary condition is a specification of the face normal gradient $g_B = \nabla_f^\perp \phi$ at the boundary, hence:

- When the discretisation requires the value ϕ_f on a boundary face the cell centre value is extrapolated to the boundary:

$$\begin{aligned} \phi_f &= \phi_P + \mathbf{d}_n \cdot \nabla_f \phi \\ &= \phi_P + |\mathbf{d}_n| g_B \end{aligned} \quad (2.19)$$

- g_B can be directly substituted in cases where the discretisation requires the face gradient to be evaluated:

$$\mathbf{S} \cdot \nabla_f \phi = |\mathbf{S}| g_B \quad (2.20)$$

The discretisation practices for the fixed gradient boundary condition are second order accurate if g_B is constant along the face. They are only first order accurate when ϕ_B varies along the face and the mesh is non-orthogonal. Here, \mathbf{d}_n usually does not point to the middle of the boundary face. However, Jasak [185] showed that an error of the same type is neglected for the internal faces of the mesh and a correction is omitted for the sake of consistency.

Zero Gradient The zero gradient boundary condition is a fixed gradient boundary condition with $g_b = 0$ and the discretisation practises outlined above are applied.

2.5 Temporal Discretisation

In the previous Section, we have described the discretisation of the volume integrals in the standard transport equation in integral form presented in Section 2.3:

$$\begin{aligned} & \int_t^{t+\Delta t} \left[\int_{V_P} \frac{\partial \rho \phi}{\partial t} dV + \int_{V_P} \nabla \cdot (\rho \mathbf{U} \phi) dV \right] dt \\ &= \int_t^{t+\Delta t} \left[\int_{V_P} \nabla \cdot (\Gamma \nabla \phi) dV + \int_{V_P} S_\phi(\phi) dV \right] dt \end{aligned} \quad (2.4)$$

Using equations (2.11), (2.12), (2.13) and (2.16) and assuming that the control volumes do not change in time, equation (2.4) can be written as:

$$\begin{aligned} & \int_t^{t+\Delta t} \left[\rho_P \frac{\phi^n - \phi^o}{\Delta t} V_P + \sum_f F \phi_{f(F,S)} \right] dt \\ &= \int_t^{t+\Delta t} \left[\sum_f \Gamma_f \mathbf{S} \cdot \nabla_f \phi + S_I V_P \phi_P + S_E V_P \right] dt \end{aligned} \quad (2.21)$$

This expression is usually referred to as a “semi-discretised” form of the transport equation [153].

We now need to consider how to treat the time integrals of equation (2.21) because there are several alternatives to express the temporal integrals. Furthermore, the temporal variations of ϕ_P , the face values and gradients have to be expressed. Reviews of different discretisation practises are given in [153, 301, 185].

It has been customary to neglect the temporal variation of ϕ_P , the face values and gradients [301]. They are assumed to be constant during a time step. However, a choice has to be made about the way ϕ_P , the face values and gradients are evaluated in terms of new and old values:

Explicit uses explicit discretisation of the spatial terms, thereby taking old values ϕ^o .

$$\phi_P = \phi_P^o \quad (2.22)$$

$$\phi_f = \phi_f^o \quad (2.23)$$

$$\mathbf{S} \cdot \nabla_f \phi = \mathbf{S} \cdot \nabla_f \phi^o = |\Delta| \nabla_f^\perp \phi^o + \mathbf{k} \cdot (\nabla \phi^o)_f \quad (2.24)$$

It is first order accurate in time and is unstable if the Courant number \mathcal{C}_o is greater than 1. The Courant number on the face is defined as:

$$\mathcal{C}_o = \frac{\mathbf{U}_f \cdot \mathbf{S}}{\mathbf{d} \cdot \mathbf{S}} \Delta t \quad (2.25)$$

where \mathbf{U}_f is a characteristic velocity, *e.g.* velocity of a wave front or the velocity of a flow.

Euler implicit uses implicit discretisation of the spatial terms, thereby taking new values ϕ^n :

$$\phi_P = \phi_P^n \quad (2.26)$$

$$\phi_f = \phi_f^n \quad (2.27)$$

$$\mathbf{S} \cdot \nabla_f \phi = \mathbf{S} \cdot \nabla_f \phi^n = |\Delta| \nabla_f^\perp \phi^n + \mathbf{k} \cdot (\nabla \phi^o)_f \quad (2.28)$$

It is first order accurate in time, guarantees the boundedness of the solution and is unconditionally stable. It should be noted, however, that in order to guarantee boundedness, the non-orthogonal correction has to be treated explicitly. This will be discussed in more detail in Section 2.6.1.

In this study, the Euler implicit method is used exclusively and the final discretised standard transport equation now reads:

$$\rho_P \frac{\phi^n - \phi^o}{\Delta t} V_P + \sum_f F \phi_{f(F,S)}^n = \sum_f \Gamma_f \mathbf{S} \cdot \nabla_f \phi^n + S_I V_P \phi_P^n + S_E V_P \quad (2.29)$$

2.6 Solution Techniques for Systems of Linear Algebraic Equations

The discretisation and linearisation procedure outlined in the previous Sections produces a linear algebraic equation for each control volume. For example, equation (2.29) is obtained for the standard transport equation (2.3). The exact form of these linear algebraic equations depends on the governing equation and the discretisation practises used, but they can be re-written in a generic form, such that:

$$a_P \phi_P^n + \sum_N a_N \phi_N^n = R_P \quad (2.30)$$

The value of ϕ_P^n depends on the values of the neighbouring cells, thus creating a system of linear algebraic equations with one equation (or row) for each cell of the space domain. These systems of linear algebraic equations can be expressed in a matrix form

as:

$$[A][\phi] = [R] \quad (2.31)$$

where $[A]$ is a sparse square matrix with coefficients a_P on the diagonal and a_N off the diagonal. $[\phi]$ is the column vector of the dependent variable and $[R]$ is the source vector. The description of $[\phi]$ and $[R]$ as “vectors” comes from matrix terminology rather than being a precise description of what they truly are: a list of values defined at the centres of the control volumes. The matrix $[A]$ can be decomposed into two matrices containing the diagonal $[D]$ and off-diagonal $[N]$ coefficients, such that:

$$[A] = [D] + [N] \quad (2.32)$$

In general, each term of a governing equation, contributes to the matrix coefficients $[A]$ and/or the source vector $[R]$. Terms which are treated implicitly always contribute to the matrix coefficients and may contribute to the source vector. Explicit terms, however, contribute only to the source vector.

The system of linear algebraic equations (2.31) is solved using an appropriate numerical technique to yield a value for ϕ . This can be done in several different ways and summaries are given in [99, 117, 379]. In essence, solution algorithms fall into two main categories: direct and iterative methods. Direct methods give the solution of the system of algebraic equations in a finite number of arithmetic operations. Iterative methods start with an initial guess and then continue to improve the current approximation of the solution until some tolerance is met. For direct methods, the number of operations necessary to reach the solution scales approximately with the cube of the number of equations/unknowns, making them prohibitively expensive for large systems [413, 99, 379, 286]. On the other hand, iterative methods are often more economical, but they usually impose some requirements on the matrix.

The matrices resulting from the discretisation discussed in this Chapter are sparse, *i.e.* most of the matrix coefficients are equal to zero. Hence, the computer memory requirements could be significantly decreased by choosing a solver which can preserve the sparseness of the matrix. Unlike direct solvers, some iterative methods preserve the sparseness of the original matrix.

Furthermore, the discretisation error is usually much larger than the accuracy of the computer arithmetic and, hence, there is no merit in solving the system to this extreme level of accuracy – a solution somewhat more accurate than the discretisation scheme is sufficient.

These properties make the use of iterative solvers very attractive and the Conjugate Gradient (CG) method, originally proposed by Hestenes and Stiefel [143] (see [117, 99]), is often utilised. The original CG method guarantees that the exact solution will be obtained in a number of iterations smaller or equal to the number of equations/unknowns in the system. The convergence rate of the solver depends on the dispersion of the eigenvalues of the matrix and can be improved through preconditioning. In this study, the Incomplete Cholesky preconditioned Conjugate Gradient (ICCG) solver is used for symmetric matrices. The method is described in detail by Jacobs [175]. The solver adopted for asymmetric matrices is the Bi-CGSTAB by Van Der Vorst [409].

Iterative solvers require diagonal dominance in order to guarantee convergence. A matrix is said to be diagonally equal if the magnitude of the diagonal coefficient is equal to the sum of magnitudes of off-diagonal coefficients, *i.e.* $|a_P| = \sum_N |a_N|$. The additional condition for diagonal dominance is that the magnitude of at least one diagonal coefficient is larger than the sum of magnitudes of the off-diagonal coefficients in its row, *i.e.* $|a_P| > \sum_N |a_N|$. In order to improve the solver convergence, it is desirable to increase the diagonal dominance of the system whenever possible.

The structure of the matrix is closely linked to the issue of boundedness. The sufficient boundedness criterion for systems of algebraic equations (see Hirsch [153]) states that the boundedness of the solution will be preserved for diagonally equal systems of equations with positive coefficients. This allows us to examine the discretised form of all the terms in the transport equation from the point of view of boundedness and diagonal dominance and identify the “troublesome” parts of discretisation.

2.6.1 Analysis of Matrix Structure

The structure of matrices arising from the discretisation procedures outlined in this Chapter has been analysed in detail by Jasak [185] and Versteeg and Malalasekera

[413]. The discussion concentrates on the analysis of the discretisation on a term-by-term basis. In reality, all of the above coefficients contribute to the matrix, thus influencing the properties of the system.

The discretisation of the temporal derivative, equation (2.11), creates only a diagonal coefficient and a source term contribution, thus increasing the diagonal dominance. Unfortunately, the sufficient boundedness criterion cannot be used to examine the boundedness of the discretisation, since it does not take into account the influence of the source term. However, this term will not cause the appearance of new extrema in the solution because of its inertial nature.

The contribution of a convection term, equation (2.12), is examined next. A requirement for boundedness of the solution is the simultaneous satisfaction of an appropriate continuity constraint. Consider the following transport equation without diffusion and additional sources:

$$\frac{\partial \rho\phi}{\partial t} + \nabla \cdot (\rho \mathbf{U}\phi) = 0 \quad (2.33)$$

Equation (2.33) can be re-written, such that:

$$\rho \left(\frac{\partial \phi}{\partial t} + (\mathbf{U} \cdot \nabla) \phi \right) + \phi \left(\frac{\partial \rho}{\partial t} + \nabla \cdot (\rho \mathbf{U}) \right) = 0 \quad (2.34)$$

The first term on the l.h.s. contains the substantive derivative of ϕ . Hence, the solution of equation (2.34) is bounded if the second term is zero. The second term vanishes only if the mass continuity equation (2.35) is satisfied simultaneously, which reads:

$$\frac{\partial \rho}{\partial t} + \nabla \cdot (\rho \mathbf{U}) = 0 \quad (2.35)$$

A similar constraint can be derived for incompressible flow, *i.e.* $\rho = \text{const}$. The transport equation (2.33) now reads:

$$\frac{\partial \phi}{\partial t} + \nabla \cdot (\mathbf{U}\phi) = 0 \quad (2.36)$$

Here, the solution will only be bounded if the transport velocity \mathbf{U} satisfies the continuity constraint:

$$\nabla \cdot \mathbf{U} = 0 \quad (2.37)$$

The continuity constraint is enforced through utilisation of “conservative” fluxes in the discretisation of a convection term, equation (2.12). A flux field is said to be conservative if it satisfies a continuity constraint such as equation (2.37) or equation (2.35).

If the flux is conservative, the convection term contributes a diagonally equal matrix only if UD is used. Any other differencing scheme is likely to create negative coefficients, violate the diagonal equality and potentially create an unbounded solution. In the case of CD on a uniform mesh, the problem is further complicated by the fact that the contribution from the convection term to the central coefficient is equal to zero.

However, it is important to note that the solution of equation (2.36) will always be limited by zero even if a non-conservative flux is used in the discretisation. This is true regardless of the initial conditions provided UD is used and the fixed boundary conditions for this problem have the same sign. For example, for a field ϕ with values between 1 and 2, the lower bound will converge towards zero in regions where the flow diverges. Furthermore, the solution is limited by the largest (or smallest negative) boundary value and is therefore not guaranteed to be physically bounded at both ends.

Nevertheless, the statement above is often used to limit the solution of equations, such as the phase continuity equation in the two-fluid methodology (see Section 3.2.6), at zero. This can be examined by considering the extreme case of a cell for which all fluxes are positive, *i.e.* no flow is entering the cell. In this case, the off-diagonal matrix coefficients are zero and the solution for this cell will therefore converge towards zero. On the other hand, consider the case of a cell for which all fluxes are negative, *i.e.* no flow is leaving the cell. In this case, the convection term does not make a contribution to the central coefficient and the value in this cell would diverge to infinity or minus infinity depending on the initial value.

The contribution of the diffusion term, equation (2.13), are examined next. Consider the following transport equation without convection and additional sources:

$$\frac{\partial \phi}{\partial t} = \nabla \cdot (\Gamma \nabla \phi) \quad (2.38)$$

Equation (2.38) is only physically meaningful and bounded for positive diffusion coefficients (assuming that the solution is carried out forward in time).

The contribution of the diffusion term is a diagonally equal matrix if the mesh

is orthogonal. However, on non-orthogonal meshes, implicit treatment of the non-orthogonal correction term in equation (2.14) would introduce the “second neighbours” of the control volume into the computational molecule with negative coefficients [185]. This violates diagonal equality and, consequently, the boundedness of the solution cannot be guaranteed. A thorough discussion and evaluation of several discretisation practices is given in Jasak [185] and Ferziger and Perić [99]. In this study, the face normal gradient is treated fully implicitly, however, the non-orthogonal correction is evaluated explicitly by interpolating cell centre gradients obtained from Gauss integration. This is expressed in equation (2.28).

Discretisation of the linear part of the source term, equation (2.16), only affects the diagonal coefficients of the matrix. If $S_I < 0$, its contribution increases the diagonal dominance and S_I is included into the diagonal coefficients. In the case of $S_I > 0$, diagonal dominance would be decreased and it is more effective to include this term into the source, which is updated when the new solution is available [99, 301]. However, this measure is not sufficient to guarantee the diagonal dominance of the matrix.

2.6.2 Under-Relaxation

In steady-state calculations, the beneficial influence of the temporal derivative on the diagonal dominance does not exist. Hence, if there is no linear source term with $S_I < 0$ which can be incorporated into the diagonal, the matrix is at best diagonally equal and not suitable for most iterative solvers. In order to enable the use of iterative solvers, the diagonal dominance needs to be enhanced in some other way, namely through under-relaxation. Consider the generic algebraic equation for each control volume presented in Section 2.6:

$$a_P \phi_P^n + \sum_N a_N \phi_N^n = R_P \quad (2.30)$$

Diagonal dominance is created through addition of an artificial term to both the left and right hand side of equation (2.30):

$$a_P \phi_P^n + \frac{1-\lambda}{\lambda} a_P \phi_P^n + \sum_N a_N \phi_N^n = R_P + \frac{1-\lambda}{\lambda} a_P \phi_P^o \quad (2.39)$$

or

$$\frac{a_P}{\lambda} \phi_P^n + \sum_N a_N \phi_N^n = R_P + \frac{1-\lambda}{\lambda} a_P \phi_P^o \quad (2.40)$$

Here, ϕ^n and ϕ^o represent the value of ϕ from the new and previous iteration, respectively. λ is the under-relaxation factor ($0 < \lambda \leq 1$). Hence, a system of linear algebraic equations can be under-relaxed by dividing the diagonal by λ and adding an additional term to the source, leaving the off-diagonal coefficients unchanged. The additional terms cancel out when the solution converges, *i.e.* $\phi^n = \phi^o$.

2.7 Finite Volume Notation

In previous Sections, the finite volume method has been introduced and the discretisation of the standard transport equation has been given as an example. However, it is often necessary to solve the governing equations in non-standard form⁴, usually, in order to guarantee boundedness of the solution. Examples for non-standard governing equations can be found in many complex physics applications like multi-phase flow and combustion. In this study, the phase fraction continuity equation in the two-fluid methodology (see Section 3.2.6) is solved non-standard form.

The extra terms of these governing equations often require special numerical treatment and the exact details of discretisation might vary for each individual term. Hence, Weller introduced a finite volume notation which allows unambiguous specification of the discretisation practices [425].

In this notation, the discretised expression arising from an implicit operator \mathcal{L} is denoted by $\llbracket \mathcal{L}[\phi] \rrbracket$. The operator might be a spatial or temporal derivative or an implicit source term. The dependent variable in the single square brackets is treated implicitly and must be identical in each term of an equation. Note that, explicit terms are not put into double brackets. In this way a distinction between implicit and explicit treatment can be made. A summary is given in Table 2.1.

Following this notation the system of linear algebraic equations arising from the

⁴A differential equation is in “non-standard” form when at least one of its terms does not correspond to a term in the standard transport equation (2.3). We will refer to these terms as “extra” terms.

Term	Term in Finite Volume Notation	Discretised Term
Time Derivative	$\left\llbracket \frac{\partial \rho[\phi]}{\partial t} \right\rrbracket$	$\frac{\rho_P^n \phi_P^n - \rho_P^o \phi_P^o}{\Delta t} V_P$
Convection Term	$\left\llbracket \nabla \cdot \left(F[\phi]_{f(F,S)} \right) \right\rrbracket$	$\sum_f F \phi_{f(F,S)}^n$
Diffusion Term	$\left\llbracket \nabla \cdot (\Gamma \nabla [\phi]) \right\rrbracket$	$\sum_f \Gamma_f \mathbf{S} \cdot \nabla_f \phi^n$
Divergence Term	$\nabla \cdot \phi$	$\sum_f \mathbf{S} \cdot \phi_f^o$
Cell Gradient Term	$\nabla \phi$	$\sum_f \mathbf{S} \phi_f^o$
Curl	$\nabla \times \phi$	$2 * (\text{skew } \nabla \phi^o)$
Implicit Source Term	$\llbracket S_I[\phi] \rrbracket$	$S_I V_P \phi^n$
Explicit Source Term	S_E	$S_E V_P$
Cell Average	$\langle \phi \rangle_{\square}$	$\frac{1}{N} \sum_{P=\square} \phi_P^o$

Table 2.1: Finite volume notation.

discretisation of the standard transport equation (2.3) can be written as:

$$\mathcal{A} := \left\llbracket \frac{\partial \rho[\phi]}{\partial t} \right\rrbracket + \left\llbracket \nabla \cdot \left(\rho \mathbf{U}[\phi]_{f(\rho, \mathbf{U}, S)} \right) \right\rrbracket = \left\llbracket \nabla \cdot (\Gamma \nabla [\mathbf{U}]) \right\rrbracket + \llbracket S_I[\phi] \rrbracket + S_E \quad (2.41)$$

where \mathcal{A} denotes a system of linear algebraic equations. The discretised equation for each cell is identical to the one previously given in equation (2.29).

Once a system of linear algebraic equations is assembled, special operators can be invoked to extract its matrix coefficients and the source vector using $\mathcal{A}_A \equiv [A]$ and $\mathcal{A}_S \equiv [R]$, respectively. Additionally, matrices containing the diagonal and off-diagonal coefficients are obtained from $\mathcal{A}_D \equiv [D]$ and $\mathcal{A}_N \equiv [N]$, respectively.

The “ H ” operator \mathcal{A}_H , introduced below, is used extensively in the numerical procedures outlined in Chapters 3 and 4. At this point, it is introduced by considering the Jacobi iteration scheme. This scheme provides a simple way of obtaining an approximate solution to the system of discretised equations by iterating over:

$$\phi \approx \mathcal{A}_D^{-1} \mathcal{A}_H = \frac{\mathcal{A}_H}{\mathcal{A}_D} \quad (2.42)$$

Note that the inversion of a diagonal matrix is trivial and that we denote this operation by the division operator for reasons of better readability. \mathcal{A}_H is the “ H ” operator defined as:

$$\mathcal{A}_H \equiv \mathcal{A}_S - \mathcal{A}_N\phi \quad (2.43)$$

2.8 Closure

In this Chapter we have described the basis of the finite volume discretisation technique adopted in this study. First, discretisation of the space and time domain were discussed, followed by the variable arrangement and its implications on the pressure-velocity coupling technique. Next, equation and temporal discretisation along with the numerical boundary condition treatment have been outlined. Furthermore, the structure of the resulting systems of linear algebraic equations has been discussed with respect to boundedness and convergence. Finally, a finite volume notation has been put forward which will be utilised in the following Chapters to describe the numerical solution procedures for the two-fluid and interface-capturing methodology in concise and unambiguous manner.

Chapter 3

Two-Fluid Methodology

In this Chapter, the two-fluid methodology is described. Firstly, the governing equations are stated along with basic turbulence and inter-phase momentum transfer modelling. Then, the numerical solution procedure is discussed and the discretised equations are presented together with the overall solution procedure. Finally, the stability and speed of the solution procedure are assessed. The test cases chosen for this purpose are: a sudden enlargement in a circular pipe; phase separation in a tank and a bubble plume.

3.1 Governing Equations

3.1.1 Averaged Phase Momentum and Continuity Equations

As outlined in Section 1.2.3, practical simulations of turbulent flows are usually carried out by solving averaged conservation equations, which describe the mean properties of the flow. In the following, the averaged conservation equations for mass and momentum for an incompressible two-phase system are presented.

Several authors [165, 121, 294, 231] derived averaged equations for the two-fluid model. The final results are very similar and in what follows we present the results of the work of Weller [426] who extended the work of Hill [147]. Both used conditional averaging based on the work of Dopazo [79]. In conditional averaging, the equations are multiplied by an indicator function, which is 1 in phase φ and 0 elsewhere, before standard averaging techniques are applied.

For incompressible fluids, the conditionally averaged momentum and continuity equations for each phase φ are given by:

$$\frac{\partial \alpha_\varphi \bar{\mathbf{U}}_\varphi}{\partial t} + \nabla \cdot (\alpha_\varphi \bar{\mathbf{U}}_\varphi \bar{\mathbf{U}}_\varphi) + \nabla \cdot (\alpha_\varphi \bar{\mathbf{R}}_\varphi^{\text{eff}}) = -\frac{\alpha_\varphi}{\rho_\varphi} \nabla \bar{p} + \alpha_\varphi \mathbf{g} + \frac{\bar{\mathbf{M}}_\varphi}{\rho_\varphi} \quad (3.1)$$

$$\frac{\partial \alpha_\varphi}{\partial t} + \nabla \cdot (\bar{\mathbf{U}}_\varphi \alpha_\varphi) = 0 \quad (3.2)$$

where the subscript φ denotes the phase, α is the phase fraction, $\bar{\mathbf{R}}_\varphi^{\text{eff}}$ is the combined Reynolds (turbulent) and viscous stress, $\bar{\mathbf{M}}_\varphi$ is the averaged inter-phase momentum transfer term. The last two terms arise from the averaging process and require modelling.

Combining equation (3.2) for two phases with $\varphi = a$ and b yields the volumetric continuity equation for the mixture, which will be utilised later to formulate an implicit equation for the pressure. The volumetric continuity equation reads:

$$\nabla \cdot \bar{\mathbf{U}} = 0 \quad (3.3)$$

where $\bar{\mathbf{U}} = \alpha_a \bar{\mathbf{U}}_a + \alpha_b \bar{\mathbf{U}}_b$.

The averaged equations representing the conservation of mass and momentum for each phase have been presented. In the two following Sections the exact form of the closure terms will be given.

3.1.2 Inter-phase Momentum Transfer

In the averaged phase momentum equations for each phase, an expression for the averaged inter-phase momentum transfer term $\bar{\mathbf{M}}_\varphi$ is needed. Conservation of global momentum dictates that the total momentum transferred between the phases is zero, *i.e.* $\sum \mathbf{M}_\varphi = 0$ where the sum is performed over all phases. Hence, after averaging, the total averaged inter-phase momentum transfer also vanishes, *i.e.* $\sum \bar{\mathbf{M}}_\varphi = 0$. Furthermore, it follows for two-phase flows that one expression accounting for the averaged inter-phase momentum transfer from or to one of the two phases is sufficient to close the system. Its derivation starts from the instantaneous forces acting on this phases.

This study deals with the simulation of dispersed flows. Hence, the instantaneous inter-phase momentum transfer is determined by assembling the forces acting on the

Dispersed Phase Elements¹ (DPEs). Its main contributions are due to drag, lift and virtual mass forces. The expressions for some of these forces are the subject of this study and a review as well as revised modelling are presented in later chapters. In this Section, only basic modelling is stated, which will be used to test the performance of the two-fluid solution procedure.

In a second step, the instantaneous inter-phase momentum transfer is averaged. In the averaging process, several additional terms may be produced, most notably the so-called turbulent drag term. In this study, the result obtained by Gosman et al. [121] is utilised.

The instantaneous inter-phase momentum transfer term can be naturally decomposed into its components indicating their different origins:

$$\frac{\mathbf{M}_a V}{\alpha} = \mathbf{F}_d + \mathbf{F}_l + \mathbf{F}_{vm} + \mathbf{F}_o \quad (3.4)$$

where the subscript a denotes the dispersed phase. V stands for the volume of the DPE and \mathbf{F}_d , \mathbf{F}_l , \mathbf{F}_{vm} and \mathbf{F}_o represent respectively the instantaneous drag, lift, virtual mass and other forces like the Basset force [260, 18], which is neglected in most practical calculations [359, 104]. The functional forms of the instantaneous forces have been subject to intensive research [274, 260, 11, 264]. In most two-fluid calculation the following functional forms are utilised:

$$\mathbf{F}_d = \frac{1}{2} \rho_b A C_d |\mathbf{U}_r| \mathbf{U}_r \quad (3.5)$$

$$\mathbf{F}_l = C_l \rho_b V \mathbf{U}_r \times (\nabla \times \mathbf{U}_b) \quad (3.6)$$

$$\mathbf{F}_{vm} = C_{vm} \rho_b V \left(\frac{D_b \mathbf{U}_b}{Dt} - \frac{D_a \mathbf{U}_a}{Dt} \right) \quad (3.7)$$

where $\mathbf{U}_r = \mathbf{U}_b - \mathbf{U}_a$ is the relative velocity. A denotes the projected area of the DPE normal to the relative velocity and $\frac{D\varphi}{Dt}$ stands for the substantive derivative which is defined as:

$$\frac{D\varphi}{Dt} = \frac{\partial}{\partial t} + \mathbf{U}_\varphi \cdot \nabla \quad (3.8)$$

The coefficients C_d , C_l and C_{vm} are usually determined empirically and depend on the properties of the DPE (spherical, rigid *etc.*). They are also functions of the local

¹In this study we use the generic term “Dispersed Phase Element” for bubbles, droplets and particles.

flow field around the DPE [56, 261]. The empirical correlations have been a subject of this work; a review as well as further developments will be presented in Chapters 6 and 7.

A set of simple and reliable models is utilised in this Chapter to study the performance of the numerical solution procedure (Section 3.3). For the drag coefficient C_d the solid particle drag model of Schiller and Naumann [340] is chosen, which reads:

$$C_d = \frac{24}{\mathcal{R}e} (1 + 0.15 \mathcal{R}e^{0.687}) \quad (3.9)$$

where $\mathcal{R}e$ is the particle Reynolds number based on the particle diameter d and the relative velocity \mathbf{U}_r and is defined as $\mathcal{R}e = \frac{\rho_b |\mathbf{U}_r| d}{\mu_b}$.

For the virtual mass coefficient C_{vm} a fixed value of 0.5 [11, 260] is used throughout the present study. In the calculations presented in this Chapter the contribution of the lift force is neglected and its coefficient is set to zero.

In their derivation of the averaged momentum equations, Gosman et al. [121] arrive at an averaged form of the momentum transfer term \mathbf{M}_a which contains an additional term, the so-called turbulent drag term. This term accounts for additional drag due to the fluctuations in the dispersed phase. However, fluctuations occurring in the virtual mass and lift forces are neglected. Their model proposed for the total inter-phase momentum transfer reads:

$$\begin{aligned} \overline{\mathbf{M}}_a &= \alpha_a C_d \frac{3}{4} \frac{\rho_b}{d_a} |\overline{\mathbf{U}}_r| \overline{\mathbf{U}}_r && \text{Drag} \\ &+ \alpha_a C_l \rho_b \overline{\mathbf{U}}_r \times (\nabla \times \overline{\mathbf{U}}_b) && \text{Lift} \\ &+ \alpha_a C_{vm} \rho_b \left(\frac{D_b \overline{\mathbf{U}}_b}{Dt} - \frac{D_a \overline{\mathbf{U}}_a}{Dt} \right) && \text{Virtual Mass} \\ &- C_d \frac{3}{4} \frac{\rho_b}{d} \frac{\nu^t}{\sigma_\alpha} |\overline{\mathbf{U}}_r| \nabla \alpha_a && \text{Turbulent Drag} \end{aligned} \quad (3.10)$$

where ν^t is the turbulent viscosity given in Section 3.1.3 and d_a is the diameter of a DPE.

Equation (3.10) cannot be used to model phase inversion or separating flows, *e.g.* in a bubble column (see Section 1.1). In such flows, regions where the originally dispersed phase becomes the continuous phase and vice versa exist simultaneously. This is not taken into account in equation (3.10), which is formulated assuming that phase a is dispersed in phase b . However, in regions where $\alpha_a \rightarrow 1$, phase b is dispersed

in phase a and, for example, a different particle diameter should be used in the drag term. This second diameter d_b is defined as the diameter of a characteristic DPE of phase b in the now continuous phase a , *e.g.* the diameter of a droplet in a gas phase.

It has been proposed by Weller [426] to use the following simple model over the full range of phase fractions for testing the numerical stability of the solution procedure:

$$\begin{aligned} \bar{\mathbf{M}}_a = & \frac{3}{4}\alpha_a\alpha_b \left(f_a \frac{C_{da}\rho_b}{d_a} + f_b \frac{C_{db}\rho_a}{d_b} \right) |\bar{\mathbf{U}}_r| \bar{\mathbf{U}}_r && \text{Drag} \\ & + \alpha_a\alpha_b f_a (C_{la}\rho_b \bar{\mathbf{U}}_r \times (\nabla \times \bar{\mathbf{U}}_a)) && \text{Lift} \quad (3.11) \\ & + \alpha_a\alpha_b f_b (C_{lb}\rho_a \bar{\mathbf{U}}_r \times (\nabla \times \bar{\mathbf{U}}_b)) \\ & + \alpha_a\alpha_b (f_a C_{vma}\rho_b + f_b C_{vmb}\rho_a) \left(\frac{D_b \bar{\mathbf{U}}_b}{Dt} - \frac{D_a \bar{\mathbf{U}}_a}{Dt} \right) && \text{Virtual Mass} \end{aligned}$$

where the modifier function f_a is a function of the phase fraction such that $f_a \rightarrow 0$ for $\alpha_a \rightarrow 0$ and $f_a \rightarrow 1$ for $\alpha_a \rightarrow 1$. f_b is given by $f_b = 1 - f_a$.

In the limit of $f_a \rightarrow 1$, the momentum transfer is modelled as if the previously continuous phase b is now dispersed in phase a . To do this realistically, a second diameter d_b as well as a second set of model coefficients, *e.g.* C_{db} , are required.

In the limit of $f_a \rightarrow 0$, equation (3.11) is equivalent to equation (3.10) except for the turbulent drag term. Close to a free surface (see Section 1.1), the phase fraction changes rapidly and its gradient is infinite. Hence, terms which are proportional to the phase fraction gradient, such as the turbulent drag term, are infinite and cause severe numerical instabilities. It should be mentioned that the turbulent drag term is not applicable the vicinity of free-surfaces, but should be applied elsewhere. However, the turbulent drag is neglected in equation (3.11) and further modelling work is required to derive a more general formulation.

Weller [426] originally proposed $f_a = \alpha_a$. However, this formulation is not very realistic when $C_{da}\rho_b d_b \ll C_{db}\rho_a d_a$ or vice versa because the terminal velocity of DPEs comprised of phase a in phase b is reduced heavily even for moderate values of the phase fraction. This problem can be overcome by choosing a stronger function of the phase fraction to calculate f_a . One possibility, which proved satisfactory in this study, is:

$$f_a = \frac{1 + \tanh(K_w(\alpha_a - K_c))}{2} \quad (3.12)$$

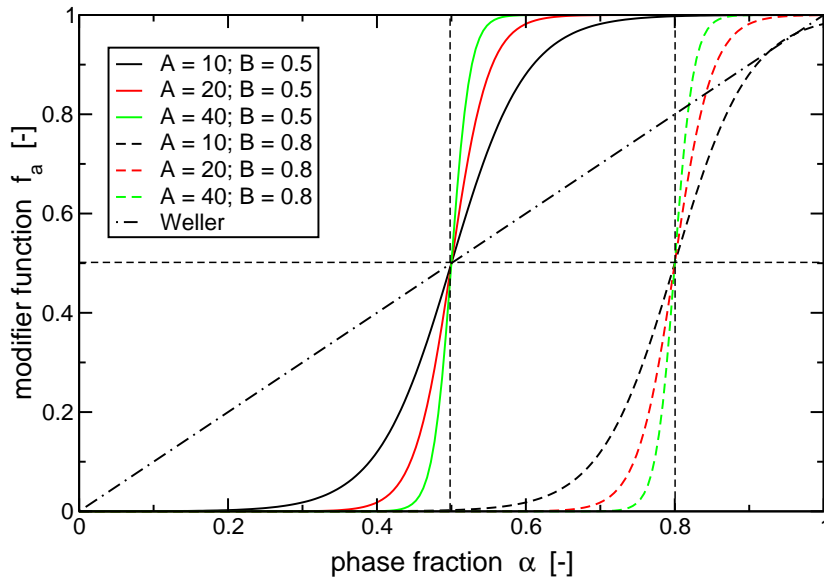


Figure 3.1: Modifier function f_a as a function of the phase fraction α for different values A and B .

where K_w and K_c define respectively the width and centre of the transition region in α space. Equation (3.12) is plotted in Figure 3.1 for several values of A and K_c . In this study, $K_w = 20$ and $K_c = 0.5$ are used.

The inter-phase momentum transfer term (3.4) can be written in a generic form, which is used in the following discussion of the solution procedure where the exact formulation of the inter-phase momentum transfer model is not important. It reads:

$$\begin{aligned}
 \bar{\mathbf{M}}_a = & A_d \bar{\mathbf{U}}_r && \text{Drag} \\
 & + A_{l_b} \bar{\mathbf{U}}_r \times (\nabla \times \bar{\mathbf{U}}_b) && \text{Lift} \\
 & + A_{l_a} \bar{\mathbf{U}}_r \times (\nabla \times \bar{\mathbf{U}}_a) && \\
 & + A_{vm} \left(\frac{D_b \bar{\mathbf{U}}_b}{Dt} - \frac{D_a \bar{\mathbf{U}}_a}{Dt} \right) && \text{Virtual Mass} \\
 & + A_\alpha \nabla \alpha && \text{Turbulent Drag}
 \end{aligned} \tag{3.13}$$

where A_d, A_l, A_{vm} and A_α are multiplier terms, which are defined by comparison with a particular inter-phase momentum transfer model, *e.g.* equation (3.10) or equation (3.11). They are summarised in Table 3.1.

multiplier term	Gosman et al. [121] equation (3.10)	Weller [426] equation (3.11)
A_d	$\alpha_a \frac{3}{4} \frac{\rho_b}{d_a} C_d \bar{\mathbf{U}}_r $	$\alpha_a \alpha_b \frac{3}{4} \left(f_a \frac{C_{da}\rho_b}{d_a} + f_b \frac{C_{db}\rho_a}{d_b} \right) \bar{\mathbf{U}}_r $
A_{la}	0	$\alpha_a \alpha_b f_a C_{la} \rho_b$
A_{lb}	$\alpha_a C_l \rho_b$	$\alpha_a \alpha_b f_b C_{lb} \rho_a$
A_{vm}	$\alpha_a C_{vm} \rho_b$	$\alpha_a \alpha_b (f_a C_{vma} \rho_b + f_b C_{vmb} \rho_a)$
A_α	$\frac{3}{4} C_d \frac{\rho_b}{d} \frac{\nu^t}{\sigma_\alpha} \bar{\mathbf{U}}_r $	0

Table 3.1: Multiplier terms in inter-phase momentum transfer term.

C_μ	C_1	C_2	C_3	σ_k	σ_ε	σ_α	C_i
0.09	1.44	1.92	1.0	1.0	1.0	1.3	C_t

Table 3.2: Coefficients in the two-phase $k - \varepsilon$ -model.

3.1.3 Turbulence Model by Gosman et al. [121]

Two-fluid turbulence models have been reviewed in Section 1.5.6. In this study, the turbulence model by Gosman et al. [121] is adopted. Recent developments of this model have been published in [172, 174, 173, 23, 24]. It consists of the standard $k - \varepsilon$ -model [230] with additional source terms to incorporate the effects of the dispersed phase on the turbulence. The modified $k - \varepsilon$ -model equations are:

$$\frac{\partial k_b}{\partial t} + (\bar{\mathbf{U}}_b \cdot \nabla) k_b - \nabla \cdot \left(\frac{\nu_b^{eff}}{\sigma_k} \nabla k_b \right) = P_b - \varepsilon_b + S_k \quad (3.14)$$

$$\frac{\partial \varepsilon_b}{\partial t} + (\bar{\mathbf{U}}_b \cdot \nabla) \varepsilon_b - \nabla \cdot \left(\frac{\nu_b^{eff}}{\sigma_\varepsilon} \nabla \varepsilon_b \right) = \frac{\varepsilon_b}{k_b} (C_1 P_b - C_2 \varepsilon_b) + S_\varepsilon \quad (3.15)$$

Here, P_b stands for the production of turbulent kinetic energy and is defined as $P_b = 2\nu_b^{eff} \left(\nabla \bar{\mathbf{U}}_b \cdot \text{dev} \left(\nabla \bar{\mathbf{U}}_b + (\nabla \bar{\mathbf{U}}_b)^T \right) \right)$. The effective viscosity of the continuous phase ν_b^{eff} is calculated from $\nu_b^{eff} = \nu_b + \nu^t$ where ν^t is given by $\nu^t = C_\mu \frac{k_b^2}{\varepsilon_b}$. The values of both the Schmidt numbers σ_k and σ_ε as well as the model coefficients C_1 and C_2 are left unchanged from those originally derived for single-phase flow. They are summarised in Table 3.2.

The additional two-phase source terms are:

$$S_k = \frac{2k_b\alpha_a A_d(C_i - 1)}{\rho_b} + \frac{A_d\nu^t}{\rho_b\sigma_\alpha} \frac{\nabla\alpha_a}{\alpha_b} \cdot \bar{\mathbf{U}}_r \quad (3.16)$$

$$S_\varepsilon = \frac{2C_3\varepsilon_b\alpha_a A_d(C_i - 1)}{\rho_b} \quad (3.17)$$

Here, the drag multiplier term A_d , which depends on the exact form the inter-phase momentum transfer, is defined in Table 3.1. The coefficient C_i is set equal to the turbulence response function C_t , *i.e.* $C_i = C_t$. C_t is defined as the ratio of the r.m.s. of dispersed phase velocity fluctuations to those of the continuous phase, given by:

$$C_t = \frac{U'_a}{U'_b} \quad (1.17)$$

where U'_a and U'_b are the r.m.s. of the fluctuations in the velocities of the dispersed and continuous phase, respectively.

Various authors have derived equations for C_t , *e.g.* [121, 171, 52, 24]. In this Chapter, we use the one proposed by Issa [171] which was validated by Hill et al. [148, 147] in a related study. It is derived by considering the Lagrangian equation of motion for a single DPE within a turbulent continuous phase and is given by:

$$C_t = \frac{3 + \beta}{1 + \beta + 2\rho_d/\rho_b} \quad (3.18)$$

$$\beta = \frac{2A_d L_e^2}{\rho_b \nu_b \mathcal{R}e_t} \quad (3.19)$$

where ν_b is the kinematic viscosity of the continuous phase and $\mathcal{R}e_t$ is the turbulence Reynolds based on the eddy length scale L_e and the r.m.s. of the liquid velocity fluctuations U'_b :

$$\mathcal{R}e_t = \frac{U'_b L_e}{\nu_b} \quad (3.20)$$

$$L_e = C_\mu \frac{k^{1.5}}{\varepsilon_b} \quad (3.21)$$

$$U'_b = \sqrt{\frac{2k_b}{3}} \quad (3.22)$$

Using the definition of C_t , the turbulent kinetic energy and the effective viscosity of the dispersed phase can be calculated from $k_a = C_t^2 k_b$ and $\nu_a^{\text{eff}} = \nu_a + C_t^2 \nu^t$, respectively. The model presented above does not take into account the effect of the phase

fraction on C_t . Hence, a modified version of this model will be developed and validated in Chapter 5.

Finally, the Reynolds stresses are obtained from the Boussinesq hypothesis [35], which models the turbulent stress-strain relation analogous to the constitutive relation of a viscous fluid. It is given by:

$$\bar{\mathbf{R}}_{\varphi}^{\text{eff}} = -\nu_{\varphi}^{\text{eff}}(\nabla \bar{\mathbf{U}}_{\varphi} + \nabla \bar{\mathbf{U}}_{\varphi}^T - \frac{2}{3}\mathbf{I}\nabla \cdot \bar{\mathbf{U}}_{\varphi}) + \frac{2}{3}\mathbf{I}k_{\varphi} \quad (3.23)$$

Basic Mixture Turbulence Model

The above turbulence model is not suitable for cases where the phases separate completely, for two reasons: firstly, the k_b and ε_b equation are not well defined when α_a approaches unity; secondly, the turbulent drag term $A_a\nabla\alpha_a$ is infinite close to a free-surface, as explained in Section 3.1.2. Hence, for the numerical tests conducted in this chapter the following simpler model, which does not exhibit these singularities, is used.

$$\frac{\partial k}{\partial t} + \nabla \cdot (\bar{\mathbf{U}}k) - \nabla \cdot \left(\frac{\nu^t}{\sigma_k} \nabla k \right) = P - \varepsilon \quad (3.24)$$

$$\frac{\partial \varepsilon}{\partial t} + \nabla \cdot (\bar{\mathbf{U}}\varepsilon) - \nabla \cdot \left(\frac{\nu^t}{\sigma_{\varepsilon}} \nabla \varepsilon \right) = \frac{\varepsilon}{k}(C_1P - C_2\varepsilon) \quad (3.25)$$

Here, k and ε are defined as mixture properties and the production term P is based on the mixture velocity defined as $\bar{\mathbf{U}} = \alpha_a \bar{\mathbf{U}}_a + \alpha_b \bar{\mathbf{U}}_b$. The model is not claimed to be rigorous and is only intended to serve as a vehicle to test numerical solution procedure under extreme conditions until a better model becomes available.

3.2 Solution Procedure

The numerical solution procedure for the two-fluid methodology is described in this Section. It is based on the procedures described by [426, 295, 147] and utilises the PISO (Pressure Implicit with Splitting of Operators) algorithm [170] to handle the pressure-velocity coupling. It involves a momentum predictor and a correction loop in which a pressure equation based on the volumetric continuity equation is solved and the momentum is corrected based on the pressure change. This part of the procedure is given in Section 3.2.1 to 3.2.4. The transport equations for the phase fraction as well as the turbulent kinetic energy and its dissipation rate are solved only once per

time step/iteration at the end of the sequence. Sections 3.2.6 and 3.2.7 deal with the details of their solution, respectively. Next, the boundary conditions are specified in Section 3.2.8 and, finally, the solution procedure is summarised in Section 3.2.9.

3.2.1 Phase-Intensive Momentum Equation

In the limit of one of the phase fractions approaching zero, the momentum equation becomes singular for that phase when written as in equation (3.1). Various numerical tricks may be used to avoid this problem, *e.g.* limiting α_φ such that $\alpha_\varphi \rightarrow \delta$ where $0 < \delta \ll 1$ or by forcing $\lim_{\alpha_\varphi \rightarrow 0} \tilde{\mathbf{U}}_\varphi = \tilde{\mathbf{U}}_\varphi^*$ where $\tilde{\mathbf{U}}_\varphi^*$ is some limiting value of $\tilde{\mathbf{U}}_\varphi$ obtained from a model.

None of these approaches is satisfactory and Weller [426] proposed to circumvent the problem by dividing the phase momentum equation by α_φ in order to produce a “phase-intensive” version of the momentum equation equation (3.1).

$$\frac{\partial \overline{\mathbf{U}}_\varphi}{\partial t} + \overline{\mathbf{U}}_\varphi \cdot \nabla \overline{\mathbf{U}}_\varphi + \nabla \cdot \overline{\mathbf{R}}_\varphi^{\text{eff}} + \frac{\nabla \alpha_\varphi}{\alpha_\varphi} \cdot \overline{\mathbf{R}}_\varphi^{\text{eff}} = -\frac{\nabla \bar{p}}{\rho_\varphi} + \mathbf{g} + \frac{\overline{\mathbf{M}}_\varphi}{\alpha_\varphi \rho_\varphi} \quad (3.26)$$

The problem has been solved in a similar fashion by Kashiwa et al. [196]. They motivate their choice of working variables as follows: “Using velocity rather than momentum; one does not have to divide out the total mass to define the velocity from the total momentum. This avoids numerical noise from creeping into the data as the phase fraction approaches zero.”

Two terms in equation (3.26), the fourth term on the l.h.s., which represents parts of the Reynolds stress term, and the inter-phase momentum transfer term, contain the phase fraction in the denominator. However, they do not become infinite when the phase fraction vanishes for the following reasons: the former term is also multiplied by the gradient of the phase fraction. As outlined by Weller [426], the ratio of the phase fraction gradient and the phase fraction approaches zero as the phase fraction vanishes and this term is discretised as outlined in Section 2.3.8 to ensure stability. The inter-phase momentum transfer term is comprised of several contribution, which are summarised for two models in Table 3.1. It is evident, that every term in the model of Weller [426] contains the product of the phase fractions $\alpha_a \alpha_b$ and, hence, can be divided by α_a or α_b without problems. On the other hand, the drag, lift and

virtual mass terms in the model by Gosman et al. [121] contain only the dispersed phase fraction. Here, problems arise for $\alpha_b \rightarrow 0$. However, it should be noted that this model is not applicable in this situation, as pointed out earlier. Similar arguments apply to the turbulent drag term: for $\alpha_a \rightarrow 0$, the turbulent drag term is proportional to $\frac{\nabla \alpha_a}{\alpha_a}$, which is finite; and for $\alpha_b \rightarrow 0$, the model is not applicable.

3.2.2 Discretisation of the Phase Momentum Equations

Let us consider the convective and diffusive transport terms, *i.e.* the l.h.s. of the phase momentum equation (3.26):

$$\frac{\partial \bar{\mathbf{U}}_\varphi}{\partial t} + \bar{\mathbf{U}}_\varphi \cdot \nabla \bar{\mathbf{U}}_\varphi + \nabla \cdot \bar{\mathbf{R}}_\varphi^{\text{eff}} + \frac{\nabla \alpha_\varphi}{\alpha_\varphi} \cdot \bar{\mathbf{R}}_\varphi^{\text{eff}} = \dots \quad (3.27)$$

For numerical implementation it is useful to decompose the Reynolds stress terms into a diffusive component and a correction:

$$\bar{\mathbf{R}}_\varphi^{\text{eff}} = \bar{\mathbf{R}}_\varphi^{\text{effD}} + \bar{\mathbf{R}}_\varphi^{\text{effC}} \quad (3.28)$$

where $\bar{\mathbf{R}}_\varphi^{\text{effD}} = -\nu_\varphi^{\text{eff}} \nabla \bar{\mathbf{U}}_\varphi$ and $\bar{\mathbf{R}}_\varphi^{\text{effC}} = \bar{\mathbf{R}}_\varphi^{\text{eff}} + \nu_\varphi^{\text{eff}} \nabla \bar{\mathbf{U}}_\varphi$.

Modelling the Reynolds stress according to the Boussinesq eddy viscosity hypothesis, equation (3.23), leads to a Reynolds stress correction term of the following form:

$$\bar{\mathbf{R}}_{\text{eff}\varphi}^{\text{C}} = -\nu_\varphi^{\text{eff}} \left(\nabla \bar{\mathbf{U}}_\varphi^T - \frac{2}{3} \mathbf{I} \nabla \cdot \bar{\mathbf{U}}_\varphi \right) + \frac{2}{3} \mathbf{I} \bar{k}_\varphi \quad (3.29)$$

Re-substitution of equation (3.28) into the l.h.s. of the phase momentum equation (3.27), gives:

$$\frac{\partial \bar{\mathbf{U}}_\varphi}{\partial t} + \bar{\mathbf{U}}_\varphi^T \cdot \nabla \bar{\mathbf{U}}_\varphi - \nabla \cdot (\nu_\varphi^{\text{eff}} \nabla \bar{\mathbf{U}}_\varphi) + \nabla \cdot \bar{\mathbf{R}}_\varphi^{\text{effC}} + \frac{\nabla \alpha_\varphi}{\alpha_\varphi} \cdot \bar{\mathbf{R}}_\varphi^{\text{effC}} = \dots \quad (3.30)$$

where a total phase velocity is defined as:

$$\bar{\mathbf{U}}_\varphi^T = \bar{\mathbf{U}}_\varphi - \nu_\varphi^{\text{eff}} \frac{\nabla \alpha_\varphi}{\alpha_\varphi} \quad (3.31)$$

Starting from equation (3.30), the convective and diffusive transport terms are discretised. The time derivative, convection and diffusion terms are handled implicitly and

the Reynolds stress correction is handled explicitly. The discretised terms for the l.h.s. of phase momentum equation then read:

$$\begin{aligned} \boldsymbol{\mathcal{T}}_\varphi &= \left[\frac{\partial[\bar{\mathbf{U}}_\varphi]}{\partial t} \right] + \left[\nabla \cdot (\phi_\varphi^\mathcal{T} [\bar{\mathbf{U}}_\varphi]_{f(\phi_\varphi^\mathcal{T}, S)}) \right] - \left[\nabla \cdot (\phi_\varphi^\mathcal{T}) [\bar{\mathbf{U}}_\varphi] \right] \\ &\quad - \left[\nabla \cdot (\nu_\varphi^{\text{eff}} \nabla [\bar{\mathbf{U}}_\varphi]) \right] + \nabla \cdot \bar{\mathbf{R}}_a^{\text{effC}} + \frac{\nabla \alpha_\varphi}{\langle \alpha_\varphi \rangle_\nabla + \delta} \cdot \bar{\mathbf{R}}_a^{\text{effC}} \end{aligned} \quad (3.32)$$

Here, $\phi_\varphi^\mathcal{T}$ denotes the total phase flux. It is calculated by interpolating equation (3.31) to the face centres, thus:

$$\phi_\varphi^\mathcal{T} = \phi_\varphi - \nu_{\varphi_f}^{\text{eff}} \frac{\nabla_f^\perp \alpha_\varphi}{\alpha_{\varphi_f} + \delta} \quad (3.33)$$

where ϕ_φ is the volumetric phase flux defined as $\phi_\varphi = \mathbf{S} \cdot (\bar{\mathbf{U}}_\varphi)_f$. However, it is a result of the pressure-velocity solution procedure outlined in Section 3.2.4 and is *not* evaluated by taking the dot product of the face area vector and the face interpolate of the velocity as this would not obey continuity

We will now focus our attention to the treatment of the terms on the r.h.s. of the phase momentum equation (3.26). They are:

$$\dots = -\frac{\nabla \bar{p}}{\rho_\varphi} + \mathbf{g} + \frac{\bar{\mathbf{M}}_\varphi}{\alpha_\varphi \rho_\varphi} \quad (3.34)$$

where $\bar{\mathbf{M}}_a = -\bar{\mathbf{M}}_b$ is given by:

$$\begin{aligned} \bar{\mathbf{M}}_a &= A_d \bar{\mathbf{U}}_r && \text{Drag} \\ &+ A_{l_b} \bar{\mathbf{U}}_r \times (\nabla \times \bar{\mathbf{U}}_b) && \text{Lift} \\ &+ A_{l_a} \bar{\mathbf{U}}_r \times (\nabla \times \bar{\mathbf{U}}_a) && \\ &+ A_{vm} \left(\frac{D_b \bar{\mathbf{U}}_b}{Dt} - \frac{D_a \bar{\mathbf{U}}_a}{Dt} \right) && \text{Virtual Mass} \\ &+ A_\alpha \nabla \alpha && \text{Turbulent Drag} \end{aligned} \quad (3.13)$$

Almost all of the terms in equation (3.34), such as the pressure gradient and inter-phase momentum transfer term, require special treatment. For example, it is well-known that careful discretisation of the pressure gradient prevents pressure-velocity decoupling and the occurrence of oscillations (checker-boarding) in the pressure field [301, 99, 413, 305, 304]. In this study, the simple cure proposed by Rhie and Chow [318] has been adopted. However, similar problems arise with other gradient terms,

in particular, the turbulent drag term, which is proportional to $\nabla\alpha_\varphi$. It is therefore treated along with the pressure gradient term in a Rhie and Chow-like manner, which is explained in detail in Sections 3.2.4 and 3.2.6. The remaining contributions to the inter-phase momentum transfer term are due to drag, lift and virtual mass forces. Section 3.2.5 is devoted to the discussion of their discretisation. The discretised terms arising from these terms are denoted \mathcal{M}_φ .

Initial estimates for the phase velocities can be obtained by solving the complete systems of discretised equations for the two momentum equations, which now read:

$$\boldsymbol{\mathcal{T}}_\varphi = -\frac{\nabla\bar{p}}{\rho_\varphi} + \mathbf{g} + \mathcal{M}_\varphi - \frac{A_\alpha \nabla\alpha_\varphi}{\rho_\varphi \alpha_\varphi} \quad (3.35)$$

The solution of equation (3.35) yields estimates for the velocity, which are not guaranteed to obey continuity. Continuity is achieved by correcting the velocities using an updated pressure field, which is chosen such that continuity is satisfied.

3.2.3 Phase Momentum Correction Equations

The phase momentum correction and pressure equation will be derived from a semi-discretised form of the momentum equation:

$$(\mathcal{A}_\varphi)_D \bar{\mathbf{U}}_\varphi = (\mathcal{A}_\varphi)_H - \frac{\nabla\bar{p}}{\rho_\varphi} - \frac{A_\alpha \nabla\alpha_\varphi}{\alpha_\varphi \rho_\varphi} \quad (3.36)$$

where the “*H*” operator $(\cdot)_H$ and diagonal $(\cdot)_D$ operator are defined in Section 2.7. \mathcal{A}_φ denotes the system of linear algebraic equations arising from the discretisation of the phase momentum equations without terms which are proportional to $\nabla\alpha_\varphi$ or $\nabla\bar{p}$:

$$\mathcal{A}_\varphi := \boldsymbol{\mathcal{T}}_\varphi = \mathbf{g} + \mathcal{M}_\varphi \quad (3.37)$$

In the spirit of Rhie and Chow [318], these gradient terms are not discretised at this stage. Rearranging equation (3.36) yields the phase momentum correction equations:

$$\bar{\mathbf{U}}_\varphi = \frac{(\mathcal{A}_\varphi)_H}{(\mathcal{A}_\varphi)_D} - \frac{\nabla\bar{p}}{\rho_\varphi (\mathcal{A}_\varphi)_D} - \frac{A_\alpha \nabla\alpha_\varphi}{\alpha_\varphi \rho_\varphi (\mathcal{A}_\varphi)_D} \quad (3.38)$$

Later, Equation (3.38) will be used to correct the velocities after an updated pressure field is obtained by solving the pressure equation.

3.2.4 Pressure Equation

In single-phase pressure correction methods the continuity equation is recast into one for pressure by substituting the momentum equation into it [301, 99, 413]. Such an equation for pressure may be derived in differential form [379]. However, subsequent discretisation of this equation may be inconsistent with the discretisation of the momentum equation and is inadvisable. Instead, a semi-discretised momentum equation is substituted into the continuity equation.

The solution of the pressure equation provides corrections for updating pressure, fluxes and velocities so that continuity is obeyed. However, in the two-fluid model, there are two phase continuity equations and, therefore, there is more freedom and more difficulty in formulating the pressure equation. A general approach is to form a mixture continuity equation by linearly combining the phase continuity equations 3.2 using appropriate weighting factors w_φ :

$$\frac{\rho_a}{w_a} \frac{\partial \alpha_a}{\partial t} + \frac{\rho_a}{w_a} \nabla \cdot (\bar{\mathbf{U}}_a \alpha_a) + \frac{\rho_b}{w_b} \frac{\partial \alpha_b}{\partial t} + \frac{\rho_b}{w_b} \nabla \cdot (\bar{\mathbf{U}}_b \alpha_b) = 0 \quad (3.39)$$

The above equation becomes the mixture mass continuity equation if the weighting factors are unity, and the volumetric mixture continuity if the weighting factors are the phase densities.

Carver [44] and Vaidya et al. [408] noted that the lighter phase is poorly conserved when the mixture mass continuity equation is used. This is due to the fact that the lighter phase hardly influences the mixture mass imbalance. This problem can be considerably alleviated by using volumetric mixture continuity instead. Following this route, we chose to solve for the mixture pressure by recasting the volumetric mixture continuity equation (3.3) into one for pressure. To achieve this, it is formulated at the cell faces, such that:

$$\nabla \cdot (\alpha_{af} \phi_a + \alpha_{bf} \phi_b) = 0 \quad (3.40)$$

Next, expressions for the volumetric phase fluxes ϕ_φ for each phase are derived by interpolating the momentum correction equation (3.38) to the face centres. Using central differencing, they are given by:

$$\phi_\varphi = \phi_\varphi^* - \left(\frac{1}{\rho_\varphi(\mathcal{A}_\varphi)_D} \right)_f |\mathbf{S}| \nabla_f^\perp \bar{p} \quad (3.41)$$

where the flux predictions ϕ_φ^* are given by:

$$\phi_\varphi^* = \left(\frac{(\mathcal{A}_\varphi)_H}{(\mathcal{A}_\varphi)_D} \right)_f \cdot \mathbf{S} - \left(\frac{1}{\rho_\varphi (\mathcal{A}_\varphi)_D} \right)_f \frac{A_{\alpha_f} |\mathbf{S}| \nabla_f^\perp \alpha_\varphi}{\alpha_{\varphi_f}} \quad (3.42)$$

The flux predictions are composed of two parts: the first contribution originates from the “H”-operator, which is evaluated by re-substituting the velocity estimates obtained earlier into their discretised equations and the second one is due to the turbulent drag term.

Now, the advantages of discretising terms which are proportional to gradients in the pressure and the phase fraction separately become apparent. Discretisation of the phase fraction gradients is performed for each face, requiring a smaller computational molecule and, hence, is more stable. However, more importantly, the pressure equation can now be constructed by substituting equation (3.41) into equation (3.40) and the pressure gradient is discretised implicitly as a diffusion term:

$$\left[\nabla \cdot \left(\left(\alpha_{af} \left(\frac{1}{\rho_a (\mathcal{A}_a)_D} \right)_f + \alpha_{bf} \left(\frac{1}{\rho_b (\mathcal{A}_b)_D} \right)_f \right) \nabla [\bar{p}] \right) \right] = \nabla \cdot (\alpha_{af} \phi_a^* + \alpha_{bf} \phi_b^*) \quad (3.43)$$

In essence, the mixture pressure field is determined in a way that guarantees continuity of the volumetric mixture flux. The individual phase fluxes are corrected after the pressure solution using equation (3.41). It has to be noted that these are not guaranteed to obey conservation at this point; this task is left to the solution of the phase continuity equations explained in detail in Section 3.2.6.

3.2.5 Practices for the Inter-phase Momentum Transfer Term

The magnitude, linearity and uniformity of the inter-phase momentum transfer term in the momentum equation (3.4) are known to affect the robustness and stability characteristics of the two-fluid solution procedure. Therefore, its numerical treatment deserves special attention. A generic equation (3.13) for the inter-phase momentum transfer term has been defined in Section 3.1.2. Its main contributions are drag, lift and virtual mass and turbulent drag. The turbulent drag term requires special treatment, which is discussed in detail in the Sections 3.2.4 and 3.2.6. Hence, no further discussion is needed here.

In the following, the terms due to drag, lift and virtual mass forces are discretised. The discretised terms are denoted \mathcal{M}_φ^d , \mathcal{M}_φ^l and \mathcal{M}_φ^{vm} and their total contribution to the discretised momentum equation (3.35) is $\mathcal{M}_\varphi = \mathcal{M}_\varphi^d + \mathcal{M}_\varphi^l + \mathcal{M}_\varphi^{vm}$.

There are many ways to implement the drag, lift and virtual mass terms and common implementation strategies are discussed next on a term-by-term basis. For the drag term $A_d \bar{\mathbf{U}}_r$, several options have been discussed in the literature:

1. The drag term is treated semi-implicitly in the dispersed phase momentum equation and fully explicitly in the continuous phase momentum equation. This treatment has been preferred by Politis [310] and is written using the finite volume notation as:

$$\mathcal{M}_a^d = \frac{\alpha_b A_d}{\rho_a} (\bar{\mathbf{U}}_b - [[\bar{\mathbf{U}}_a]]) \quad (3.44)$$

$$\mathcal{M}_b^d = \frac{\alpha_a A_d}{\rho_b} \bar{\mathbf{U}}_r \quad (3.45)$$

2. The drag term are treated semi-implicitly in both the dispersed and continuous phase momentum equations and the discretised terms read:

$$\mathcal{M}_a^d = \frac{\alpha_b A_d}{\rho_a} (\bar{\mathbf{U}}_b - [[\bar{\mathbf{U}}_a]]) \quad (3.46)$$

$$\mathcal{M}_b^d = \frac{\alpha_a A_d}{\rho_b} (\bar{\mathbf{U}}_a - [[\bar{\mathbf{U}}_b]]) \quad (3.47)$$

3. The partial elimination method of Spalding [356] uses the discretised momentum equations to partially eliminate the phase velocities from the drag terms. Variations of this method have been used by [135, 134, 294, 296] in their two-phase flow solution procedure and implementation details are given there.
4. For highly non-linear drag situations, Hill [147] proposed to solve the difference of the discretised momentum equations for $\bar{\mathbf{U}}_r$ iteratively on a point-by-point basis. The updated values are then used in the partial elimination method (option 3) to construct \mathcal{M}_φ^d .

The first three options have been investigated by Oliveira and Issa [296]. They came to the conclusion that although options 1 and 3 behave similarly when the drag multiplier is not too large, only option 3 ensures convergence when it is high or very

non-uniform. However, this is not the case in the present study and option 2 is used throughout this study.

Treatments for the virtual mass term $A_{vm} \left(\frac{D_b \bar{\mathbf{U}}_b}{Dt} - \frac{D_a \bar{\mathbf{U}}_a}{Dt} \right)$ have not been discussed in the literature, but a semi-implicit treatment similar to option 2 for drag is used in this study. It reads:

$$\mathcal{M}_a^{vm} = \frac{\alpha_b A_{vm}}{\rho_a} \left(\frac{D_b \bar{\mathbf{U}}_b}{Dt} - \left[\left[\frac{D_a [\bar{\mathbf{U}}_a]}{Dt} \right] \right] \right) \quad (3.48)$$

$$\mathcal{M}_b^{vm} = \frac{\alpha_a A_{vm}}{\rho_b} \left(\frac{D_a \bar{\mathbf{U}}_a}{Dt} - \left[\left[\frac{D_b [\bar{\mathbf{U}}_b]}{Dt} \right] \right] \right) \quad (3.49)$$

where the explicit substantive derivatives are given by:

$$\frac{D_a \bar{\mathbf{U}}_a}{Dt} = \frac{\partial \bar{\mathbf{U}}_a}{\partial t} + \nabla \cdot (\phi_a \bar{\mathbf{U}}_{af(\phi_a, S)}) - \bar{\mathbf{U}}_a \nabla \cdot (\phi_a) \quad (3.50)$$

$$\frac{D_b \bar{\mathbf{U}}_b}{Dt} = \frac{\partial \bar{\mathbf{U}}_b}{\partial t} + \nabla \cdot (\phi_b \bar{\mathbf{U}}_{bf(\phi_b, S)}) - \bar{\mathbf{U}}_b \nabla \cdot (\phi_b) \quad (3.51)$$

Note that the third terms on the r.h.s. of equations (3.50) and (3.51), can be important in gas-liquid flows despite the fact that their values are usually quite small. This is the case for the explicit part of equation (3.48) where the substantive derivative of the continuous phase velocity is multiplied by 500 because of the large density ratio.

Unfortunately, the functional form of the lift force $-A_l \bar{\mathbf{U}}_r \times (\nabla \times \bar{\mathbf{U}}_b)$, which has a pronounced effect on the phase fraction distribution in some cases, makes its implicit treatment extremely difficult. Although an explicit treatment is known to compromise convergence, it has been adopted in this study:

$$\mathcal{M}_a^l = -\frac{A_{la}}{\alpha_a \rho_a} \bar{\mathbf{U}}_r \times (\nabla \times \bar{\mathbf{U}}_b) - \frac{A_{lb}}{\alpha_a \rho_a} \bar{\mathbf{U}}_r \times (\nabla \times \bar{\mathbf{U}}_b) \quad (3.52)$$

$$\mathcal{M}_b^l = \frac{A_{la}}{\alpha_b \rho_b} \bar{\mathbf{U}}_r \times (\nabla \times \bar{\mathbf{U}}_b) + \frac{A_{lb}}{\alpha_b \rho_b} \bar{\mathbf{U}}_r \times (\nabla \times \bar{\mathbf{U}}_b) \quad (3.53)$$

3.2.6 Solution of the Phase Continuity Equations

The phase fractions are obtained from the solution of the phase continuity equation (3.2). The discretisation of these should be efficient and most importantly yield a conservative and bounded result. Several approaches have been proposed over the years and, recently, some of them have been tested by Vaidya et al. [408] and Oliveira [295]:

1. The obvious way to advance the phase fraction field is to solve one of the phase continuity equations in its original form, *i.e.* equation (3.2):

$$\frac{\partial \alpha_a}{\partial t} + \nabla \cdot (\bar{\mathbf{U}}_a \alpha_a) = 0 \quad (3.54)$$

It is then discretised as:

$$\left[\left[\frac{\partial [\alpha_a]}{\partial t} \right] \right] + \left[\left[\nabla \cdot \left(\phi_a [\alpha_a]_{f(\phi_a, S)} \right) \right] \right] \quad (3.55)$$

where ϕ_a is the volumetric flux of phase a obtained from the momentum correction equation (3.38) after the solution of the pressure equation.

This approach has been utilised in the previous BRITE projects [147, 310] and the following deficiencies have been identified. Although, α_a in equation (3.54) can easily be bounded by zero, boundedness by one cannot be guaranteed since ϕ_a is non-conservative. This has been discussed in detail in Section 2.6.1. In this context, Carver [43] proposed to locally adjust the under-relaxation factors for cells where α_a approaches one. This can lead to convergence problems in steady-state calculations and is clearly not suitable for transient calculations.

2. In order to solve the problem of unboundedness, Spalding [358] suggested that equation (3.54) should be solved for α_a and its counterpart for α_b , the solutions should then be recombined:

$$\alpha_a^* = \frac{\alpha_a}{\alpha_a + \alpha_b} \quad (3.56)$$

The new phase fraction field α_a^* will be bounded by zero and one only if α_a and α_b are both larger than zero and it follows that appropriate differencing is essential.

In effect, equation (3.56) overwrites the phase continuity equations (3.54). Therefore, phase continuity is not guaranteed until convergence, *i.e.* $\alpha_a + \alpha_b = 1$. This is not an issue in steady-state calculations, but has to be considered in transient applications.

3. Another drawback of the approach of straightforward solution of the α_a equation is that it takes insufficient account of the coupling between the phases. Carver [43, 45] therefore suggested to handle the interaction between the phases via a

composite solution for α_a and α_b . In this, the two phase continuity equations are subtracted and the resulting equation for α_a reads:

$$2\frac{\partial \alpha_a}{\partial t} + \nabla \cdot (\bar{\mathbf{U}}_a \alpha_a) + \nabla \cdot (\bar{\mathbf{U}}_b \alpha_a) - \nabla \cdot (\bar{\mathbf{U}}_b) = 0 \quad (3.57)$$

Vaidya et al. [408] compared this approach with the recombination method by Spalding [358] and found no significant differences in the convergence rate for a steady-state two-phase flow in a U-bend, but preferred Carver's approach because it is computationally more efficient since it requires the construction and solution of only one transport equation instead of two. A major disadvantage of this approach is that even the converged solution is neither strictly conservative nor bounded.

4. Weller [426] re-arranged the phase continuity equation (3.2) so that all terms are in conservative form and α_a can be bounded at both ends, as follows:

$$\frac{\partial \alpha_a}{\partial t} + \nabla \cdot (\bar{\mathbf{U}} \alpha_a) + \nabla \cdot (\bar{\mathbf{U}}_r \alpha_a (1 - \alpha_a)) = 0 \quad (3.58)$$

where $\bar{\mathbf{U}} = \alpha_a \bar{\mathbf{U}}_a + \alpha_b \bar{\mathbf{U}}_b$ and $\bar{\mathbf{U}}_r = \bar{\mathbf{U}}_a - \bar{\mathbf{U}}_b$. This approach also couples the two phases more implicitly through the presence of the relative velocity $\bar{\mathbf{U}}_r$ in the third term.

Equation (3.58) is discretised as follows:

$$\left[\left[\frac{\partial [\alpha_a]}{\partial t} \right] \right] + \left[\left[\nabla \cdot (\phi [\alpha_a]_{f(\phi,S)}) \right] \right] + \left[\left[\nabla \cdot (\phi_{r_a} [\alpha_a]_{f(\phi_{r_a},S)}) \right] \right] = 0 \quad (3.59)$$

where $\phi_{r_a} = \alpha_{bf(-\phi_r,S)} \phi_r$ and $\phi_r = \phi_a - \phi_b$.

In the second term, α_a is bounded at zero as well as one, since the volumetric mixture flux ϕ satisfies the mixture continuity equation exactly. In the third term, bounding of α_a is achieved by using ϕ_r in the convection scheme to interpolate α_a to the face and $-\phi_r$ in the face interpolation of α_b . This treatment is quite diffusive if UD is used. However, using an higher order differencing scheme instead, reduces the numerical diffusion, but might compromise the boundedness of the solution.

The most serious limitation of this approach stems from the fact that equation (3.58) is non-linear in α_a . Therefore, boundedness at both limits can only

be guaranteed if the equation is solved fully implicitly α_a and α_b . Thus, solution with linear solvers requires iteration. Unfortunately, experience has shown that the iteration is not always convergent, especially when the Courant number is not sufficiently small. This is usually not so much of an issue for transient problems because a low Courant number is required for time accuracy. However for steady-state problems, where boundedness is of paramount importance and a conservative solution is only required when overall convergence is achieved, the approach by Spalding [358] could be used in conjunction with the modified α -equations.

5. The inter-phase momentum transfer term (3.4) may contain a turbulent drag term, which is proportional to $\nabla \alpha_a$ and has a diffusive effect on the phase fraction distribution. This term can lead to decoupling of the momentum and phase continuity equation, compromising convergence especially in steady-state situations, as shown in Section 3.3.1. In essence, the problem is very similar to the well-known problem of pressure-velocity coupling solved by the Rhie and Chow technique [318] and an analogous solution is proposed here. The diffusive nature of the turbulent drag term can be shown by substituting the phase momentum correction equation (3.38) for phase a into the phase fraction equation (3.54), such that:

$$\frac{\partial \alpha_a}{\partial t} + \nabla \cdot \left(\frac{(\mathcal{A}_a)_H}{(\mathcal{A}_a)_D} \right) - \nabla \cdot \left(\frac{1}{\rho_a (\mathcal{A}_a)_D} \nabla \bar{p} \right) - \nabla \cdot \left(\frac{A_\alpha}{\rho_a (\mathcal{A}_a)_D} \nabla \alpha_a \right) = 0 \quad (3.60)$$

The problems arise from the last term, *i.e.* fourth term on the l.h.s., since it is not discretised implicitly. A simple solution is to treat this term implicitly as a diffusion term. However, this remedy suffers from the same deficiencies as option 1, in the sense that the flux featuring in the second term is non-conservative and, consequently, boundedness of the solution can not be guaranteed. This situation can be overcome by starting from equation (3.58) instead of equation (3.54).

Furthermore, the discretisation of the second and third term on the l.h.s. of equation (3.60) can be avoided by correcting the phase velocities for the contributions

of the turbulent drag term which are now treated implicitly in the diffusion term. The corrected phase velocities read:

$$\bar{\mathbf{U}}_\varphi^\# = \bar{\mathbf{U}}_\varphi + \frac{A_\alpha}{\rho_\varphi(\mathcal{A}_\varphi)_D} \nabla \alpha_\varphi \quad (3.61)$$

Sustitution of equation (3.61) into equation (3.58) yields:

$$\begin{aligned} \frac{\partial \alpha_a}{\partial t} + \nabla \cdot (\bar{\mathbf{U}} \alpha_a) + \nabla \cdot (\bar{\mathbf{U}}_r^\# \alpha_a (1 - \alpha_a)) \\ - \nabla \cdot \left(A_\alpha \left(\frac{\alpha_b}{\rho_a(\mathcal{A}_a)_D} + \frac{\alpha_a}{\rho_b(\mathcal{A}_b)_D} \right) \nabla \alpha_a \right) = 0 \end{aligned} \quad (3.62)$$

where $\bar{\mathbf{U}}_r^\# = \bar{\mathbf{U}}_a^\# - \bar{\mathbf{U}}_b^\#$.

This transport equation for the phase fractions α_a is discretised along the guidelines given for option 4, equation (3.59), resulting in:

$$\left[\left[\frac{\partial [\alpha_a]}{\partial t} \right] \right] + \left[\nabla \cdot \left(\phi[\alpha_a]_{f(\phi, S)} \right) \right] + \left[\nabla \cdot \left(\phi_{r_a}^\# [\alpha_a]_{f(\phi_{r_a}^\#, S)} \right) \right] - \left[\nabla \cdot \left(\nu_{\alpha_f} \nabla [\alpha_a] \right) \right] = 0 \quad (3.63)$$

where $\phi_{r_a}^\# = \alpha_{b_f(-\phi_{r_a}^\#, S)} \phi_{r_a}^\#$. The diffusion coefficient ν_{α_f} is evaluated at the cell faces as:

$$\nu_{\alpha_f} = A_{\alpha_f} \left(\alpha_{b_f} \left(\frac{1}{\rho_a(\mathcal{A}_a)_D} \right)_f + \alpha_{a_f} \left(\frac{1}{\rho_b(\mathcal{A}_b)_D} \right)_f \right) \quad (3.64)$$

The corrected relative flux $\phi_r^\#$ is then calculated by removing the contribution of the turbulent drag term from the volumetric phase fluxes. This result is:

$$\phi_r^\# = \phi_r + \frac{\nu_{\alpha_f}}{\alpha_{a_f} \alpha_{b_f} + \delta} |\mathbf{S}| \nabla_f^\perp \alpha_a \quad (3.65)$$

The solution of a diffusion term does not compromise boundedness if its coefficient is positive, which is always the case, since the diagonal coefficients used in equation (3.64) are positive (a requirement of the iterative solvers). It follows that the solution of equation (3.63) is guaranteed to be bounded under the same conditions as previously outlined for equation (3.59).

It has been found that solving only for the dispersed phase fraction is adequate for most cases. However, for cases where there are significant regions where the dispersed

phase fraction is very high, it has proven to be advantageous [295] to solve for both α_a and α_b and then to correct for unboundedness (option 2). However, this treatment does not guarantee phase continuity until overall convergence and should, if possible, only be used in steady-state simulations. In this study, options 4 and 5 are utilised; sometimes in conjunction with option 2, if necessary.

3.2.7 Solution of the $k - \varepsilon$ -Turbulence Model

The two transport equations for the $k_b - \varepsilon_b$ turbulence model are discretised in straightforward manner: the unconditionally negative source terms are treated implicitly, thus strengthening the diagonal dominance of the matrix, whereas the positive source terms are incorporated explicitly. The result reads:

$$\left[\frac{\partial[k_b]}{\partial t} \right] + \left[\nabla \cdot \left(\phi_b [k_b]_{f(\phi_b, S)} \right) \right] - \left[\nabla \cdot (\phi_b) [k_b] \right] - \left[\nabla \cdot \left(\frac{\nu_b^{\text{eff}}}{\sigma_k} \nabla [k_b] \right) \right] = P_b - \left[\frac{\varepsilon_b}{k_b} [k_b] \right] + \left[\frac{2\alpha_a A_d (C_i - 1)}{\rho_b} [k_b] \right] + \frac{A_d \nu^t}{\rho_b \sigma_\alpha} \frac{\nabla \alpha_a}{\alpha_b} \cdot \bar{\mathbf{U}}_r \quad (3.66)$$

$$\left[\frac{\partial[\varepsilon_b]}{\partial t} \right] + \left[\nabla \cdot \left(\phi_b [\varepsilon_b]_{f(\phi_b, S)} \right) \right] - \left[\nabla \cdot (\phi_b) [\varepsilon_b] \right] - \left[\nabla \cdot \left(\frac{\nu_b^{\text{eff}}}{\sigma_\varepsilon} \nabla [\varepsilon_b] \right) \right] = C_1 P_b \frac{\varepsilon_b}{k_b} - \left[C_2 \frac{\varepsilon_b}{k_b} [\varepsilon_b] \right] + \left[\frac{2C_3 \alpha_a A_d (C_i - 1)}{\rho_b} [\varepsilon_b] \right] \quad (3.67)$$

The discretised equation for the basic mixture turbulence models are not given here, but are easily obtained by replacing the working variables, fluxes and source terms in the above equations. The transport equation have to be complemented by appropriate boundary condition, which are outlined in the next section.

3.2.8 Boundary Conditions

The specification of boundary conditions is an interpretation of the true behaviour because real boundary conditions are generally defined by some physical attributes rather than the numerical descriptions given in Section 2.4. The numerical representation of the boundary conditions used with the two-fluid methodology is very similar to the practises used for laminar single-phase flow [147]. However, two issues require further discussion here: the pressure boundary condition at a no-slip impermeable wall and near-wall turbulence.

Pressure Boundary Condition at Walls

In single-phase flow the dynamic pressure gradient at the wall is specified to be zero, implying that the pressure gradient at the wall equals $\rho\mathbf{g}$. In the two-fluid methodology, difficulties arise from the fact that the system is modelled in such a way that it has only a single pressure, but two fluids with possibly very different densities. Consider the averaged momentum equations presented in Section 3.1.1:

$$\frac{\partial \alpha_\varphi \bar{\mathbf{U}}_\varphi}{\partial t} + \nabla \cdot (\alpha_\varphi \bar{\mathbf{U}}_\varphi \bar{\mathbf{U}}_\varphi) + \nabla \cdot (\alpha_\varphi \bar{\mathbf{R}}_\varphi^{\text{eff}}) = -\frac{\alpha_\varphi}{\rho_\varphi} \nabla \bar{p} + \alpha_\varphi \mathbf{g} + \frac{\bar{\mathbf{M}}_\varphi}{\rho_\varphi} \quad (3.1)$$

For a no-slip impermeable stationary wall, the velocities at the wall are zero and the l.h.s. of the above equation as well as the momentum transfer term vanish. The remaining pressure gradient and buoyancy term can be rearranged, yielding expressions for the pressure boundary conditions:

$$(\nabla \bar{p})_f = \rho_\varphi \mathbf{g} \quad (3.68)$$

The problem is now immediately noticeable. In order to satisfy the momentum equations at a non-vertical wall, the pressure gradient has got to be different for each phase. This is of course impossible in a single pressure system and the problem can only be shifted from one equation to another.

Consider a bubbly jet impinging downwards onto a horizontal wall. The density ratio is large and equation (3.68) consequently demands that the wall pressure gradient in the lighter phase is much smaller than that in the heavier phase. However, the phase fraction close to the wall is very small if the jet is not strong enough to drag the bubbles towards the wall. In this situation, the momentum equation for the lighter phase is singular near the wall. This is not the case for the heavier phase and in fact the correct pressure gradient is needed here to ensure that the flow aligns with the wall. On the other hand, for a high speed jet, the phase fraction close to the wall could be appreciable. In this case, it is not obvious how to set the wall pressure gradient – a correct specification for both phases is impossible in a single pressure system.

The specification of pressure boundary conditions depends on the exact definition of pressure. In incompressible flow calculations, the pressure is often modified to remove possibly steep gradient arising from hydrostatic effects as well as simplifying

the specification of the wall pressure boundary condition. This route is adopted here, and we define a modified mixture pressure according to our earlier choice as:

$$\bar{p}^* = \bar{p} - \rho_b \mathbf{g} \cdot \mathbf{x} \quad (3.69)$$

where ρ_b is the density of the heavier phase and \mathbf{x} is the position vector. After substitution into equation (3.34) and some rearrangements, the r.h.s. of the momentum equations read:

$$\dots = -\frac{\nabla \bar{p}^*}{\rho_a} + \left(1 - \frac{\rho_b}{\rho_a}\right) \mathbf{g} + \frac{\bar{\mathbf{M}}_a}{\alpha_a \rho_a} \quad (3.70)$$

$$\dots = -\frac{\nabla \bar{p}^*}{\rho_b} + \frac{\bar{\mathbf{M}}_b}{\alpha_b \rho_b} \quad (3.71)$$

Near-wall Turbulence

The physics of turbulence in the vicinity of walls is considerably different from that in the other parts of the flow. It is therefore necessary to use appropriate modelling in the near-wall region. In this study, the near-wall region of high gradients is bridged by using the so-called wall-function approach by Launder and Spalding [230], which creates an additional term in the momentum equation in order to compensate for the increased shear stress at the wall. The additional drag is treated as a change in the effective viscosity at the “wall face”, carrying the difference between the assumed linear and the logarithmic velocity profile between the cell centre and the wall. For the k and ε transport equations, the situation is somewhat different: wall-functions use the local equilibrium assumption and prescribe the generation of k and the value of ε in the near-wall cell.

Very little is known about the exact nature of turbulent boundary layer in two-phase flow, so the validity of the wall-function approach is not known. Following Politis [310], it is assumed that the effects of the second phase on the turbulent boundary layer are adequately accounted for by including the phase fraction to account for the effective reduction of the wall surface area in contact with the considered phase.

Summary of Boundary Conditions

In this study, the following types of boundary conditions are utilised and the corresponding numerical boundary conditions for each variable are summarised in Table 3.3:

Variable	Wall	Inlet	Outlet	Symmetry Plane
\bar{U}_a	Fixed Value	Fixed Value	Zero Gradient	Mirror Image
\bar{U}_b	Fixed Value	Fixed Value	Zero Gradient	Mirror Image
α_a	Zero Gradient	Fixed Value	Zero Gradient	Zero Gradient
\bar{p}	Zero Gradient	Zero Gradient	Fixed Value	Zero Gradient
k	Fixed Value	Fixed Value	Zero Gradient	Zero Gradient
ε	Fixed Value	Fixed Value	Zero Gradient	Zero Gradient

Table 3.3: Boundary conditions applied to each equation for each boundary type.

Inlet The velocity fields at the inlet are supplied and, for consistency, the boundary condition on the modified pressure is zero gradient. In addition, fixed value conditions for the dispersed phase fraction, the turbulence kinetic energy as well as its dissipation rate are specified;

Outlet The modified pressure field at the outlet is supplied and a zero gradient boundary condition on velocity is specified. Furthermore, zero gradient boundary conditions are applied to the dispersed phase fraction, turbulence kinetic energy as well as its dissipation rate;

No-slip impermeable wall The velocities of the fluids are equal to that of the wall, *i.e.* a fixed value condition is specified. The dynamic pressure is specified to be zero gradient since the flux through the wall must be zero. Zero gradient boundary conditions are also used for the additional scalars if appropriate;

Symmetry plane In a problem whose solution domain and boundary conditions are symmetric about a plane, usually only half of the domain to one side of the symmetry plane is modelled. The boundary condition for any field is obtained by considering its mirror image as outlined in [255], which simplifies to a zero normal gradient condition for scalar fields.

3.2.9 Sequence of Solution

The sequence of operation for the solution procedure is summarised in Table 3.4. The solution procedure is based on the PISO algorithm [170] to handle the pressure-velocity coupling. This requires a momentum predictor and a correction loop in which the

1. Calculate coefficients A_d , A_l and A_{vm} , defined in equation (3.13).
2. Solve the momentum equations, equation (3.35).
3. PISO-Loop:
 - (a) Predict fluxes using equation (3.42).
 - (b) Construct and solve the pressure equation (3.43).
 - (c) Correct fluxes, equation (3.41).
 - (d) Correct velocities, equation (3.38).
4. Correct the substantive derivatives using equations (3.50) and (3.51).
5. Solve $k - \varepsilon$ equations equations (3.66) and (3.67) (if required).
6. Solve the α_a -equation (3.58).

Table 3.4: Two-phase numerical solution procedure.

pressure equation is solved and the momentum corrected based on the pressure change. The exact equations solved have been discussed in detail in the preceding Sections.

There are many variations on this theme, especially for steady-state calculations where the stabilising influence of the time derivative is missing from the equations. In this study, steady-state calculations are performed in two ways: either by under-relaxing the equations and using just one iteration in the PISO loop as employed in the SIMPLE (Semi-Implicit Method for Pressure-Linked Equations) algorithm [302, 301] or by keeping the time derivative and using a large time step ($C_o > 1$) to march through time until steady-state is reached. Again, only one iteration is performed in the PISO loop and it follows that the solution is not time accurate because of the non-linearity inherent in the “H”-operator. This is referred to as a pseudo-transient steady-state calculation. The SIMPLE algorithm offers more flexibility, since each of the equations can be under-relaxed individually. This can be utilised to reduce the number of time steps needed to reach a certain residual tolerance.

Several options for the treatment of the phase continuity equation and the inter-phase momentum transfer term have been outlined in the previous Sections. The choices made in this study are summarised as follows. In the momentum predictor, the drag (option 2) and the virtual mass terms are both treated semi-implicitly. The lift term is treated explicitly.

The phase continuity equation is solved once per time step/iteration at the end of the sequence. Its position in the solution procedure is not important, but simplifies the coding of option 5, which requires the diagonal coefficients of the momentum matrices, which only become available after step 2. The exact equations solved are given in Section 3.2.6.

3.2.10 Solution Procedure of Weller

It will be shown in Section 3.3 that the pressure-velocity handling as outlined in Section 3.2.4 is not sufficient when the flow exhibits regions where the phase fractions changes abruptly and the densities of the two-fluids are very different, for example, a bubbly flow where complete phase separation occurs. The problem is not specific to the two-fluid methodology and has also been recognised by Brennan [39] who computed a flow in a settling tank using a simplified two-fluid model.

The problem stems from the choice of the collocated variable arrangement and does not occur if a staggered variable arrangement were used. For this reason, the staggered arrangement has been utilised in most solution procedures for the two-fluid methodology [357, 376, 152, 231], partly because of the its stability properties and partly because of the fact that most of the geometries under consideration have been fairly simple. The collocated variable arrangement is currently used by the groups at Imperial College [147, 294] and Los Alamos [196] as well as some commercial CFD codes. It has been noted, however, that special care has to be exercised to ensure adequate pressure-velocity coupling, especially when the flow exhibits rapid changes in the phase fraction [196, 295].

To overcome the problem Weller [423] revised the previously described solution procedure so that it mimics the operation of a solution procedure devised for a staggered variable arrangement, but keeping the collocated variables. The structure of this new procedure is very similar to the previous one, in the sense that it consists of a momentum predictor and a correction loop in which the pressure equation is solved and the momentum corrected based on the pressure change. The key novelty is that the velocities are obtained from the corrected flux fields using a reconstruction procedure. This reflects the view that the flux should be the primary variable representing

the velocity, since it is located in such a way that pressure-velocity decoupling cannot occur. The cell-centred velocity is merely regarded as a secondary variable, which is used in the construction of the momentum equation.

This alternative solution procedure will now be outlined, following the same pattern as the derivation of the previous solution procedure. The discretised momentum equations are identical to those used in the previous solution procedure, with the exception that the buoyancy term and explicit part of the drag term are treated at the cell-faces. For the derivation of the momentum correction and pressure equation, a semi-discretised form of the momentum equations is used:

$$(\mathcal{A}_a)_D \bar{\mathbf{U}}_a = (\mathcal{A}_a)_H - \frac{\nabla \bar{p}}{\rho_a} - \frac{A_\alpha \nabla \alpha_a}{\alpha_a \rho_a} + \mathbf{g} + \frac{A_d \bar{\mathbf{U}}_b}{\alpha_a \rho_a} \quad (3.72)$$

$$(\mathcal{A}_b)_D \bar{\mathbf{U}}_b = (\mathcal{A}_b)_H - \frac{\nabla \bar{p}}{\rho_b} + \frac{A_\alpha \nabla \alpha_a}{\alpha_b \rho_b} + \mathbf{g} + \frac{A_d \bar{\mathbf{U}}_a}{\alpha_b \rho_b} \quad (3.73)$$

where \mathcal{A}_a and \mathcal{A}_b denote the systems of linear algebraic equations arising from the discretisation of the phase momentum equations without the turbulent drag term, the pressure gradient term, the buoyancy term and the explicit part of the drag term. They are given by:

$$\mathcal{A}_\varphi := \mathcal{T}_\varphi = \mathcal{M}_\varphi^{vm} + \mathcal{M}_\varphi^l + \left[\left[\frac{\alpha_b A_d}{\rho_\varphi} [\mathbf{U}_\varphi] \right] \right] \quad (3.74)$$

where \mathcal{T}_φ denotes the discretised terms due to convective transport and diffusion, *i.e.* the l.h.s. of the phase momentum equations and is defined in equation (3.32). \mathcal{M}_φ^{vm} and \mathcal{M}_φ^l stand for the discretised terms arising from the contribution of the virtual mass and lift forces to the inter-phase momentum transfer, respectively.

Rearranging equations (3.72) and (3.73) yields the phase momentum correction equations, which are not used in this solution procedure, but are needed in the derivation of the flux predictor and corrector as well as the pressure equation:

$$\bar{\mathbf{U}}_a = \frac{(\mathcal{A}_a)_H}{(\mathcal{A}_a)_D} - \frac{\nabla \bar{p}}{\rho_a (\mathcal{A}_a)_D} - \frac{A_\alpha \nabla \alpha_a}{\alpha_a \rho_a (\mathcal{A}_a)_D} + \frac{\mathbf{g}}{(\mathcal{A}_a)_D} + \frac{A_d \bar{\mathbf{U}}_b}{\alpha_a \rho_a (\mathcal{A}_a)_D} \quad (3.75)$$

$$\bar{\mathbf{U}}_b = \frac{(\mathcal{A}_b)_H}{(\mathcal{A}_b)_D} - \frac{\nabla \bar{p}}{\rho_b (\mathcal{A}_b)_D} + \frac{A_\alpha \nabla \alpha_a}{\alpha_b \rho_b (\mathcal{A}_b)_D} + \frac{\mathbf{g}}{(\mathcal{A}_b)_D} + \frac{A_d \bar{\mathbf{U}}_a}{\alpha_b \rho_b (\mathcal{A}_b)_D} \quad (3.76)$$

The flux predictor and corrector are then derived by interpolating the momentum correction equations using central differencing:

$$\phi_\varphi = \phi_\varphi^* - \left(\frac{1}{\rho_\varphi (\mathcal{A}_\varphi)_D} \right)_f |\mathbf{S}| \nabla_f^\perp \bar{p} \quad (3.77)$$

1. Calculate coefficients A_d , A_l and A_{vm} , defined in equation (3.13).
2. Construct \mathcal{A}_φ , equation (3.74).
3. PISO-Loop:
 - (a) Predict fluxes using equations (3.78) and (3.79).
 - (b) Construct and solve the pressure equation (3.43).
 - (c) Correct fluxes, equation (3.77).
 - (d) Reconstruct velocities.
4. Correct the substantive derivatives using equations (3.50) and (3.51).
5. Solve $k - \varepsilon$ equations equations (3.66) and (3.67).
6. Solve the α_a -equation (3.58).

Table 3.5: Two-phase numerical solution procedure of Weller [423].

where the flux predictions ϕ_φ^* are expressed by:

$$\begin{aligned} \phi_a^* = & \left(\frac{(\mathcal{A}_\varphi)_H}{(\mathcal{A}_a)_D} \right)_f \cdot \mathbf{S} - \left(\frac{1}{\rho_a (\mathcal{A}_a)_D} \right)_f \frac{A_{af} |\mathbf{S}| \nabla_f^\perp \alpha_a}{\alpha_{af}} \\ & + \left(\frac{1}{(\mathcal{A}_a)_D} \right)_f \mathbf{g} \cdot \mathbf{S} + \left(\frac{A_d}{\alpha_a \rho_a (\mathcal{A}_a)_D} \right)_f \phi_b \end{aligned} \quad (3.78)$$

$$\begin{aligned} \phi_b^* = & \left(\frac{(\mathcal{A}_\varphi)_H}{(\mathcal{A}_b)_D} \right)_f \cdot \mathbf{S} + \left(\frac{1}{\rho_b (\mathcal{A}_b)_D} \right)_f \frac{A_{bf} |\mathbf{S}| \nabla_f^\perp \alpha_b}{\alpha_{bf}} \\ & + \left(\frac{1}{(\mathcal{A}_b)_D} \right)_f \mathbf{g} \cdot \mathbf{S} + \left(\frac{A_d}{\alpha_b \rho_b (\mathcal{A}_b)_D} \right)_f \phi_a \end{aligned} \quad (3.79)$$

The sequence of solution for this procedure is summarised in Table 3.5. The solution sequence is almost identical to that of the previous solution procedure summarised in Table 3.4. The alternative procedure requires modification to steps 2, 3a, 3c and 3d. In steps 3a and 3c the new flux predictor, equations (3.78) and (3.79), as well as the new flux corrector, equation (3.77), are used. In step 3d, the velocity corrector is replaced by a procedure, which reconstructs the cell-centred phase velocities from the phase fluxes. This reconstruction procedure is outlined in more detail in [255].

Finally, it has been found that the solution of the momentum predictor in step 2 may destabilise the solution procedure for challenging test cases and, hence, the discretised momentum equations are only constructed, but not solved. This imposes a restriction on the time step in transient calculations. However, this has not been found

to be a serious limitation so far. However, it should also be noted that not solving the momentum predictor may slow down convergence of steady-state calculations.

3.3 Basic Tests of the Solution Procedure

In this Section, the stability and speed of the solution procedure outlined in the previous Section are assessed. The test cases chosen for this purpose are: a sudden enlargement in a circular pipe, phase separation in a tank and a bubble plume.

3.3.1 Test Case: Sudden Enlargement in a Circular Pipe

The case studied here is that of a turbulent bubbly air/water upward flow through a pipe with a sudden enlargement, for which experiments have been carried out by Bel F'dhila [25]. Several authors used his results to validate their solution procedures and models [228, 393, 418, 416, 295, 25, 27]. The following Section investigates convergence problems associated with the turbulent drag term and demonstrates the benefits of the modified phase fraction equation with implicit diffusion treatment (option 5) introduced in Section 3.2.6.

Setup

The geometry is depicted in Figure 3.2. The diameters of the two pipe section are 50 mm and 100 mm, respectively. In the experiments, the profiles of mean and r.m.s. velocities (axial and radial components) and of the phase fraction are measured at six cross-sections ($x = -20, 70, 130, 180, 250$ and 320 mm).

Several sets of measurements for different liquid and gas flow rates have been conducted by Bel F'dhila [25]. Here, we chose to compare with the data for case 1.2, for which the maximum local phase fraction is measured to 25%. At the inlet, the mean liquid and relative velocity between the liquid and the gas phase are 1.57 and 0.3 m/s, respectively. The Reynolds number based on the smaller pipe diameter and the mean liquid velocity is $\mathcal{R}e = 78500$. The bubble diameter is estimated at $d_a = 2$ mm.

This problem is essentially two-dimensional and the calculations are therefore performed on a two-dimensional axi-symmetric geometry. In the radial direction, the

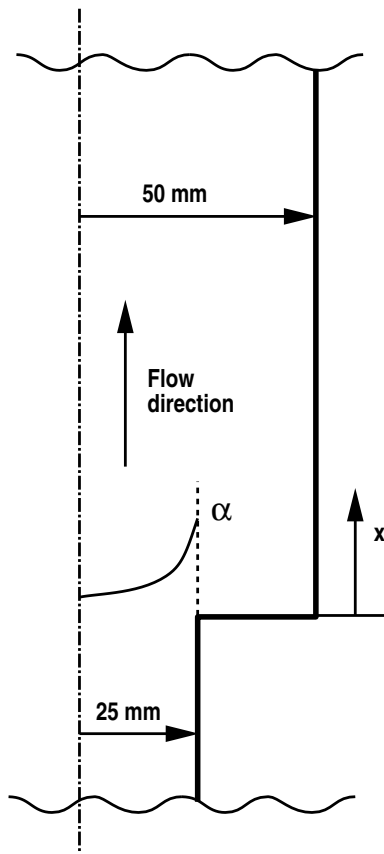


Figure 3.2: Sketch of the setup for the sudden enlargement test case.

large pipe radius is represented by 20 and 40 cells for the coarse and fine mesh, respectively. In axial direction, the space domain extends from $x = -20$ to 700 mm in order to ensure negligible influence of the outlet boundary on the region of interest. Furthermore, the mesh is graded in order to provide a higher mesh density towards the sudden enlargement. Altogether, the computational meshes comprised approximately 1900 and 6200 cells for the coarse and fine version, respectively. The lower section of the fine mesh up to $x \approx 225$ mm is plotted in Figure 3.3a.

The inlet conditions for the gas phase fraction and the liquid velocity are taken directly from the measurements at $x = -20$ mm. The turbulence kinetic energy of the liquid phase is calculated from the axial velocity fluctuations assuming isotropy. Measurements of the gas phase velocity and dissipation rate of kinetic energy of the liquid phase are not available. Therefore, the gas phase velocity is calculated by assuming that drag and buoyancy are in balance, whereas the dissipation rate of the kinetic energy is inferred from a mixing length hypothesis.

The numerical solution procedure as well as the models are described in the pre-

α_b	\mathbf{U}_a	\mathbf{U}_b	p	k	ε
⊕	0.7	0.7	0.3	0.9	0.9

Table 3.6: Under-relaxation factors λ used for the sudden enlargement test case. ⊕ denotes values that are varied in the calculations.

vious Sections. The models utilised in the calculations are therefore only stated briefly. The calculations are obtained using standard inter-phase transfer modelling (3.10), including drag, virtual mass and turbulent drag, but neglecting lift. The detrimental effect of the lift term has been noted by many authors and will be discussed in detail in Chapter 7. Drag is modelled using the simple drag model by Schiller and Naumann [340] given in equation (3.9). The turbulence model by Gosman et al. [121] is used, as outlined in Section 3.1.3.

Two options for the solution of the phase continuity equations are investigated. These are options 4 and 5 of Section 3.2.6. The flow is nominally steady and the steady-state solution is obtained by using SIMPLE as well as by pseudo-transient time marching. Both solution procedures are outlined in Section 3.2.9. The under-relaxation factors are given in Table 3.6. The value of the under-relaxation factor for the phase fraction is varied in this study and its value will be given along with the results. All the results are obtained using the standard pressure-velocity solution procedure and upwind differencing on all convection terms.

Results

Figure 3.3b shows the vector field of the mean liquid velocity $\overline{\mathbf{U}}_b$. As expected, there is a large recirculation zone behind the enlargement, similar to the behaviour in a single-phase flow. In Figure 3.3c, the distribution of the gas phase fraction is pictured. It is highest close to the wall of the small pipe section and diffuses slowly further downstream. As outlined in Section 1.5.5, the accumulation of bubbles at the wall is characteristic for certain vertical pipe flows and is often referred to as a “wall peak” distribution. Its prediction remains a difficult task because of the coupled effects of shear, wake phenomena and deformation on the lift force as well as the turbulence of the liquid phase. However, in the calculations presented here, the phase fraction profile at the inlet has been prescribed according to the measurements and no attempt

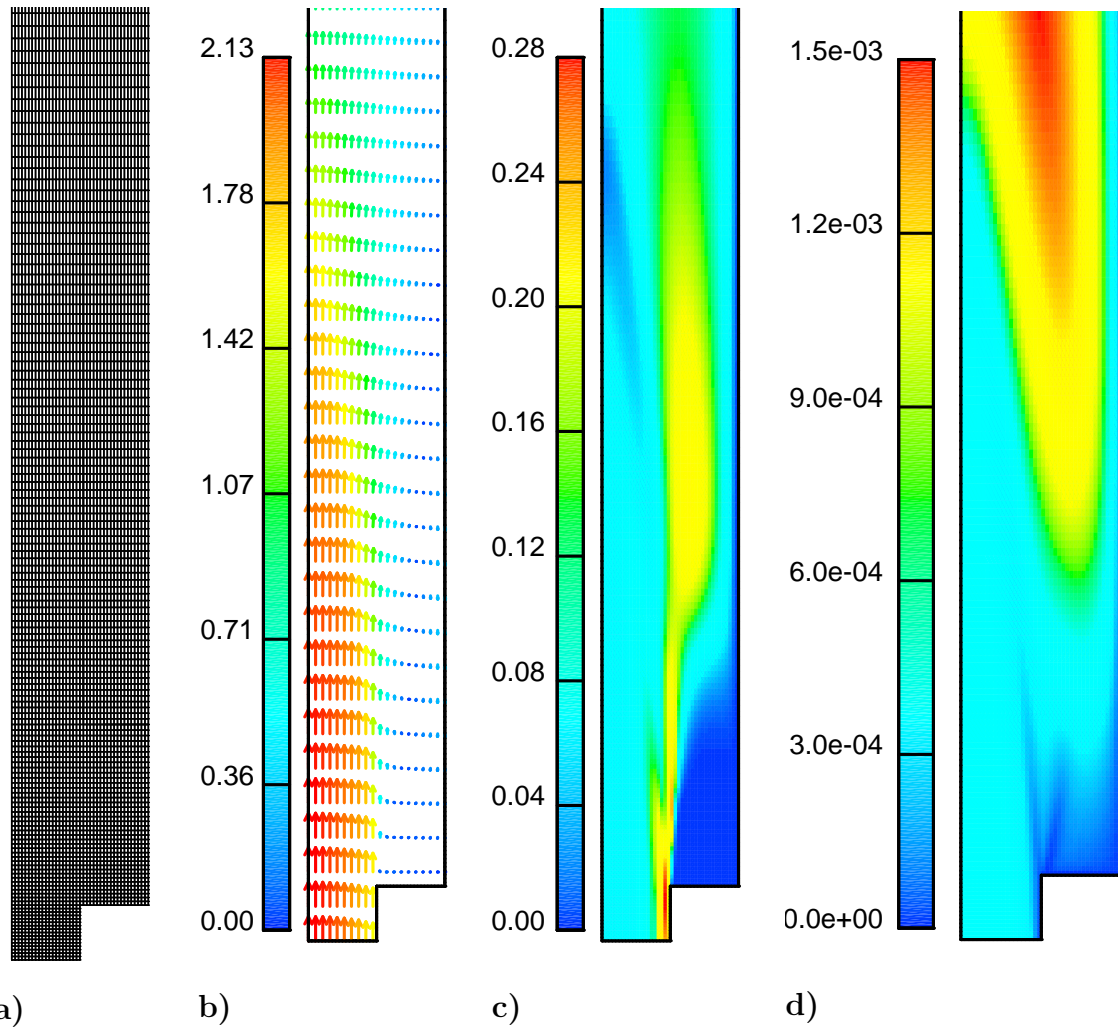


Figure 3.3: Results for the sudden enlargement test case: **a)** lower section of the computational mesh; **b)** mean liquid velocity \bar{U}_b ; **c)** gas phase fraction α_a ; **d)** turbulent viscosity ν^t .

is made to predict the “wall peak”. In the region just behind the enlargement the gas phase fraction is very small, since the recirculation is not strong enough to drag bubbles back towards the enlargement and in this way to support an accumulation of bubbles in this region. This shows the effectiveness of using the phase-intensive momentum equations instead of standard ones for cases where one of the phases is not present locally. The turbulent viscosity ν^t is shown in Figure 3.3d. It is noticeable that most of the turbulent diffusion is produced far away from the enlargement. This is due to bubble-induced turbulence, which is represented by the additional two-phase source terms in the $k - \varepsilon$ -model, *i.e.* (3.16) and (3.17).

The residuals for the gas phase fraction are shown in Figure 3.4. For pseudo-transient time marching, convergence is very smooth and residuals of the order of 10^{-7}

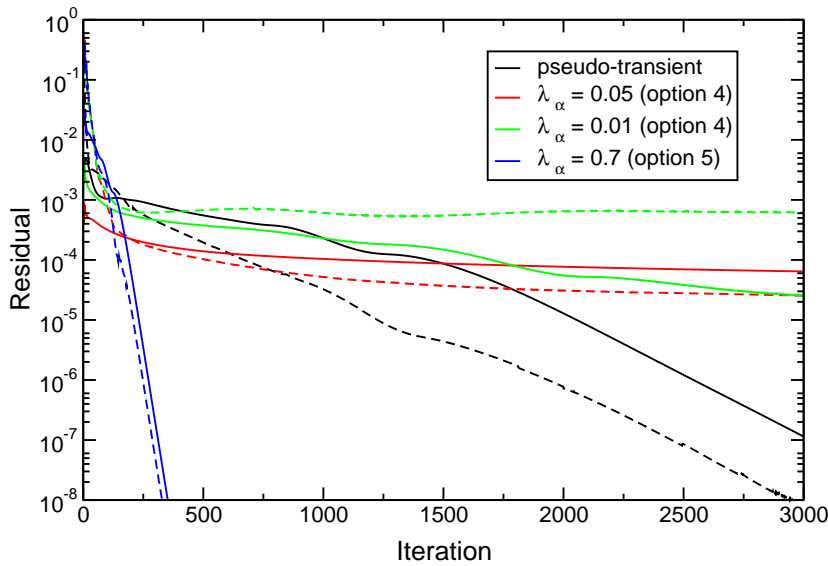


Figure 3.4: Residuals in the dispersed phase continuity equation for the coarse mesh. Residuals for the phase continuity and the pressure equation are denoted by solid and broken lines, respectively.

are obtained after approximately 3000 time steps. The large number of iterations can be explained by the fact that the solution is advanced with a small time step of $\Delta t = 1 \times 10^{-4}$ s; resulting in a maximum Courant number of $\mathcal{C}o = 0.86$. However, it has been found that the time step cannot be increased without compromising the stability of the solution process. This imposes a serious limitation on the rate of convergence. Nevertheless, this is an improvement over the previous solution procedure used by Hill [147] where convergence could not be obtained to this level, as shown by Oliveira [295].

The problem has been analysed further using the SIMPLE algorithm, since it allows us to adjust the rate of convergence for each transport equation individually through the under-relaxation parameters. Interestingly, it was found that a converged result cannot be obtained even if the under-relaxation factors are reduced to very small values and that the problem does not occur when the turbulent drag term is excluded from the calculations. This suggests that the treatment of this term is not adequate.

Evidence of the problem is pictured in Figure 3.5 where the cell values of the dispersed phase fraction are shown for the last few rows of cells close to the outlet. The distribution of phase fraction field is checker-boarded and the oscillations increase with the increasing under-relaxation factors. It could be argued that this problem is related to the implementation of the outlet boundary condition. However, various

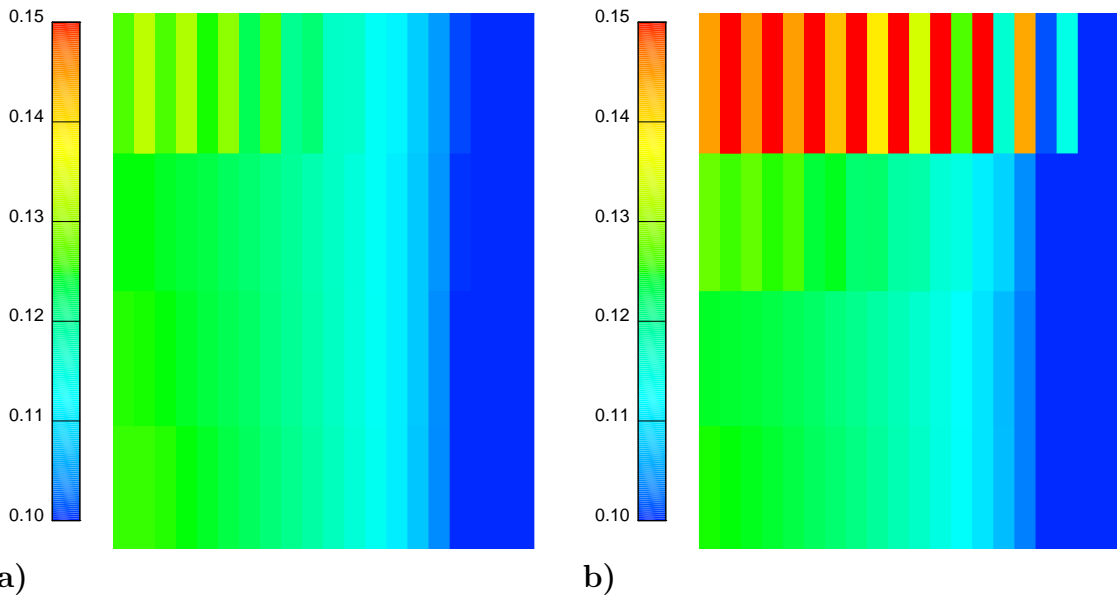


Figure 3.5: Cell values of the dispersed phase fraction at the outlet of the sudden enlargement for dispersed phase fraction under-relaxation factors of **a)** $\lambda = 0.05$ and **b)** $\lambda = 0.25$.

alternative implementations have been tried out with no success. Therefore, a more physical approach was sought and it was found that treating the turbulent drag term implicitly cures the problem effectively. This has been described in detail as option 5 in Section 3.2.6. Using option 5 for the solution of the phase continuity equation removes the limitations on the under-relaxation factor for the dispersed phase fraction and it can now be advanced using under-relaxation factors similar to those used for ordinary scalars. The enormous benefits in terms of solution efficiency are shown in Figure 3.4 for the coarse mesh and in Figure 3.6 for the fine mesh. Numerical instabilities in the residual of the pressure equation are noticeable for the fine mesh results using pseudo-transient time marching. These have to be attributed to the inadequate discretisation of the turbulent drag term, but disappear if option 5 is used to solve for the phase fraction equation.

3.3.2 Test Case: Phase Separation in a Tank

Complete phase separation, where the phase fraction approaches 0 or 1, has proven to be a very challenging test case for the stability of the numerical scheme. The setup of the test case is very simple and consists of a tank, which is initially filled with a mixture of air and water left for gravitational separation. Here, we simulate a square

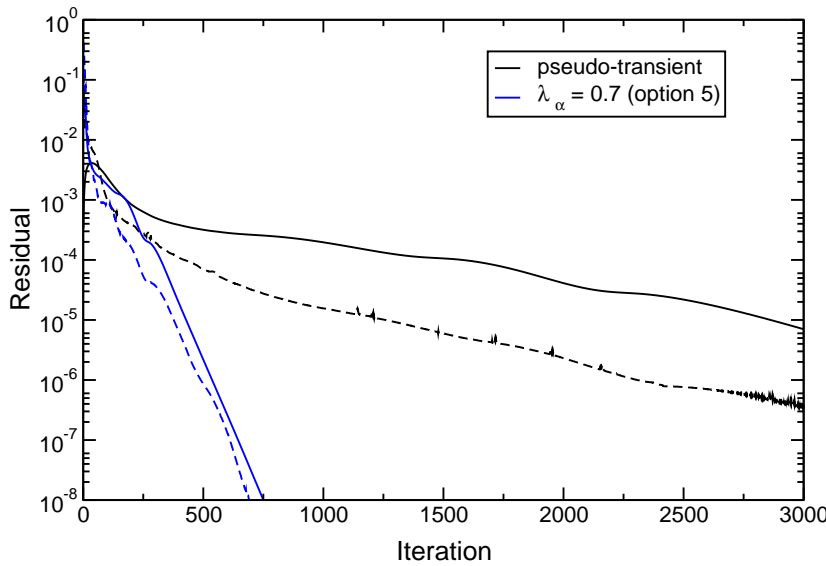


Figure 3.6: Residual in the dispersed phase continuity equation for the fine mesh. Residuals for the phase continuity and the pressure equation are denoted by solid and broken lines, respectively.

cross-section of $1 \text{ m} \times 1 \text{ m}$, which is discretised using 20 cells in each direction. The difficulties in this test case are twofold:

1. The two phase momentum equation becomes singular in the limit of the phase fractions approaching the extrema. This leads to numerical oscillations and the stability of the solution procedure is easily destroyed. This problem is overcome by utilising the phase-intensive momentum equations, as described in Section 3.2.1.
2. The pressure-velocity coupling becomes increasingly troublesome when the densities are very different. This stems from the fact that the pressure gradient changes rapidly across the free-surface. In fact, the ratio of the pressure gradients in the pure fluids is of the order of the density ratio. Therefore, any inconsistencies in the pressure-velocity coupling quickly result in erroneous results. The solution procedure of Weller [423] outlined in Section 3.2 solves this problem and in this Section its performance is compared against the standard solution procedure.

The calculations start from the bubbly mixture, but eventually regions of pure phases are generated as expected. Hence, appropriate modelling has to be used. The inter-phase momentum transfer is modelled using equation (3.11). This model neglects

the turbulent drag force to avoid numerical difficulties in the proximity of the free-surface. Drag is modelled using the simple drag model by Schiller and Naumann [340] given by equation (3.9). Furthermore, the basic $k - \varepsilon$ -model given by equations (3.24) and (3.25) is utilised. All calculations are obtained running in the transient mode. Gamma differencing [186, 185] with $\Gamma = 0.5$ is used on all convection terms.

The phase fraction is solved for using option 4 in conjunction with option 2, as described in Section 3.2.6, in order to ensure boundedness of the solution in this extreme case.

Results

The time evolutions of the liquid and gas velocity fields (vectors) as well as phase fraction distribution (iso-lines) are shown in Figure 3.7 for a density ratio of 20 using the Weller [423] solution procedure. The time step used in the calculations is $\Delta t = 0.02$ s and the time difference between each picture is 2 s. During the process, the “gas” bubbles rise and a sharp front between the pure gas and the mixture is formed at the top of the tank. A second front is evident between the mixture and the pure liquid. Eventually, the gas separates completely from the liquid and the free surfaces between the gas and the liquid is resolved over less than two cells. No numerical difficulties are evident in the velocity field. It is interesting to note that the liquid velocity in the pure gas phase does not vanish, but instead approaches the terminal velocity of droplets. A similar effect can be noticed for the gas velocity in the pure liquid, which is equal to the terminal velocity of bubbles. Of course, these velocities are fictitious because the phase fraction vanishes.

Figure 3.8 shows results for the standard solution procedure at $t = 4$ s. The gas and liquid velocities are staggered, *i.e.* they point in different directions from one row of cells to another. Furthermore, their magnitude increases rapidly with the height of the column. Interestingly, examination of the gas phase fluxes (not shown) revealed that they are zero within the solution tolerance in the upper part of the column. The pressure field (not shown), however, oscillates widely around the analytical (hydrostatic) solution. Note that the time step had to be reduced by a factor of 20 to $\Delta t = 0.001$ s in order to stabilise the solution procedure and to cope with the unphysical oscillations.

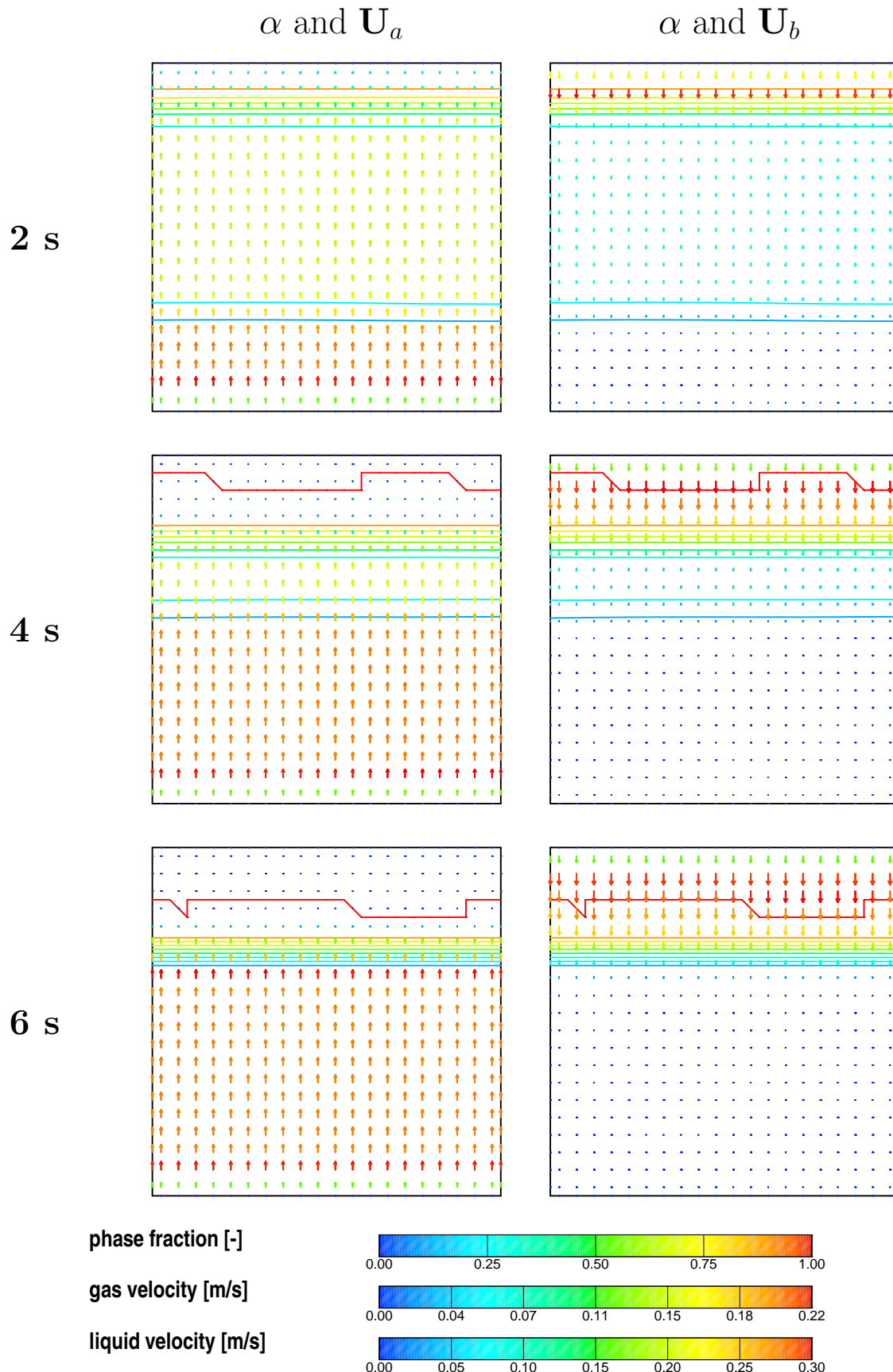


Figure 3.7: Time sequence of the phase fraction (iso-lines) and the velocity fields (vectors) for the complete separation test case using the Weller [423] solution procedure. $\rho_b/\rho_a = 20$.

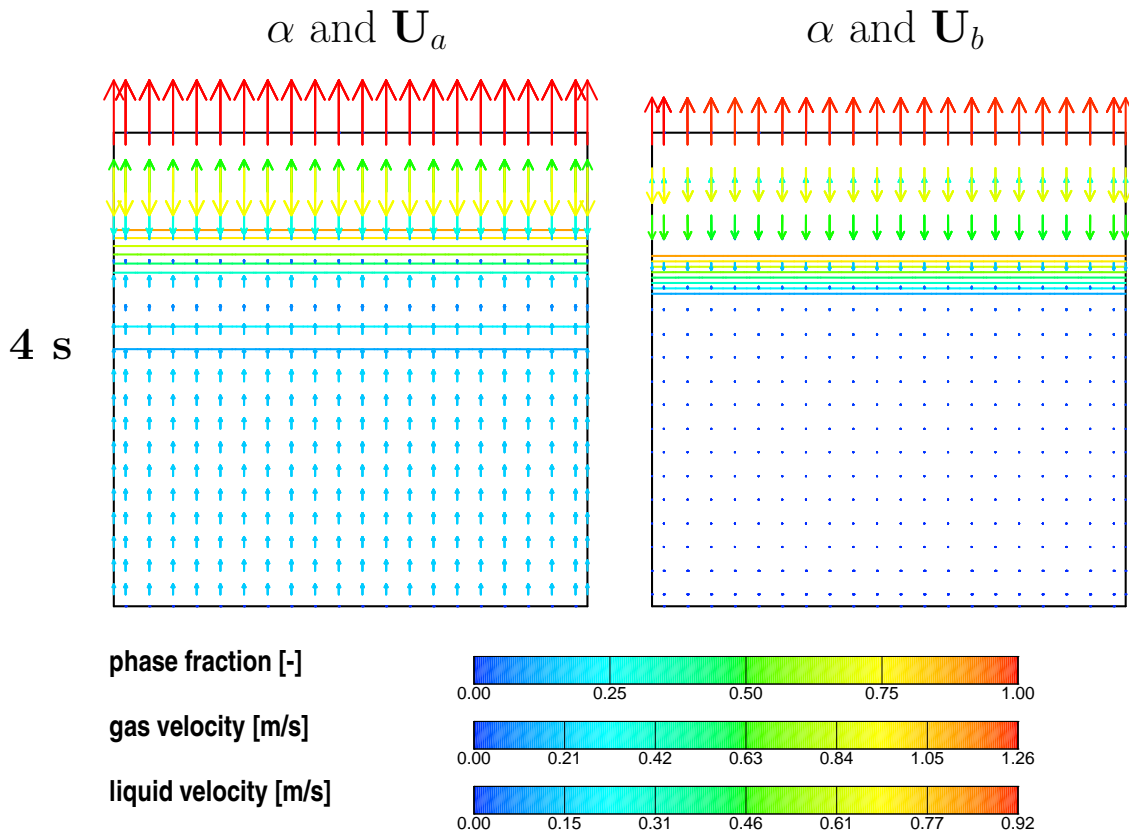


Figure 3.8: Time sequence of the phase fraction (iso-lines) and the velocity fields (vectors) for the phase separation test case using the standard solution procedure. $\rho_b/\rho_a = 20$.

The strength of the Weller [423] solution procedure is further demonstrated in the Figure 3.9 where the density ratio is increased to a more practical value of 1000. No oscillation in the velocity fields are noticeable and this technique has therefore been adopted for cases where free surfaces are present.

3.3.3 Test Case: Bubble Plume

The third test case is that of a bubble plume produced by injecting air through a sparger at the base of a rectangular vessel. Usually, in multi-phase flow calculations attempts are made to create some kind of “top-surface” boundary condition, which does not allow the liquid to leave the domain but allows the gas to escape. If one considers a typical startup condition where the column is initially only filled with liquid, it is not clear how the liquid displaced by the in-flowing gas is dealt with and one has to assume that some sort of continuity error is compensating for the effect.

However, with the capabilities of the Weller [423] solution procedure, this case can

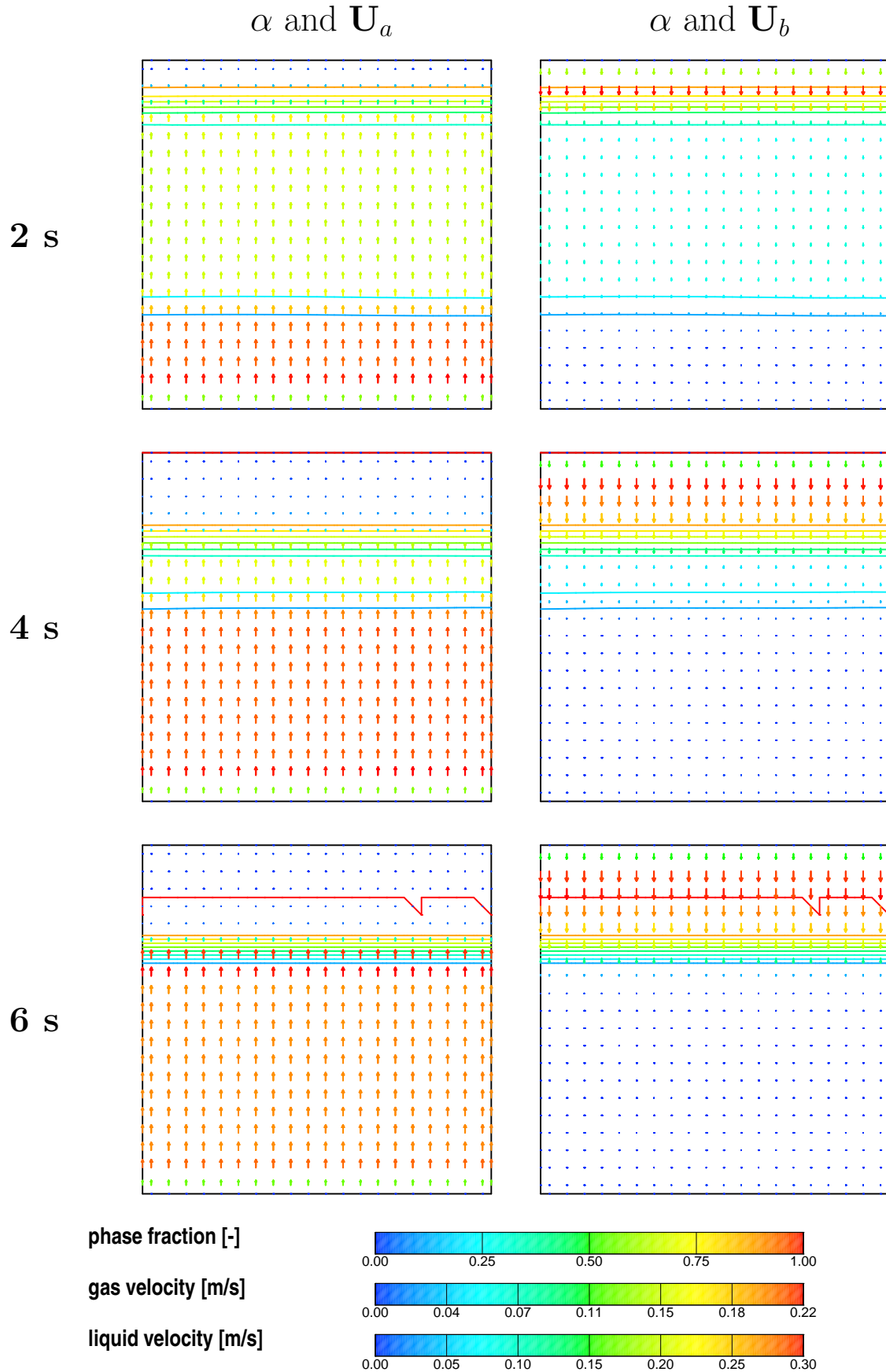


Figure 3.9: Time sequence of the phase fraction (iso-lines) and the velocity fields (vectors) for the phase separation test case using the Weller [423] solution procedure. $\rho_b/\rho_a = 1000$.

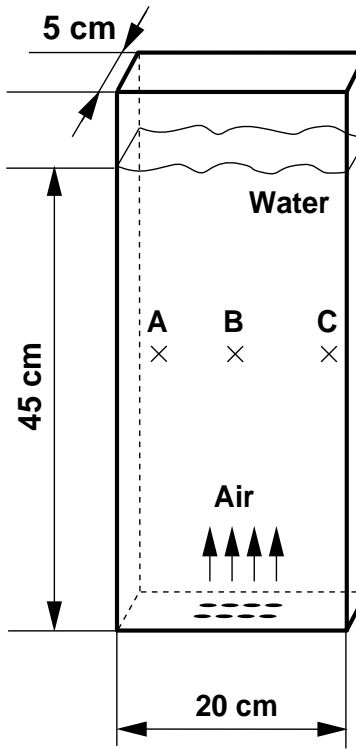


Figure 3.10: Sketch of the setup for the bubble plume test case.

be calculated by including the region above the liquid in the domain, with the position of the free-surface being determined as part of the calculation wherever necessary. A simple outlet boundary is imposed at the top of the domain to allow the gas to escape.

Setup

The domain chosen corresponds to the column investigated by Gomes et al. [118] and Pfleger et al. [306]. The apparatus is a flat laboratory-scale bubble column with the main dimension $20 \times 100 \times 5$ cm ($W \times H \times D$). Initially the column is filled with tap water and the static water level is 45 cm. Compressed air is injected through a plate, which has 8 holes with a diameter of 0.4 mm in a rectangular configuration. The air flow rate is varied between 20 and 180 l/h, but in this study, calculations were only performed for 20, 48 and 90 l/h. The mean phase fraction in the column is of the order of 1%, but local values exceed 5%. The bubble size is approximately 2 mm.

Measurements of the liquid velocities were taken by means of Laser Doppler Anemometry (LDA) at various locations inside the column. Three points (A, B and C) have been selected for comparison. All three points are located 25 cm above the

base and in the middle of the back and front wall. The locations only vary in their position from the vertical centreline: $x = -4, 0$ and 9.8 cm for locations A, B and C, respectively.

The domain is decomposed into $25 \times 60 \times 7$ control volumes, giving a total of 10^4 cells. The air is injected into five cells in the centre of the base. Here, a phase fraction of 10% is assumed and the inlet velocity is then chosen to match the given volume flux.

As mentioned before, the calculations are performed for the bubbly mixture as well as the region above the free-surface. Therefore, modelling has to be used, which can handle situations where complete separation of the phases occurs. In fact, the modelling and numerical solution procedure is identical to the one for the previous test case. The time step is set to $\Delta t = 0.01$ s; resulting in a maximum Courant number between $Co = 0.18$ and 0.33 depending on the gas flow rate.

The phase fraction is solved for using option 4 in conjunction with option 2, as described in Section 3.2.6, in order to ensure boundedness of the solution in this extreme case.

Results

The motion of the bubble plume is transient and typical results for the phase fraction (iso-lines) as well as the gas and liquid velocities (vectors) are shown in Figures 3.11 and 3.12 for an air flow rate of 48 l/h. A periodic meandering motion of the plume is clearly visible. A large vortex spanning about half of the height of the column is induced by the rising bubbles on one side of the plume. On the opposite, outwards bent side of the plume two small vortices, one close to the free-surface and one close to the base, are generated. An animation of the time sequence has been produced and is available on the CD-ROM accompanying this thesis.

The time averaged results for the phase fraction, liquid and gas velocity are shown in Figure 3.13. On average, the gas rises in the centre of the column, dragging the liquid along and generating a large scale recirculating motion of the liquid, which is clearly evident from the plot.

The liquid velocity in the vertical direction at locations A, B and C is plotted

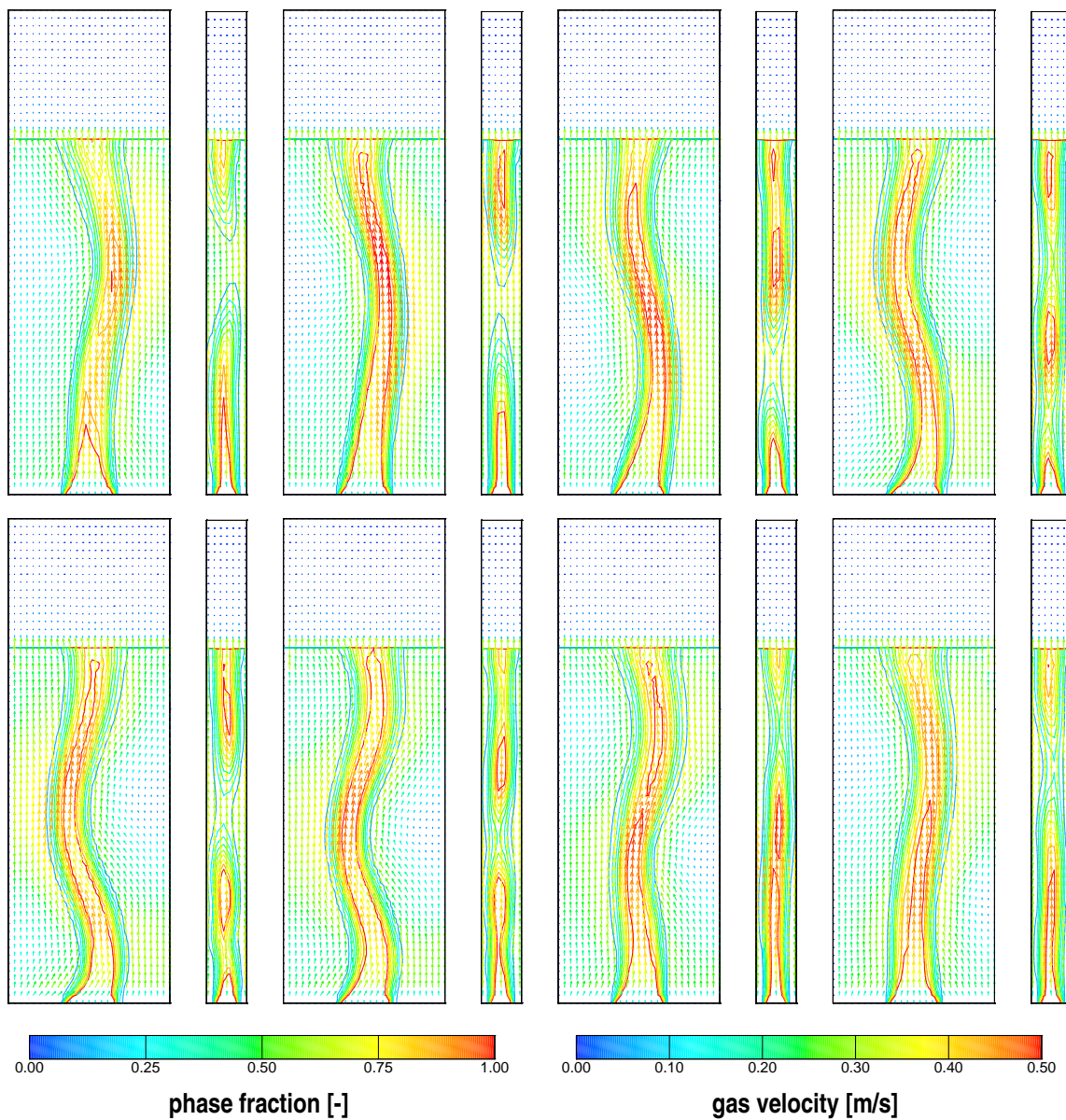


Figure 3.11: Time sequence of the phase fraction (iso-lines) and the gas velocity field (vectors) for the bubble plume test case. Narrow pictures show a side view onto the $x = 0$ cm plane. The air flow rate is 48 l/h and the time difference between each picture is $\Delta t = 2$ s.

in Figure 3.14. The periodic signals induced by the plume are clearly noticeable. The mean velocity is highest at location B, the centre of the plume, and lowest at location C, close to the side wall. This is expected and explained by the recirculating motion of the liquid. Furthermore, the period and amplitude of the fluctuating motion is influenced by the air volume flux. This will be investigated next by spectrum analysis.

Figure 3.15 pictures the Fourier transforms of the velocity signals in vertical direction presented earlier in Figure 3.14. The different curves represent different air

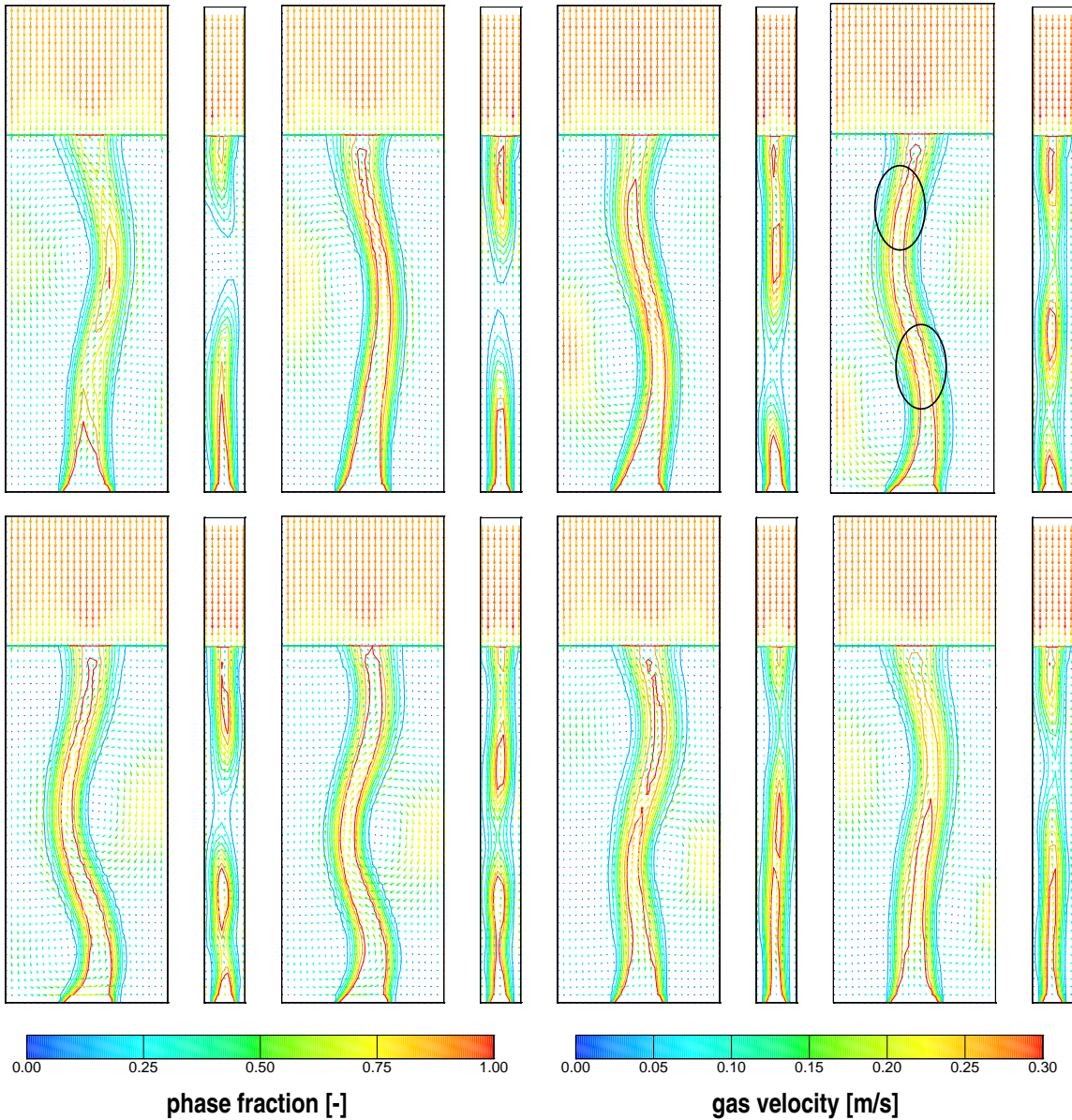


Figure 3.12: Time sequence of the phase fraction (iso-lines) and the liquid velocity field (vectors) for the bubble plume test case. Narrow pictures show a side view onto the $x = 0$ cm plane. The air flow rate is 48 l/h and the time difference between each picture is $\Delta t = 2$ s.

flow rates and locations within the column. With the increasing air flow rate, the period of the dominant frequencies is reduced, *i.e.* the plume plume oscillates more violently. The periods at location B on the centreline (solid lines) are approximately half of those at location A on the l.h.s. of the column (broken lines). This is explained by the fact that location B is affected equally well by the vortices travelling down on either side of the column increasing the liquid velocity on the centreline, as indicated by the ellipses in Figure 3.12, and causing the halving of the period of the dominant

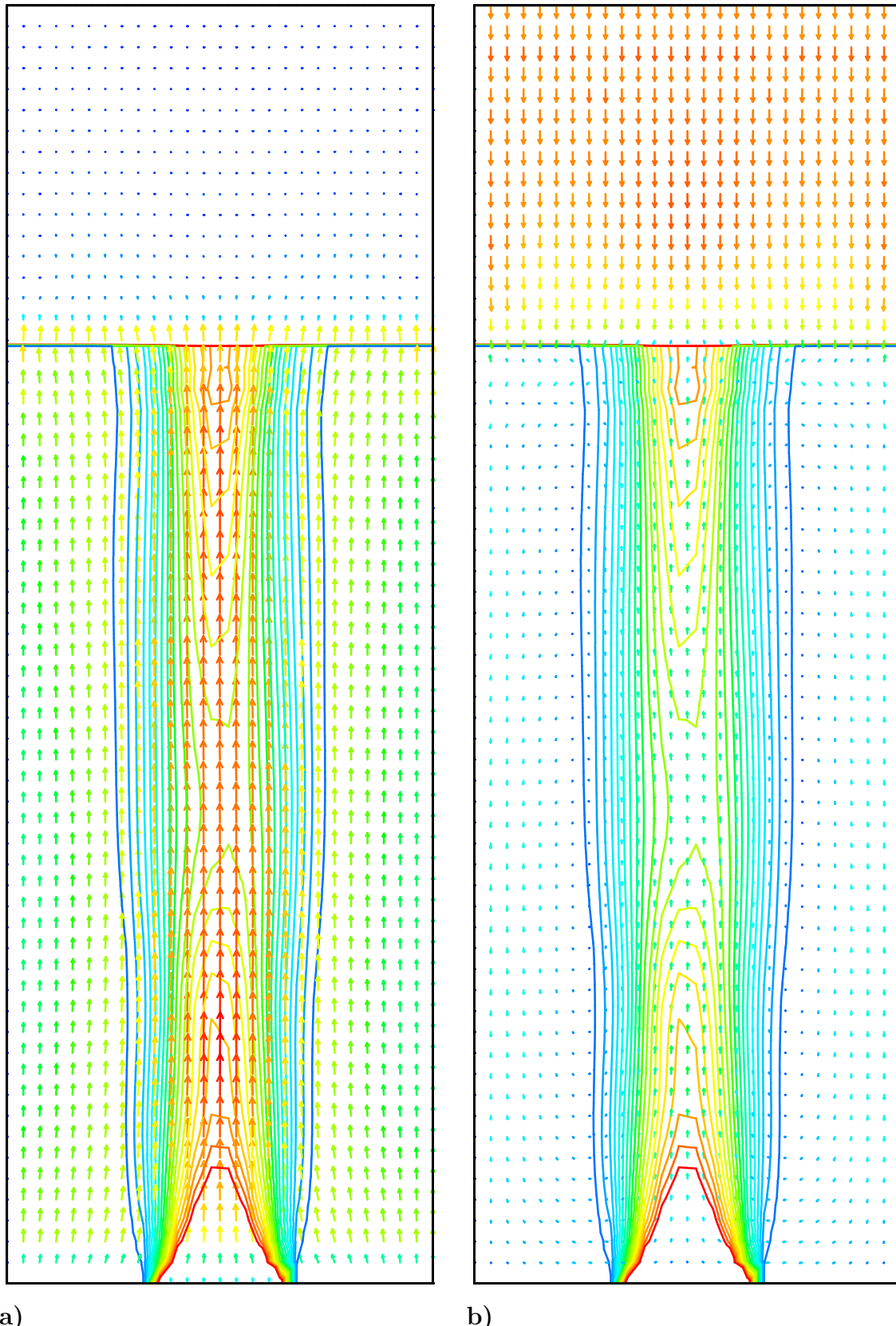


Figure 3.13: Time averaged phase fraction (iso-lines) and the velocity fields (vectors) for the bubble plume test case. The air flow rate is 48 l/h: **a)** gas velocity; **b)** liquid velocity.

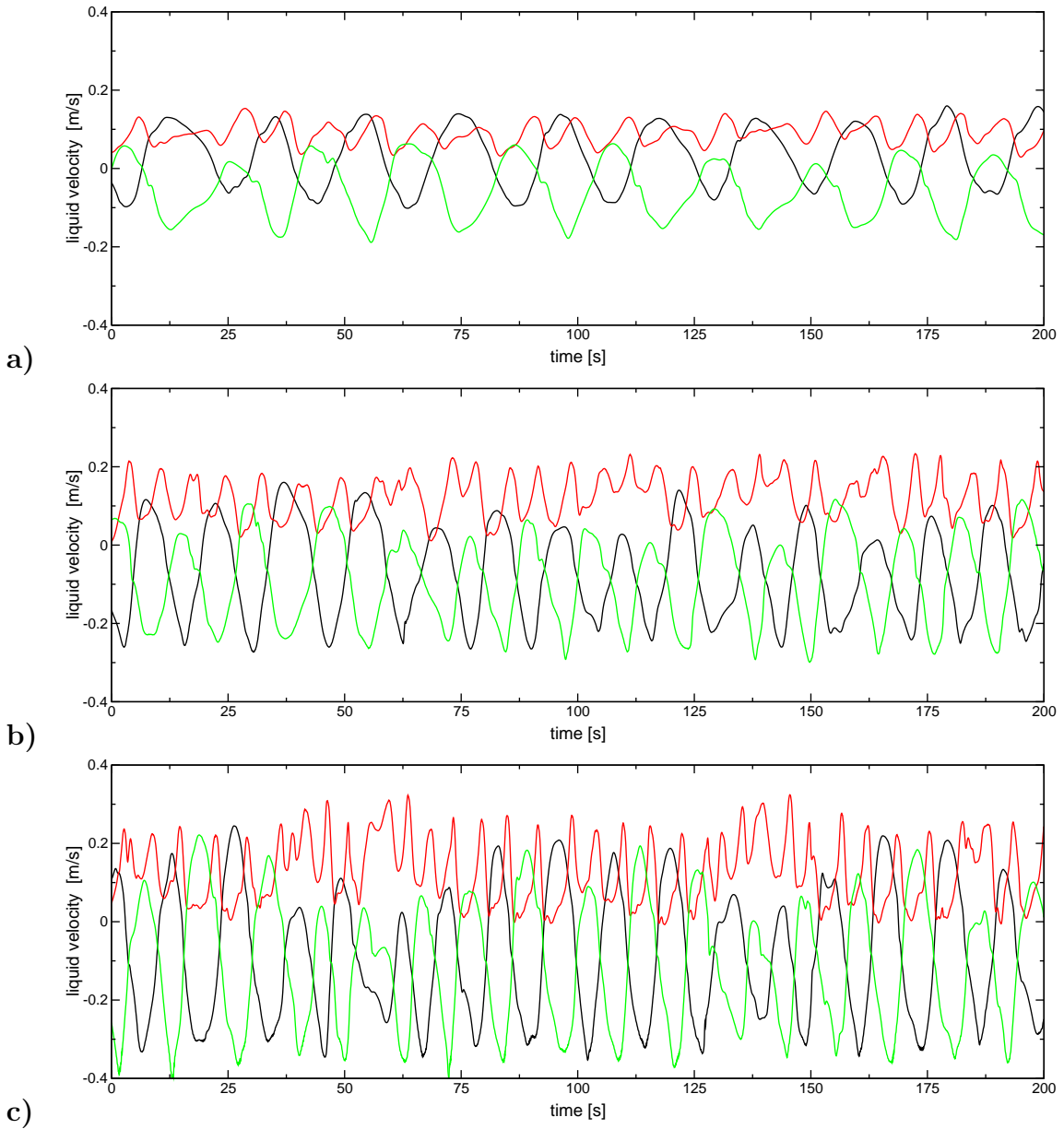


Figure 3.14: Liquid velocity in the vertical direction at three locations (location A: black; B: red and C: green). The air flow rate is: **a)** 20 l/h; **b)** 48 l/h; **c)** 90 l/h.

frequency.

The periods determined from the liquid velocity in the horizontal and vertical direction at locations A and B are plotted as a function of the gas flow rate in Figure 3.16. The periods are reduced by the increasing air flow rate, as shown earlier in Figure 3.14, and are in good agreement with the experimental data, which are denoted by the circles.

It has been noted earlier that the periods of the vertical motion of the liquid at location B are half of those at location A. This is also evident from Figure 3.16.

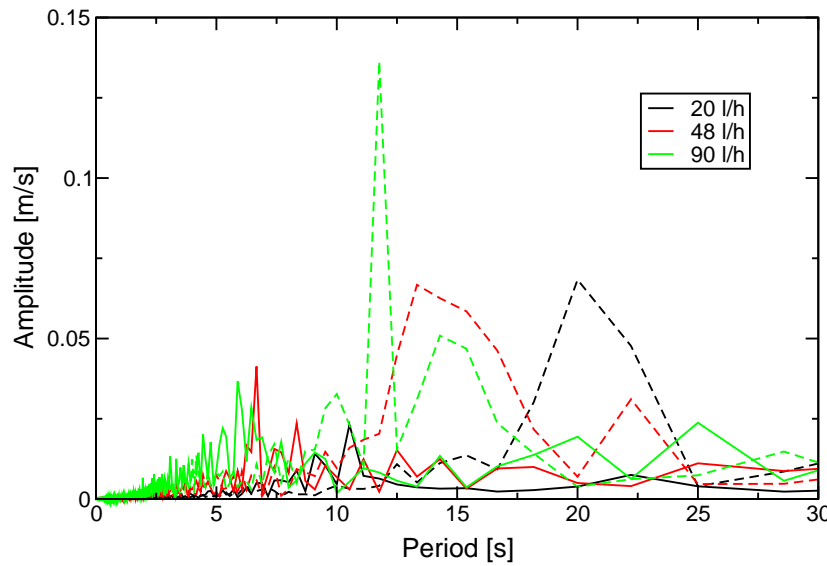


Figure 3.15: Fourier transform of the liquid velocity in the vertical direction at two locations (location A: broken lines; and B: solid lines) and different air flow rates.

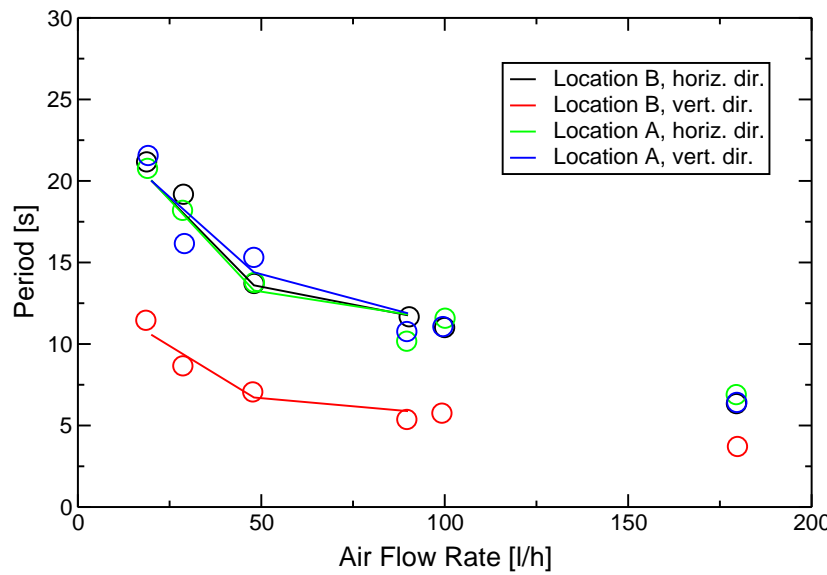


Figure 3.16: Variation of period of the vertical liquid velocity with the air flow rate at locations A and B. The circles denote the experimental data.

However, a similar reduction is not noticeable for the periods of the liquid's motion in the horizontal direction. This can be explained by the fact that the vortices on each side of the bubble plume act in concert to generate the liquid flow in horizontal direction.

3.4 Closure

This Chapter described the basic two-fluid methodology used later in this study. First, the governing equations of the two-fluid model were stated and turbulence and basic inter-phase momentum transfer modelling were introduced. Then, the numerical solution procedure was discussed. The discretised equations were presented along with the overall solution procedure. Here, several options for the numerical treatment of the drag term, phase continuity equation as well as the pressure-velocity coupling were summarised.

Finally, solutions for three challenging test cases were obtained to assess the stability and speed of the solution procedure. Some preliminary comparison with experimental data was also conducted. The numerical results are in good agreement with the experiments. However, further modelling efforts are needed, in particular, regarding the inter-phase momentum transfer term and the influence of the phase fraction on it. Those will be dealt with in later Chapters.

Chapter 4

Interface-Capturing Methodology

This Chapter presents the interface-capturing methodology utilised later to perform direct numerical simulations to examine the influence of shear on the motion of air bubbles in water. First, the governing equations are stated. The space domain is translated along with the rising bubble in order to minimise the computational effort and an additional acceleration term has to be included into the momentum equation in order to account for this motion. Then, the discretised equations are presented and the numerical solution procedure is discussed. This Section is complemented with an outline of the numerical treatment of the boundary conditions as well as two adjustment procedures: the first procedure updates the velocity of the moving frame of reference; and the second adjusts the time step of the simulation. The discussion of the numerical solution procedure concludes with a summary of the overall solution procedure. Finally, the complete methodology is validated for two test cases where experimental data are available. The first case is that of single air bubbles of different sizes in quiescent water and the second one deals with single air bubbles in glycerol-water solutions under the influence of shear.

4.1 Governing Equations

In this Section, a mathematical representation of the simultaneous flow of two immiscible, incompressible fluids, each having a constant viscosity, is presented. This mathematical representation includes surface tension, but neglects heat and mass transfer.

It is based on writing one set of conservation equations for the whole flow field where the material properties and the flow field are, in general, discontinuous across the boundary (or interface) between the fluids. An alternative, however equivalent, representation can be found in most standard textbooks. It is obtained by writing down the conservation equations separately for each fluid and matching them at the interface.

In this single-field representation, the fluids are identified by a step (Heaviside) function H , which is 1 in one particular fluid and 0 elsewhere. Hence, the density as well as any other material property, can be written in terms of their constant values on either side of the interface and the Heaviside function:

$$\rho(\mathbf{x}, t) = \rho_a H(\mathbf{x}, t) + \rho_b (1 - H(\mathbf{x}, t)) \quad (4.1)$$

where t is the time, \mathbf{x} is the position vector and ρ_φ stands for the density in phase φ .

The interface itself is marked by a non-zero value of the gradient of the step function. The representation of inter-facial phenomena such as surface tension is achieved by adding the appropriate interface terms to the governing equations. Since these terms are concentrated at the interface, they are represented by three-dimensional δ -functions. The three-dimensional δ -function is constructed by repeated multiplication of one-dimensional Dirac δ -functions:

$$\delta(\mathbf{x}) = \delta(x)\delta(y)\delta(z) \quad (4.2)$$

4.1.1 Momentum and Continuity Equations

The fluid motion is assumed to be governed by the Navier-Stokes equations for an incompressible fluid. Nevertheless, in a single-field formulation, the conservation equations have to account for both the differences of the material properties as well as the surface tension force acting at the interface. The mass continuity and momentum equations read [394, 395]:

$$\nabla \cdot \mathbf{V} = 0 \quad (4.3)$$

$$\frac{\partial \rho \mathbf{V}}{\partial t} + \nabla \cdot (\rho \mathbf{V} \mathbf{V}) = -\nabla p + \nabla \cdot \boldsymbol{\tau} + \rho \mathbf{f} + \int_{S(t)} \sigma \kappa' \mathbf{n}' \delta(\mathbf{x} - \mathbf{x}') dS \quad (4.4)$$

where t is the time, \mathbf{V} is the velocity field, $\boldsymbol{\tau}$ is the stress tensor and \mathbf{f} stands for the acceleration due to body forces. In this study, the only body force acting on the system is gravity, *i.e.* $\mathbf{f} = \mathbf{g}$.

The last term in equation (4.4) represents the source of momentum due to surface tension. It only acts at the interface as indicated by the integral of a three-dimensional δ -function over the entire surface of the interface $S(t)$, *i.e.* $\int_{S(t)} \delta(\mathbf{x} - \mathbf{x}') dS$. Of course, this integration is neither practical nor necessary for every point in the flow and we shall rewrite this term in Section 4.2.2 before numerical implementation. The other variables in this term denote the surface tension coefficient σ as well as the curvature κ and the normal vector \mathbf{n} of the interface. Primed variables denote values at the interface.

It should be noted that equations (4.3) and (4.4) are valid for the whole flow field including the interface. As outlined earlier, an alternative, however equivalent, representation can be found by writing down the conservation equation separately for each fluid and matching them at the interface. The boundary conditions can be obtained by integrating the equations over a small volume enclosing the interface. Integrating the momentum equation (4.4) in normal direction to the interface yields the usual statement that the normal stresses are balanced by surface tension. Integrating the tangential component shows continuity of the tangential stresses across the interface and integrating the mass continuity equation (4.3) shows that the normal velocities are also continuous.

The Navier-Stokes equations have to be supplemented by an equation, which relates the deformations and the stresses within the fluids. The fluids investigated in this study obey the Newtonian law of viscosity. Hence, the stress tensor is given by:

$$\boldsymbol{\tau} = \mu (\nabla \mathbf{V} + \nabla \mathbf{V}^T) \quad (4.5)$$

where μ is the kinematic viscosity.

4.1.2 Indicator Function

As outlined in Section 1.5.1, the interface-capturing methodology employs the volume fraction as an indicator function to mark the different fluids. The interface is not

defined as a sharp boundary and a transition region exist where the fluid is treated as some mixture of the two fluids on each side of the interface. In reality, this transition region is a discontinuous step. The indicator function is defined as:

$$\gamma = \begin{cases} 1 & \text{for a point inside fluid a} \\ 0 < \gamma < 1 & \text{for a point in the transitional region} \\ 0 & \text{for a point inside fluid b} \end{cases} \quad (4.6)$$

where γ is the indicator function. It is associated with each fluid and is hence propagated with them as a Lagrangian invariant [155]. Therefore, it obeys a transport equation of the form:

$$\frac{\partial \gamma}{\partial t} + (\mathbf{V} \cdot \nabla) \gamma = 0 \quad (4.7)$$

Using the indicator function, the local density ρ and the local viscosity μ of the fluid are given by:

$$\rho = \gamma \rho_a + (1 - \gamma) \rho_b \quad (4.8)$$

$$\mu = \gamma \mu_a + (1 - \gamma) \mu_b \quad (4.9)$$

where the subscripts a and b denote the different fluids.

4.1.3 Non-Inertial Frame of Reference

In this study, the space domain is moved along with the rising bubble and its velocity is adjusted so that the bubble is kept centred within the domain. In this way, the domain size can be minimised and local refinement can be applied to increase mesh resolution in the vicinity of the bubble. However, the frame of reference of the space domain is now non-inertial and its acceleration has to be accounted for in the momentum equation. In the case of steady rotating motion, this results in the familiar Coriolis and centrifugal terms (see Batchelor [19, p. 139]).

Figure 4.1 depicts the situation for a bubble rising in a quiescent liquid. The bubble rises with respect to the inertial frame of reference ($x - y$), but remains centred within the space domain with its non-inertial frame of reference ($\hat{x} - \hat{y}$). The velocities on the boundary of the space domain \mathbf{U}_B are equal to the negative velocity of the

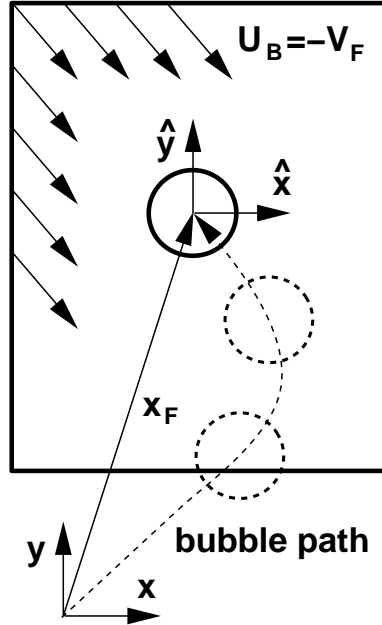


Figure 4.1: Sketch of the space domain and its non-inertial frame of reference ($\hat{x} - \hat{y}$) relative to the inertial frame ($x - y$).

moving reference frame. The velocity and acceleration of the moving reference frame relative to the inertial reference frame are given by:

$$\mathbf{V}_F = \frac{d\mathbf{x}_F}{dt} \quad (4.10)$$

$$\mathbf{a}_F = \frac{d\mathbf{V}_F}{dt} \quad (4.11)$$

where \mathbf{x}_F , \mathbf{V}_F and \mathbf{a}_F denote the position, velocity and acceleration of the moving reference frame, respectively. The velocity of the moving reference frame is adjusted in at the beginning of each time step. Its position and acceleration are then evaluated numerically. This adjustment procedure will be outlined in Section 4.2.6.

We noted before, that the acceleration of the moving reference frame has to be accounted for in the momentum equation (4.4). In our case, the moving reference frame is translated with a variable velocity, but not rotated. Hence, only a linear acceleration term a_F has to be added on the l.h.s. [19, p.139]:

$$\frac{\partial \rho \mathbf{U}}{\partial t} + \rho \mathbf{a}_F + \nabla \cdot (\rho \mathbf{U} \mathbf{U}) = \dots \quad (4.12)$$

Note that the momentum equation is now expressed in terms of the velocity relative to the moving reference frame \mathbf{U} and that the same transformation has to be applied to the transport equation for the indicator function, equation (4.7).

This completes the mathematical description of the system. The solution procedure is described next.

4.2 Solution Procedure

The numerical solution procedure for the interface-capturing methodology is presented in this Section. It has been developed by Weller [424] and it is similar to that proposed by Ubbink [403, 404]. Its main ingredients are outlined next: first, a bounded compression technique for the indicator function γ is described in Section 4.2.1. Then, the calculation of the surface tension term from a smoothed indicator function is outlined in Section 4.2.2. Next, the solution procedure of Weller [423] presented in Section 3.2.10 is adapted to handle the pressure-velocity coupling. This requires the construction of the discretised momentum equation and a correction loop in which the pressure equation is solved and the momentum corrected based on the pressure change. This part of the procedure is given in Section 4.2.4. Finally, the boundary conditions as well as the adjustment procedures for the frame velocity and time step are given in Sections 4.2.5, 4.2.6 and 4.2.7, respectively. After detailed description of the ingredients, the overall solution procedure is summarised in Section 4.2.8.

4.2.1 Indicator Equation with Bounded Compression

The choice of the phase fraction as an indicator function is a popular one, but it is prone to problems associated with the convection of a step function. Many researchers have proposed techniques for this purpose and some alternatives are reviewed in [403, 404, 320]. In the Weller scheme [424], the necessary compression of the interface is not achieved by using a compressive differencing scheme, but rather by introducing an extra, artificial compression term (the third term on the l.h.s. of equation (4.13) below) into the indicator function equation:

$$\frac{\partial \gamma}{\partial t} + \nabla \cdot (\mathbf{U}\gamma) + \nabla \cdot (\mathbf{U}_r\gamma(1-\gamma)) = 0 \quad (4.13)$$

Here, \mathbf{U}_r is a velocity field suitable to compress the interface. The artificial term is only active in the thin interface region because of the multiplication term

$\gamma(1 - \gamma)$. Therefore, it does not affect the solution significantly outside this region. The advantage of equation (4.13) is that its solution for γ can be bounded between zero and one using the discretisation practises discussed in Section 3.2.6. Note that Equation (4.13) is identical to equation (3.58). Following the practices outlined in option 4 of Section 3.2.6, the discretised transport equation for the indicator function reads:

$$\left[\left[\frac{\partial[\gamma]}{\partial t} \right] + \left[\nabla \cdot (\phi[\gamma]_{f(\phi,S)}) \right] + \left[\nabla \cdot (\phi_{r_b}[\gamma]_{f(\phi_{r_b},S)}) \right] \right] = 0 \quad (4.14)$$

where ϕ is the volumetric flux and ϕ_{r_b} stands for $\phi_{r_b} = (1 - \gamma)_{f(-\phi_r,S)} \phi_r$. The volumetric flux is defined as $\phi = \mathbf{S} \cdot \mathbf{U}_f$. It is a result of the pressure-velocity solution procedure outlined in Section 4.2.4 and is *not* evaluated by taking the dot product of the face area vector and the face interpolate of the velocity as this would not obey continuity.

There are many possible formulations for the compression velocity \mathbf{U}_r . In this study, we use one that is based on the maximum velocity magnitude in the transition region. The compression should act perpendicular to the interface. This is achieved by multiplying the maximum velocity magnitude by the normal vector of the interface:

$$\phi_r = K_c \mathbf{n}^* \max \frac{|\mathbf{n}^* \phi|}{|\mathbf{S}|^2} \quad (4.15)$$

where K_c is an adjustable coefficient which determines the magnitude of the compression. Preliminary studies have shown that $K_c = 1.5$ gives good results. The unit normal vector \mathbf{n}^* of the interface is evaluated from the smoothed indicator function. This is explained in the next Section.

One of the desirable properties of the indicator function γ is that of a sharp interface, with the transition region being as thin as possible. However, this requirement renders the accurate determination of its gradient impossible. This gradient is needed to calculate the unit normal vector of the interface, which is then used in the calculation of the curvature of the interface. In order to alleviate this problem, many authors followed Brackbill et al. [37] and convolve γ with a smooth kernel to construct a smoothed function γ^* from which to obtain the gradients and curvature more accurately. The accuracy and convergence properties of some of these kernels have been discussed by Williams et al. [431]. In this study, the smoothed indicator function is

obtained by elliptic relaxation:

$$\left\| \nabla \cdot \left(\left(\frac{w_\gamma}{|\mathbf{d}|} \right)^2 \nabla [\gamma^*] \right) \right\| = [[[\gamma^*]]] + \gamma \quad (4.16)$$

where \mathbf{d} denotes the vector between the centre of the cell of interest P and the centre of a neighbouring cell N , as shown in Figure 2.2. w_γ is an adjustable coefficient related to the width of the transition region of the smoothed indicator function γ^* . Preliminary studies have shown that $w_\gamma = 0.5$ gives good results. After this smoothing operation, the interface unit normal vector is evaluated at the cell faces from the smoothed indicator function. It is given by:

$$\mathbf{n}^* = \frac{(\nabla \gamma^*)_f}{|(\nabla \gamma^*)_f| + \delta} \quad (4.17)$$

where \mathbf{n}^* is the interface unit normal vector and δ is a small number in order to stabilise the calculation in regions outside the transition region where $|\nabla \gamma^*| \rightarrow 0$. Throughout this study, $\delta = 10^{-5}$ is used.

4.2.2 Calculation of Surface Tension

The surface tension force acts on the interface between the two phases. However, in the interface-capturing methodology (and other volume methods) the interface is not tracked explicitly and, consequently, its exact shape and location are unknown. Therefore, the surface integral in equation (4.4), which represents the source of momentum due to surface tension, cannot be evaluated directly. Brackbill et al. [37] overcame this problem with their continuum surface force (CSF) model, which represents the surface tension effects as a continuous volumetric force acting within the transition region. It reads:

$$\int_{S(t)} \sigma \kappa' \mathbf{n}' \delta(\mathbf{x} - \mathbf{x}') dS \approx \sigma \kappa \nabla \gamma \quad (4.18)$$

where κ is the curvature of the interface, given by:

$$\kappa = \nabla \cdot \left(\frac{\nabla \gamma}{|\nabla \gamma|} \right) \quad (4.19)$$

It should be noted that the CSF model neglects the effects of a variable surface tension coefficient. In the solution procedure, the curvature is calculated from the

interface unit normal vector such that:

$$\kappa = -\nabla \cdot \mathbf{n}^* \quad (4.20)$$

It should be noted that the total surface tension force over a closed surface equals to zero [395, 394, 311], *i.e.* $0 = \int_{S(t)} \sigma \kappa \mathbf{n} dS$. This property is important and errors result in an unphysical net force. However, it cannot be ensured in this technique and evidence of this problem is given in Section 4.3.1. Unfortunately, the problem is fundamental because, as mentioned above, the surface is not defined as a sharp boundary in volume methods such as interface-capturing and surface integrals such as above can therefore neither be evaluated accurately nor strictly obeyed. In fact, the above also applies to the closedness constraint, *i.e.* $0 = \int_{S(t)} \mathbf{n} dS$, which is not enforced in the current method. On the other hand, constraints based on the surface can be enforced in surface and moving mesh methods. However, as noted in Section 1.5.1, it is impossible to strictly conserve the volume of each fluid in surface methods. The strict, simultaneous assertion of both, conservation of volume and surface constraints, can only be achieved in some moving mesh methods.

4.2.3 Final Form of the Momentum Equation

Before discretisation, two terms of the momentum equation (4.4) are reformulated: firstly, the modified pressure is introduced into the equation; and secondly, the viscous stress term is expanded. The final form of these terms is presented in this Section. Furthermore, the modelling introduced in the previous Section is substituted into the momentum equation.

The specification of the pressure boundary conditions is simplified if the modified pressure is used as a dependent variable. It is defined as:

$$p^* = p - \rho \mathbf{g} \cdot \mathbf{x} \quad (4.21)$$

where p^* stands for the modified pressure, which is obtained by removing the hydrostatic pressure from the pressure. Hence, assuming a quiescent liquid, the modified pressure is zero far away from the bubble. This is advantageous for the specification of the pressure at the boundaries of the space domain. However, this change of working

variables has to be accounted for in the momentum equation. This is achieved by taking the gradient of equation (4.21) and substituting the result into the momentum equation. The gradient of equation (4.21) reads:

$$\begin{aligned}\nabla p^* &= \nabla p - \nabla(\rho \mathbf{g} \cdot \mathbf{x}) \\ &= \nabla p - \rho \mathbf{g} - \mathbf{g} \cdot \mathbf{x} \nabla \rho\end{aligned}\quad (4.22)$$

In addition to the advantage of a simpler specification of the pressure boundary condition, this treatment enables efficient numerical treatment of the steep density jump at the interface by including the term $\mathbf{g} \cdot \mathbf{x} \nabla \rho$ into the Rhie and Chow interpolation. This is explained in the next section.

The viscous stress term is reformulated because its numerical evaluation is more efficient in this way. It reads:

$$\begin{aligned}\nabla \cdot \boldsymbol{\tau} &= \nabla \cdot \left(\mu \left(\nabla \mathbf{U} + (\nabla \mathbf{U})^T \right) \right) \\ &= \nabla \cdot (\mu \nabla \mathbf{U}) + \nabla \cdot \left(\mu (\nabla \mathbf{U})^T \right) \\ &= \nabla \cdot (\mu \nabla \mathbf{U}) + (\nabla \mathbf{U}) \cdot \nabla \mu + \mu \nabla (\nabla \cdot \mathbf{U}) \\ &= \nabla \cdot (\mu \nabla \mathbf{U}) + (\nabla \mathbf{U}) \cdot \nabla \mu\end{aligned}\quad (4.23)$$

Finally, the final form of the momentum equation is assembled. Starting from equation (4.4) and utilising equations (4.12), (4.18), (4.22) and (4.23), the momentum equation expressed for the non-inertial frame of reference (see Section 4.1.3) used in this study reads:

$$\begin{aligned}\frac{\partial \rho \mathbf{U}}{\partial t} + \rho \mathbf{a}_F + \nabla \cdot (\rho \mathbf{U} \mathbf{U}) \\ = -\nabla p^* + \nabla \cdot (\mu \nabla \mathbf{U}) + (\nabla \mathbf{U}) \cdot \nabla \mu - \mathbf{g} \cdot \mathbf{x} \nabla \rho + \sigma \kappa \nabla \gamma\end{aligned}\quad (4.24)$$

Note that the second term on the l.h.s. is due to the acceleration of the moving frame as discussed in Section 4.1.3.

4.2.4 Pressure-Velocity Solution Procedure

The solution of the pressure-velocity system is obtained by adapting the alternative pressure-velocity solution procedure of Weller [423] outlined in Section 3.2.10. Use of this technique is necessary because of the large density ratios encountered in gas-liquid

flows. The problem arises in conjunction with the collocated variable arrangement and has been discussed earlier in Sections 2.2 and 3.2.10.

It should be noted at this point that the collocated variable arrangement has not been adopted by the interface tracking community [394, 214, 311] with the noteworthy exception of Ubbink [403]. There are two reasons for this: firstly, the requirements in terms of mesh complexity are usually very low as most calculations are performed on very simple geometries. Secondly, the preservation of sharp an interface between the fluids is a key goal of the numerical techniques, putting an extra burden onto the pressure-velocity coupling.

The derivation of the pressure-velocity solution procedure follows the one in Section 3.2.10. Special attention needs to be given to the discretisation of the surface tension and buoyancy terms to avoid unphysical oscillations as well as spurious currents.

The momentum correction and pressure equation will be derived from a semi-discretised form of the momentum equation:

$$\mathcal{A}_D \mathbf{U} = \mathcal{A}_H - \nabla p^* - \mathbf{f} \cdot \mathbf{x} \nabla \rho + \sigma \kappa \nabla \gamma \quad (4.25)$$

where the “ H ” operator $(\cdot)_H$ and diagonal $(\cdot)_D$ operator are defined in Section 2.7. \mathcal{A} denotes the system of linear algebraic equations arising from the discretisation of the phase momentum equations without surface tension and buoyancy terms. It reads:

$$\mathcal{A} := \left[\left[\frac{\partial \rho[\mathbf{U}]}{\partial t} \right] \right] + \rho \mathbf{a}_F + \left[\left[\nabla \cdot (\rho_f \phi [\mathbf{U}]_{f(\rho_f \phi, S)}) \right] \right] = \left[\left[\nabla \cdot (\mu_f \nabla [\mathbf{U}]) \right] \right] + (\nabla \mathbf{U}) \cdot \nabla \mu_f \quad (4.26)$$

The momentum correction equation is obtained by decomposing the semi-discretised momentum equation in equation (4.26) into diagonal and “ H ” parts and rearranging. This yields:

$$\mathbf{U} = \frac{\mathcal{A}_H}{\mathcal{A}_D} - \frac{\nabla p^*}{\mathcal{A}_D} - \frac{\mathbf{f} \cdot \mathbf{x} \nabla \rho}{\mathcal{A}_D} + \frac{\sigma \kappa \nabla \gamma}{\mathcal{A}_D} \quad (4.27)$$

The flux predictor and corrector are then derived by interpolating the momentum correction equation using central differencing:

$$\phi = \phi^* - \left(\frac{1}{\mathcal{A}_D} \right)_f |\mathbf{S}| \nabla_f^\perp p^* \quad (4.28)$$

where the flux prediction ϕ^* is expressed by:

$$\phi^* = \left(\frac{\mathcal{A}_H}{\mathcal{A}_D} \right)_f \cdot \mathbf{S} - \left(\frac{1}{\mathcal{A}_D} \right)_f (\mathbf{f} \cdot \mathbf{x})_f |\mathbf{S}| \nabla_f^\perp \rho + \left(\frac{1}{\mathcal{A}_D} \right)_f (\sigma \kappa)_f |\mathbf{S}| \nabla_f^\perp \gamma \quad (4.29)$$

The continuity equation is then recast into one for pressure. This is achieved by formulating the continuity equation (4.3) at the cell faces and substituting the flux corrector equation (4.28) into it. The final result reads:

$$\left[\nabla \cdot \left(\left(\frac{1}{\mathcal{A}_D} \right)_f \nabla [p^*] \right) \right] = \nabla \cdot \phi^* \quad (4.30)$$

The solution of the pressure equation (4.30) provides corrections for updating fluxes and velocities so that continuity is obeyed.

4.2.5 Boundary Conditions

As outlined in Section 4.1.3, the space domain is moving along with the rising bubble and its velocity is adjusted so that the bubble is kept centred within the domain. This is depicted in Figure 4.1 for a rising bubble in quiescent liquid. In this case, the velocities on the boundary of the space domain \mathbf{U}_B are equal to the negative velocity of its moving reference frame. Next, consider a space domain moving in a simple linear shear, given by:

$$\mathbf{V} = \begin{pmatrix} 0 \\ \omega x \\ 0 \end{pmatrix} \quad (4.31)$$

where ω stands for the shear rate. In this case, the velocities on the boundary of the space domain are given by:

$$\mathbf{U}_B = -\mathbf{U}_F + \begin{pmatrix} 0 \\ \omega x_F \\ 0 \end{pmatrix} + \begin{pmatrix} 0 \\ \omega \hat{x} \\ 0 \end{pmatrix} \quad (4.32)$$

where \mathbf{U}_B denotes the boundary velocity, x_F stand for the x-component of the position vector relative to the inertial frame \mathbf{x}_F and \hat{x} is the x-component of the position vector relative to the moving reference frame $\hat{\mathbf{x}}$. These quantities are defined with reference to Figure 4.1. The first term on the r.h.s. of equation (4.32) arises from the motion of the non-inertial frame of reference. The second is due to the frame position within the inertial frame of reference. The last term imposes a linear shear onto the velocity boundary conditions.

In principle, equation (4.32) could now be applied at all boundaries using an inlet boundary condition, as described in Section 3.2.8. However, this treatment does not allow the vorticity generated by the bubble to be convected out of the domain. To solve this problem an outlet boundary condition must be applied where the flow is leaving the space domain. The problem is complicated further if the bubble follows a complex, *e.g.* helical, trajectory. In this situation, the boundaries to the side of the bubble are inlets or outlets depending on the instantaneous lateral motion of the bubble.

In order to overcome the above difficulties, inlet or outlet boundary conditions are applied on a face by face basis depending on the direction of the flow given by equation (4.32). For faces where $\mathbf{U}_B \cdot \mathbf{S} < 0$ (*i.e.* inflow) an inlet boundary condition is used. For the other faces, an outlet boundary condition is applied.

4.2.6 Motion of the Moving Reference Frame

This Section gives details regarding the numerical calculation of the position, velocity and acceleration of the moving reference frame. As outlined in Section 4.1.3, the space domain and the frame of reference connected to it are translated along with the rising bubble. Their velocity is adjusted so that the bubble is kept centred within the space domain. This can be achieved in many ways. In this study, a correction for the velocity of the moving reference frame is obtain from the following expression:

$$\Delta \mathbf{V}_F = \lambda_{Ff} \frac{\hat{\mathbf{x}}_d^f - \hat{\mathbf{x}}_d}{\Delta t} - \lambda_{Fo} \frac{\hat{\mathbf{x}}_d - \hat{\mathbf{x}}_d^o}{\Delta t} \quad (4.33)$$

where $\Delta t = t - t^o$ is the current time step and $\hat{\mathbf{x}}_d$ is the centre of mass of the bubble relative to the moving reference frame calculated from equation (A.3). The superscripts *f* and *o* denote values at the first and the previous time step. λ_{Ff} and λ_{Fo} stand for appropriate under-relaxation factors.

The first term in equation (4.33) represents the velocity, which would be sufficient to translate the bubble back to its original position relative to the moving reference frame within a single timestep. However, this term on its own leads to overshoots even when under-relaxation is applied. The reason for this lies in the fact that the corrections are accumulating until the bubble reaches its original position. Hence, the second term is introduced, which represents the bubble velocity relative to the moving

reference frame. When this term cancels with the first one, no correction is applied. For example, this is the case when the bubble moves towards its original position with a velocity equal to that given by the first term. Furthermore, the second term applies a correction in situations where the bubble has reached its original bubble position, but is still travelling with a finite velocity. Damping of the two terms is provided through the under-relaxation factors λ_{Ff} and λ_{Fo} . It was found that $\lambda_{Ff} = \lambda_{Fo} = 0.1$ yields good results.

The acceleration and position of the moving reference frame have to be evaluated during the course of the interface tracking calculation because they appear in the momentum equation (4.12) and equation (4.32) for the boundary velocity. In order to obtain their values the time derivative of the frame velocity as well as its integral over time have to be determined. This is done by evaluating the following expressions:

$$\mathbf{a}_F = -\frac{\Delta \mathbf{V}_F}{\Delta t} \quad (4.34)$$

$$\mathbf{x}_F = \left(\frac{1}{2} \Delta \mathbf{V}_F + \mathbf{V}_F^o \right) \Delta t + \mathbf{x}_F^o \quad (4.35)$$

where \mathbf{V}_F^o and \mathbf{x}_F^o stand for the frame velocity and frame position at the old time step.

The numerical scheme to determine the frame acceleration given in equation (4.34) is only first order accurate. However, this is consistent with the discretisation of the time derivative and, hence, there is no need to improve the accuracy of this term.

4.2.7 Time Step Control

At the beginning of each (time) iteration, the time step is adjusted such that it is sufficiently small in order to ensure stability of the numerical solution procedure. The time step restrictions of a numerical solution procedure are usually expressed in dimensionless form of a maximum Courant number. The local Courant number \mathcal{C}_o at a cell face is defined in Section 2.5 as:

$$\mathcal{C}_o = \frac{\mathbf{U}_f \cdot \mathbf{S}}{\mathbf{d} \cdot \mathbf{S}} \Delta t \quad (2.25)$$

The time step should be adjusted in a smooth fashion such that the maximum \mathcal{C}_o is around a predefined target value \mathcal{C}_o_t which ensures the stability of the numerical

solution procedure and some under-relaxation has proved to be beneficial in achieving this goal. However, if the maximum $\mathcal{C}o$ is much smaller than its target value, for example, during start-up when the calculation is initialised with a very small time step, the new time step could be several times larger than the previous one even with under-relaxation. In this case, the new time step should be limited to an appropriate multiple of the old time step. On the other hand, more drastic adjustments are needed if the maximum $\mathcal{C}o$ overshoots by a specified tolerance. In this case, the time step is set to the one given by the target $\mathcal{C}o$. A suitable prescription for the new time step is found to be:

$$\Delta t^n = \begin{cases} \min(\Delta t^o + \lambda_t (\Delta t_t - \Delta t^o), 2\Delta t^o) & \text{for } \mathcal{C}o^o \leq K_l \mathcal{C}o_t \\ \Delta t_t & \text{for } \mathcal{C}o^o > K_l \mathcal{C}o_t \end{cases} \quad (4.36)$$

where $\mathcal{C}o_t$, λ_t and K_l are the target Courant number, the under-relaxation factor and the limit for overshoots, respectively. $\Delta t_t = \frac{\mathcal{C}o_t}{\mathcal{C}o^o} \Delta t^o$ is the time step given by the target Courant number $\mathcal{C}o_t$. $\mathcal{C}o^o$ stands for the maximum Courant number evaluated from the results of the last time step.

Experience has shown that the stability of the numerical solution procedure is ensured if the Courant number is kept below 0.5. In this study, good results are obtained by using $\mathcal{C}o_t = 0.5$, $K_l = 1.05$ and $\lambda_t = 0.1$.

4.2.8 Sequence of Solution

The sequence of operation for the solution procedure is summarised in Table 4.1. The solution procedure is based on the PISO algorithm [170] to handle the pressure-velocity coupling.

At the beginning of each time step, adjustments of the time step and the frame velocity are carried out. This is done in steps 1 and 2. The position of the moving reference frame is needed to update the boundary conditions (step 4) and the acceleration of the reference frame has to be accounted for in the momentum equation. They are calculated in step 3. Next, the transport equation for the indicator function is solved in step 5. The result is then smoothed before the unit normal vector and curvature are evaluated (step 6). The pressure-velocity algorithm requires the construction of the

1. Adjust time step, equation (4.36).
2. Adjust frame velocity, equation (4.33).
3. Calculate frame position and acceleration, equations (4.35) and (4.34).
4. Adjust boundary conditions, equation (4.32).
5. Solve the γ -equation (4.14).
6. Smooth γ field and calculate the unit normal vector as well as curvature, equations (4.16), (4.20) and (4.17).
7. Construct \mathcal{A} , equation (4.26).
8. PISO-Loop:
 - (a) Predict fluxes using equation (4.29).
 - (b) Construct and solve the pressure equation (4.30).
 - (c) Correct fluxes, equation (4.28).
 - (d) Reconstruct velocities.

Table 4.1: Interface-capturing numerical solution procedure.

discretised momentum equation (step 7) and a correction loop (step 8) in which the pressure equation is solved and the momentum corrected based on the pressure change.

4.3 Test of Numerical Methodology

4.3.1 Free Rising Bubbles

The dynamics of free rising single bubbles in quiescent liquids have been investigated by several authors. Detailed measurements of rise velocity, shape and trajectory are available in the literature. In this Section, the motion of bubbles of different sizes is compared with experimental results from two sources: firstly, the predicted rise velocities are compared with the empirical correlation proposed by Tomiyama et al. [384, 383]; and secondly, the transient bubble motion is compared with recent measurements by Ellingsen and Risso [88, 87].

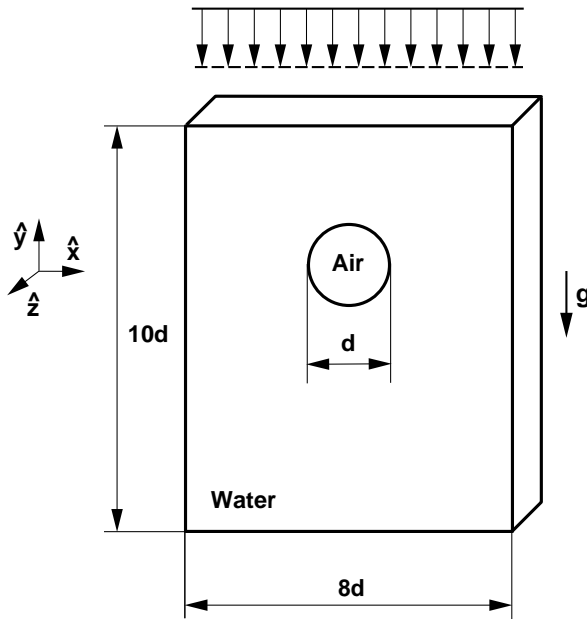


Figure 4.2: Sketch of the setup for free rising bubbles in a quiescent liquid.

Setup

The simulations are for air bubbles in water. The Morton number (see equation (1.7)) for this system is $\log(\mathcal{M}_o) = -11$. Bubbles with nominal diameters between 1 and 5 mm are investigated. The nominal diameter is defined as the diameter of a sphere having the same volume as the bubble. The Eötvös numbers \mathcal{E}_o (see equation (1.6)) for these bubbles vary between 0.14 and 3.50 and the Reynolds numbers \mathcal{R}_e (see equation (1.5)) lie between 300 and 1200.

The three-dimensional space domain is depicted in Figure 4.2. Its size of $8d \times 10d \times 8d$ ($W \times H \times D$) has been chosen so that the boundaries do not interfere with the flow field of the bubble. Here, d is the nominal diameter of the bubble. In the region around the bubble, the computational mesh is refined by cell splitting (embedded refinement) so that the close proximity of the bubble is resolved using 15 cells across the diameter. The total number of cells is approximately 10^5 .

As outlined in Section 4.2.7, the time step is adjusted such that the maximum Courant number is approximately 0.5. Therefore, the time step is a function of the flow field and the cell size which both vary for different bubble sizes. The time step also fluctuates over the duration of the calculation as a result of the unsteady motion of the bubble. The mean time steps for the calculations conducted in this Section fall

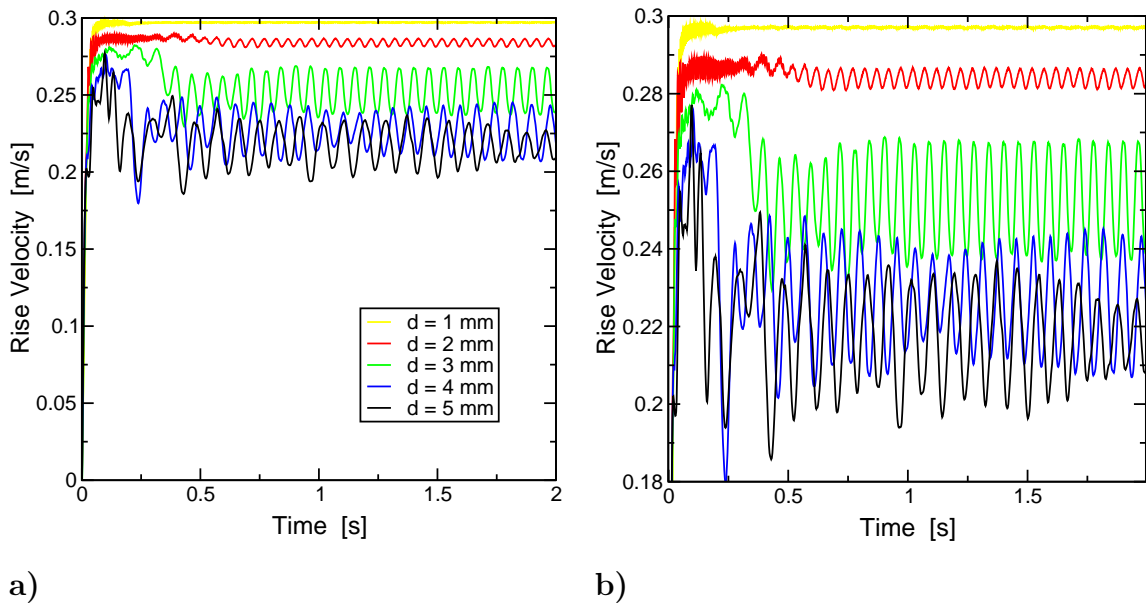


Figure 4.3: Rise velocity as a function of time for bubbles with nominal diameters between 1 and 5 mm: **a)** Overview; **b)** Close-up.

between $\Delta t = 7.7 \times 10^{-5} \text{ s}$ and $4.1 \times 10^{-4} \text{ s}$ for bubbles with a nominal diameter of 1 and 5 mm, respectively.

Results

In Figure 4.3, the rise velocity relative to the inertial frame of reference is given as a function of time for bubbles with nominal diameters between 1 and 5 mm. It is evident that the motion of bubbles with a nominal diameter of 1 mm is stable. For larger bubbles a transition occurs shortly after the start of the calculation and the rise velocity oscillates smoothly. It can also be seen that the average rise velocity decreases with increasing bubble diameter.

This transition can also be observed by examination of the velocity fields shown in Figure 4.4. It is evident that a stable wake is formed behind the bubble when the bubble is sufficiently small. However, as the size of the bubble increases, a transition occurs and the wake of the bubble oscillates from side to side which in turn decreases its rise velocity as discussed earlier. This transition is also evident in the bubble shapes as pictured in Figure 4.4. The smaller bubbles are almost spherical because of dominant surface tension forces. In fact, the magnitude of the surface tension term scales inversely proportional to the square of the bubble diameter.

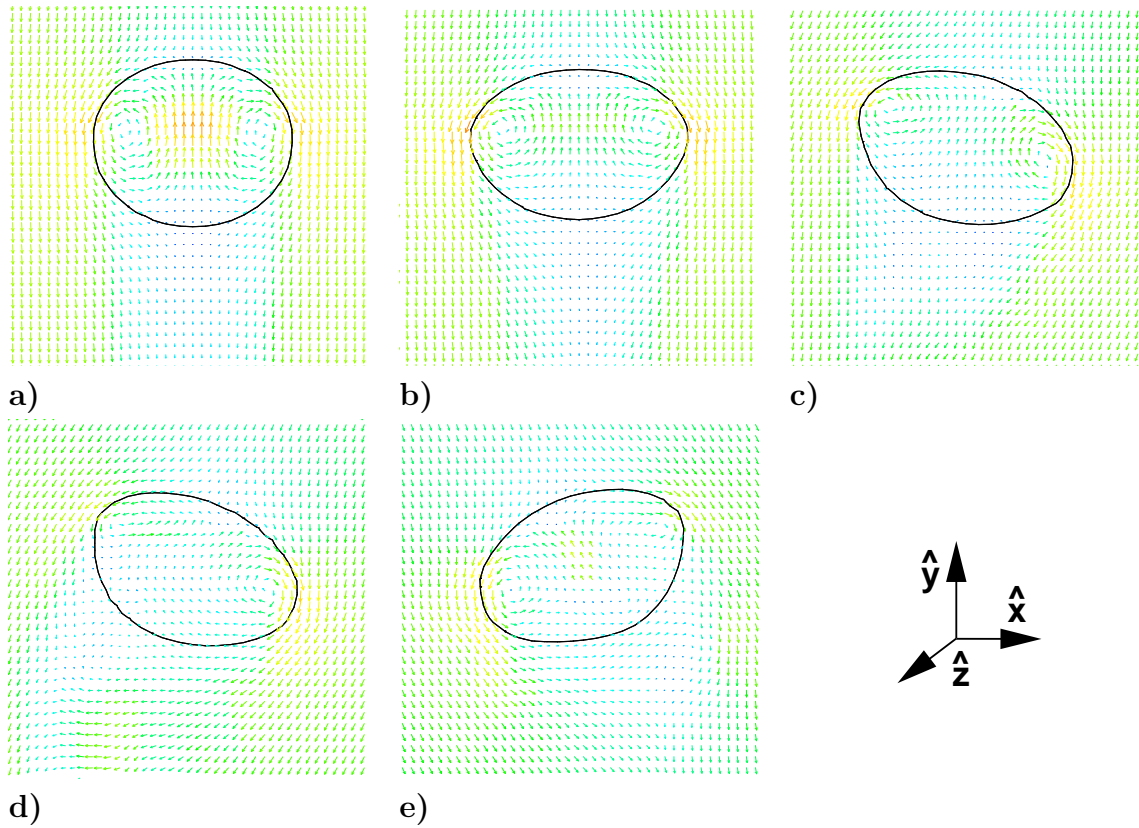


Figure 4.4: Characteristic velocity fields around free rising bubbles, $\log(\mathcal{M}_o) = -11$: **a)** $d = 1$ mm; **b)** $d = 22$ mm; **c)** $d = 3$ mm; **d)** $d = 4$ mm; **e)** $d = 5$ mm.

In Figure 4.5, a top view of the bubble trajectories is plotted. After an initial acceleration phase, bubbles with a nominal diameter of 2 mm and 3 mm prescribe a zigzag trajectory. For larger bubbles, this motion turns into a helical one. The existence of these types of bubble motion as well as their preferred occurrence for similar bubble sizes is well established in the literature, *e.g.* [334, 12, 258, 88, 387] (see Section 1.5.3) and are reproduced here numerically. The motion of the bubble with a nominal diameter of 2.5 mm has been analysed further in the light of the experiments conducted by Ellingsen and Risso [88] and the results are discussed towards the end of this Section.

The trajectories in the vertical $x - y$ plane are shown in Figure 4.6. There is evidence of a periodic lateral motion (zigzag or helical) for most bubbles. However, for the 2 mm bubble, the zigzag motion evident in Figure 4.5a is not noticeable in Figure 4.6a because it is aligned with the vertical $y - z$ plane.

Inspection of the trajectory of the smallest bubble ($d = 1$ mm) reveals that it drifts in x -direction with a constant velocity. This is shown in Figure 4.5a as well as

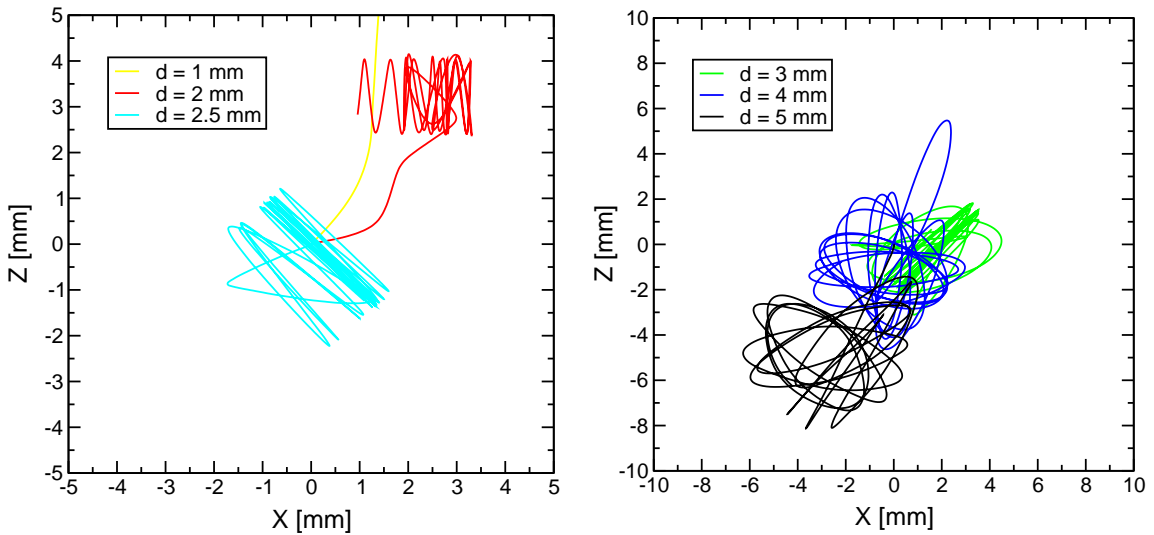


Figure 4.5: Bubble trajectories in the horizontal $x - z$ plane for bubbles with nominal diameters between 1 to 5 mm: **a)** $1 \leq d \leq 2.5$ mm; **b)** $3 \leq d \leq 5$ mm.

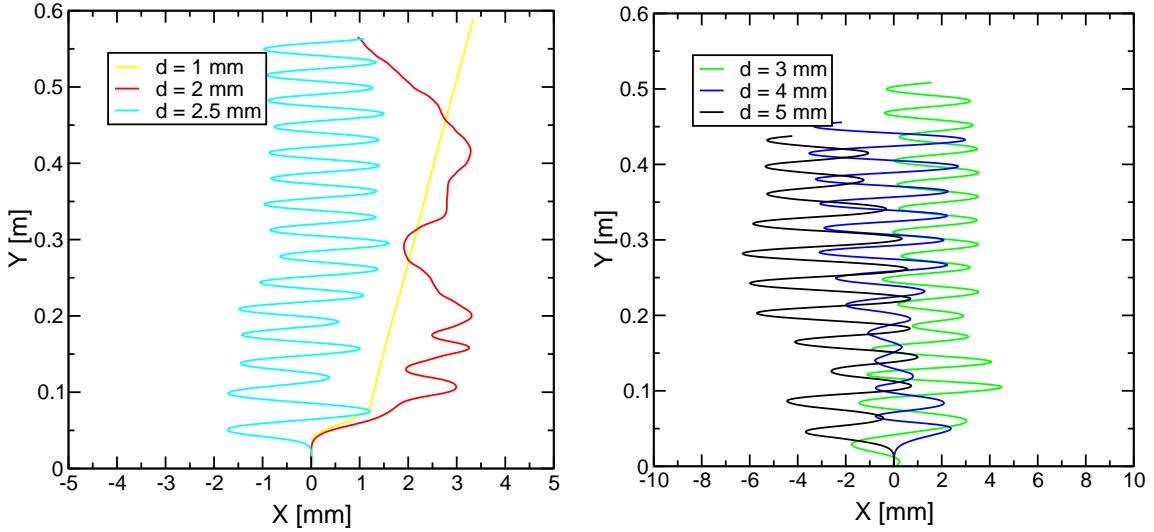


Figure 4.6: Bubble trajectories in the vertical $x - y$ plane for bubbles with nominal diameters between 1 to 5 mm: **a)** $1 \leq d \leq 2.5$ mm; **b)** $3 \leq d \leq 5$ mm.

Figure 4.6a. It should be noted that in this case the magnitude of the lateral velocity is only 6% of the rise velocity. However, this is a deficiency of the numerical solution procedure. It stems from the fact that the discretisation of the surface tension term does not guarantee that its surface integral over a closed surface equals zero. This has been explained in Section 4.2.2.

Figure 4.7 shows a comparison of the calculated and measured $\mathcal{R}e$ as a function of $\mathcal{E}o$ for bubbles with diameters in the range of 1 to 5 mm. Also shown are Tomiyama et al.'s [384] empirical formulae for clean, slightly contaminated and contaminated

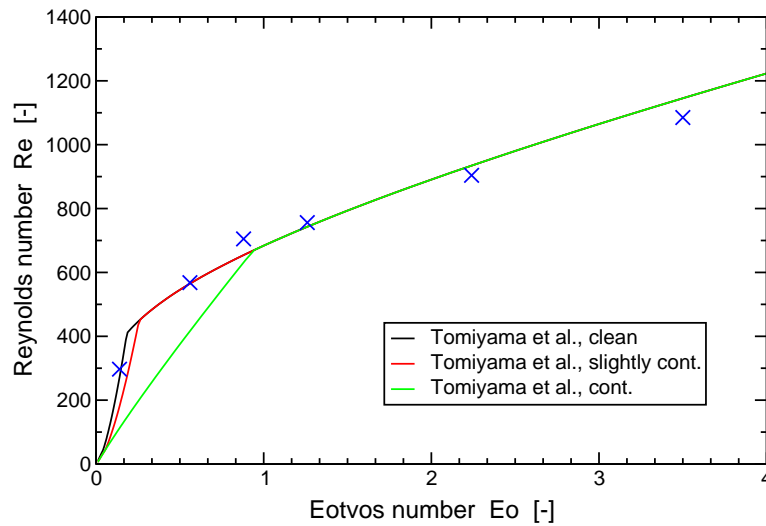


Figure 4.7: Calculated and measured bubble $\mathcal{R}e$ as a function of $\mathcal{E}o$.

d [mm]	U^{To} [m/s]	$U^{E\&R}$ [m/s]	\bar{v}^C [m/s]	$\frac{U^C - U^{To}}{U^{To}}$
1.0	0.275		0.297	+8.0%
2.0	0.283		0.284	+0.4%
2.5	0.261	0.309	0.282	+7.6%
3.0	0.248		0.252	+1.6%
4.0	0.234		0.226	-3.4%
5.0	0.231		0.217	-6.1%

Table 4.2: Comparison of calculated and measured bubble rise velocities.

water, equations (6.30), (6.35) and (6.36), respectively. Typical numerical values for the mean rise velocity and relative differences with Tomiyama et al.'s [384] correlation for clean systems are given in Table 4.2. The agreement with the empirical formula for clean water is excellent and the relative differences are within 8%.

Recently, Ellingsen and Risso [88, 87] measured the motion of a bubble with a nominal diameter of 2.5 mm rising in water using two high speed video cameras. They observed that the bubble dynamics involves two modes. A primary mode develops first, leading to a zigzag trajectory. A secondary mode then grows, causing the trajectory to progressively change into a circular helix. They went on to characterise this motion. For the first mode, the measured trajectories in the principal plane varied very little from a sin-curve. This holds even when the second mode develops. The principal plane is then rotating around the vertical axis. In addition, it was found that the vertical

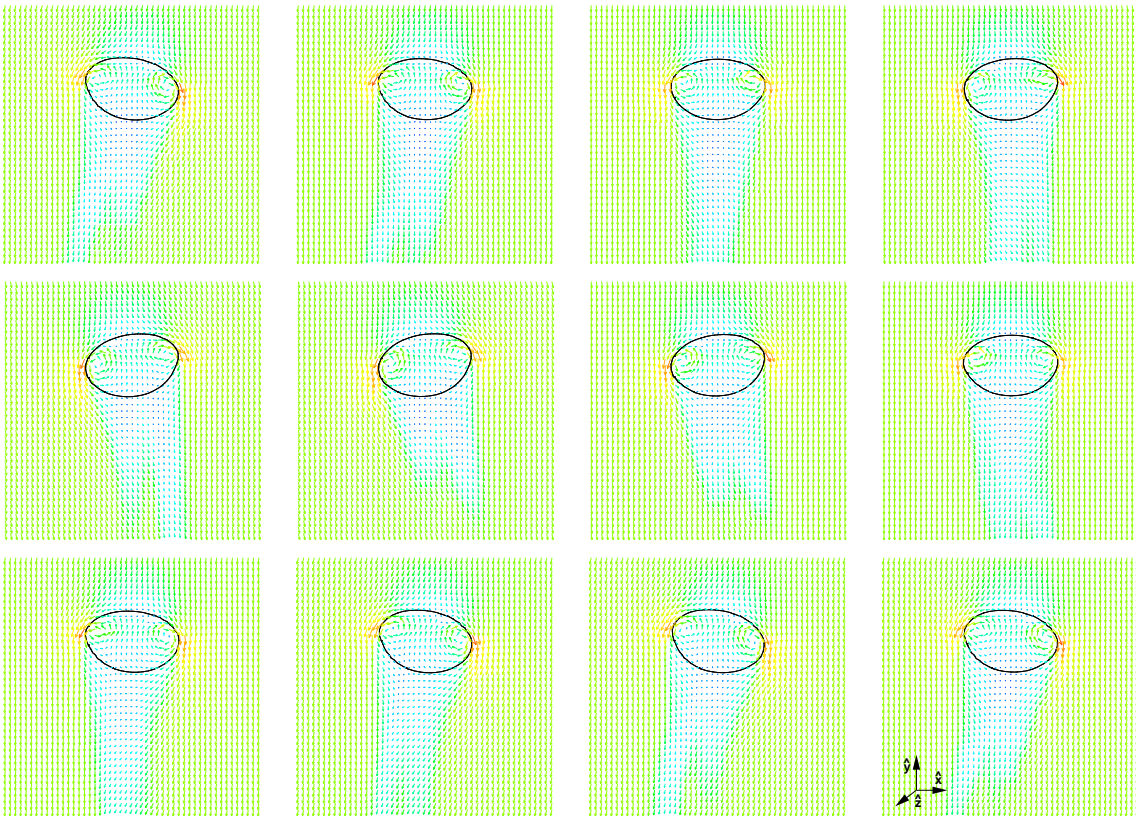


Figure 4.8: Time sequence of the velocity fields around a free rising bubble, $d = 2.5$ mm, $\log(\mathcal{M}_0) = -11$. The time difference between the pictures is $\Delta t = 18$ ms.

motion exhibits weak oscillations at twice the frequency of the horizontal motion.

They then determined the periods $\Delta T_{rise} = 80.6$ ms and $\Delta T_{lat} = 161$ ms for the motion in vertical direction as well as in the principal plane, respectively. The amplitudes were measured as $A_{rise} = 13.7$ mm/s and $A_{lat} = 84.5$ mm/s. The mean rise velocity of this bubble was 0.309 m/s, which is 18% larger than the value given by Tomiyama's correlation, as shown in Table 4.2. However, the present numerical result is only 8.7% smaller than Ellingsen and Risso's measurements.

A time sequence showing the velocity field and the shape of a bubble with a nominal diameter of 2.5 mm is shown in Figure 4.8. The deformation and the wake of the bubble are clearly visible. The shape of the bubble is that of an ellipsoid with a flattened front. An animation of the time sequence has been produced and is available on the CD-ROM accompanying this thesis.

The trajectory of a bubble with a nominal diameter of 2.5 mm in the horizontal $x-z$ plane is shown in Figure 4.5a. It is evident that the motion is confined to a plane,

i.e. a zigzag trajectory. During the duration of the computation (2 s), a transition into the second mode as observed by Ellingsen and Risso [88, 87] does not take place. However, helical motion is predicted for larger bubbles with nominal diameter between 3 and 5 mm, as evidenced in Figure 4.5. For the 3 mm bubble, the motion is initially a zigzag trajectory which is then developing into a helical one. It can therefore be concluded that the model is able to capture the principle modes of bubble motion. The reason for the absence of the second mode for the 2.5 mm bubble might lie in the short simulation time (2 s). It is possible that transition occurs at a later stage of the calculations because the disturbances did not have enough time to grow sufficiently during the course of the calculation. Another reason might be sought in the relatively coarse mesh.

The computed rise and lateral velocity variations for a bubble with a nominal diameter of 2.5 mm are plotted in Figures 4.9 and 4.10, respectively. The periodic movements in vertical as well as lateral direction are clearly evident. The velocities in the two lateral directions are shifted by $\pi/2$. This is further evidence that the bubble is moving in a zigzag trajectory, as shown earlier in Figure 4.5. However, this is fortunate for the quantitative analysis since it is easier to determine the amplitude and frequency of a zigzag trajectory than a helical one, but it should be noted that Ellingsen and Risso [88] developed a method to analyse helical bubble motion.

The present velocity oscillations have been analysed by spectrum analysis and their Fourier transforms are depicted in Figure 4.11. As expected, the periods of the oscillations in the two lateral directions are identical. This is also true for the amplitudes, indicating that the bubble is oscillating in a plane which forms an angle of 45° with $x - z$ plane. This is probably due to numerical reasons and might explain why transition to an helical motion as observed in some of the experiments is delayed. Further investigations, especially employing finer meshes, are needed to resolve this issue, but could not be carried out in the course of this study due to limited computer resources.

Table 4.3 compares the calculated and measured periods and amplitudes. The vertical motion exhibits oscillations at twice the frequency of the horizontal motion which is in agreement with the experiments. However, the calculated periods are

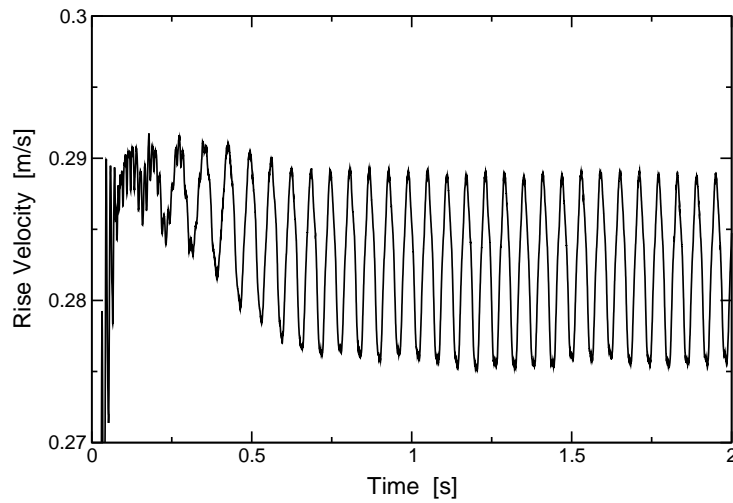


Figure 4.9: Rise velocity of bubble with a nominal diameter of 2.5 mm as a function of time.

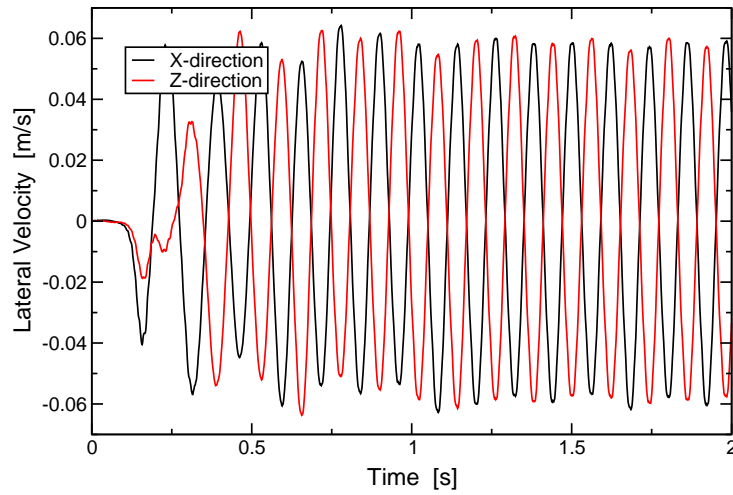


Figure 4.10: Lateral velocities of bubble with a nominal diameter of 2.5 mm as a function of time.

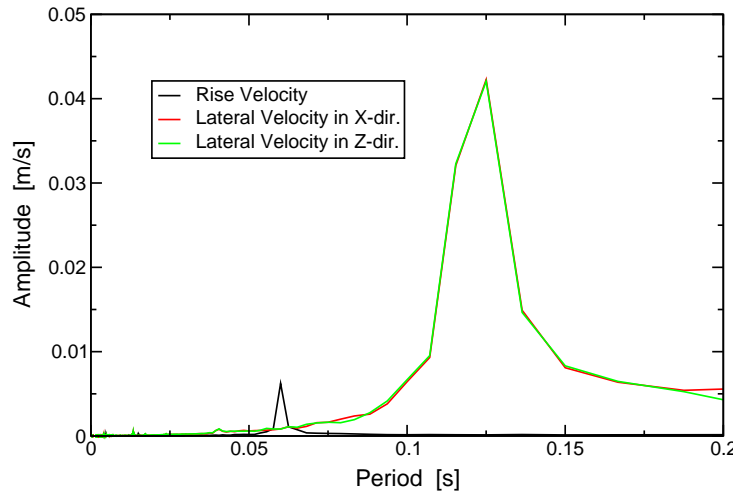


Figure 4.11: Fourier transform of the rise and lateral velocity of a bubble with a nominal diameter of 2.5 mm.

	meas.	calc.	$\frac{\text{meas.} - \text{calc.}}{\text{meas.}}$
$\Delta T_{rise} [\text{ms}]$	80.6	60	+26%
$\Delta T_{lat} [\text{ms}]$	161	125	+22%
$A_{rise} [\text{mm/s}]$	13.7	6.0	+56%
$A_{lat} [\text{mm/s}]$	84.5	60.1	+29%

Table 4.3: Comparison of calculated and measured velocity periods and amplitudes for a bubble with a nominal diameter of 2.5 mm.

somewhat smaller than what has been measured.

The calculated amplitude of the lateral velocity is also smaller than the measured one. Note that the amplitudes in x - and z -direction have been combined to give the amplitude of the oscillation in the principal plane, *i.e.* $\sqrt{2} \cdot A_{lat} = \sqrt{2} \cdot 42.5 \text{ mm/s} = 60.1 \text{ mm/s}$. The measured value is 84.5 mm/s and the relative error is therefore 29%. Some of these discrepancies can be explained by the fact that the calculated bubble rise velocity is smaller than the measured one by 8.7%, as shown in Figure 4.2. However, some of the error has to be attributed to the relatively coarse mesh. In contrast, the amplitude of the rise velocity is under-predicted by 56%. This large error is not too surprising considering that the oscillations are much weaker in this direction. It is likely that better results could be obtained by refining the mesh.

4.3.2 Free Rising Bubbles in Linear Shear

Very few experiments have been carried out to measure the dynamics of bubbles in shear flow. Recently, Tomiyama et al. [389] conducted detailed measurements of trajectories of single bubbles in linear shear. Their experimental setup and results are outlined in Section 7.2.5 and it is this test case which has been chosen to validate the interface-capturing methodology for cases where shear has an effect on the bubble dynamics.

Setup

The setup is very similar to that used in the previous Section for the free rising bubbles. In particular, the three-dimensional space domain, which is depicted in Figure 4.12, is identical to that used in the previous calculations and consists of approximately 10^5 cells. Its size of $8d \times 10d \times 8d$ ($W \times H \times D$) has been found to be large enough to ensure

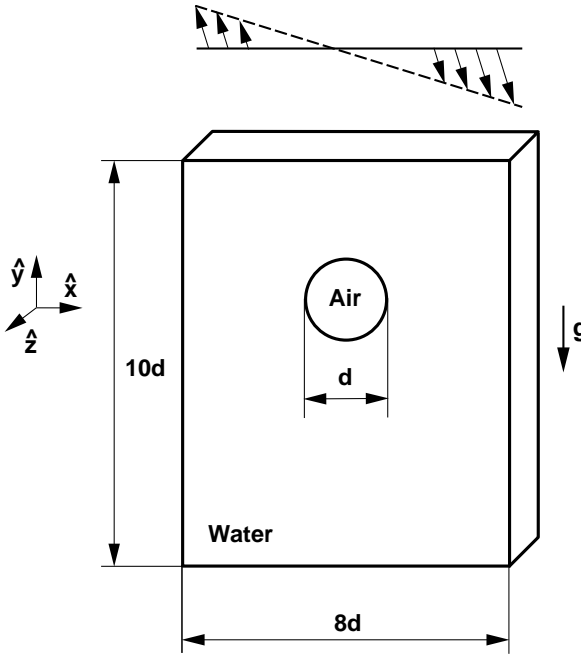


Figure 4.12: Sketch of the setup for free rising bubble in linear shear.

negligible effects by the boundary conditions on the flow field of the bubble. However, the simulations differ in two important points: firstly, a linear shear is imposed which is given by:

$$\mathbf{V}_c = \begin{pmatrix} 0 \\ \omega_x \\ 0 \end{pmatrix} \quad (4.37)$$

where ω and x denote the shear rate and x -coordinate, respectively.

Secondly, the simulations are now obtained for air bubbles in glycerol-water solutions. The viscosities of the glycerol-water solutions chosen by Tomiyama et al. [389] are approximately 18 to 80 times higher than that of water in order to suppress the oscillating motion frequently encountered for bubbles in low viscosity fluids. \mathcal{M}_o for these systems are between $\log(\mathcal{M}_o) = -5.3$ and -2.8 . In comparison, \mathcal{M}_o for an air-water system is approximately $\log(\mathcal{M}_o) = -11$. Calculations for free rising air-water bubbles in a linear shear flow are presented in Section 7.5.

Characteristic results of Tomiyama et al.'s [389] experiments are shown in Figure 7.5, which were then used to infer the lift coefficient C_l (see equation (1.15)) and the projected diameter. These properties are also not immediate results of the simulations and some post-processing is required to extract their values. To determine C_l from the calculated bubble trajectory, a procedure similar to the one employed by Sridhar and

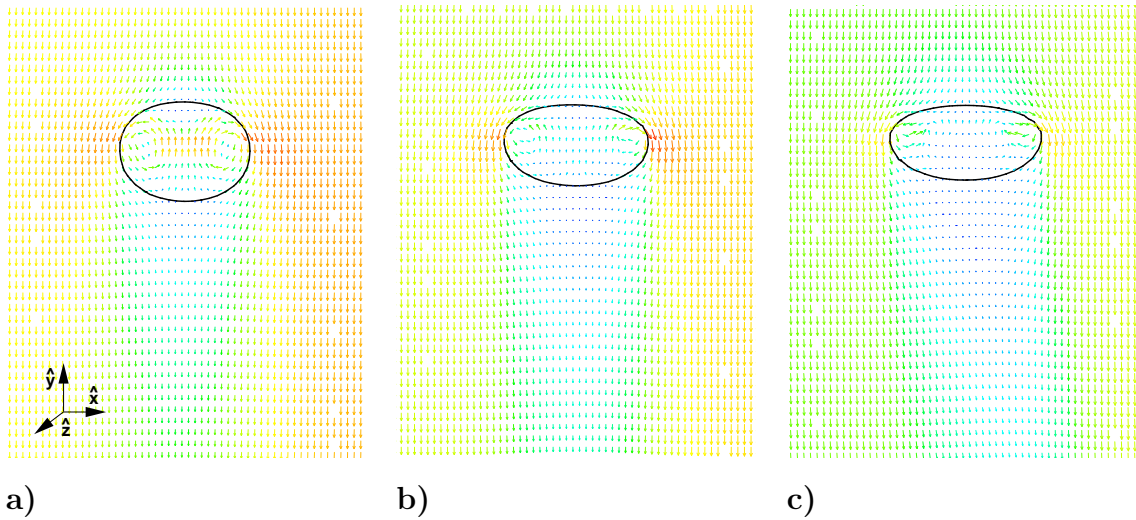


Figure 4.13: Velocity field around sheared free rising bubbles, $\log(\mathcal{M}_0) = -5.3$, $\omega = -3.8$ 1/s: **a)** $d = 2.84$ mm; **b)** $d = 4.16$ mm; **c)** $d = 4.85$ mm.

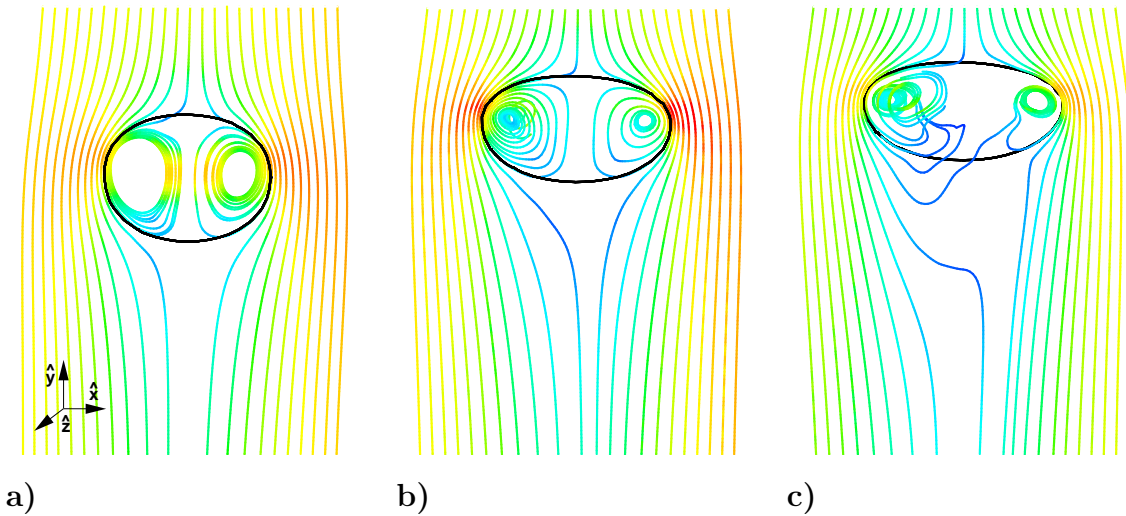


Figure 4.14: Streak-lines coloured by velocity magnitude around sheared free rising bubbles, $\log(\mathcal{M}_0) = -5.3$, $\omega = -3.8$ 1/s: **a)** $d = 2.84$ mm; **b)** $d = 4.16$ mm; **c)** $d = 4.85$ mm.

Katz [359] is utilised. The projected diameter has to be calculated from the phase fraction distribution and, in this study, is obtained by comparing the moments of inertia of the calculated bubble and an ellipsoid. Details on these post-processing procedures are given in Appendices A and B, respectively.

Results

The velocity fields and the shapes of bubbles with nominal diameters of 2.84, 4.16 and 4.85 mm are shown in Figure 4.13. The corresponding \mathcal{E}_0 are 1.65, 4.40 and

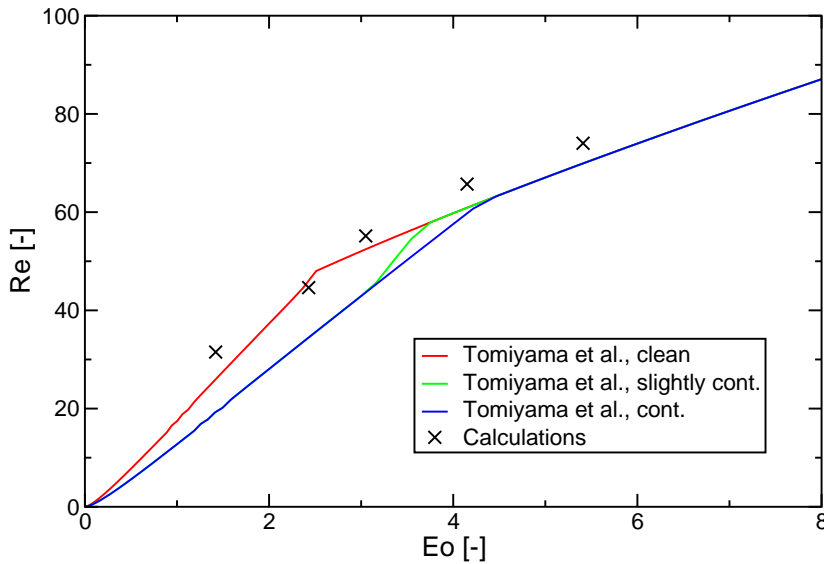


Figure 4.15: Calculated and measured Reynolds number $\mathcal{R}e$ as a function of Eötvös number $\mathcal{E}o$, $\log(\mathcal{M}o) = -5.3$, $\omega = -3.8 \text{ 1/s}$.

6.57, respectively. The shear rates ω and $\mathcal{M}o$ are both set constant at $\omega = -3.8 \text{ 1/s}$ and $\log(\mathcal{M}o) = -5.3$, respectively. The imposed shear is noticeable in that the y -component of the velocity decreases in direction of \hat{x} . Furthermore, the deformations of the bubble shapes and the wakes of the bubbles are clearly evident.

Figure 4.14 shows streak-lines coloured by velocity magnitude around the fore-mentioned bubbles. For the smallest bubble the flow is practically symmetric with respect to the $\hat{y}-\hat{z}$ plane, but for larger bubbles an appreciable asymmetry is noticeable. It is also interesting to note that some of the streak-lines enter the bubble, mainly through the rear. This is not physical and can be attributed to numerical errors in the procedure for generating the streak-lines.

A comparison of the calculated and measured $\mathcal{R}e$ as a function of $\mathcal{E}o$ based on the nominal diameter is shown in Figure 4.15. The nominal diameters of the bubbles are 2.84, 3.52, 4.16, 4.85 and 5.54 mm. Also shown are Tomiyama et al.'s [384] correlations for the rise velocity of bubbles in clean, slightly contaminated and contaminated systems, equations (6.30), (6.35) and (6.36), respectively. The agreement with the empirical formula for clean systems is very good with the relative differences within 7% for larger bubbles. However, the relative difference for the 2.84 mm bubbles is slightly higher at 15%.

Figure 4.16 shows the trajectories in the $x - y$ plane for the fore-mentioned

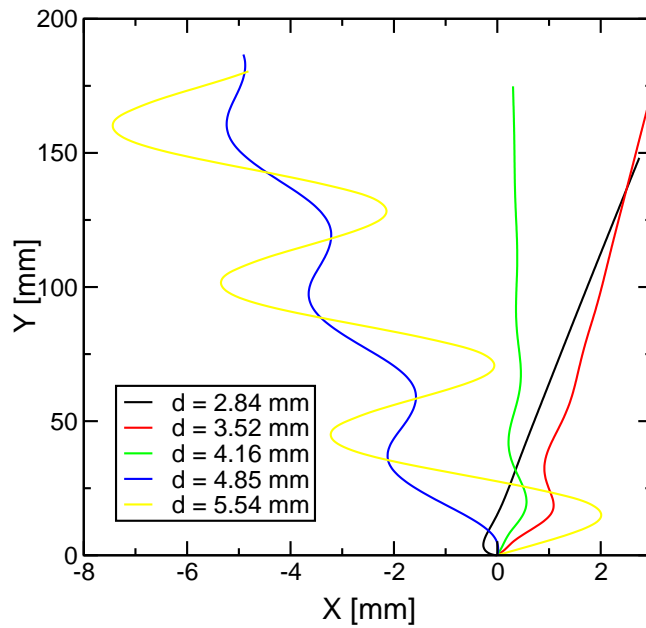


Figure 4.16: Bubble trajectories in the vertical x - y plane for bubbles with nominal diameters between 2.84 and 5.54 mm, $\log(\mathcal{M}_o) = -5.3$, $\omega = -3.8$ 1/s.

bubbles. The smaller bubbles up to a nominal diameter of $d = 4.16$ mm rise in a straight line, whereas the larger bubbles oscillate periodically. Further evidence of the transition into unsteady bubble motion in Figure 4.17 which shows the lift coefficient C_l as a function of time. On the other hand, for higher \mathcal{M}_o , the bubbles always rise in a straight line (not shown) even for the largest bubbles investigated in this study. The same transition has been confirmed experimentally by Tomiyama et al. [389], as evident from Figure 7.5. However, they found that it occurs at $\log(\mathcal{M}_o) = -5.5$ and $d = 5.68$ mm, *i.e.* for slightly larger bubbles in a slightly less viscous fluid. The discrepancy is probably due to perturbations induced by the numerical technique used in this study, but no effort has been made to investigate it further because the accuracy of the technique is sufficient for the purpose of this study.

Furthermore, it is evident from Figure 4.16 that the direction of the lateral motion changes when the diameter increases sufficiently. Smaller bubbles migrate towards the r.h.s., *i.e.* “positive” lift, whereas larger ones move in the opposite direction.

Next, the results for different \mathcal{M}_o and \mathcal{E}_o are summarised in Figure 4.18. For most data points, $C_l(t = 0.75$ s) is plotted as a function of \mathcal{E}_o , but for unsteady bubbles the time-average is taken and the data point is denoted by filled symbols. The circles denote results for the smallest ω investigated by Tomiyama et al. [389]. ω is kept constant

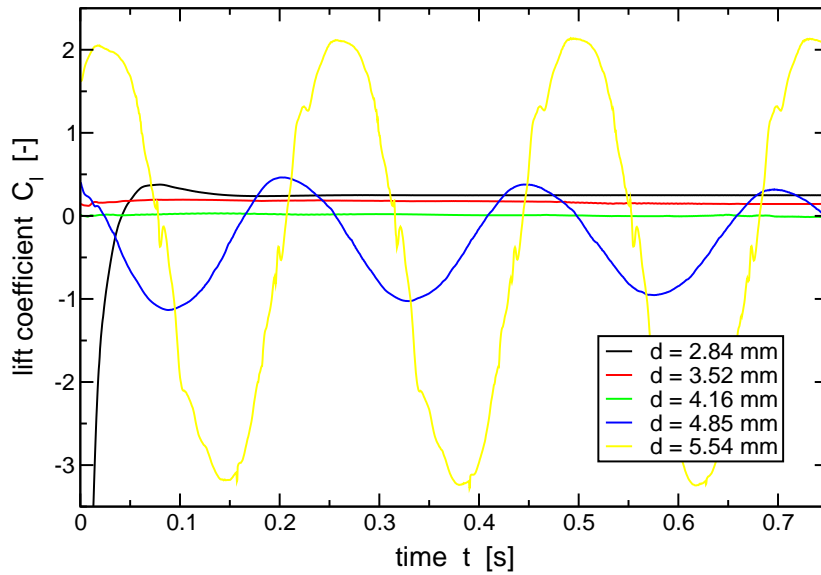


Figure 4.17: Lift coefficient C_l as a function of time for bubbles with nominal diameters between 2.84 and 5.54 mm, $\log(\mathcal{M}o) = -5.3$, $\omega = -3.8$ 1/s.

for constant $\mathcal{M}o$, but varies slightly with $\mathcal{M}o$ such that $\omega = -3.0$ 1/s, -3.1 1/s, -3.7 1/s and -3.8 1/s for $\log(\mathcal{M}o) = -2.8$, -3.6 , -4.2 and -5.3 , respectively. For $\log(\mathcal{M}o) = -5.3$, results for $\omega = -6.2$ 1/s have also been obtained which are denoted by $+-$ -symbols. Also plotted are Tomiyama et al.'s [389] experimental results, denoted by \times -symbols, as well as their curve fit, equation (7.19).

It is evident from the results for $\log(\mathcal{M}o) = -5.3$ that for the low and high shear rate, *i.e.* blue lines with circles and plus-symbols, that C_l is not affected by ω . This result confirms the findings of Tomiyama et al. [389] who found that C_l is independent of ω for all $\mathcal{M}o$ and ω investigated by them. The calculated C_l are somewhat smaller, but still in reasonable agreement with the experimental findings. However, they deteriorate as $\mathcal{M}o$ becomes higher and bigger differences, including qualitative ones, are apparent. This result is in contrast to Tomiyama et al.'s [389] findings who found no appreciable influence of $\mathcal{M}o$ on C_l .

The discrepancy between the calculations and measurements needs further investigation, but it is possible that viscous effects in the vicinity of the bubbles surface are not taken fully into account for the high $\mathcal{M}o$ where $\mathcal{R}e$ is around 10. However, it is important to note that the results for lower $\mathcal{M}o$ are in reasonable agreement with the experimental findings. This gives some confidence to the results presented in Section 7.5 where the lift coefficients of air-water bubbles (a system with a low $\mathcal{M}o$) are

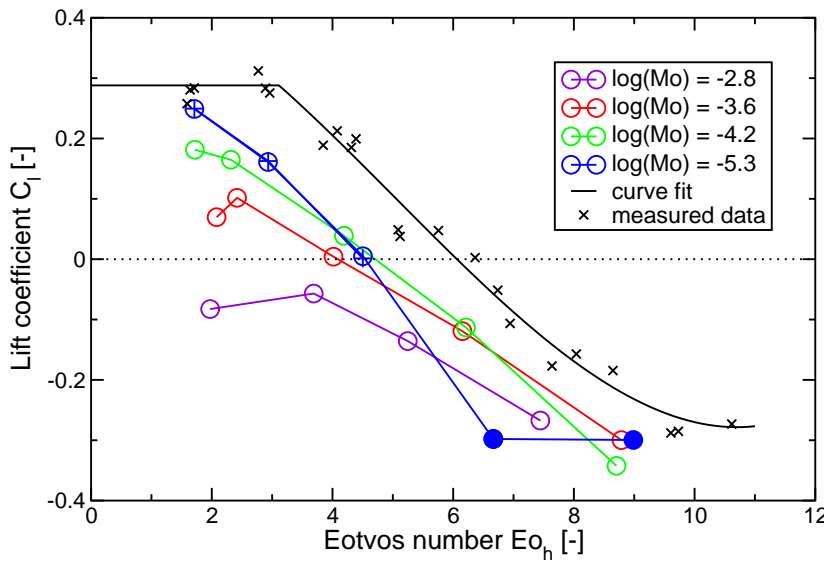


Figure 4.18: Calculated and measured lift coefficient C_l as a function of the Eötvös number Eo_h . Circles and plus-symbols denote results for low and high ω , respectively. Filled symbols denote results where the bubble exhibits unsteady periodic motion.

investigated.

The experimental findings show a change of the direction of the lift force for bubbles with an Eo larger than 6, which is manifested in a change of the sign of the lift coefficient. The same trend is evident in the numerical results, however, at smaller Eo . So far this phenomenon has not been fully explained, but it seems likely that the interplay of small bubble deformations and the wake dynamics is responsible for this drastic effect.

4.4 Closure

This Chapter described the interface-capturing methodology, for which further results are presented later in this thesis. First, the governing equations were stated, followed by the discussion of the numerical solution of the partial differential equations. The discretised equations were presented along with the overall solution procedure due to Weller [424]. Finally, direct numerical simulations were carried out to investigate the dynamics of single bubbles. Free rising bubbles in quiescent water and under the influence of shear were calculated and the results were compared against experimental data.

As a result, it became apparent that the new numerical solution procedure is

capable of predicting the dynamics of bubbles accurately if the Morton number is sufficiently small ($\log(\mathcal{M}o) \leq -4.2$). The main experimental findings of Tomiyama et al. [389] have been confirmed numerically: firstly, the lift coefficient is independent of the shear rate in the regime investigated; and secondly, the lift changes sign for large Eötvös numbers. The methodology has also been used to tackle the problem of lift on air-water bubbles, which has been identified to be an important factor for the correct prediction of the phase fraction distribution in cases where large shear occurs. These results are presented in Section 7.5.

Chapter 5

Turbulence Response Coefficient Modelling

In Chapters 3 and 4, the two-fluid and interface-capturing methodologies have been presented and validated. These will be utilised in the following Chapters to test and improve the modelling of dispersed two-phase flows. This Chapter is concerned with the modelling of two-phase turbulence at high phase fractions. The two-phase turbulence is expressed in this study through the model by Gosman et al. [121] presented in Section 3.1.3. It is based on a concept that relates the dispersed phase turbulence to that of the continuous phase through a turbulence response coefficient C_t , which is defined as the ratio of the dispersed phase velocity fluctuations to those of the continuous phase (1.17).

At low phase fractions, expressions for C_t have been put forward by various authors [121, 310, 171, 174, 52] by considering simplified equations of motion for single DPEs encountering a turbulence eddy within the continuous phase. However, recent experimental data [109, 227, 7] suggest that both phases fluctuate in unison as one entity when the phase fraction is high. Consequently, C_t approaches a constant value close to unity as the phase fraction increases. This effect is not taken into account in the current C_t -models and a modified expression will be proposed in the following Section.

The new formulation is then implemented in the two-fluid methodology and validated against two gas-liquid test cases: the sudden enlargement of a circular pipe (at

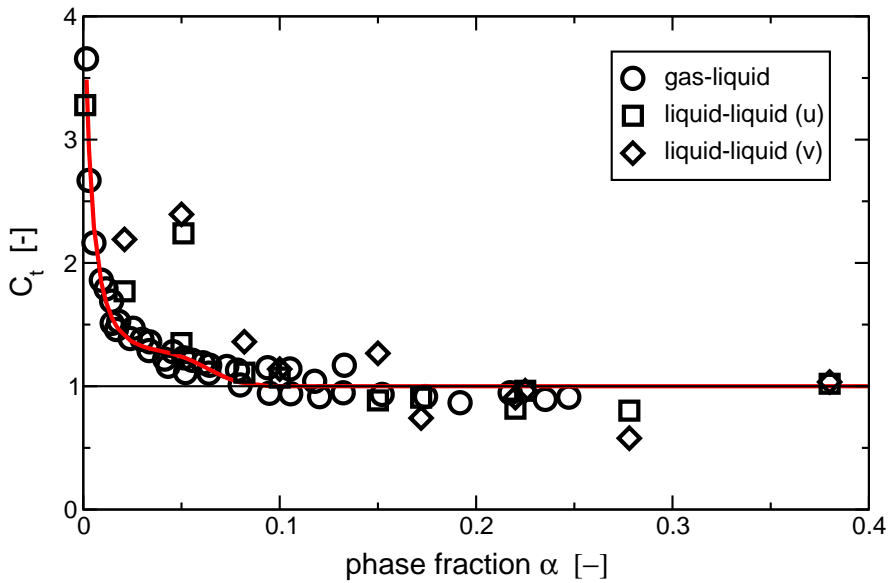


Figure 5.1: Turbulence response function as a function of the phase fraction.

high gas phase fraction) and the plane mixing layer (at low gas phase fraction). Even without taking into account the effect of α on C_t , the results for the latter, low phase fraction case are already in good agreement with the experimental data and the reason for reexamining it is to verify that the new formulation for C_t remains valid.

5.1 Turbulence Response Coefficient at High Phase Fractions

Recently, Larue de Tournemine et al. [227] and Augier [7] measured C_t for turbulent gas-liquid and liquid-liquid flows at high phase fractions, respectively. Their results are shown in Figure 5.1. It is evident that for both classes of flow C_t is a strong and nearly identical function of the phase fraction and approaches a constant value close to unity for phase fractions as low as 6%. Similar results have been obtained independently by Garnier et al. [109] for a different gas-liquid flow.

A correlation for the above data is proposed here that takes into account the effect of α on C_t and reverts to the dilute model (3.18) when $\alpha \rightarrow 0$. It is plotted in

Figure 5.1 and takes the form:

$$C_t(\alpha_a) = 1 + (C_{t0} - 1)e^{-f(\alpha_a)} \quad (5.1)$$

$$f(\alpha_a) = 180\alpha_a - 4.71 \times 10^3\alpha_a^2 + 4.26 \times 10^4\alpha_a^3 \quad (5.2)$$

where $C_{t0} = C_t(k, \varepsilon, U_r, d, \dots)$ stands for the limiting value of C_t when $\alpha_a \rightarrow 0$. This is determined from equation (3.18) and is recovered by the new correlation as α_a approaches zero, as evident from equation (5.1). The coefficients in $f(\alpha_a)$ are determined by minimising its r.m.s. deviation from the data using the non-linear fitting procedure implemented in the graph plotting package “grace” [125].

5.2 Two-Fluid Methodology: Sudden Enlargement of a Circular Pipe

The case studied here is that of a bubbly air/water upward flow through a pipe with a sudden enlargement, for which experiments have been carried out by Bel F’dhila [25]. This case has been utilised in Section 3.3.1 to test the two-fluid solution procedure and is described there. In this Section, it is used to assess the effects of the phase fraction dependence of C_t .

Setup

The setup of this case and the modelling utilised in the calculations are essentially the same as outlined in Section 3.3.1. The only difference between the two calculations presented in this Section is that they use different formulations for C_t , *i.e.* the dilute formulation (3.18) and the phase fraction dependent one (5.1).

Results

The development of the two-phase flow behind the sudden enlargement has been illustrated in Section 3.3.1 and the results obtained in the present calculations show no qualitative differences, so the presentation will focus on qualitative comparisons.

Profiles of the axial liquid velocity at five cross-sections at $x = 70, 130, 180, 250$ and 320 mm downstream of the sudden enlargement are shown in Figure 5.2. For

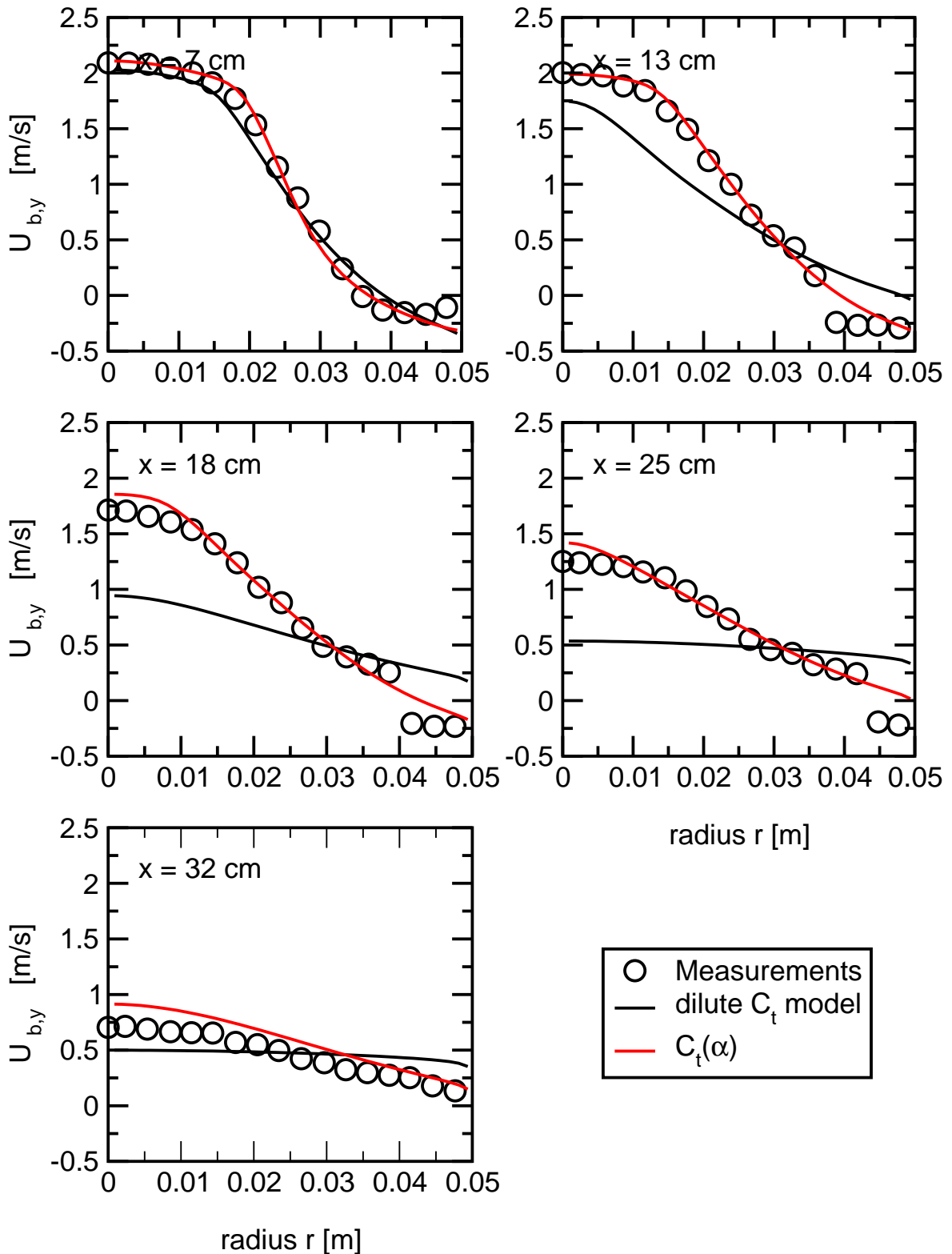


Figure 5.2: Results for the sudden enlargement test case: predicted profiles of the mean axial liquid velocity compared with experimental data (circles). The lines represent predictions with the dilute and the phase fraction dependent C_t -model.

the dilute C_t -model, the velocity difference generated by the enlargement is quickly diffused and further downstream at $x = 250$ mm the velocity profile is almost uniform over the pipe radius. These results are not in agreement with the experimental data, but generally improved predictions are obtained for the phase fraction dependent C_t -formulation, especially closer to the inlet and away from the centreline. Here, the agreement between the calculations and the measurements is excellent. However, some discrepancies are noticeable towards the outlet. For example, at the last station, the centreline velocity is overpredicted by 31%. This may be attributed to other deficiencies in the turbulence modelling.

In Figure 5.3, the results for the gas phase fraction field are shown. The peak at the first measuring location at $x = 70$ mm originates from an accumulation of bubbles at the wall of the small pipe section. This “wall peak” distribution is characteristic for vertical pipe flow and has been prescribed in the calculations as a boundary condition according to the measurements, as outlined in Section 3.3.1.

The dilute C_t -formulation overpredicts the accumulation of bubbles shortly behind the recirculation zone at $x = 70$ mm. Although the profile at $x = 320$ mm is predicted correctly by the dilute model, the experimental data upstream shows a slower replenishment on the centreline. In fact, the calculated centreline phase fraction diminishes between $x = 70$ and 180 mm before it recovers rapidly between $x = 180$ and 250 mm.

With the present model, the phase fraction profiles are better predicted at stations close to the inlet, but the discrepancies with the experimental data increase towards the outlet. In particular, the rate of development towards fully developed pipe flow is underpredicted. The reduced bubble diffusion is a consequence of a smaller turbulent viscosity ν_t , which affects the phase fraction through the turbulent drag term as well as the velocities. The deficiencies are somewhat surprising in the light of the vastly improved velocity predictions, as shown in Figure 5.2. However, it is possible that the deficiency lies in the correlations for the drag and lift coefficients, which will be investigated further in Chapters 6 and 7.

Turbulent kinetic energy profiles are shown in Figure 5.4. A significant improvement is obtained with the present C_t -formulation throughout the flow, which predicts

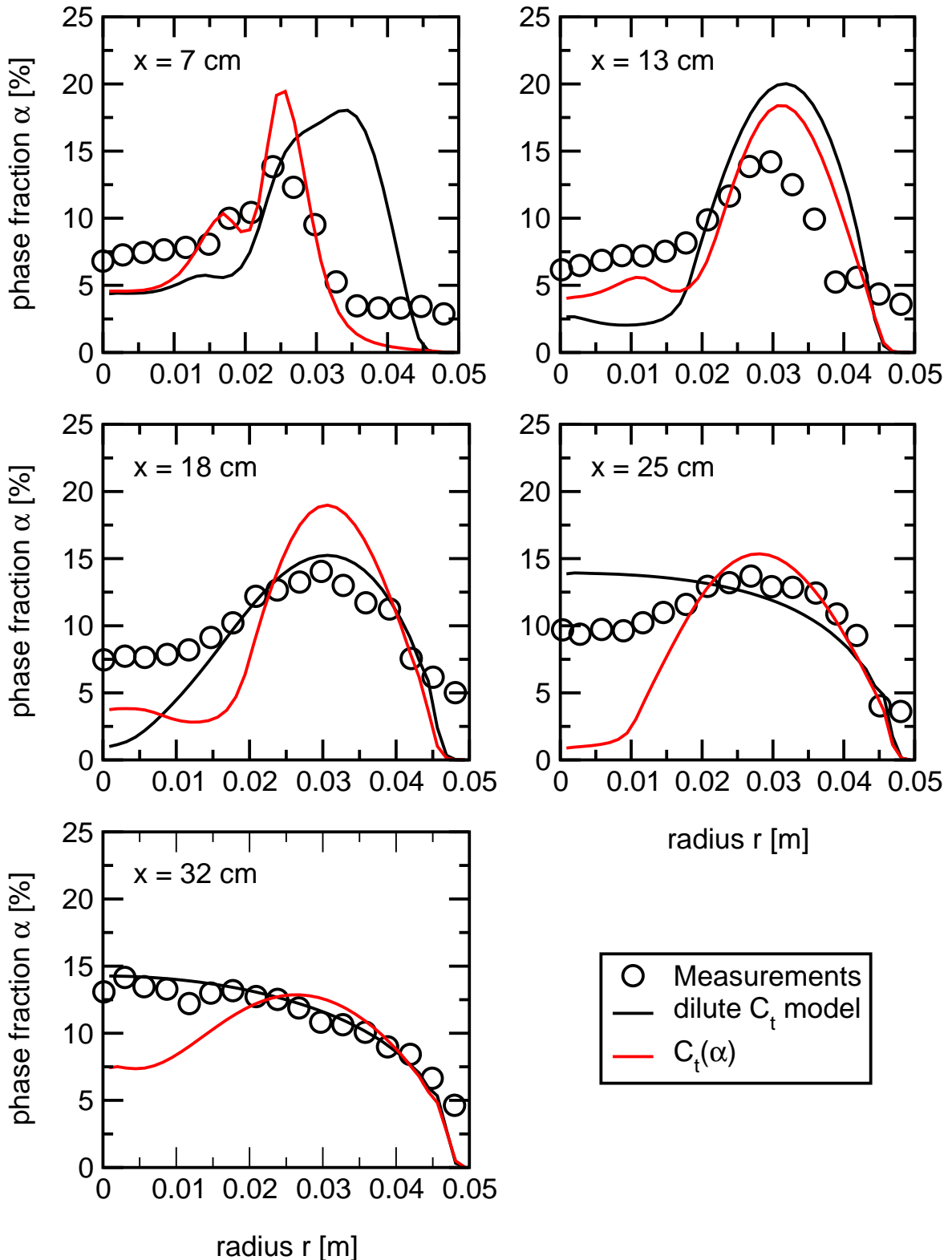


Figure 5.3: Results for the sudden enlargement test case: predicted phase fraction profiles compared with experimental data (circles). The lines represent predictions with the dilute and the phase fraction dependent C_t -models.

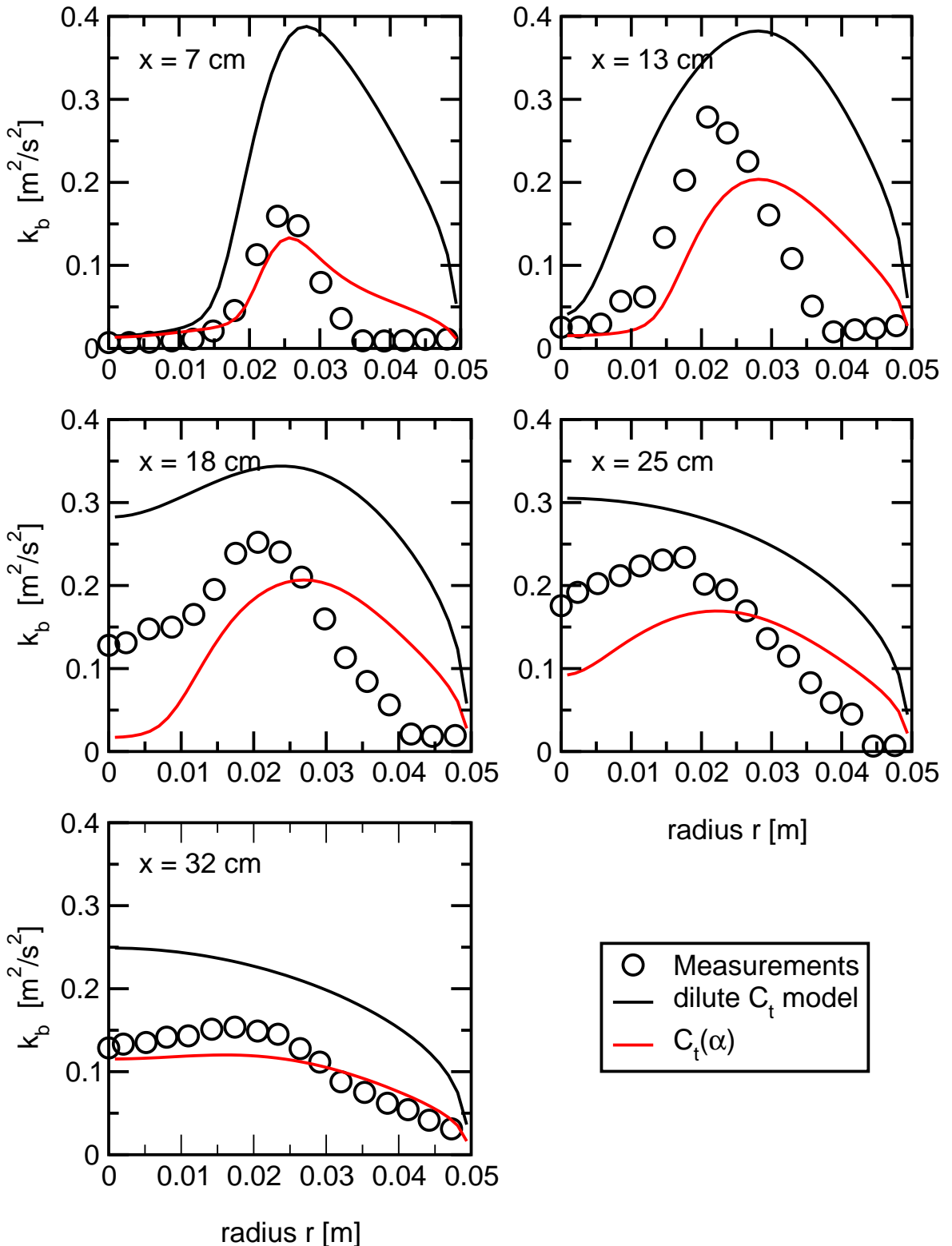


Figure 5.4: Results for the sudden enlargement test case: predicted profiles of the turbulent kinetic energy of the continuous phase compared with experimental data (circles). The lines represent predictions with the dilute and the phase fraction dependent C_t -models.

a lower level of turbulent kinetic energy compared with the overpredictions of the dilute model. However, there is still room for further improvements, especially on the centreline at $x = 180$ and 250 mm. The overall reduction of the kinetic energy is expected for the range of α_a values in this test case because C_t is close to unity thereby diminishing the two-phase turbulence production terms given in equations (3.16) and (3.17). Lower turbulent kinetic energy results in smaller turbulent viscosities and, therefore, less diffusion of momentum and bubbles, as pointed out earlier for Figures 5.2 and 5.3, respectively.

5.3 Two-Fluid Methodology: Plane Mixing Layer

The case studied here is that of a bubbly air/water upward flow of two separate inlet streams brought together to form a plane mixing layer within a square duct. A series of 8 experiments were carried out by Roig [328, 329, 222] and several authors have used this test case to validate their two-fluid models, *e.g.* [228, 393, 147, 148, 328]. In this study, only the data from one of the experiments is simulated because it is representative for the other experiments, which are also carried out at similarly low mean phase fractions.

Setup

The geometry of the plane mixing layer is shown schematically in Figure 5.5. Two separate inlet streams, initially separated by a 2 mm thick splitter plate, which is tapered at its trailing edge to reduce the influence of the wake, are brought together to form a plane mixing layer within a square test section of $2w \times 2w = 400 \text{ mm} \times 400 \text{ mm}$. The experimental apparatus provides independent control of both liquid and gas flow rates in each stream. Air is introduced uniformly into the flow via three perforated injection tubes for each stream positioned normal to the splitter plate, which produce bubbles of approximately 1.5 to 2.5 mm diameter. In the predictions, a uniform bubble diameter of $d = 2 \text{ mm}$ is assumed.

In the experiment selected for comparison, the average liquid velocities were 0.94 m/s and 0.60 m/s for the right and left inlet stream, respectively. The phase frac-

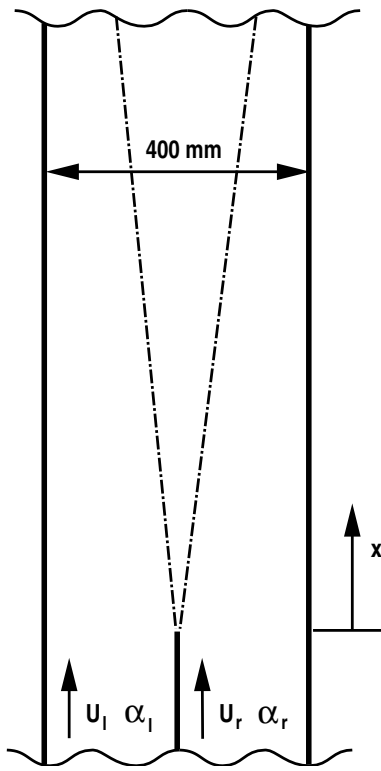


Figure 5.5: Sketch of the setup for the plane mixing layer test case.

tion was set to a uniform 1.9% in both inlets. The mean and fluctuating velocities for both phases were measured in flow direction at five cross-sections ($x = -10, 60, 200, 400$ and 600 mm) using Laser Doppler Anemometry (LDA). In addition, the local phase fraction was measured at the same locations using a fibre-optic probe. The Reynolds numbers for the right and left inlet stream are $\mathcal{R}e_r = 251000$ and $\mathcal{R}e_l = 160000$, respectively, based on the average liquid velocity and the hydraulic diameter d_{hyd} of each stream. The latter is $d_{hyd} = \frac{4}{3}w$ for a rectangular inlet stream of $w \times 2w$.

The calculations are performed on a 2D geometry. In the flow direction, the space domain extends from $x = -10$ to 1100 mm in order to ensure negligible influence of the outlet boundary conditions. The duct is subdivided by a mesh with 80×104 cells in the lateral and flow directions, respectively. Furthermore, the mesh is graded towards the splitter plate as well as the inlets in order to provide higher mesh density in these regions of large flow gradients. Altogether, the resulting computational mesh, plotted in Figure 5.6d, consists of approximately 8300 cells, which provides adequate resolution, as shown by Hill [147].

The inlet conditions for the gas phase fraction and the liquid velocity are taken

directly from the measurements at $x = -10$ mm. The turbulent kinetic energy k_b of the liquid phase is calculated from the velocity fluctuations of the liquid assuming isotropy.

Measurements of the gas phase velocity and dissipation rate of kinetic energy of the liquid are not available and their values at the inlet are estimated as follows: for the determination of the gas phase velocity, it is assumed that the bubbles are in equilibrium and rise with their terminal velocity, which is estimated at 0.3 m/s. To obtain the gas velocity, the terminal velocity is simply added to that of the liquid. The dissipation rate of the kinetic energy ε_b is inferred from a mixing length hypothesis [413, 151]:

$$\varepsilon_b = C_\mu \frac{k_b^{1.5}}{L_m} \quad (5.3)$$

where L_m stands for the mixing length, which has to be prescribed.

Hill [147] found that the accurate representation of the boundary layers on either side of the splitter plate is crucial for the simulation of this test case and used the following expression for the mixing length which is based on Nikuradse's formula [413, 151]:

$$L_m = \begin{cases} \kappa x^* & 0 \leq \frac{x^*}{\delta} < \frac{\lambda}{\kappa} \\ \lambda \delta & \frac{\lambda}{\kappa} \leq \frac{x^*}{\delta} < 1 \\ \frac{w}{2} \left(0.14 - 0.08 \left(1 - \frac{2x^*}{w} \right)^2 - 0.06 \left(1 - \frac{2x^*}{w} \right)^4 \right) & 1 \leq \frac{x^*}{\delta} \end{cases} \quad (5.4)$$

Here, w stands for width of the inlet streams and x^* is the normal distance to the closest wall. The boundary layer δ is prescribed independently for each boundary layer on the left and right hand side of the splitter plate by inspection of the experimental velocity profiles. δ_l and δ_r were determined to 30 and 8 mm, respectively. The boundary layers in vicinity of the outer walls are neglected because they are expected to have a negligible influence on the development of the mixing layer. Finally, κ and λ stand for the von Kármán constant and a constant of the mixing length model, which take values of 0.435 and 0.09, respectively.

The modelling utilised to calculate this case is essentially the same as that used for the previous one. However, it should be noted that lift force is now accounted for in the interface momentum transfer term because it is essential in order to accurately

predict the phase fraction distribution in this test case, as noted by [147, 148]. The effect of the lift force on the results will be discussed in more detail in Chapter 7.

Results

In Figure 5.6a, the distribution of the gas phase fraction is pictured. Although the phase fraction was set to an average 1.9%, it is much larger in vicinity of the splitter plate. This accumulation of gas is a result of the migration of bubbles towards the wall and is often termed the “wall peak” phenomenon. It is characteristic of vertical pipe flow and originates from lift effects, as discussed in Section 1.5.5. In the present calculations, no attempt is made to predict it accurately, but the peak has been prescribed at the inlets at $x = -10$ mm according to the measurements. Figure 5.6b shows the vector field of the mean liquid velocity $\bar{\mathbf{U}}_b$. As expected, the sharp velocity jump generated at the inlet is diffused slowly upstream. This behaviour is similar to a single-phase flow. The turbulent viscosity ν^t is given in Figure 5.6c. It is largest immediately upstream of the splitter plate because the shear rate is largest in this region.

Profiles of the measured and calculated gas phase fraction at five cross-sections ($x = -10, 60, 200, 400$ and 600 mm) are shown in Figure 5.7. As mentioned before, the inlet profiles have been prescribed from the measurements and are therefore identical. Around the splitter plate, the aforementioned wall peak is noticeable, which is slowly diffused further downstream. Overall, excellent agreement between the calculations and the measurements is found. The differences between the two C_t -formulations are negligible. This is fortunate, since the results obtained without taking into account the effect of the phase fraction on C_t are already in good agreement with the experimental data.

Figure 5.8 displays profiles of the liquid velocity at the aforementioned cross-sections. The profile at $x = -10$ mm is shown in the first picture and has been prescribed using the experimental data. The velocity jump between the two inlet streams as well as the boundary layers on either side of the splitter plate are clearly noticeable. Further downstream, the boundary layers are diffused slowly, but there is evidence of the velocity jump at all stations. The calculations are in excellent agreement with the experimental data and differences between the dilute and the phase fraction

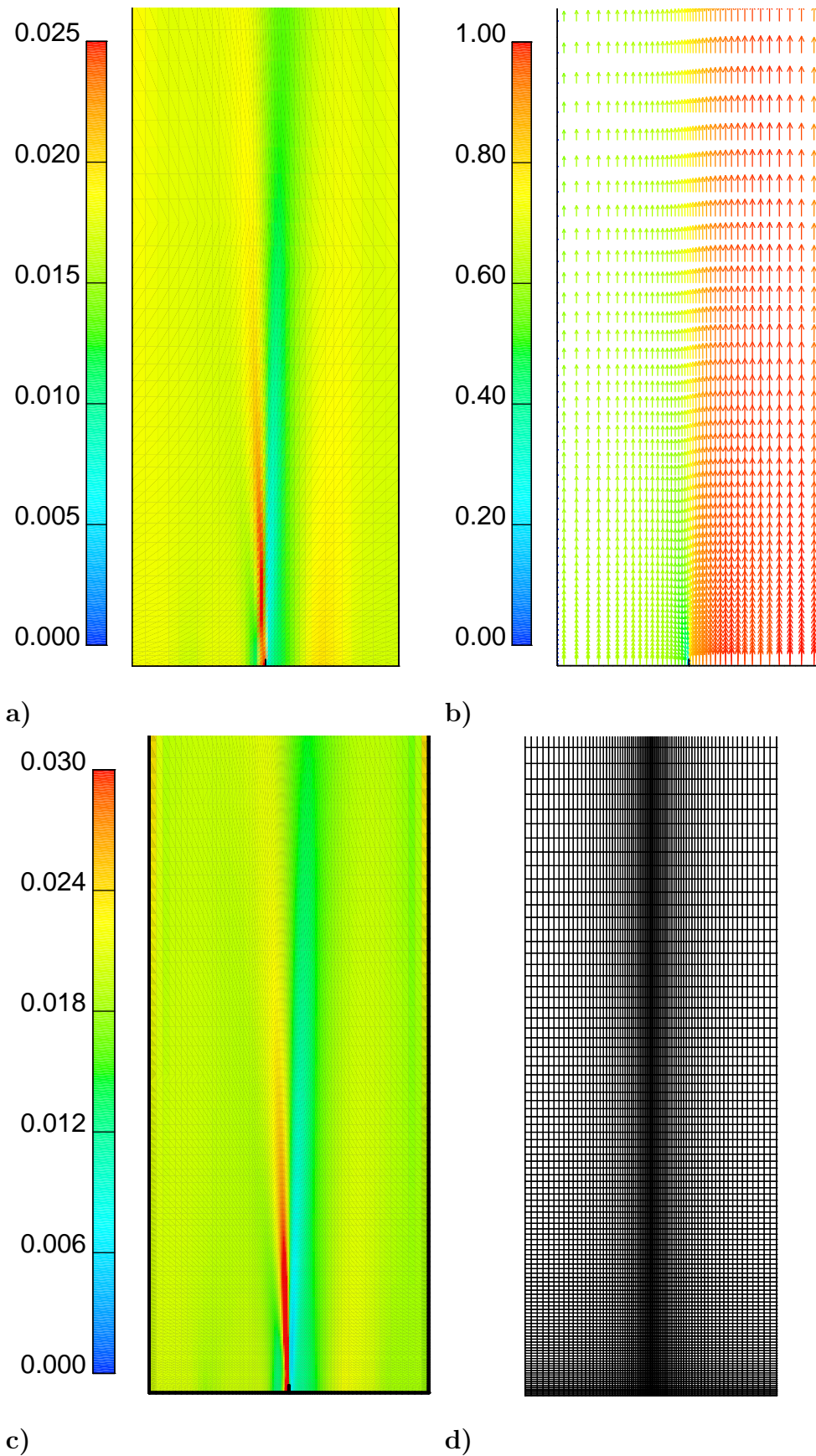


Figure 5.6: Results for the mixing layer test case: **a)** gas phase fraction α_a ; **b)** mean liquid velocity $\overline{\mathbf{U}}_b$; **c)** turbulent viscosity ν^t ; **d)** computational mesh.

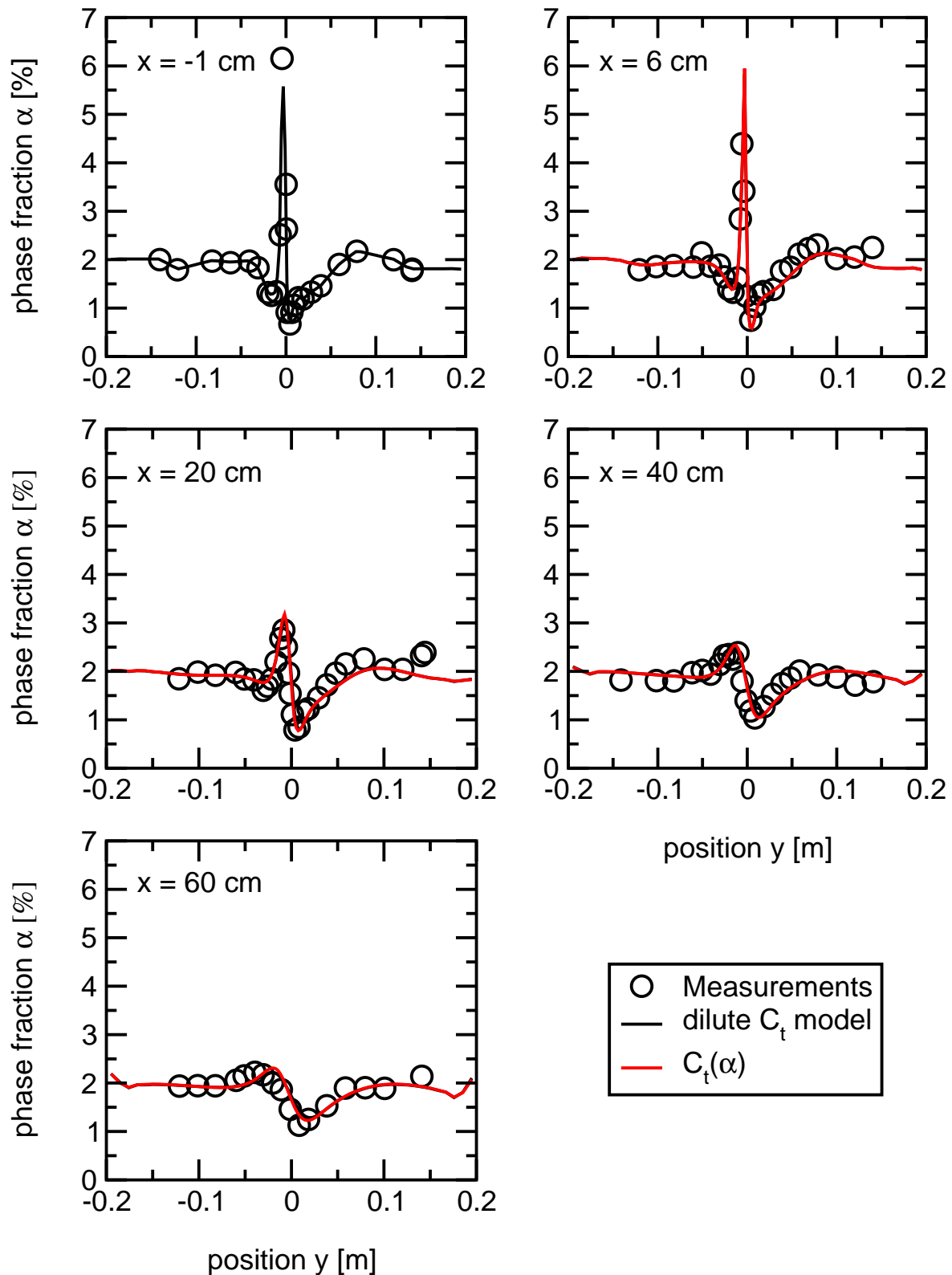


Figure 5.7: Results for the mixing layer test case: predicted phase fraction profiles compared with experimental data (circles). The lines represent predictions with the dilute and the phase fraction dependent C_t -models.

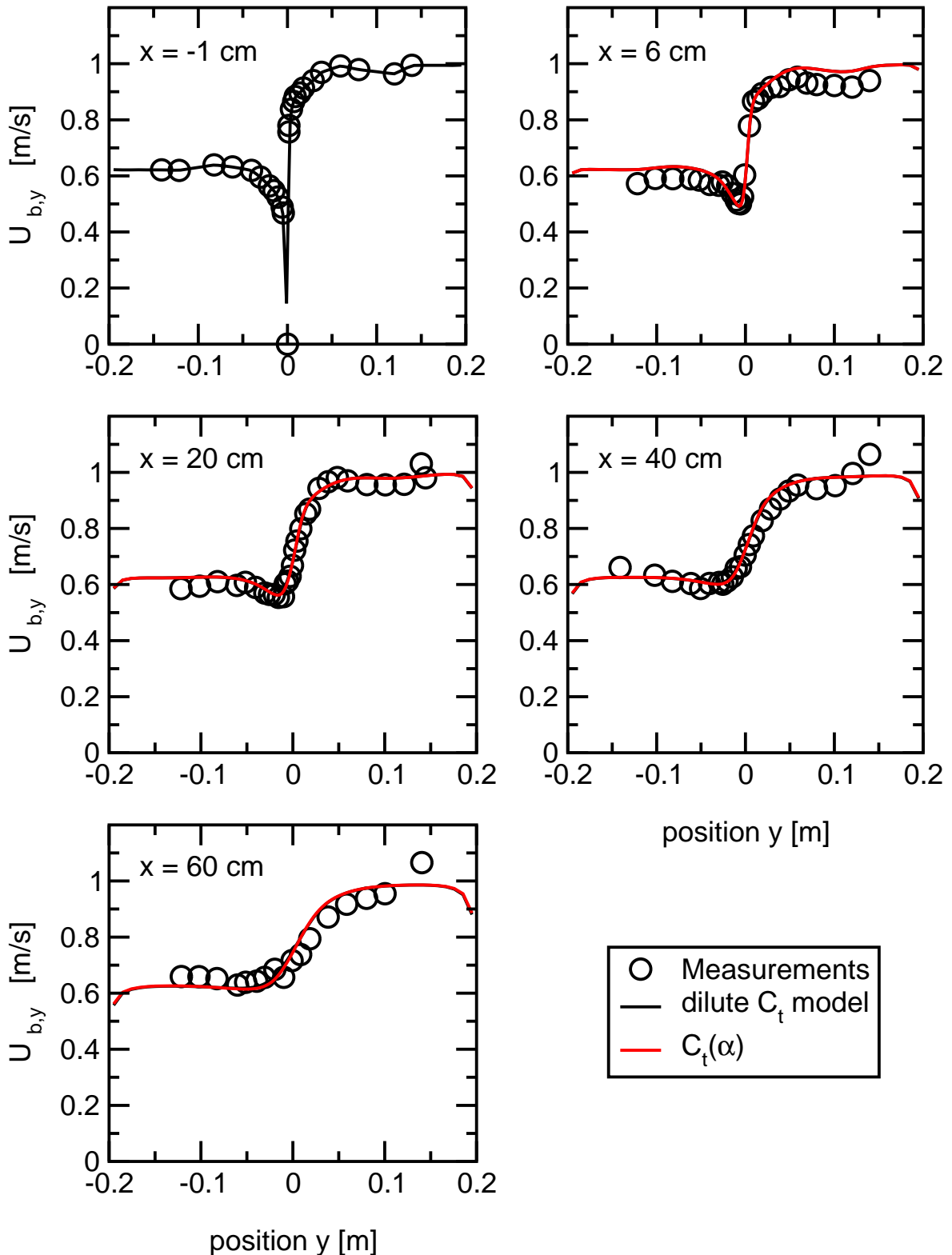


Figure 5.8: Results for the mixing layer test case: predicted profiles of the mean liquid velocity in x -direction compared with experimental data (circles). The lines represent predictions with the dilute and the phase fraction dependent C_t -models.

dependent formulations for C_t are again not noticeable.

In Figure 5.9, the profiles for the turbulent kinetic energy in the liquid phase k_b are given. Inspection of the measured k_b on the centreline reveals that the peak evident at the inlet, is quickly diffused and not apparent at $x = 60$ mm. However, turbulent kinetic energy is generated within the mixing layer and an increase of k_b is evident at later stations. Furthermore, the level of k_b is reduced between $x = -10$ and 60 mm and then stays almost constant further downstream.

Similar trends are evident from the calculated profiles, but some differences between the measured and calculated profiles are noticeable. For example, the decay of k_b is less rapid in the calculations and is still taking place towards the end of the test section. Furthermore, a peak in k_b is apparent on the centerline at $x = 60$ mm, whereas it is not evident in the measurements as pointed out earlier. The overall agreement with the measured data is reasonable for both C_t -formulations, especially towards the later stations. However, the present model is in better agreement with the experimental data because it predicts an enhanced dissipation of k_b . The differences between the two models are not as drastic as for the sudden enlargement flow because α_a is lower and, consequently, the present correlation for C_t yields values close to C_{t0} .

5.4 Closure

In this Chapter, a new correlation for the turbulence response coefficient C_t was put forward, which takes into account the influence of the phase fraction and was derived using recent experimental data. This model was then implemented in the two-fluid methodology and assessed for two gas-liquid flows, *i.e.* in a plane mixing layer and a sudden enlargement of a circular pipe.

With the present C_t -formulation the already excellent predictions for the plane mixing layer, in particular for the phase fraction and liquid velocity, did not change. Furthermore, the results for the turbulent kinetic energy improved slightly. On the other hand, the predictions for the sudden enlargement flow were generally better, especially for the turbulent kinetic energy and the liquid velocity. Some discrepancies with the experimental data were noticeable in the turbulence predictions for both cases.

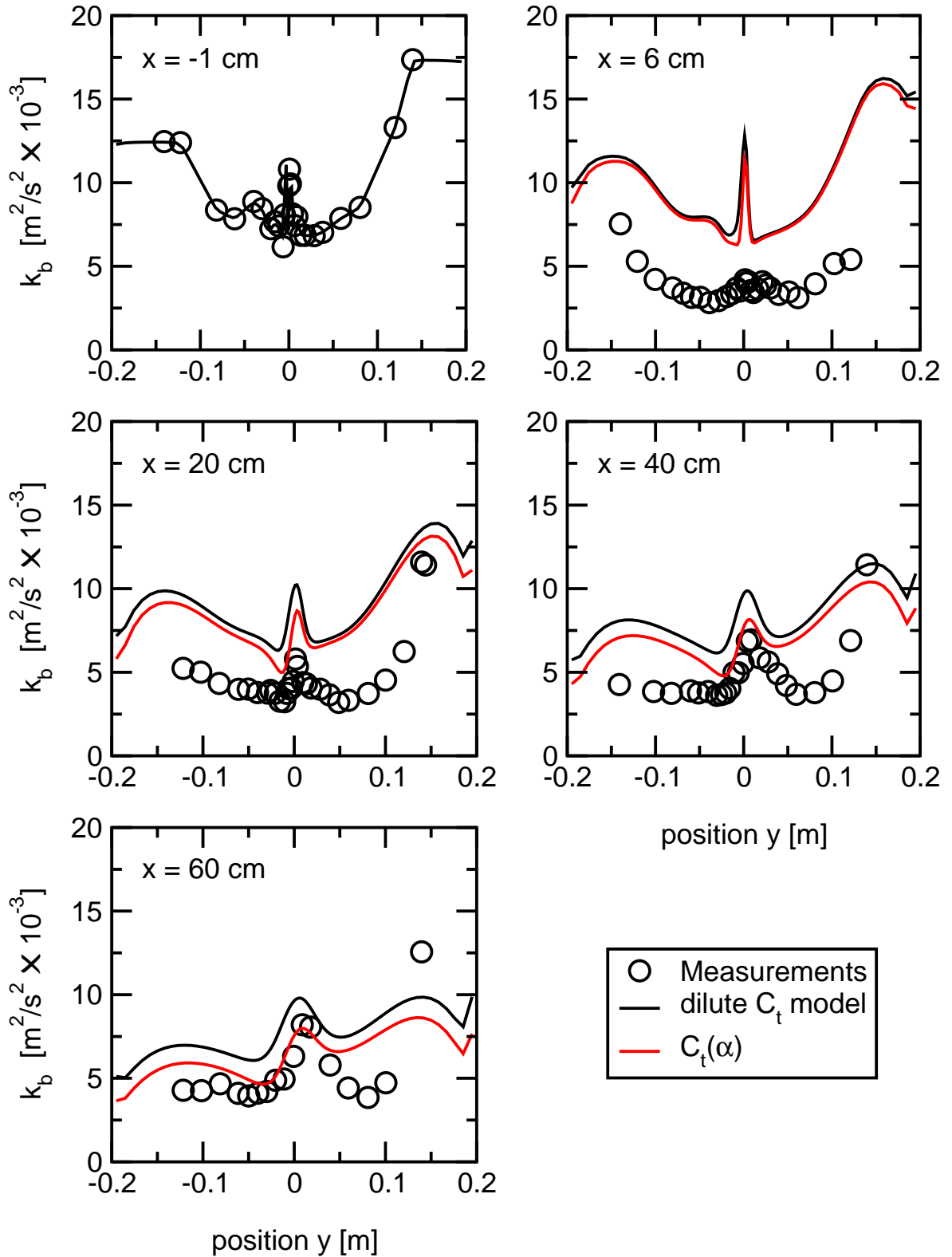


Figure 5.9: Results for the mixing layer test case: predicted profiles of the turbulent kinetic energy of the liquid compared with experimental data (circles). The lines represent predictions with the dilute and the phase fraction dependent C_t -models.

There are many possible causes including weaknesses of the C_t concept and modelling, the basic model $k - \varepsilon$ -model as well as the additional source terms that incorporate the two-phase effects. However, this has not been investigated further in the present study.

The results for the phase fraction improved close to the inlet and away from the centreline, but discrepancies with the experimental data on the centreline increased towards the outlet where the development towards fully developed pipe flow was underpredicted. It is possible that the deficiency lies in the correlation for the drag or lift coefficients, which will be investigated further in the following Chapters.

Chapter 6

Drag Modelling

In the modelling of dispersed two-phase flow, closure laws to represent the inter-phase momentum transfer are needed. They are usually described by simple correlations for the forces, *e.g.* drag, lift and virtual mass, acting on a single DPE in an infinite medium, which are derived either empirically or from simple analysis. However, a number of important industrial processes are carried out at higher phase fractions where the presence of surrounding DPEs has an influence. Hence, it is the objectives of this Chapter to identify correlations to determine the drag force on a DPE at high α . These correlations are intended for the two-fluid methodology presented in Chapter 3, but the same formulations can be used in other CFD methodologies for the prediction of the dynamics of two-phase flows, *e.g.* the discrete DPE model outlined in Section 1.2.2.

An appropriate drag correlation should be applicable to dispersed flow at high as well as low phase fractions simultaneously. The latter is important because regions of low and high phase fraction co-exist in many two-phase flows. However, the conventional approach to develop a correlation which spans a parameter range is to divide it into several distinct regimes and fit the experimental data in each separately. Consequently, the resulting correlations do not match at the boundaries between the regimes unless care is exercised. These discontinuities are clearly not physical and can lead to difficulties in numerical calculations [147].

In the introduction to this thesis, some definitions and modelling strategies have been outlined in Sections 1.5.3 and 1.5.4. In this Chapter, the literature related to the modelling of the drag coefficient in dispersed systems at all phase fractions is

reviewed more thoroughly and the equations are quoted. Correlations applicable to a single DPE are included in this review because they are often invoked to construct models for higher phase fractions. Consequently, the accuracy of the drag predictions at high phase fractions hinges on those for a single DPE. Unfortunately, an up to date and comprehensive review on the drag on single DPEs does not exist to the author's knowledge and is hence presented below. In addition, new correlations for the influence of the phase fraction on the drag on particles, droplets and bubbles will be proposed.

The correlations are then compared with data from the literature in order to assess their validity. Finally, the most promising ones are implemented in the two-fluid methodology and validated against two gas-liquid test cases: the plane mixing layer (at low gas phase fraction) and the sudden enlargement of a circular pipe (at high gas phase fraction).

6.1 Definitions

The drag coefficient C_{d0} on a single DPE in an infinite fluid is governed primarily by the Reynolds \mathcal{Re} , Eötvös \mathcal{Eo} and Morton \mathcal{Mo} numbers [56]. The definitions of these dimensionless groups have been given in Section 1.5.3 and are repeated here for convenience:

$$C_{d0} = \frac{F_{d0}}{\frac{1}{2}\rho_c A U_{r0}^2} = \frac{\text{Drag force}}{\text{Dynamic pressure force}} \quad (1.4)$$

$$\mathcal{Re}_0 = \frac{\rho_c U_{r0} d}{\mu_c} = \frac{\text{Inertia}}{\text{Viscous}} \quad (1.5)$$

$$\mathcal{Eo} = \frac{g_{\text{eff}} |\Delta\rho| d^2}{\sigma} = \frac{\text{Gravity}}{\text{Surface Tension}} \quad (1.6)$$

$$\mathcal{Mo} = \frac{g_{\text{eff}} \mu_c^4 |\Delta\rho|}{\rho_c^2 \sigma^3} = \text{Material Group} \quad (1.7)$$

$$\kappa = \frac{\mu_d}{\mu_c} \quad (1.9)$$

In the definitions given above, μ_c and ρ_c are the dynamic viscosity and density of the continuous phase, respectively. σ is the surface tension and $\Delta\rho$ is the density difference between the continuous and dispersed phases, *i.e.* $\Delta\rho = \rho_d - \rho_c$. g_{eff} denotes the magnitude of the effective acceleration given by $g_{\text{eff}} = |\mathbf{g}_{\text{eff}}| = |\mathbf{g} - \frac{D_c \mathbf{U}_c}{Dt}|$ where $\frac{D_c}{Dt}$ is the substantive derivative defined in equation (3.8). F_d and U_{r0} are the magnitudes

of the drag force \mathbf{F}_{d0} and the relative velocity \mathbf{U}_{r0} vectors, respectively. The latter is defined as $\mathbf{U}_{r0} = \mathbf{U}_c - \mathbf{U}_d$. A stands for the projected area normal to \mathbf{U}_{r0} , which, for practical reasons outlined in Section 1.5.3, is usually calculated from $A = \pi \frac{d^2}{4}$ where d is the nominal diameter, *i.e.* the diameter of a sphere having the same volume V as the DPE. Hence, the influences of the shape, deformation or orientation on the projected area are neglected.

Several authors work with the Morton number in its original form \mathcal{G} , which is defined as follows:

$$\mathcal{G} = \frac{g\mu_c^4}{\rho_c \sigma^3} = \frac{\rho_c}{|\Delta\rho|} \mathcal{Mo} \quad (6.1)$$

An alternative set of dimensionless groups to the Eötvös and Morton numbers is formed by the Weber \mathcal{We} and Laplace \mathcal{La} numbers, which are widely used when break-up and coalescence are considered. Their definitions are also given here because they are used in some drag models for bubbles:

$$\mathcal{We} = \frac{\rho_c d U_{r0}^2}{\sigma} = \mathcal{Re}_0^2 \sqrt{\frac{\mathcal{Mo}}{\mathcal{Eo}}} = \frac{\text{kin. Energy}}{\text{surface energy}} \quad (6.2)$$

$$\mathcal{La} = \frac{\rho_c \sigma d}{\mu_c^2} = \frac{\text{Surface Tension}}{\text{Viscous}} \quad (6.3)$$

For a single DPE moving steadily with the terminal velocity in an uniform, infinite medium, only the buoyancy and drag forces have to be considered. In this case, the equation of motion for a single DPE (B.1) simplifies to:

$$0 = V (\rho_d - \rho_c) \mathbf{g} + \frac{1}{2} \rho_c A C_{d0} |\mathbf{U}_{r0}| \mathbf{U}_{r0} \quad (6.4)$$

The above can be re-written in non-dimensional form in terms of the Archimedes and Reynolds number as:

$$\mathcal{Ar} = \frac{3}{4} C_{d0} \mathcal{Re}_0^2 \quad (6.5)$$

where the Archimedes number is defined as:

$$\mathcal{Ar} = \frac{d^3 g \rho_c |\Delta\rho|}{\mu_c^2} = \sqrt{\frac{\mathcal{Eo}^3}{\mathcal{Mo}}} \quad (6.6)$$

At higher phase fractions, the drag coefficient for a DPE in a cluster of DPEs is expressed in the same way as for single DPEs, *i.e.* equation (1.4). However, the

subscript 0 is now dropped in order to indicate the fact that we are now dealing with multiple DPEs. Hence, the definition of the drag coefficient is:

$$C_d = \frac{F_d}{\frac{1}{2}\rho_c A U_r^2} \quad (6.7)$$

Some authors prefer to use a friction coefficient C_f to express the inter-phase momentum transfer due to drag in the momentum equation (3.1) directly as:

$$\mathbf{M}_{d,a} = C_f \mathbf{U}_r \quad (1.11)$$

where $\mathbf{M}_{d,a}$ denotes the inter-phase momentum transfer due to drag per volume. Note that C_f is not dimensionless, which is undesirable.

The analysis of the motion of single DPEs can be extended to clusters of DPEs if the differences are properly recognised and accounted for. As outlined in Section 1.5.4, the average hydrostatic pressure gradient is affected by the presence of the other DPEs. Consequently, the buoyancy force has been calculated using the density of the mixture, not the continuous phase. The balance between buoyancy and drag, previously given by equation (6.4) now becomes [208, 15, 441]:

$$0 = V (\rho_d - \rho_c) (1 - \alpha) \mathbf{g} + \frac{1}{2} \rho_c A C_d |\mathbf{U}_r| \mathbf{U}_r \quad (6.8)$$

This equation can be re-written in non-dimensional form in terms of the Archimedes and Reynolds number as:

$$Ar (1 - \alpha) = \frac{3}{4} C_d Re^2 \quad (6.9)$$

where the Archimedes number and Reynolds number are defined in equations (6.6) and (1.5), respectively.

6.2 Models for Single DPEs

Comprehensive reviews of correlations available from the literature for the drag on single DPEs can be found in Clift et al. [56] and Wallis [414]. Unfortunately, these are fairly dated and do not reflect the newer literature. More recent results for the drag on bubbles have been reviewed by Fan and Tsuchiya [95, chapter 2] and Tomiyama et al. [384]. Some analytical results obtained for droplets and bubbles have been summarised by Harper [140].

6.2.1 Analytical Results

Analytical solutions to the Navier-Stokes equation are difficult to obtain and such solutions are only known for a small number of geometrically simple cases and under certain assumptions. A well known example is Stokes' law for the creeping flow ($\mathcal{Re}_0 \ll 1$) around a solid sphere which has been outlined in Section 1.5.3. Later, his work was generalised by Hadamard [131] and Rybczynski [332] to fluid spheres. Under the assumption that the surface of the fluid sphere is completely free of contaminants allowing it to be completely mobile, the drag coefficient is given by:

$$C_{d0} = \frac{24}{\mathcal{Re}_0} K^{H\&R} = \frac{24}{\mathcal{Re}_0} \frac{2 + 3\kappa}{3 + 3\kappa} \quad (6.10)$$

where $K^{H\&R}$ is termed the Hadamard-Rybczynski correction and κ stands for the viscosity ratio given by equation (1.9). For $\kappa \rightarrow \infty$, equation (6.10) reduces to the expression originally obtained by Stokes [363] for solid spheres. The other extreme $\kappa \rightarrow 0$ corresponds to negligible viscosity of the dispersed phase, *i.e.* to bubbles.

For high \mathcal{Re} , Levich [241] obtained a first order approximation for the drag on clean spherical bubbles by calculating the viscous energy dissipation from the flow field determined from potential flow theory, giving:

$$C_{d0} = \frac{48}{\mathcal{Re}_0} \quad (6.11)$$

The above result has been subsequently extended by Moore [278] who solved the boundary layer equations analytically to include the contribution from the boundary layer and the wake. The drag coefficient is then given as:

$$C_{d0} = \frac{48}{\mathcal{Re}_0} \left(1 - \frac{2.21}{\sqrt{\mathcal{Re}_0}} + \mathcal{O}\left(\mathcal{Re}_0^{-5/6}\right) \right) \quad (6.12)$$

This equation holds for $80 < \mathcal{Re}_0 < 500$ to 700, where the bubble deformation is not too large. An extension of this theory to take into account bubble deformation has been presented by Moore [279] and Harper [140].

When the bubbles are very large, the effects of surface tension and viscosity are negligible. While the shape of a large fluid particle cannot be predicted analytically, the terminal velocity can be obtained by solving for the potential flow around a specified shape. Using this approach, Davies and Taylor [73] give for spherical-cap bubbles and

droplets:

$$\mathbf{U}_{r0} = 1.00 \sqrt{\frac{gd}{2} \frac{|\Delta\rho|}{\rho_c}} \quad (6.13)$$

which is equivalent to:

$$C_{d0} = \frac{8}{3} \quad (6.14)$$

This result is valid when the Reynolds number is sufficiently large ($\mathcal{Re}_0 > 150$) and the fluid particle has the shape of a spherical-cap. The latter applies when $\mathcal{Eo} > 40$.

Mendelson [270] suggested an analogy with wave theory in order to express the terminal velocity of single bubbles at intermediate Reynolds numbers where the bubble rise is still dominated by surface tension, expressed via the Eötvös number. Their result has been extended for droplets by Marruci et al. [263], who found:

$$\mathbf{U}_{r0} = \sqrt{\frac{2\sigma}{\rho_c d} + \frac{gd}{2} \frac{|\Delta\rho|}{\rho_c}} \quad (6.15)$$

This can be recast into:

$$C_{d0} = \frac{8}{3} \frac{\mathcal{Eo}}{\mathcal{Eo} + 4} \quad (6.16)$$

Note that the Davies-Taylor equation (6.13) is a special case of equation (6.15) for very large bubbles.

Although Mendelson's [270] simple wave analogy works reasonably well, no rational explanation has been given to justify its derivation. However, it is interesting that Lehrer [239] derived an almost identical equation based on an energy argument with the only difference being that the coefficient in the first term (surface tension) of equation (6.15) changes from 2 to 3.

6.2.2 Empirical Correlations for Particles

For the past 80 years, considerable attention has been paid to the determination of the terminal velocity and the drag coefficient of particles. Clift et al. [56] critically reviewed the older published data and presented a correlation based on it (see [56, p. 112]), which is piecewise and consists of ten separate equations with a total of 18 fitted constants. It is valid up to $\mathcal{Re}_0 \approx 10^6$, but also fairly complex, expensive to evaluate

and exhibits small jumps (< 1%) as well as gradient discontinuities due to the piecewise fit. Therefore, the simpler expressions presented next should be used instead which offer a similar degree of accuracy and range of applicability while being continuous.

In many particle-fluid systems of practical interest the particle Reynolds number is less than 1000 and the drag coefficient may be expressed after Schiller and Naumann [340] as:

$$C_{d0} = \frac{24}{Re_0} (1 + 0.15 Re_0^{0.687}) \quad (3.9)$$

which fits the experimental data to within $\pm 5\%$. For Re greater than about 1000, the drag is approximately constant up to the critical point with the value $C_{d0} = 0.44$ as suggested by Wallis [414, p. 178].

Clift and Gauvin [54, 55] extended Schiller and Naumann's [340] expression for the sub-critical region $Re_0 < 3 \times 10^5$ and give:

$$C_{d0} = \frac{24}{Re_0} (1 + 0.15 Re_0^{0.687}) + \frac{0.42}{1 + 4.2 \times 10^4 Re_0^{-1.16}} \quad (6.17)$$

where $Re_0 < 3 \times 10^5$. The deviation in C_{d0} from the measurements is given by Clift et al. [56, p. 112] as +6 to -4%.

Recently, two new correlations have been developed by Flemmer and Banks [101] and Turton and Levenspiel [402]. The former propose:

$$C_{d0} = \frac{24}{Re_0} 10^{0.261 Re_0^{0.369} - 0.105 Re_0^{0.431} - \frac{0.124}{1 + (\log_{10} Re_0)^2}} \quad (6.18)$$

where $Re_0 < 3 \times 10^5$. The coefficients in the above have been determined using experimental data from two sources. The number of data points used to fit the correlation has not been given by the authors. The deviation in C_{d0} is approximately between +4 and -8%.

Turton and Levenspiel [402] re-fitted the parameters in Clift and Gauvin's expression to obtain:

$$C_{d0} = \frac{24}{Re_0} (1 + 0.173 Re_0^{0.657}) + \frac{0.413}{1 + 1.63 \times 10^4 Re_0^{-1.09}} \quad (6.19)$$

where $Re_0 < 2 \times 10^5$.

The expression of Turton and Levenspiel [402] performs better than that given by Clift et al. [56, p. 112] when compared to 408 data points from 18 sources reported

in the literature: 90.4% of the data points fall within $\pm 10\%$. It combines simplicity, accuracy and a wide-range of applicability and is therefore recommended by Karamanov and Nikolov [194] for use as a standard drag curve for solid spheres in the sub-critical regime.

6.2.3 Empirical Correlations for Droplets

Harmathy [138] obtained an empirical correlation for the drag coefficient of large droplets and bubbles in turbulent flows. He assumed that the drag coefficient on a fluid particle is only a function of the shape, *i.e.* viscous effects are negligible and the drag coefficient is only a function of the Eötvös number. From a fit to experimental data, he then obtained:

$$C_{d0} = 0.57\sqrt{\mathcal{E}_o} \quad (6.20)$$

This result is valid when the Reynolds number is sufficiently large ($\mathcal{R}e_0 > 500$) and the Eötvös number is in the range $1 < \mathcal{E}_o < 13$.

Early attempts to correlate the terminal velocities of droplets in liquids (mainly water) have been made by Klee and Treybal [200] and Hu and Kinter [159]. Johnson and Braida [189] extended the modelling approach of Hu and Kinter [159] to systems of organic liquids falling in a glycerol solution. Their result is given by two empirical expressions for stable and oscillating drops, respectively:

$$\mathcal{J} = \begin{cases} 0.798\mathcal{H}^{0.784} & \text{for } 2 < \mathcal{H} \leq 70 \\ 3.70\mathcal{H}^{0.422} & \text{for } 70 > \mathcal{H} \end{cases} \quad (6.21)$$

where

$$\mathcal{J} = \mathcal{R}e_0 \mathcal{M}o^{0.15} + 0.75 \quad (6.22)$$

$$\mathcal{H} = \frac{4}{3}\mathcal{E}_o \mathcal{M}o^{-0.15} \left(\frac{\mu}{\mu_w} \right)^{-0.14} \quad (6.23)$$

and μ_w is the viscosity of water, which is taken as $9 \times 10^{-4} [\text{Pa s}]$. The data used in the fitting process covers the range $1.3 \times 10^{-11} < \mathcal{M}o < 1.7 \times 10^{-6}$ and $3 < \mathcal{R}e_0 < 1100$. Hu and Kinter's [159] expression can be recovered by setting $\frac{\mu}{\mu_w} = 1$. A potential problem arises from the fact that equation (6.21) is not valid for $\mathcal{H} < 2$, *i.e.* for small particle

sizes because \mathcal{H} is proportional to \mathcal{E}_0 , as can be seen from equation (6.23). The use outside this range yields negative relative velocities, which is clearly unphysical.

Grace et al. [124] collected a large body of experimental data (~ 1700 data points) for droplets as well as bubbles and applied three types of correlation to it, namely: the one proposed by Klee and Treybal [200]; that given by Hu and Kinter [159] and its extension by Johnson and Braida [189] as well as the wave analogy suggested by Mendelson [270] which had been extended to drops by Marruci et al. [263]. They found that the type of correlation used of Hu and Kinter [159] and Johnson and Braida [189] gave the best fit, after adjustment of the coefficients. They obtained:

$$\mathcal{J} = \begin{cases} 0.94\mathcal{H}^{0.757} & \text{for } 2 < \mathcal{H} \leq 59.3 \\ 3.42\mathcal{H}^{0.441} & \text{for } 59.3 > \mathcal{H} \end{cases} \quad (6.24)$$

where

$$\mathcal{J} = \mathcal{R}e_0 \mathcal{M}o^{0.149} + 0.857 \quad (6.25)$$

$$\mathcal{H} = \frac{4}{3} \mathcal{E}_0 \mathcal{M}o^{-0.149} \left(\frac{\mu}{\mu_w} \right)^{-0.14} \quad (6.26)$$

This equation holds in the range $1.5 \times 10^{-12} < \mathcal{M}o < 10^{-3}$, $\mathcal{E}_0 < 40$ and $\mathcal{R}e_0 > 0.2$ and is recommended by Clift et al. [56, p. 176] for calculating the drag coefficients of bubbles and droplets, since none of the earlier correlations covers such a broad range of conditions. Grace et al. [124] also give a modification for pure systems.

Grace et al.'s [124] expression suffers from the same potential problem as that of Johnson and Braida since it yields negative relative velocities for $\mathcal{H} < 2$, corresponding to small $\mathcal{R}e$.

6.2.4 Empirical Correlations for Bubbles in Clean Water

For the case of clean bubbles, Moore's [278] classic analysis may be applied in the range $80 < \mathcal{R}e_0 < 500$ to 700 where the Reynolds number is large enough for boundary layer theory to be valid. However, the bubble has to be small enough that its deformation is not significant. Lain et al. [218] decided to use Moore's [278] result in their correlation

for bubbles in clean water. They propose:

$$C_{d0} = \begin{cases} 16\mathcal{R}e_0^{-1} & \text{for } \mathcal{R}e_0 \leq 1.5 \\ 14.9\mathcal{R}e_0^{-0.78} & \text{for } 1.5 < \mathcal{R}e_0 \leq 80 \\ \frac{48}{\mathcal{R}e_0} \left(1 - \frac{2.21}{\sqrt{\mathcal{R}e_0}}\right) & \text{for } 80 < \mathcal{R}e_0 \leq 700 \\ 1.86 \times 10^{-15}\mathcal{R}e_0^{4.756} & \text{for } 700 < \mathcal{R}e_0 \leq 1530 \\ 2.61 & \text{for } 1530 < \mathcal{R}e_0 \end{cases} \quad (6.27)$$

Unfortunately, Lain et al. [218] did not compare their correlation with experimental data. Furthermore, the piecewise correlations do not match exactly at $\mathcal{R}e_0 = 1.5$ and 80 which could lead to instabilities in numerical calculations. To avoid this problem, the regime transitions should be modified to $\mathcal{R}e_0 = 1.38$ and 56.9, respectively.

At larger Reynolds numbers ($Re > 500$), the bubble rise is dominated by surface tension, *i.e.* the Eötvös number. In this regime, Mendelson [270] suggested an analogy with wave theory in order to determine the terminal velocity of single bubbles (see equation (6.15)). No rational explanation has been given to justify this, therefore it seems reasonable to fit the coefficients to experimental data. This has been done by Clift et al. [56, p. 172] with the result:

$$C_{d0} = \frac{2.65\mathcal{E}_0}{\mathcal{E}_0 + 4.26} \quad (6.28)$$

for $500 < \mathcal{R}e_0 < 5000$. Johansen and Boysan [187] used this equation as a basis for a correlation for finite α (see Section 6.3.3). In this situation the Morton numbers are usually extremely low ($\mathcal{M}o \approx 10^{-13}$) and one can expect spherical-cap bubbles.

Wang [416] derived expressions to fit the experimental data obtained by Haberman and Morton [130] for clean bubbles in distilled water by using a least squares method. This correlation was used during the BRITE-II project [416, 146]. Wang's [415] expression for the drag coefficient reads:

$$\log_e C_{d0} = \begin{cases} \log_e 24 - \log_e \mathcal{R}e_0 & \text{for } \mathcal{R}e_0 \leq 1 \\ 2.70 - 0.336 \log_e \mathcal{R}e_0 - 7.14 \times 10^{-2}(\log_e \mathcal{R}e_0)^2 & \text{for } 1 < \mathcal{R}e_0 \leq 456 \\ -51.8 + 13.2 \log_e \mathcal{R}e_0 - 0.824(\log_e \mathcal{R}e_0)^2 & \text{for } 456 < \mathcal{R}e_0 \leq 4000 \end{cases} \quad (6.29)$$

Tomiyama *et al.* [384, 383, 381] developed empirical correlations for the drag coefficient of a single bubble. They combined and modified the correlations given by Hadamard and Rybczynski at low Reynolds numbers, Schiller and Naumann at intermediate Reynolds numbers and Mendelson at high Reynolds numbers. The proposed correlation consists of three equations, which respectively correspond to pure, slightly-contaminated and contaminated systems. The correlations for contaminated systems are given in the next Section; the one for pure systems is:

$$C_{d0} = \max \left(\min \left(\frac{16}{\mathcal{R}e_0} (1 + 0.15 \mathcal{R}e_0^{0.687}), \frac{48}{\mathcal{R}e_0} \right), \frac{8}{3} \frac{\mathcal{E}_0}{\mathcal{E}_0 + 4} \right) \quad (6.30)$$

Tomiyama et al. [384, 383] used the dataset of Grace [123], who collected 247 data points for 21 air-liquid system from 8 sources covering $10^{-3} < \mathcal{R}e_0 < 10^5$, $10^{-14} < \mathcal{M}_o < 10^7$ and $10^{-2} < \mathcal{E}_0 < 10^3$ to assess the validity of their approach. They also found that it gives better fits than that proposed by Peebles and Garber [303] and Ishii and Zuber [168].

6.2.5 Empirical Correlations for Bubbles in Contaminated Water

The aforementioned results are only applicable to clean systems, where the concentration of surfactants is negligible. However, it should be noted that even small amounts of surfactants have an enormous effect on bubbles in the range $d < 1 - 2$ mm because their interfaces are quickly saturated with surfactants. Furthermore, bubbles of this size are almost spherical and, consequently, the standard drag law for solid particles can be used. For example, Schiller and Naumann's [340] expression has been used by Mudde and Simonin [284] and Thai Van et al. [376] in order to calculate various bubbly two-phase flows. Some authors also incorporated this correlation into their own (Tomiyama et al. [384], Lain et al. [218]). Lain et al.'s [218] correlation is:

$$C_{d0} = \begin{cases} \frac{24}{\mathcal{R}e_0} (1 + 0.15 \mathcal{R}e_0^{0.687}) & \text{for } \mathcal{R}e_0 \leq 700 \\ 9.5 \times 10^{-5} \mathcal{R}e_0^{1.397} & \text{for } 700 < \mathcal{R}e_0 \leq 1500 \\ 2.61 & \text{for } 1500 < \mathcal{R}e_0 \end{cases} \quad (6.31)$$

As for their clean bubble correlation, Lain et al. [218] did not compare with experimental data.

The terminal velocity of rising bubbles in liquids has been investigated by Peebles and Garber [303]. They obtained 146 data points for 22 gas-liquid systems, used to derive the following empirical correlation:

$$C_{d0} = \begin{cases} 24\mathcal{R}e_0^{-1} & \text{for } \mathcal{R}e_0 \leq 2 \\ 18.7\mathcal{R}e_0^{-0.68} & \text{for } 2 < \mathcal{R}e_0 \leq 4.02\mathcal{G}^{-0.214} \\ 0.0275\mathcal{G}\mathcal{R}e_0^4 & \text{for } 4.02\mathcal{G}^{-0.214} < \mathcal{R}e_0 \leq 3.1\mathcal{G}^{-0.25} \\ 0.82\mathcal{G}^{0.25}\mathcal{R}e_0 & \text{for } 3.1\mathcal{G}^{-0.25} < \mathcal{R}e_0 \end{cases} \quad (6.32)$$

Here, \mathcal{G} is the Morton number in its original form as defined in equation (6.1). Peebles and Garber [303] give the following descriptions for the various regimes:

- Region 1: Stokes regime, spherical bubbles moving on rectilinear paths; drag coefficients agree with the Stokes' law;
- Region 2: spherical bubbles moving on rectilinear paths with drag coefficients slightly lower than those of an equal-volume solid sphere;
- Region 3: deformed bubbles of ellipsoidal shape moving in zigzag or helical paths with drag coefficients increasing sharply with Reynolds number;
- Region 4: Greatly deformed bubbles assuming mushroom like shape, rising in a nearly rectilinear path with drag coefficients increasing with Reynolds number, but not so sharp as for Region 3.

Peebles and Garber's [303] data do not extend very far into the spherical-cap regime and it is therefore not surprising that their correlation does not obey the spherical-cap limit obtained by Davies and Taylor [73], namely $C_{d0} = \frac{8}{3}$. Glaeser and Brauer [113] modified Peebles and Garber's [303] correlation to give this behaviour, thus:

$$C_{d0} = \begin{cases} 16\mathcal{R}e_0^{-1} & \text{for } \mathcal{R}e_0 \leq 1.4 \\ 14.9\mathcal{R}e_0^{-0.78} & \text{for } 1.4 < \mathcal{R}e_0 \leq 3.73\mathcal{G}^{-0.209} \\ 0.0275\mathcal{G}\mathcal{R}e_0^4 & \text{for } 3.73\mathcal{G}^{-0.209} < \mathcal{R}e_0 \leq 3.1\mathcal{G}^{-0.25} \\ 2.61 & \text{for } 100 < 3.1\mathcal{G}^{-0.25} < \mathcal{R}e_0 \end{cases} \quad (6.33)$$

Kuo and Wallis [211] studied the terminal velocity of bubbles in water. For $\mathcal{Re}_0 < 100$, they found that the drag coefficient is only a function of the Reynolds number, whereas it is only a function of the Weber number when the bubble become very distorted. They propose:

$$C_{d0} = \begin{cases} 16\mathcal{Re}_0^{-1} & \text{for } \mathcal{Re}_0 < 0.49 \\ 20.68\mathcal{Re}_0^{-0.643} & \text{for } 0.49 < \mathcal{Re}_0 < 100 \\ 6.3\mathcal{Re}_0^{-0.385} & \text{for } \mathcal{Re}_0 > 100 \\ \frac{\mathcal{We}}{3} & \text{for } \mathcal{Re}_0 > 2065.1/\mathcal{We}^{2.6} \\ \frac{8}{3} & \text{for } \mathcal{We} > 8 \end{cases} \quad (6.34)$$

This correlation is valid for bubbles in tap water and has been used by Boisson and Malin [32] in their calculation of a bubble column. It should be noted that a similar correlation is available for clean water

As mentioned earlier, Tomiyama *et al.* [384, 383, 381] developed empirical correlations for the drag coefficient of a single bubble in pure, slightly-contaminated and contaminated water. The correlation for pure systems has been presented in the previous Section; the ones for slightly contaminated and contaminated systems are

$$C_{d0} = \max \left(\min \left(\frac{24}{\mathcal{Re}_0} (1 + 0.15\mathcal{Re}_0^{0.687}), \frac{72}{\mathcal{Re}_0} \right), \frac{8}{3} \frac{\mathcal{Eo}}{\mathcal{Eo} + 4} \right) \quad (6.35)$$

and

$$C_{d0} = \max \left(\frac{24}{\mathcal{Re}_0} (1 + 0.15\mathcal{Re}_0^{0.687}), \frac{8}{3} \frac{\mathcal{Eo}}{\mathcal{Eo} + 4} \right) \quad (6.36)$$

, respectively.

6.2.6 Other Empirical Correlations for Bubbles

As has been shown, the conventional approach to develop a correlation is to divide the whole parameter range into several distinct regimes and fit the experimental data in each. This can lead to difficulties in numerical calculations [147] when the correlations do not match at the boundaries between one regime and another separately. In this context, it is noteworthy that Fan and Tsuchiya [95, p. 43] developed a correlation

that is continuous in all of its derivatives. It is based on the well-known equations of Stokes [363] and Mendelson [270] with re-fitted coefficients and reads:

$$U_{r0} = \frac{1}{\sqrt[n]{(U_r^{St})^{-n} + (U_r^{Me})^{-n}}} \quad (6.37)$$

$$U_r^{St} = \frac{\rho_c g d^2}{K_b \mu_c} \quad (6.38)$$

$$U_r^{Me} = \sqrt{\frac{2c\sigma}{\rho_c d} + \frac{gd}{2}} \quad (6.39)$$

Here, K_b , c and n are empirical coefficients fitted to experimental data sets for air bubbles in 20 different liquids from three sources in the range $10^{-12} < \mathcal{M}_o < 10^5$. The subscripts S and M stand for the laws of Stokes [363] and Mendelson [270], respectively.

Fan and Tsuchiya [95] found that the values for c and n can be determined for a specific liquid at a given level of contamination. It is recommended to use $c = 1.2$ and 1.4 for mono-component and multicomponent liquids, respectively. The recommended values for n range from 0.6 to 1.6 depending on liquid purity and have been tabulated by the authors. The value of K_b was found to vary from one liquid to another, ranging from 12 to 40 . The behaviour of K_b can be correlated by the following relation $K_b = K_{b0}\mathcal{M}_o^{0.038}$, where $K_{b0} = 14.7$ and 10.2 for aqueous solution (and water) and organic solvents/mixtures, respectively. The best fit for air bubbles in water was obtained with $K_b = 37$ and $c = 1.2$. The coefficient n was set to $n = 1.6$ and 0.8 for clean and contaminated water, respectively.

Equation (6.37) approaches equation (6.38) for small Reynolds numbers and equation (6.39) for large ones. These equations can be reformulated to give the drag coefficient in terms of the Reynolds number, resulting in:

$$C_d^{St} = \frac{4K_b}{3\mathcal{R}e_0} \quad (6.40)$$

$$C_d^{Me} = \frac{8}{3} \frac{\mathcal{E}_o}{\mathcal{E}_o + 4c} \quad (6.41)$$

It has been noted earlier that Fan and Tsuchiya [95] choose K_b as a fitting parameter. With their recommended value for bubbles in water $K_b = 37$, equation (6.40) becomes $C_d^{St} = 49.3\mathcal{R}e_0^{-1}$. This is somewhat different from the analytical results of Stokes [363], Hadamard [131] and Rybczynski [332] for creeping flow and closer to the results of Levich for slightly higher Reynolds numbers ($10 < \mathcal{R}e_0 < 100$). This leads

to the conclusion that Fan and Tsuchiya's [95] expression is not strictly valid at small Reynolds numbers and should not be applied there.

Recently, Tomiyama et al. [387] challenged the view that the variation of the rise velocity for a fixed bubble diameter from one experiment to another can be explained by the presence of surfactants. His group conducted experiments with air bubbles in clean, tap and contaminated water and found that multiple stable states exist. For each of these states, the bubble assumes a particular shape and possesses a characteristic rise velocity falling into the shaded area of Figure 1.5. These results have been presented in more detail Section 1.5.3. They then derived a correlation for the bubble rise velocity as a function of the aspect ratio E of the bubble which is given by:

$$U_{r0} = \frac{\sin^{-1} \sqrt{1 - E^2} - E\sqrt{1 - E^2}}{1 - E^2} \sqrt{\frac{8\sigma}{\rho_c d} E^{4/3} + \frac{|\Delta\rho|gd}{2\rho_c} \frac{E^{2/3}}{1 - E^2}} \quad (6.42)$$

Unfortunately, E is itself an dependent variable and seems to depend on the history of the bubble. Hence, Tomiyama conducted additional work to identify the dimensionless groups which govern the aspect ratio. However, no final conclusion was presented.

6.3 Influence of Phase Fraction on the Drag Coefficient

Up to date and comprehensive reviews of correlations for the drag on multiple DPEs are not available. However, the older literature for particles, droplets and bubbles has been reviewed by Wallis [414]. More results for bubbles can be found in Lahey et al. [217] and in Steiner and Hartland [361] for droplets. Drag models often used in CFD calculations have been listed by Hjertager [156] and Jakobsen et al. [178].

The majority of the correlations presented in the following Sections are empirical and the data used in their derivation have often been obtained from fluidisation and/or sedimentation experiments [15]. In the former, the DPEs are suspended in a column by a stream of fluid. Once steady-state is reached, the drag and buoyancy forces are (on average) in equilibrium and the phase fraction is determined from the height of the bed formed by the suspended DPEs. On the other hand, in a sedimentation experiment,

the two-phase mixture is left for gravitational settling and the height of the mixture is then recorded over time.

The fluidisation/sedimentation experiments are relatively easy to conduct with particles, but they are much more complicated if droplets or bubbles are investigated for two reasons: firstly, the fluid particles are usually generated during the experiment; and secondly, their size might change in the course of the experiment due to break-up and coalescence. Hence, their size has to be obtained in the experiment, *e.g.* photographically.

Experimental investigations on droplets are often carried out in spray columns [361, 308]. In this device, the droplets are dispersed into the continuous fluid through a distributor. The dispersed phase velocity is either measured directly, *e.g.* cinematically, or calculated from the dispersed phase throughput and the phase fraction where the latter is determined by sudden isolation of a section of the column.

6.3.1 Empirical Correlations for Particles

For fluidised and sedimenting particles, the relationship between the relative velocity and the phase fraction has been investigated by several authors, *e.g.* [197, 5, 15, 110, 362, 319, 429, 428, 240, 168].

Drift flux models have been widely used to represent the influence of the phase fraction on drag. See Wallis [414] for a general introduction. In general these models take the following form:

$$\frac{j}{U_{r0}} = \alpha(1 - \alpha)^n \quad (1.12)$$

where n is an empirical coefficient and j is the drift flux defined as:

$$j = \alpha(1 - \alpha)U_r \quad (1.13)$$

Equation (1.12) can be recast in terms of the drag coefficient, thus:

$$C_d = C_{d0}(1 - \alpha)^{3-2n} \quad (6.43)$$

where C_{d0} is the drag coefficient for a single DPE in an infinite medium.

For particles, Wallis [414, p. 182] has given the following empirical formula for n , which compares very well with the earlier ones obtained by Richardson and Zaki [319]:

$$n = 4.7 \frac{1 + 0.15\mathcal{R}e^{0.687}}{1 + 0.253\mathcal{R}e^{0.687}} \quad (6.44)$$

Barnea and Mizrahi [15] used a mixture approach to express the drag at elevated phase fraction. They define the Reynolds number and drag coefficient as:

$$\mathcal{R}e_m = \frac{\rho_d U_r d}{\mu_m} \quad (6.45)$$

$$C_{dm} = \frac{F_m}{\frac{1}{2}\rho_c A U_r^2 (1 + \alpha^{1/3})} \quad (6.46)$$

where subscript m denotes mixture.

Here, μ_m is the effective mixture viscosity of the suspension:

$$\mu_m = \mu_c \exp \left(\frac{5\alpha}{3(1 - \alpha)} \right) \quad (6.47)$$

With these definitions their drag correlation is:

$$C_{dm} = \left(0.63 + \frac{4.8}{\sqrt{\mathcal{R}e_m}} \right)^2 \quad (6.48)$$

This can be recast in terms of C_d using the following relationship:

$$C_d = C_{dm} (1 + \alpha^{1/3}) \quad (6.49)$$

In their study, Garside and Al-Diboui [110] observed that the relative velocity normalised by the terminal velocity of a single particle can be fitted by the following equation:

$$\frac{U^* - K_A}{K_B - U^*} = 0.06 \mathcal{R}e_0^{1.2-\alpha} \quad (6.50)$$

where U^* is the normalised velocity magnitude $U^* = \frac{U_r}{U_{r0}}$ and the empirical coefficients are the following functions of α : $K_A = (1 - \alpha)^{4.14}$ and $K_B = (1 - \alpha)^{2.65}$ for $\alpha < 0.15$ or $K_B = 0.8(1 - \alpha)^{1.28}$ for $\alpha \geq 0.15$. The coefficients were obtained from the best fit for 379 data points from 17 sources in the range $10^{-3} < \mathcal{R}e_0 < 3 \times 10^4$ and $0.01 < \alpha < 0.62$ with a standard deviation of 9%. Equation (6.50) can be reformulated to give an expression for C_d , thus:

$$C_d = C_{d0}(1 - \alpha) \left(\frac{1 + 0.06 \mathcal{R}e_0^{1.2-\alpha}}{K_A + 0.06 K_B \mathcal{R}e_0^{1.2-\alpha}} \right)^2 \quad (6.51)$$

Garside and Al-Diboui [110] compared their relationship with the one of Richardson and Zaki [319] and Barnea and Mizrahi [15] and found better agreement with the experimental data.

Wen and Yu [429] proposed a model for the drag on particles at elevated phase fractions by assuming that the ratio of the multi-particle and single-particle drag coefficient C_d/C_{d0} can be expressed as a function of phase fraction. They found:

$$C_d = \frac{24}{\mathcal{R}e_s} (1 + 0.15\mathcal{R}e_s^{0.687}) (1 - \alpha)^{-1.7} \quad (6.52)$$

where the Reynolds number $\mathcal{R}e_s$ is based on the superficial velocity, *i.e.* $\mathcal{R}e_s = \frac{(1-\alpha)\rho_c U_r d}{\mu_c}$. Note that for low Reynolds numbers this equation reverts to that of Richardson and Zaki [319]. The correlation has been validated against experimental data from 4 sources. It has also been used by Simonin *et al.* [27, 284] to calculate drag on bubbles at elevated phase fractions.

Andersson [5] modified the classic Ergun [90] equation for packed beds by including a tortuosity factor q and a cross-section factor z . Both of those are phase fraction dependent. The result is presented in the form given by Mewes [273]:

$$C_{d0} = \begin{cases} \frac{24(zq^2)}{\mathcal{R}e_0} \frac{\alpha}{1-\alpha} & \text{for } \mathcal{A}r \leq 1 \\ \frac{24(zq^2)}{\mathcal{R}e_0} \frac{\alpha}{1-\alpha} + 8C_{d0}^* q^3 & \text{for } \mathcal{A}r > 1 \end{cases} \quad (6.53)$$

where

$$C_{d0}^* = \frac{1}{8} \left(C_{d0} - \frac{24}{\mathcal{R}e_0} \right) \quad (6.54)$$

$$zq^2 = \frac{1-\alpha}{2\alpha} \exp \left(\frac{2.5\alpha}{1-0.61\alpha} \right) \quad (6.55)$$

$$q^3 = 5 \left(\frac{\alpha}{1-\alpha} \right)^{0.45} \quad (6.56)$$

and $6 \times 10^{-2} < \mathcal{A}r < 6 \times 10^5$ and $0.05 < \alpha < 0.55$. C_{d0} is the drag coefficient on a single particle. Various expressions for the latter are given in Section 6.2.2 and Turton and Levenspiel's [402] expression is used in the present study. However, it is unfortunate that the equation diverges for low phase fractions, as will be shown in Section 6.4.3. This renders it unsuitable for CFD calculations, where generality and robustness are key requirements.

It has been noted by Pilhofer and Mewes [308] that Andersson's [5] correlations were able to predict particle swarm velocities more reliably than that of Barnea and Mizrahi [15]. They therefore decided to extend Andersson's [5] correlation to liquid-liquid systems.

Ishii and Zuber [168] (see [166, 167]) studied the drag on DPEs and proposed several models for the drag coefficient for wide ranges of the phase fraction, Reynolds number and flow regime. They identified the following flow regimes: the **Undistorted** regime for particles, droplets and bubbles; the **Distorted** regime for droplet and bubbles; the **Newton** regime for particles; and the **Churn Turbulent** regime for bubbles. In the undistorted and Newton regime, the confinement effect of the surrounding DPEs is represented using a mixture viscosity approach, in which the latter is calculated from:

$$\mu_m = \mu_c \left(1 - \frac{\alpha}{\alpha^*}\right)^{2.5\alpha^* \frac{\mu_d + 0.4\mu_c}{\mu_d + \mu_c}} \quad (6.57)$$

where α^* is the maximum phase fraction, which takes a value of approximately 0.62 for solid particles and 1.0 for fluid particles.

In this Section, only correlations applicable to particles are given, whereas Ishii and Zuber's [168] correlations applicable to fluid particles will be presented in Sections 6.3.2 and 6.3.3. For particles in the undistorted and Newton regimes, they give the following correlations based on the mixture viscosity:

$$C_d = \begin{cases} \frac{24}{Re_m} (1 + 0.1 Re_m^{0.75}) & \text{Undistorted DPE regime} \\ 0.45 K_1(\alpha) & \text{Newton's regime} \end{cases} \quad (6.58)$$

In the undistorted regime, Ishii and Zuber assume that a complete similarity exists between C_d based on Re_0 for a single DPE and C_d based on Re_m for a cloud of DPEs. Therefore the multi-particle drag coefficient can be determined from the single-particle one using Re_m instead of Re and a drag law similar to that proposed by Schiller and Naumann's [340] is used for this purpose.

However, in the Newton regime, C_d is assumed to depend only on the phase fraction, *i.e.* the effect of the neighbouring particles is through the phase fraction alone. Hence, the relation between C_d and C_{d0} , *i.e.* $K_1(\alpha)$, can be obtained by considering a special case of the terminal velocity particles in an infinite medium. Briefly, the terminal velocities for single-particle and multi-particle systems are compared at the

	Fluid particle system		Solid particle system	
	Bubble in liq.	Drop in liq.	Drop in gas	
α^*	≈ 1	≈ 1	0.62 to 1	≈ 0.62
$\frac{\mu_d+0.4\mu_c}{\mu_d+\mu_c}$	0.4	≈ 0.7	1	1
μ_m/μ_c	$\approx (1-\alpha)^{-1}$	$\approx (1-\alpha)^{-1.75}$	$\approx (1-\alpha)^{-2.5}$	$\approx (1-\alpha)^{-1.55}$
$K_2(\alpha)$	$\approx (1-\alpha)^{1.5}$	$\approx (1-\alpha)^{2.25}$	$\approx (1-\alpha)^3$	n/a

Table 6.1: Magnitudes of various terms in the model of Ishii and Zuber [168]

transition point between the undistorted and the Newton regime. At this point, the relative velocity given by the two models should be identical. From this argument the following function for K_1 is obtained:

$$K_1(\alpha) = \left(\frac{1 + 17.6 (K_2(\alpha))^{6/7}}{18.67 K_2(\alpha)} \right)^2 \quad (6.59)$$

where K_2 is defined as $K_2(\alpha) = \sqrt{1-\alpha} \frac{\mu_c}{\mu_m}$. The magnitudes of the terms in the model of Ishii and Zuber [168] for bubble, droplet and solid particle flows are given in Table 6.1.

6.3.2 Empirical Correlations for Droplets

The drag force on droplets at high phase fractions has often been expressed by extending models for particle systems. For example, Pilhofer [307] based his model on the ideas of Andersson [5], whereas Barnea and Mizrahi [16] extended their mixture viscosity approach by taking into account the circulation within the droplets, but not their deformed shapes. The latter give:

$$\mu_m = \mu_c K_B \frac{\frac{2}{3} K_B + \frac{\mu_d^*}{\mu_c}}{K_B + \frac{\mu_d^*}{\mu_c}} \quad (6.60)$$

where μ_d^* is the “apparent” viscosity of the dispersed phase, $K_A = \frac{\mu_c+2.5\mu_d}{2.5\mu_c+2.5\mu_d}$ and $K_B = \exp\left(\frac{5\alpha K_A}{3(1-\alpha)}\right)$. With these definitions, equation (6.46) can be applied. However, no way was found of evaluating μ_d^* , so Barnea and Mizrahi [16] recommend to use μ_d instead. Kumar et al. [209] also addressed this problem and suggested to avoid the evaluation μ_d^* by using the equation of Leviton and Leighton [242] instead of equation (6.47):

$$\mu_m = \mu_c \exp\left(2.5 \frac{0.4\mu_c + \mu_d}{\mu_c + \mu_d} (\alpha + \alpha^{5/3} + \alpha^{11/3})\right) \quad (6.61)$$

Kumar et al. [209] simplified the approach of Barnea and Mizrahi [16] and redefined the drag coefficient for the mixture as:

$$C_{dm} = \frac{F_d}{\frac{1}{2}\rho_c A U_r^2 \left(\frac{1+\alpha^{1/3}}{1-\alpha} \right)^n} \quad (6.62)$$

C_d is related to C_{dm} via:

$$C_d = C_{dm} \left(\frac{1+\alpha^{1/3}}{1-\alpha} \right)^n \quad (6.63)$$

where C_{dm} and n have constant values of 0.49 and 1.834, respectively. These correlations were validated against experimental results consisting of 591 data points for 16 liquid-liquid systems from 8 sources covering the range $7 < \mathcal{R}e < 2450$ and $0.01 < \alpha < 0.75$. Kumar et al. [209] also compared their predictions with those of Pilhofer's [307] and Barnea and Mizrahi's [16] correlations and found that their correlation predicts 69.5% of the data points to within a deviation of 10%, whereas the other two correlations only predict 35.7% and 34.7% of the data sets with this accuracy..

It is interesting to note that Kumar et al.'s [209] correlation is independent of the droplet Reynolds number for all phase fractions. This is clearly not physical in the single droplet limit. Kumar and Hartland [208] later rectified this problem and presented another empirical expression for the prediction of the droplet rise velocity which is a function of the Reynolds number. The new correlation, which is not based on Barnea and Mizrahi's [16] approach, is:

$$\mathcal{R}e = -\frac{12}{K_1} + \sqrt{\left(\frac{12}{K_1} \right)^2 + \frac{4\mathcal{A}r}{3K_1} f(\alpha)} \quad (6.64)$$

$$f(\alpha) = \frac{1-\alpha}{1+k\alpha^n} \quad (6.65)$$

where $k = 4.56$, $K_1 = 0.53$ and $n = 0.73$ and C_d can then be expressed as:

$$C_d = \left(K_1 + \frac{24}{\mathcal{R}e} \right) (1+k\alpha^n) \quad (6.66)$$

This correlation has been validated against 998 published experimental results for 29 liquid-liquid systems from 14 different sources covering the range $9 \times 10^{-3} < \alpha < 0.75$, $0.16 < \mathcal{E}o < 6.41$ and $0.16 < \mathcal{R}e < 3169$.

Pilhofer [307] (see [308, 209]) extended the approach of Andersson [5] from particles to droplets. He obtained for $\mathcal{Ar} \leq 1$:

$$C_d = \frac{24(zq^2)}{\mathcal{Re}} \frac{\alpha}{1-\alpha} \quad (6.67)$$

$$zq^2 = \frac{1-\alpha}{2\alpha} \exp\left(\frac{2.5\alpha}{1-0.61\alpha}\right) K^{H\&R} \quad (6.68)$$

where $\alpha > 0.06$ and $K_{H\&R}$ is the Hadamard-Rybczynski correction given in equation (6.10).

For higher Archimedes numbers ($\mathcal{Ar} > 1$), C_d is given by:

$$C_d = \frac{24(zq^2)}{\mathcal{Re}} \frac{\alpha}{1-\alpha} + 8C_{d0}^* q^3 \quad (6.69)$$

$$C_{d0}^* = \frac{1}{6} \frac{\mathcal{Ar}}{\mathcal{Re}_0^2} - 3K_{HR}\mathcal{Re}_0 \quad (6.70)$$

$$zq^2 = \begin{cases} \frac{1-\alpha}{2\alpha} \exp\left(\frac{2.5\alpha}{1-0.61\alpha}\right) K_{HR} & \text{for } 0.06 < \alpha \leq 0.55 \\ 2.2 \frac{1-\alpha}{\alpha} \exp\left(\frac{0.44\alpha}{1-0.61\alpha}\right) K_{HR} & \text{for } 0.55 < \alpha < 0.74 \end{cases} \quad (6.71)$$

$$q^3 = 5 \left(\frac{\alpha}{1-\alpha}\right)^{0.45} K_{HR}^{1.5} \quad (6.72)$$

where \mathcal{Re}_0 is calculated from Hu and Kinter's [159] equation (6.21). Note that for oscillating bubbles/droplets with $\mu_c < \mu_d$ and $\mathcal{H} > 70$, C_{d0}^* has to be multiplied by an additional correction factor $1 - \alpha^{1.29} \left(\frac{\mathcal{Ar}-394\mathcal{M}_0-0.275}{394\mathcal{M}_0-0.275}\right)^{-1.74}$.

Pilhofer's [307] approach suffers from the same deficiency as Andersson's [5] in the sense that it diverges for low phase fractions and, therefore, lacks the necessary generality required for use in a CFD code.

As outlined in Section 6.3.1, Ishii and Zuber [168] developed a unified model for particles, droplet and bubbles. In what follows the formulation for his distorted particle regime (droplets) is given. In this regime, the drag coefficient for a single fluid particle is assumed to depend only on the Eötvös number and the phase fraction, but not on the Reynolds number, *i.e.* Harmathy's [138] result for large droplets and bubbles is used. However, it should be noted that Ishii and Zuber [168] modified the constant given by Harmathy from 0.57 to 0.66.

Ishii and Zuber [168] express the dependence of the drag coefficient on the phase fraction by making the assumption that the increase in drag can be determined by the expression used for particles in the Newton regime for particles. In other words,

they assumed that regardless of the difference in C_{d0} in these regimes, the effect of increased drag in the distorted particle regime can be predicted by using the same function $K_1(\alpha)$. This model is:

$$C_d = \begin{cases} \frac{24}{\mathcal{R}e_m} (1 + 0.1 \mathcal{R}e_m^{0.75}) & \text{Undistorted DPE regime} \\ \frac{2}{3} \sqrt{\mathcal{E}o} K_1(\alpha) & \text{Distorted DPE regime} \end{cases} \quad (6.73)$$

where $K_1(\alpha)$ is defined in equation (6.59). $\mathcal{R}e_m$ is based on the mixture viscosity defined in equation (6.57) in which α^* takes a value of 1.0 for droplets, extending the range of application for densely packed systems. During the BRITE-II project Hill [147, 145] used this correlation for the calculation of liquid-liquid flows in a pipe mixer, but neglected the influence of α on the drag coefficient because the phase fraction was low.

The use of Drift flux models for droplets in fluids has not been studied as extensively as for bubbly flow (see Section 6.3.3 for details). However, Wallis [414, p. 382] presented considerable evidence that a direct analogy between bubbly and droplet flow can be assumed and suggests to use $n = 2.0$ in equation (1.12).

6.3.3 Empirical Correlations for Bubbles

Drift flux models for bubbly flow have been discussed by Wallis [414, p. 252]. He made the simple assumption that the relative velocity decreases linearly with the phase fraction and, therefore, recommended $n = 2.0$. However, there are strong indications that the value of n is not always 2.0. Zuber and Hench [442] (see [414, p. 255]) presented analytical as well as experimental results and recommended the following values for n depending on the regimes used by Peebles and Garber [303]:

$$n = \begin{cases} 2.0 & \text{for } \mathcal{R}e_0 \leq 2 & \text{Region 1} \\ 1.75 & \text{for } 2 < \mathcal{R}e_0 \leq 4.02 \mathcal{G}^{-0.214} & \text{Region 2} \\ \text{not given} & \text{for } 4.02 \mathcal{G}^{-0.214} < \mathcal{R}e_0 \leq 3.1 \mathcal{G}^{-0.25} & \text{Region 3} \\ 1.5 & \text{for } 3.1 \mathcal{G}^{-0.25} < \mathcal{R}e_0 & \text{Region 4} \end{cases} \quad (6.74)$$

Unfortunately, a value for the very important regime 3, which covers 1 to 10 mm air bubbles in water, was not given. Here, Tomiyama et al. [382] used a constant

value of $n = 1.75$ in their calculation of a transient bubble-induced circulation in a bubble column.

Schwarz and Turner [341] presented a very simple model for the rise velocity of contaminated bubbles in liquids. It is given in the form of a constant friction factor which is defined in equation (1.11):

$$C_f = 5 \times 10^4 \left[\frac{kg}{m^3 s} \right] \quad (6.75)$$

This corresponds to a constant relative velocity of about 0.2 m/s and is a good approximation to the terminal velocity of single air bubbles in water when the diameter is in the range of 1 to 10 mm. The slip velocity is almost constant over this range of diameters because of increasing non-sphericity. The correlation can be cast into a relation for C_d :

$$C_d = 6.7 \times 10^4 (1 - \alpha) \frac{d}{\rho_c |\mathbf{U}_r|} \left[\frac{kg}{m^3 s} \right] \quad (6.76)$$

This correlation has been used for CFD calculations of bubble columns by [352, 353, 391] and of gas-stirred baths by [341].

Johansen and Boysan [187] studied bubble stirred metallurgical ladles and modified equation (6.28) by using Tsuji et al.'s [401] experimental data on the drag coefficients of two spheres behind each other for $\mathcal{R}e < 200$ in order to account for phase fraction effects. Their equation for the drag coefficient, in the form presented by Hjertager [156], reads:

$$C_d = C_{d0} (1 - \alpha^{0.667}) = \frac{2.65 \mathcal{E}_o}{\mathcal{E}_o + 4.26} (1 - \alpha^{0.667}) \quad (6.77)$$

valid for $500 < \mathcal{R}e < 5000$.

The model predicts a reduction of the drag coefficient with increasing phase fraction. This is not in agreement with the trend predicted by many other well established models, *e.g.* Wallis [414, p. 382] and Tomiyama et al. [382] which give $\frac{C_d}{C_{d0}} = (1 - \alpha)^{-0.5}$ and $(1 - \alpha)^{-1}$, respectively. Furthermore, the experimental data presented in Section 6.4 confirms that the drag coefficient increases with increasing phase fraction. Therefore, Johansen and Boysan's [187] model does not seem to be appropriate under these conditions.

The model of Ishii and Zuber [168] has been used by several authors [282, 103] to correlate the drag on bubbles. It is applicable to particles, droplets as well as bubbles, but only the correlations applicable to bubbles are given here:

$$C_d = \begin{cases} \frac{24}{\mathcal{R}e_m} (1 + 0.1 \mathcal{R}e_m^{0.75}) & \text{Undistorted DPE regime} \\ \frac{2}{3} \sqrt{\mathcal{E}o} K_1(\alpha) & \text{Distorted DPE regime} \\ \frac{8}{3} (1 - \alpha)^2 & \text{Churn turbulent regime} \end{cases} \quad (6.78)$$

where $K_1(\alpha)$ is defined in equation (6.59). $\mathcal{R}e_m$ is based on the mixture viscosity defined in equation (6.57) in which α^* takes a value of 1.0 for bubbles.

Ishii and Zuber's [168] correlation only gives criteria for transition from the undistorted particle to distorted particle regime. Therefore, Morud and Hjertager [282], who used it in order to calculate bubbly air-water flow in a stirred vessel, assumed the flow to be in the distorted particle regime (bubbles) for $\alpha \leq 0.3$, in the churn turbulent regime (see Section 1.5.4) for $0.3 < \alpha \leq 0.7$ and again in the distorted particle regime (droplets) for $\alpha > 0.7$.

6.3.4 New Correlations

Most of the correlation discussed in the previous Sections suffer from the limitation that they do not revert to a single DPE drag correlation when the phase fraction approaches zero. Even if they incorporate a single DPE model, it often does not represent the current state of the art. This is especially the case for correlations for systems of droplets.

It therefore seems desirable in the present study to formulate the effects of the presence of other DPEs independently from the model used in the low phase fraction limit. In this respect, this new correlation is similar to the drift flux approach. In the new correlation, the drag coefficient is expressed as a correction to the drag coefficient of a single DPE:

$$C_d = C_{d0} f(\alpha, Ar, \dots) \quad (6.79)$$

where f is a function of the phase fraction, the Archimedes number and other parameters of the flow. An obvious constraint on f is that it must approach unity when the phase fraction vanishes.

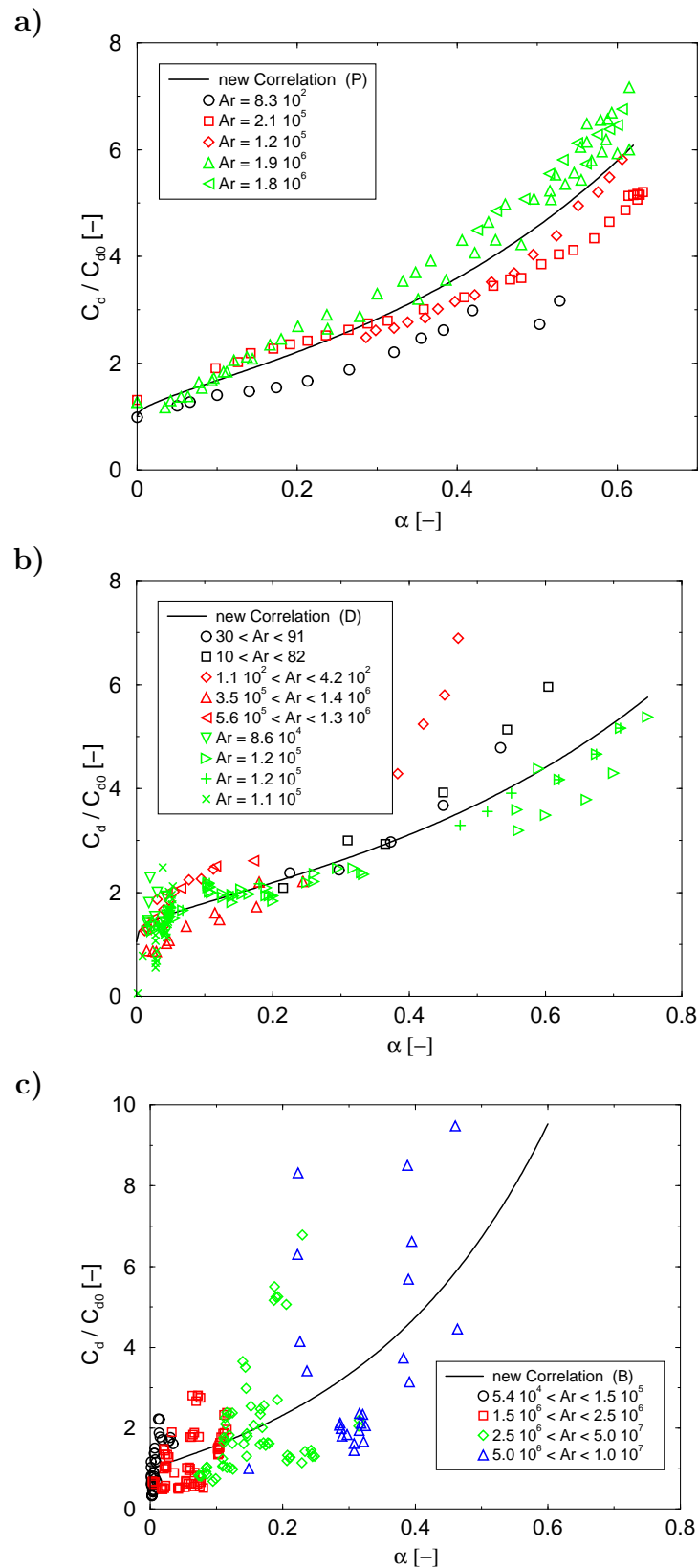


Figure 6.1: Experimental values of the ratio C_d/C_{d0} and best fits to equation (6.80). **a)** Particles; **b)** Droplets; **c)** Bubbles.

Plots of the ratio C_d/C_{d0} versus α derived from the experimental data are presented in Figure 6.1 for particles, droplets and bubbles. The selection of the experimental data as well as the evaluation of C_d/C_{d0} from it is described in Section 6.4. In general, the relative velocity of a DPE surrounded by other DPEs decreases, as discussed in Section 1.5.4 and, therefore, the ratio C_d/C_{d0} increases with increasing phase fraction. It is also evident, that it tends to unity for very low phase fractions, although for bubbles there is a large amount of scatter indicating that not all of the important effects are taken fully into account in the single bubble drag law. This will be discussed further in Section 6.4.5.

For particles, a weak dependency on the Archimedes number is noticeable from Figure 6.1a in that C_d/C_{d0} takes larger values with increasing Archimedes numbers. Unfortunately, this dependency cannot be confirmed for fluid particles, as can be seen from Figure 6.1b and c, where other effects seem to have a much stronger influence on the multi-particle dynamics.

The experimental data in Figure 6.1 suggests that C_d/C_{d0} is primarily a function of the phase fraction. The increasing influence of Ar is weak for particles, but cannot be confirmed for droplets and bubbles. Therefore, in a first step, it is assumed in the present study that f is only a function of α . Hereby, a suitable functional form is chosen for f in the light of the experimental data. Its coefficients are evaluated by minimising its r.m.s. deviation from the data using the non-linear fitting procedure implemented in the graph plotting package “grace” [125].

It is evident from Figures 6.1a and b that f increases exponentially for high phase fractions, whereas for values up to $\alpha \approx 0.3$, f seems to rise initially and then tail off. Therefore, a combination of a power law and an exponential function is chosen as a fitting function, thus:

$$f(\alpha) = \exp(K_1\alpha) + \alpha^{K_2} \quad (6.80)$$

The coefficients K_1 and K_2 have been determined for the different systems using the non-linear fitting procedure implemented in the graph plotting package “grace” [125]. The resulting values are tabulated in Table 6.2.

It should be mentioned that the new correlations derived in this Section are for dispersed flows. However, a gas-liquid flow at very high phase fractions ($\alpha > 0.3$)

	Particles	Droplets	Bubbles
K_1	2.68	2.10	3.64
K_2	0.430	0.249	0.864

Table 6.2: Coefficients in new correlations.

might be in the churn turbulent rather than the dispersed flow regime, as discussed in Section 1.5.4. In this case, different correlations must be used.

6.4 Model Selection and Testing

The objective of this Section is to select drag correlations from those presented in Sections 6.2 and 6.3 for implementation into the two-fluid methodology described in Chapter 3. The selected correlations are then implemented in the two-fluid methodology and validated against two test cases for which experimental data are available: the plane mixing layer (at low phase fraction) and the sudden enlargement of a circular pipe (at high phase fraction).

The final expressions have to be applicable to two-phase systems at the full range of phase fractions. However, many drag correlations are based on those for single DPEs and, therefore, the best of the latter have to be selected first. The drag correlations for single particles have been validated extensively against experimental data by several authors [56, 101, 402, 194] and further work in this field is outside the scope of this study. Hence, *we follow Karamanov and Nikolov’s [194] recommendation to use the correlation of Turton and Levenspiel [402]*. However, less work has been conducted for single bubbles and droplets, and the correlations presented earlier are therefore compared against each other in Sections 6.4.1 and 6.4.2, respectively, in order to assess their validity.

Finally, the correlations for particles, droplets and bubbles at high phase fractions are assessed against each other as well as experimental data from the literature in Sections 6.4.3, 6.4.4 and 6.4.5, respectively.

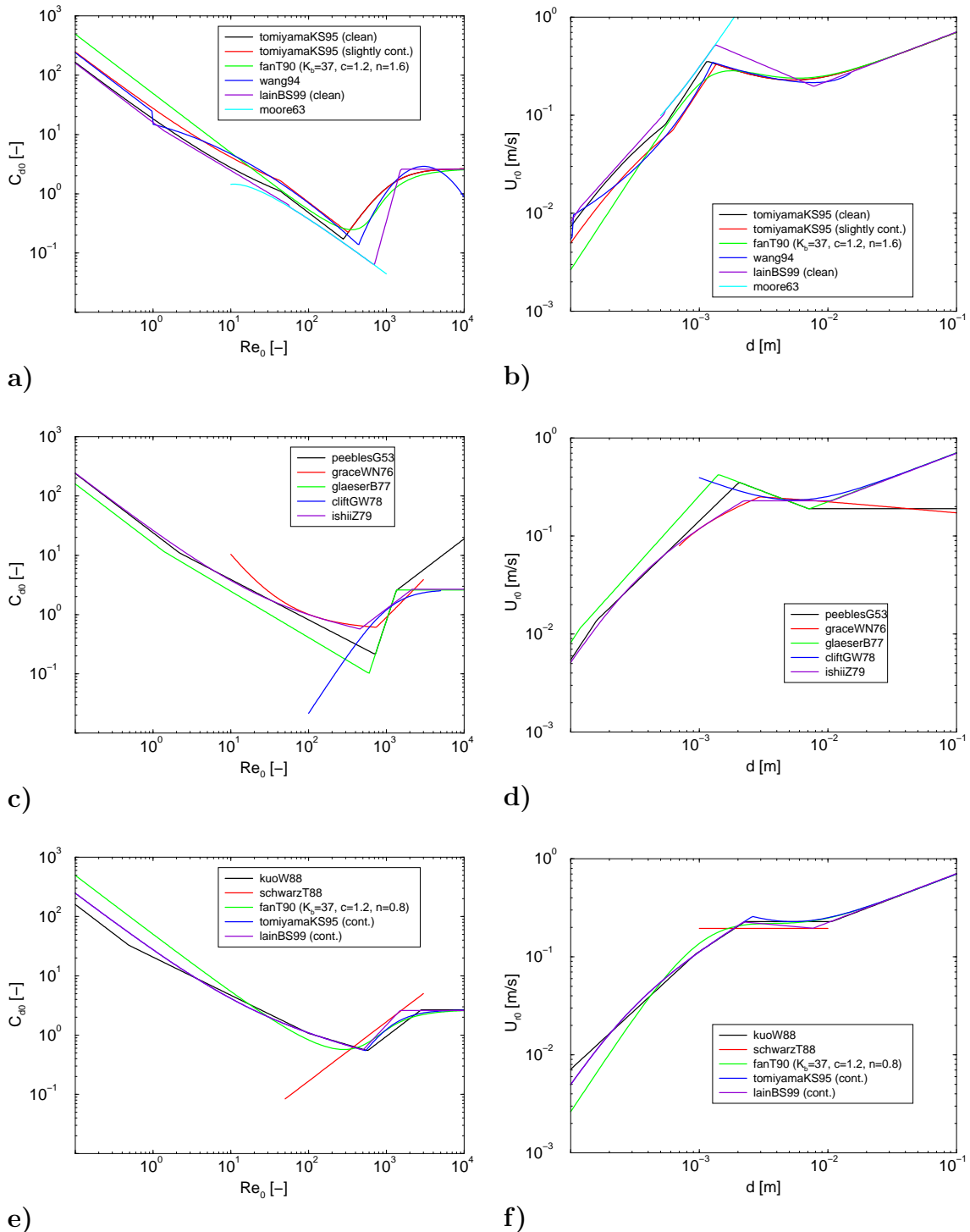


Figure 6.2: Plot of $C_{d0} - \mathcal{R}e_0$ (l.h.s.) and $U_{r0} - d$ (r.h.s.) from various drag correlations for bubbles in clean (a) and (b)) and contaminated (c) to (f)) water.

6.4.1 Bubbles at Low Phase Fraction

The performance of the various drag correlations is best analysed by plotting the drag coefficient C_{d0} as a function of the Reynolds number $\mathcal{R}e_0$ and the relative velocity U_{r0} as a function of the diameter of the DPE d . For this purpose, equation (6.5) is solved numerically using the Newton-Raphson method, [313, p. 376][272, p. 278]. Properties of an air-water system under atmospheric conditions are used in the calculations.

Figure 6.2a and b show the results for correlations suitable for clean gas-liquid systems, *i.e.* those proposed by Tomiyama et al. [384], Fan and Tsuchiya [95], Wang [415], Lain et al. [218] as well as the analytical result of Moore [278]. Very good agreement between the correlations for U_{r0} can be observed for larger bubbles with $d > 1$ mm or $\mathcal{R}e_0 > 400$, although that of Lain et al. [218] seems to somewhat overestimate in the intermediate regime. Nearly all models obey the limit for spherical-cap bubbles, *i.e.* $C_{d0} \approx \frac{8}{3}$, except that of Wang [415], as this one is only valid up to a Reynolds number of 5000.

On the other hand, appreciable differences are apparent for $d < 1$ mm or $\mathcal{R}e_0 < 400$, when the bubbles maintain their spherical shape. For extremely pure systems C_{d0} should approach $16\mathcal{R}e_0^{-1}$. This has been recognised in the correlation of Tomiyama et al. [384] (clean systems) and in that of Lain et al. [218]. Nevertheless, even very small amounts of contaminants immobilise the surface of very small bubbles. In this case, C_{d0} should approach $24\mathcal{R}e_0^{-1}$ as used by Tomiyama et al. [384] (slightly contaminated) and Wang [415]. However, in the latter case the limit was added at a later stage of the modelling after the curve fit for $\mathcal{R}e_0 > 1$ had been obtained, leaving an unmatched regime transition at $\mathcal{R}e_0 = 1$. Fan and Tsuchiya's [95] correlation predicts drag coefficient that are somewhat higher than those given by the other models because it approaches $C_{dS} = 49.3\mathcal{R}e_0^{-1}$ for small Reynolds numbers, as shown in Section 6.2.6. Hence, this expression is not strictly valid at small Reynolds numbers ($\mathcal{R}e_0 < 40$) and should not be applied there.

Figure 6.2c to f show the results for correlations suitable for contaminated gas-liquid systems, *i.e.* those proposed by Peebles and Garber [303], Grace et al. [124], Glaeser and Brauer [113], Clift et al. [56], Ishii and Zuber [168], Kuo and Wallis [211], Schwarz and Turner [341], Fan and Tsuchiya [95], Tomiyama et al. [384] as well as

Lain et al. [218]. By comparing Figure 6.2c and d with Figure 6.2e and f it is apparent that the more recent correlations dating from the 80's and 90's are in better agreement with each other than the earlier ones. Two of the very early expressions suffer from the deficiency that the spherical-cap regime is not recovered for high $\mathcal{R}e$. These are the ones of Peebles and Garber [303] and Grace et al. [124]. However, Glaeser and Brauer [113] seem to have rectified this problem in their correlation, but it gives higher values for the rise velocity for small bubbles than any other model. It is interesting that Peebles and Garber's [303] formulation for region 3 ($C_{d0} = 0.0275\mathcal{G}\mathcal{R}e_0^4$) seems to be more appropriate for contaminated systems, where a noticeable decrease in the rise velocity is found for moderate bubbles sizes of $1 \text{ mm} < d < 10 \text{ mm}$.

The correlation proposed by Grace et al. [124] has a relatively small range of applicability, but it is also applicable to liquid-liquid flows. As mentioned earlier, its functional form leads to unphysical behaviour when used outside its bounds for moderately small Reynolds numbers as indicated in Figure 6.2c.

From Figure 6.2b it is evident that Schwarz and Turner's [341] assumption of a constant friction factor is a good approximation for air-water bubbles in contaminated water of the size $2 \text{ mm} < d < 10 \text{ mm}$. Interestingly, it gives slightly smaller rise velocities than the other models. Nevertheless, it lacks the necessary generality.

Again, there seems to be some confusion in the low Reynolds number limit in the earlier as well as in the more recent expressions, but in the light of the previous comments we simply note that $C_{d0} = 24\mathcal{R}e_0^{-1}$ should be used for bubbles in contaminated systems. This was done by Peebles and Garber [303], Ishii and Zuber [168], Tomiyama et al. [384] and Lain et al. [218].

The correlations proposed by Ishii and Zuber [168] (contaminated systems), Fan and Tsuchiya [95] (clean and contaminated systems), Tomiyama et al. [384] (clean and contaminated systems) and Lain et al. [218] (contaminated systems) capture the overall trends very well. Tomiyama et al. [384] validated their model slightly more thoroughly than Fan and Tsuchiya [95], although both references used the extensive data set collected of Haberman and Morton [130], but Lain et al. [218] unfortunately did not conduct a validation study. Tomiyama et al. [384] note that their correlation performs better than that of Ishii and Zuber [168], which has the advantage of being

applicable to higher phase fractions. *Overall, we recommend the use of Tomiyama et al.’s [384] correlation for clean as well as contaminated single bubbles.*

6.4.2 Droplets at Low Phase Fraction

Essentially, two correlations have been proposed in the literature for the rise velocity of single droplets, namely those of Harmathy [138] and Grace et al. [124]. It has been shown in the previous Section that the functional form of the latter leads to unphysical behaviour when used outside its bounds for moderately small Reynolds numbers. Similar restrictions apply to Harmathy’s [138] expression which is only valid in the range $1 < \mathcal{E}_0 < 13$. *Therefore, it has to be concluded that a general correlation for the terminal velocity of a single droplet in an infinite medium is not available at present.*

6.4.3 Particles at High Phase Fraction

The dynamics of falling particles have been researched quite extensively and a large body of literature is available which has been reviewed by [15, 110]. The data selected for comparison have been obtained from fluidisation experiments. This type of experiment has been outlined in Section 6.3 and yields the mean phase fraction and the mean relative velocity on a macroscopic scale, *e.g.* for whole column. The experimental data have been obtained by 3 authors and have been chosen so that a wide range of the Archimedes number is covered. They are assembled in 4 data sets which are tabulated in Table 6.3.

The data are compared with the following correlations which are described in Section 6.3.1: drift flux model (equation (6.44)), Ishii and Zuber [168] (undistorted and Newton regime), Barnea and Mizrahi [15], Andersson [5], Wen and Yu [429], Garside and Al-Dibou [110] as well as the formula developed in the present study which is denoted “new correlation”. Some formulations require an expression for the drag on a single particle and we use the best available to us – in this case the one of Turton and Levenspiel [402]. As mentioned earlier, Andersson’s [5] correlation is not valid for $\alpha < 0.05$ and we use dashed lines to indicate this. The performance of the various formulations is analysed by plotting $C_d - \alpha$ and $U_r - \alpha$. The predictions for C_d

Data Set	Reference	System	$\mathcal{A}r$
P1	Hanratty and Bandukwala [133]	steel spheres, glass spheres in glycerine-water solution	< 1
P2	Wilhelm and Kwauk [430]	sea sand in water	8.3×10^2
P3	Wilhelm and Kwauk [430]	sacony beads in water	2.1×10^5
	Wen and Yu [429]	glass spheres in water	1.2×10^5
P4	Wilhelm and Kwauk [430]	glass beads in water	1.9×10^6
	Wen and Yu [429]	glass spheres in water	1.8×10^6

Table 6.3: Data sets chosen for comparison with drag correlations for particles at high phase fraction.

and U_r are obtained using the same numerical techniques as outlined in the previous Section, but equation (6.9) is now solved instead of equation (6.5). Equation (6.9) is also utilised to calculate C_d from the experimental data, which usually contains only U_r , as pointed out earlier. The properties utilised in the calculations are taken from the references mentioned above. In addition, the data is normalised by the model's prediction for $\alpha = 0$, *i.e.* C_d/C_{d0} and U_r/U_{r0} . However, this is not possible for the formula of Andersson [5] because it is not defined in the single particle limit. Instead, Turton and Levenspiel's [402] expression is utilised.

Figure 6.3 shows the drag coefficient and the relative velocity as well as their normalised (by single particle values) values as functions of the phase fraction for data set P1. This is for glass and steel spheres falling in glycerine-water solution for which the Archimedes number is less than 1. The corresponding Reynolds numbers are of the order of 10^{-2} for data points close to the single particle limit and 10^{-3} when the suspension is dense. The flow is therefore in the creeping flow regime. Unfortunately, Hanratty and Bandukwala [133] published only the normalised relative velocity and it is therefore impossible to calculate U_r or C_d for this data set.

It is evident from Figure 6.3a that all correlations predict roughly the same trend, namely that the drag coefficient rises when the phase fraction increases. However, there are large differences in behaviour in the proximity of the maximum packing limit (approximately 0.62 for particles). Here, the expressions of Barnea and Mizrahi [15] and Ishii and Zuber [168] predict a sharp increase of the drag coefficient. Reference to equation (6.57) reveals that the model of Ishii and Zuber [168] is actually singular at

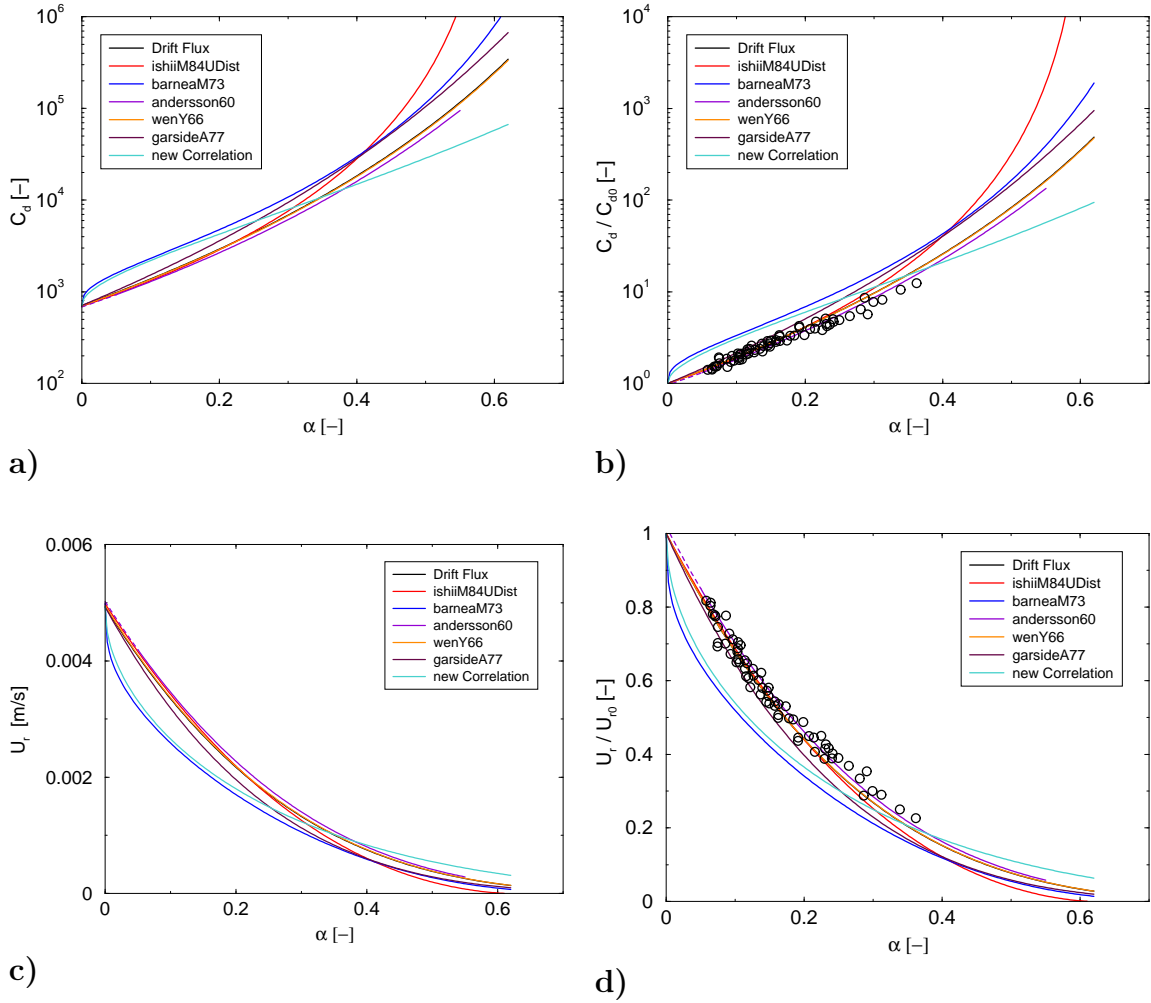


Figure 6.3: Comparison of the predictions of various drag correlations for particles with data set P1 ($\text{Ar} < 1$): **a)** $C_d - \alpha$; **b)** $C_d/C_{d0} - \alpha$; **c)** $U_r - \alpha$; **d)** $U_r/U_{r0} - \alpha$.

this point. This behaviour is not physical because the pressure drop and, consequently, the drag coefficient in a packed bed of particles are always finite. The former is given to good approximation by the well-known Ergun [90] equation.

It is further noticeable from the plot that the correlation of Barnea and Mizrahi [15] and that proposed in the present study give slightly higher values for low phase fractions, although the differences are fairly small. In particular, they predict a sudden increase in the drag coefficient for small α which will be discussed further in the light of the other experimental data at the end of this Section.

The relative velocity and its normalised value are shown in Figure 6.3c and d, respectively. As expected, the rise in the drag coefficient with increasing phase fraction corresponds to a decrease of the relative velocity with increasing phase fraction. This

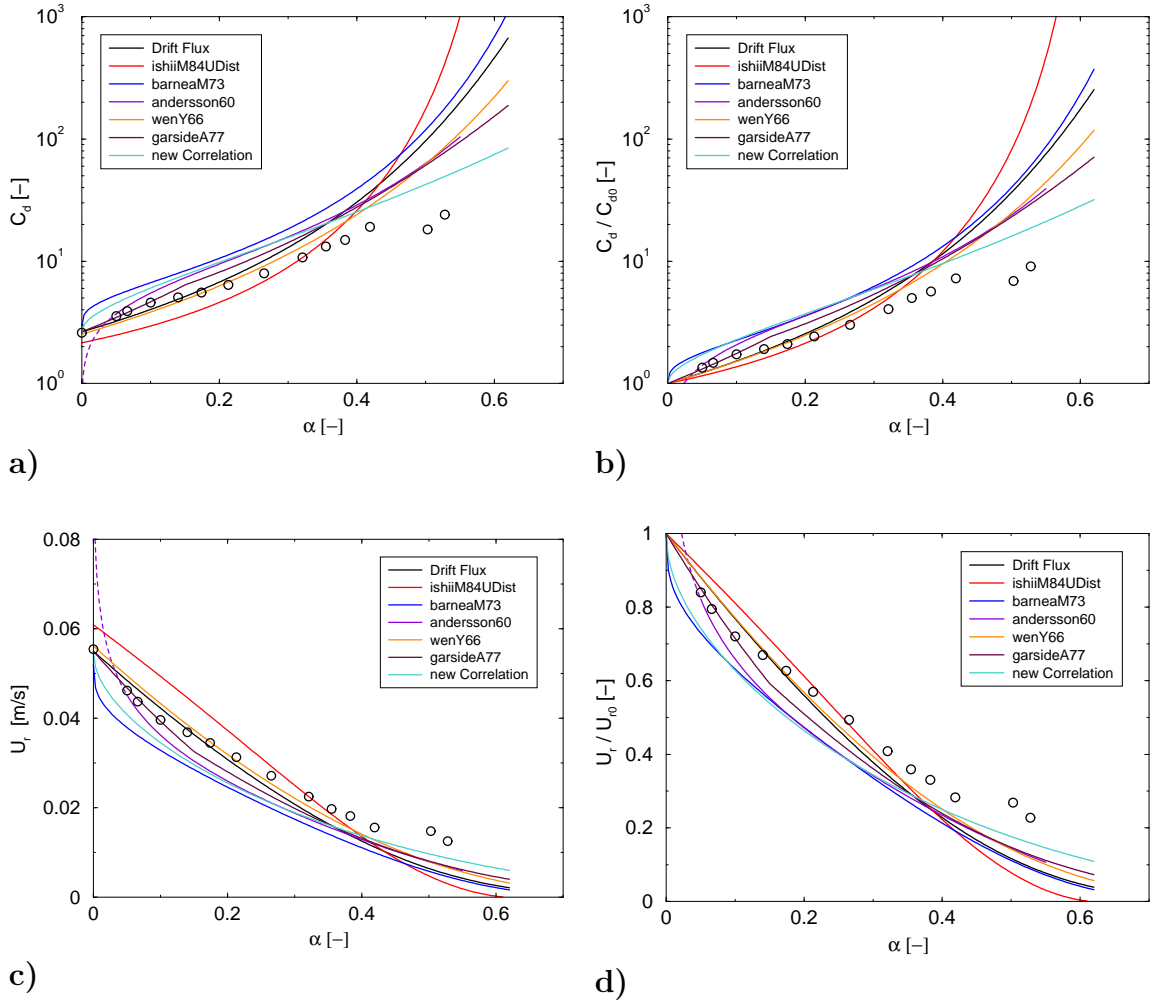


Figure 6.4: Comparison of the predictions of various drag correlations for particles with data set P2 ($Ar = 8.3 \times 10^2$): **a)** $C_d - \alpha$; **b)** $C_d / C_{d0} - \alpha$; **c)** $U_r - \alpha$; **d)** $U_r / U_{r0} - \alpha$.

is shown in Figure 6.3a and c. The results of the different correlations are very similar, although some predict slightly smaller relative velocities for $\alpha < 0.3$ most notably that of Barnea and Mizrahi [15] and that developed in the present study. However, it should be mentioned that all models produce nearly identical values for the terminal velocity in the single particle limit, *i.e.* they all revert to Stokes' law. Very good agreement can also be found for the normalised relative velocity as a function of α , as shown in Figure 6.3d. All correlations predict the normalised relative velocity within the scatter of the experimental data, with the exception of that of Barnea and Mizrahi [15] and that proposed in the present study which give slightly lower values for $\alpha < 0.3$.

Figure 6.4 shows the same comparison for data set P2. The Archimedes number for this set is higher than for set P1. Therefore buoyancy is more important which

results in larger relative velocities. The Reynolds number is now approximately 20 for data points close to the single particle limit.

The predictions for the drag coefficient, plotted in Figure 6.4a, are in reasonable agreement with the experimental results. However, none of the expressions captures the trend indicated by the two data points around $\alpha \approx 0.42$; those are assumed to be anomalous. From the plot, it is evident that the model of Ishii and Zuber [168] gives lower values when $\alpha < 0.4$, whereas that of Barnea and Mizrahi [15] and that developed in the present study predict larger ones. The best agreement is obtained for the correlation of Wen and Yu [429] and the drift flux model.

The relative velocity is shown in Figure 6.4c. Some discrepancies are noticeable even for the single particle limit. Here, the drift flux model can be taken as a reference, since it is based on the single particle drag model by Turton and Levenspiel [402] which is deemed to be the most recent and accurate. The relative differences between the predictions of the drift flux model and those of the models of Ishii and Zuber [168] and Barnea and Mizrahi [15] are +10% and -6%, respectively. The relative differences in the drag coefficient are -18% and +13%. This level of uncertainty should be kept in mind when assessing the predictions for droplets and bubbles in Sections 6.4.4 and 6.4.5.

Figure 6.5 shows C_d and U_r as well as their normalised values for data set P3, for which the Archimedes number is approximately 10^5 . The set contains data from two sources and some variation between them is evident. This is probably due to the slightly different Archimedes numbers. The Reynolds numbers for this data set are in the range of 120 to 750, for high and low phase fractions, respectively. At this \mathcal{Re} , the use of Ishii and Zuber's [168] model for the Newton regime is justified and results for this model are included into the graphs.

Reasonable agreement is obtained for all correlations except for those of Ishii and Zuber [168] which substantially underpredict the drag coefficient for $\alpha \approx 0.4$ and, hence, overestimates the relative velocity by up to 100%. Furthermore, the correlations of Ishii and Zuber [168] predict that the relative velocity is a concave function of α , *i.e.* $\frac{\partial^2 U_r}{\partial \alpha^2} \leq 0$, which is not in agreement with the other expressions nor the experimental data. For high values of the phase fraction, they also give a sharp increase of the

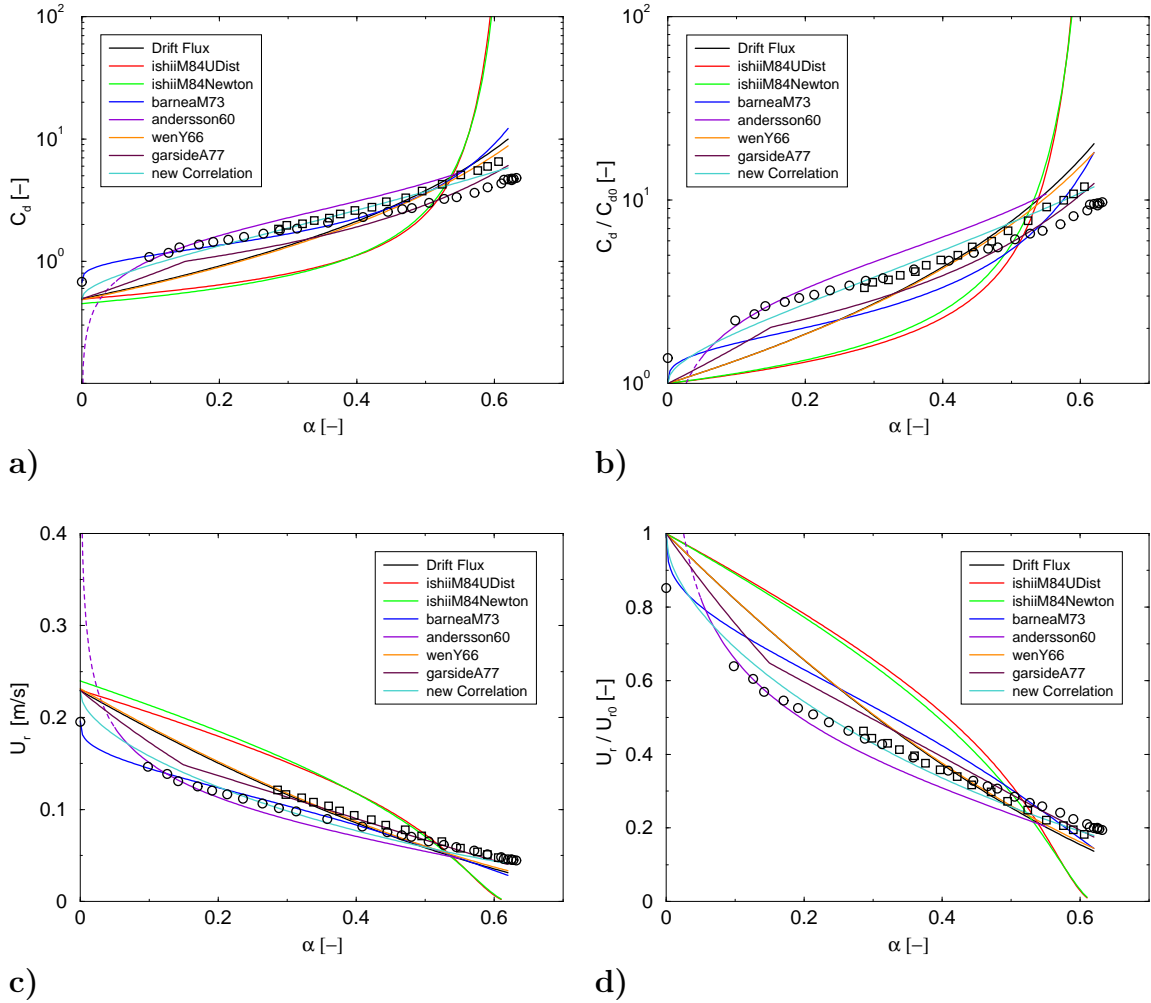


Figure 6.5: Comparison of the predictions of various drag models for particles with data set P3 ($\mathcal{Ar} \approx 1.6 \times 10^5$). Wilhelm and Kwauk [430] (circles), Wen and Yu [429] (squares): **a)** $C_d - \alpha$; **b)** $C_d / C_{d0} - \alpha$; **c)** $U_r - \alpha$; **d)** $U_r / U_{r0} - \alpha$.

drag coefficient amounting to an underprediction of the relative velocity by an order of magnitude for $\alpha \approx 0.6$. There is virtually no difference between the two formulations for the undistorted and the Newton regime.

The other expressions are in much better agreement with the experimental data, although some differences are noticeable in the range $0.1 < \alpha < 0.3$, where those of Andersson [5] and Barnea and Mizrahi [15] as well as that proposed in the present study seem to match the data better than the expression of Wen and Yu [429] and the drift flux model.

The results for data set P4 are plotted in Figure 6.6. These relate to an Archimedes number of approximately 10^6 and \mathcal{Re} in the range 420 to 2500. As

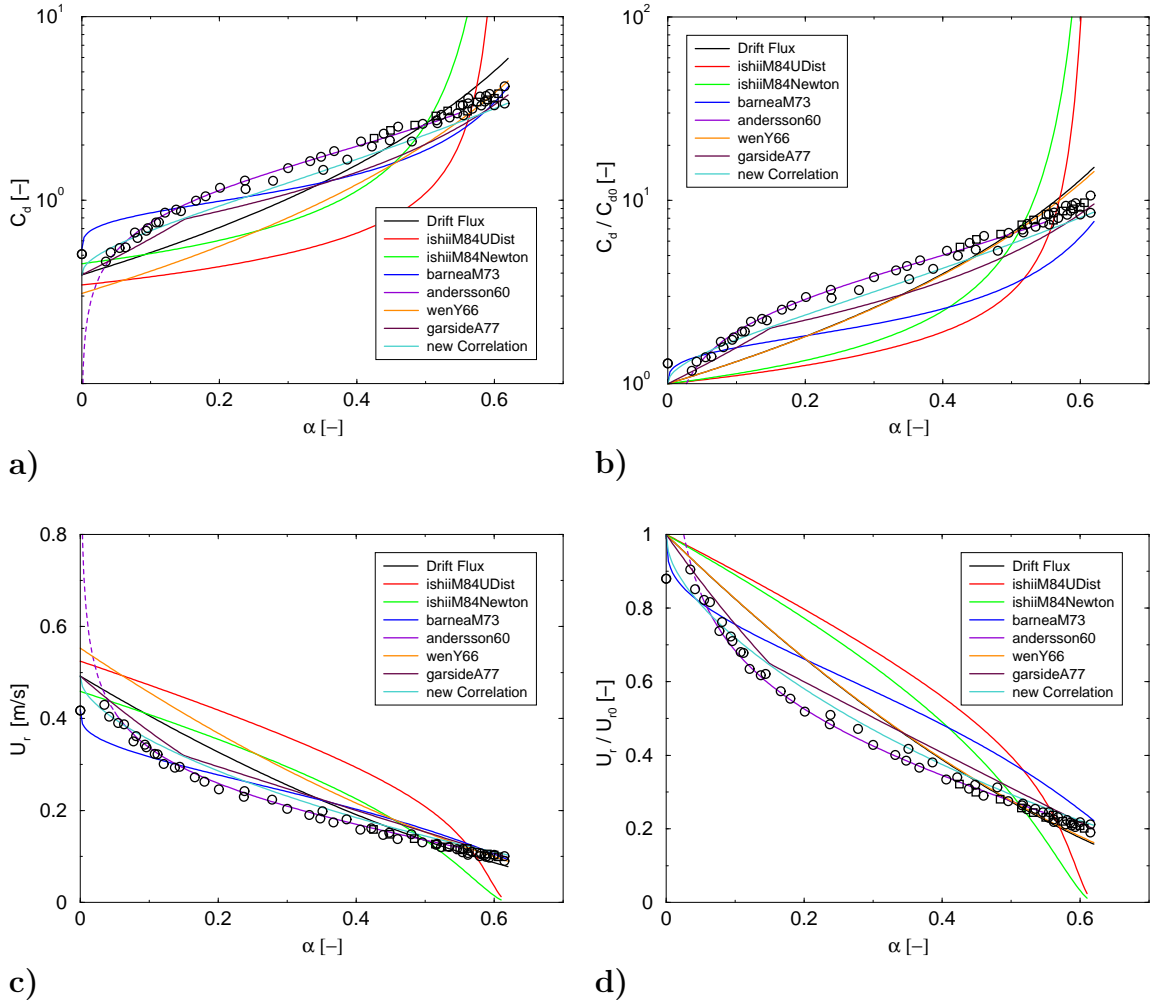


Figure 6.6: Comparison of the predictions of various drag correlations for particles with data set P4 ($\mathcal{Ar} = 1.9 \times 10^6$). Wilhelm and Kwauk [430] (circles), Wen and Yu [429] (squares): **a)** $C_d - \alpha$; **b)** $C_d / C_{d0} - \alpha$; **c)** $U_r - \alpha$; **d)** $U_r / U_{r0} - \alpha$.

previously evidenced for data set P3, the Ishii and Zuber's [168] model substantially underpredicts the drag for low phase fractions and overpredicts it for large ones. There is now a noticeable difference between the formulations for the undistorted and Newton regime, largely due to the different formulations in the single particle limit.

The expression of Wen and Yu [429] performs well for data set P3, but the predictions for data set P4 substantially overestimate the relative velocity for $\alpha < 0.4$. This seems to be due to the underlying single particle model; they used that of Schiller and Naumann [340] which is only valid for $\mathcal{Re}_0 < 1000$. Much better agreement with the experimental data is obtained for the correlation developed in the present study as well as that of Garside and Al-Dibou [110], especially for lower phase fractions. Nearly

perfect agreement is noticeable for the formula proposed by Andersson [5].

In essence, the correlations of Ishii and Zuber predicts larger relative velocities at $\alpha < 0.4$ than the other models. This is especially the case for higher Archimedes numbers, *i.e.* data sets P3, P4 and to lesser extent for P2. Furthermore, it was found that the $U_r - \alpha$ relationship is a concave function of α which is not in agreement with the experimental findings or the predictions of the other expressions. This problem stems from the formulation of the mixture viscosity, which seems is underestimated at low phase fractions and overestimated at high values. Barnea and Mizrahi [15], whose formula also uses a mixture viscosity approach, seem to compensate for this deficiency by modifying the definition for C_d with an additional factor of $(1 - \alpha)^{1/3}$, as evident from equation (6.49). This leads to a sharp increase in the drag coefficient for small α which yields better agreement with the experimental data for high Archimedes numbers (P3, P4), but introduces a problem at low Archimedes numbers where the relative velocity for $\alpha < 0.2$ is underpredicted (P1).

It is interesting to note, that the effect of the phase fraction on the drag coefficient diminishes with higher Archimedes and Reynolds numbers, as evidenced by comparing the normalised drag coefficient in figures 6.3d, 6.4d, 6.5d and 6.6d.

Overall, the expressions proposed by Garside and Al-Dibouい [110] and Andersson [5] seem to give the best results for the terminal velocity of particles falling in liquids. However, Andersson's [5] formula suffers from the deficiency that it cannot be applied to systems at low phase fraction (less than 5%), as mentioned earlier. The new correlation yields reasonable results and could be improved if the influence of the Archimedes number was taken into account. Hence, it lacks generality and *we recommend to use the correlation by Garside and Al-Dibouい [110]*.

6.4.4 Droplets at High Phase Fraction

Fluid-fluid systems have been researched extensively and there are approximately 17 sources of data available in the literature on the velocity of falling or rising droplets in multi-droplet systems. Reviews of these data sets are given in [308, 208]. In this study, four sets have been chosen so that a wide range of the Archimedes numbers ($30 < Ar < 1.4 \times 10^6$) is covered. Unfortunately, the data for intermediate Archimedes

Data Set	Reference	System	$\mathcal{A}r_{min}$	$\mathcal{A}r_{max}$
D1	Barnea and Mizrahi [15]	brine in butanol	30	91
D2	Vedaiyan et al. [412]	methyl iso-butyl ketone in water	1.1×10^5	4.2×10^5
D3	Vedaiyan et al. [412]	benzene in water	3.5×10^5	1.4×10^6
D4	Loutaty et al. [254]	kerosene in water	8.6×10^4	3.0×10^5
D5	Garwin and Smith [111]	benzene in water	3.4×10^5	1.0×10^6

Table 6.4: Data sets chosen for comparison with drag correlations for droplets at high phase fraction.

numbers was not available to the author. In the experiments, the size of a droplet and bubble cannot be fixed easily and is a result of the generation process as well as secondary effects, *e.g.* break-up and coalescence. Therefore, the Archimedes number is no longer a constant for a given system. The data sets are tabulated in Table 6.4 together with the range of Archimedes numbers prevailing. All of the experiments were carried out in spray columns and the diameter of the droplets was obtained photographically.

The data are compared with the following correlations which are described in Section 6.3.2: drift flux model (equation (1.12)), Ishii and Zuber [168], Barnea and Mizrahi [16], Pilhofer [307], Kumar et al. [209], Kumar and Hartland [208] as well as the formula developed in the present study which is denoted “new correlation”. Some formulations require an expression for the drag on a single droplet and, as previously, we use the best available to us – in this case the one of Grace et al. [124]. However, this expression is not valid when \mathcal{H} , as defined in equation (6.26), is smaller than 2 and the standard particle drag law is used instead. This is justified since in this case \mathcal{Re} is usually small and Stokes’ law should apply. As mentioned earlier, Pilhofer [307] derived his correlation from that proposed by Andersson [5] for multi-particle systems and, hence, it is not valid for $\alpha < 0.06$. Again, a dashed line indicates this and Grace et al.’s [124] correlation is used to calculate the normalised quantities.

Figure 6.7 shows the comparison for data set D1, which is for relatively small brine droplets ($0.5 \text{ mm} < d < 1.0 \text{ mm}$) falling in butanol. The Archimedes number is of the order of $30 - 90$. The corresponding Reynolds numbers are of the order of 0.7 for a single droplet and 0.2 for a dense suspension.

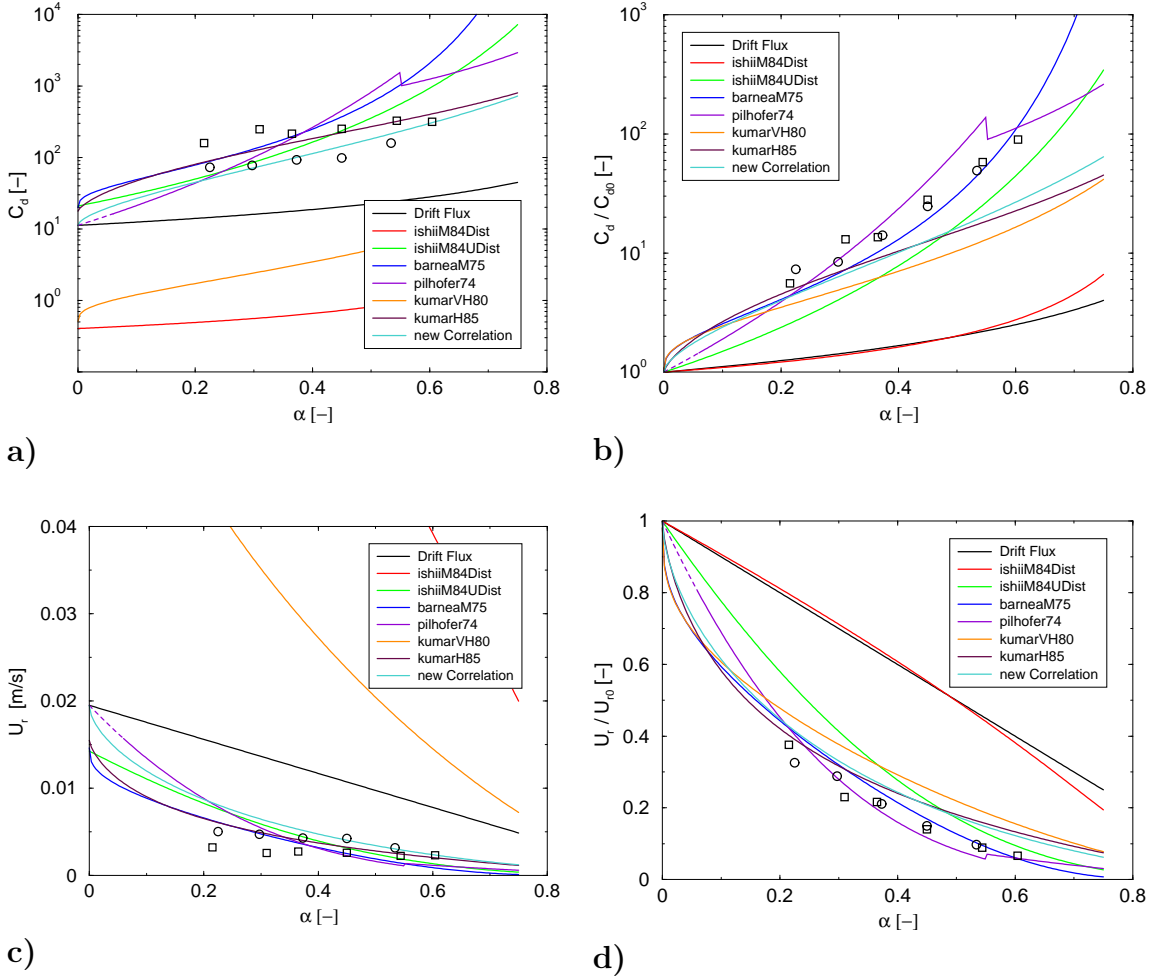


Figure 6.7: Comparison of the predictions of various drag correlations for droplets with data set D1 ($30 < Ar < 91$): **a)** $C_d - \alpha$; **b)** $C_d/C_{d0} - \alpha$; **c)** $U_r - \alpha$; **d)** $U_r/U_{r0} - \alpha$.

The drag coefficient and its normalised value are plotted in Figure 6.7a and b. Similar to the results for particle systems, C_d increases with increasing phase fraction, but it is evident from Figure 6.7a that the differences between the correlations are much larger than for particle systems. The differences extend over the whole range of the phase fraction and even in the single droplet limit they can be as large as an order of magnitude.

The predictions of the model of Ishii and Zuber [168] (distorted regime) and Kumar et al. [209] are particularly low. This can be explained by examination of the expression used in the single droplet limit, which is that of Harmathy [138]. It was derived for large drops and bubbles and the Eötvös number should be larger than 1 for it to be applicable. This is not the case for data set D1 where the Eötvös number

is approximately 0.37 and clearly a different correlation should be used instead to determine the single droplet drag coefficient.

For Kumar et al.'s [209] expression, it is fair to note that the conditions of set P1 are outside its range of applicability, because it has only been validated for $\mathcal{R}e > 7$, where for data set D1 the Reynolds number is lower than 0.7. They addressed this problem in the revised version of their model Kumar and Hartland [208].

From Figure 6.7a and b it is noticeable that Pilhofer's [307] correlation exhibits a jump at $\alpha = 0.55$. This is due to the fact that equation (6.71) for zq^2 is constructed in two discontinuous parts. The problem is less noticeable for higher Archimedes numbers; however, it could lead to serious numerical problems when used in CFD calculations.

The relative velocity and its normalised value are shown in Figure 6.7c and d. Reasonable agreement is obtained for the correlations of Barnea and Mizrahi [16], Kumar and Hartland [208] and Pilhofer [307] as well as that proposed in the present study. The one of Ishii and Zuber [168] (undistorted regime) also gives quite accurate predictions since the small droplets in this data set can be approximated reasonably well by solid spheres.

Data set D2 contains data for methyl iso-butyl ketone droplets in water. The droplet diameter varies between 3.5 and 5.4 mm and the Archimedes number is much higher than for data set D1, lying in the range of 1.1×10^5 and 4.2×10^5 . The Reynolds numbers are between 130 and 600 in the dense and dilute limit, respectively.

The results are given in Figure 6.8. Large differences between the correlations are apparent and most of them yield drag coefficients that are smaller than the measurements. This is especially the case for Ishii and Zuber's [168] model (undistorted regime) which does not seem to be appropriate for this set, probably because of the high Reynolds numbers. Only the models of Ishii and Zuber [168] (distorted regime), Kumar et al. [209], Pilhofer [307] and the new correlation give reasonable results.

Figure 6.9 shows the comparison for data set D3 relating to benzene droplets rising in water. The droplet diameter is between 5.0 and 9.3 mm and the Archimedes number ranges between 3.5×10^5 and 1.3×10^6 . The corresponding Reynolds numbers are of the order of 1300 for a single droplet and 300 for the dense system. It is noticeable that the expressions of Pilhofer [307] and Kumar et al. [209] as well as the new correlation

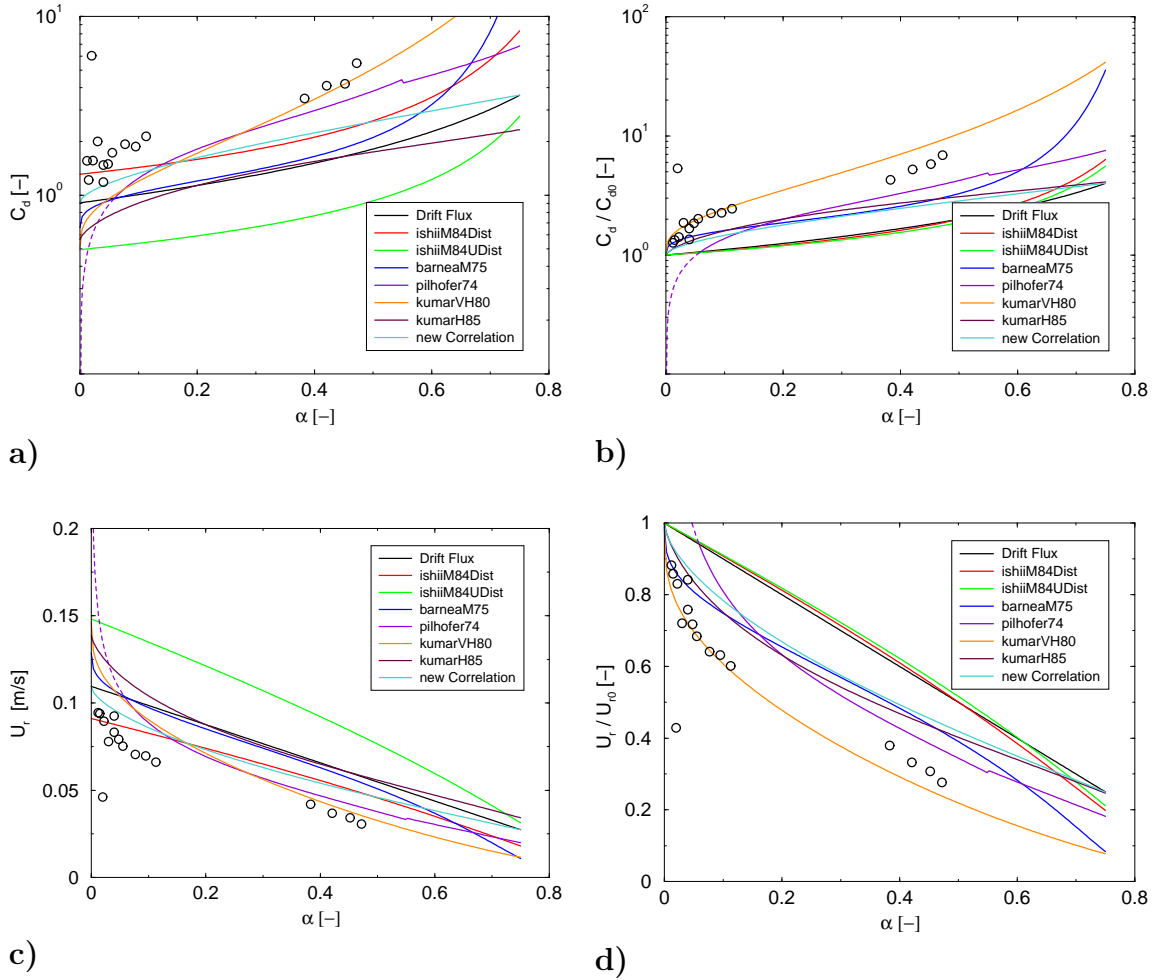


Figure 6.8: Comparison of the predictions of various drag correlations for droplets with data set D2 ($1.1 \times 10^3 < \mathcal{Ar} < 4.2 \times 10^3$): **a)** $C_d - \alpha$; **b)** $C_d/C_{d0} - \alpha$; **c)** $U_r - \alpha$; **d)** $U_r/U_{r0} - \alpha$.

give the best results. However, it is evident from Figure 6.8c and d that the model of Kumar et al. [209] agrees accidentally because it underpredicts the normalised relative velocity and by doing so, gives reasonable predictions for the relative velocity.

Plots showing the results for kerosene droplets rising in water are given in Figure 6.10 (data set D4). Here, the Archimedes number is around 6×10^5 and the corresponding Reynolds numbers are 730 and 130 in the dilute and dense limit, respectively. The relative velocity is plotted in Figure 6.10c. The correlations of Pilhofer [307], Kumar and Hartland [208], Barnea and Mizrahi [16] as well as the new correlation are in good agreement with the experimental results. Barnea and Mizrahi's [16] expression predicts very small rise velocities for $\alpha > 0.6$ which are not supported by the experimental findings.

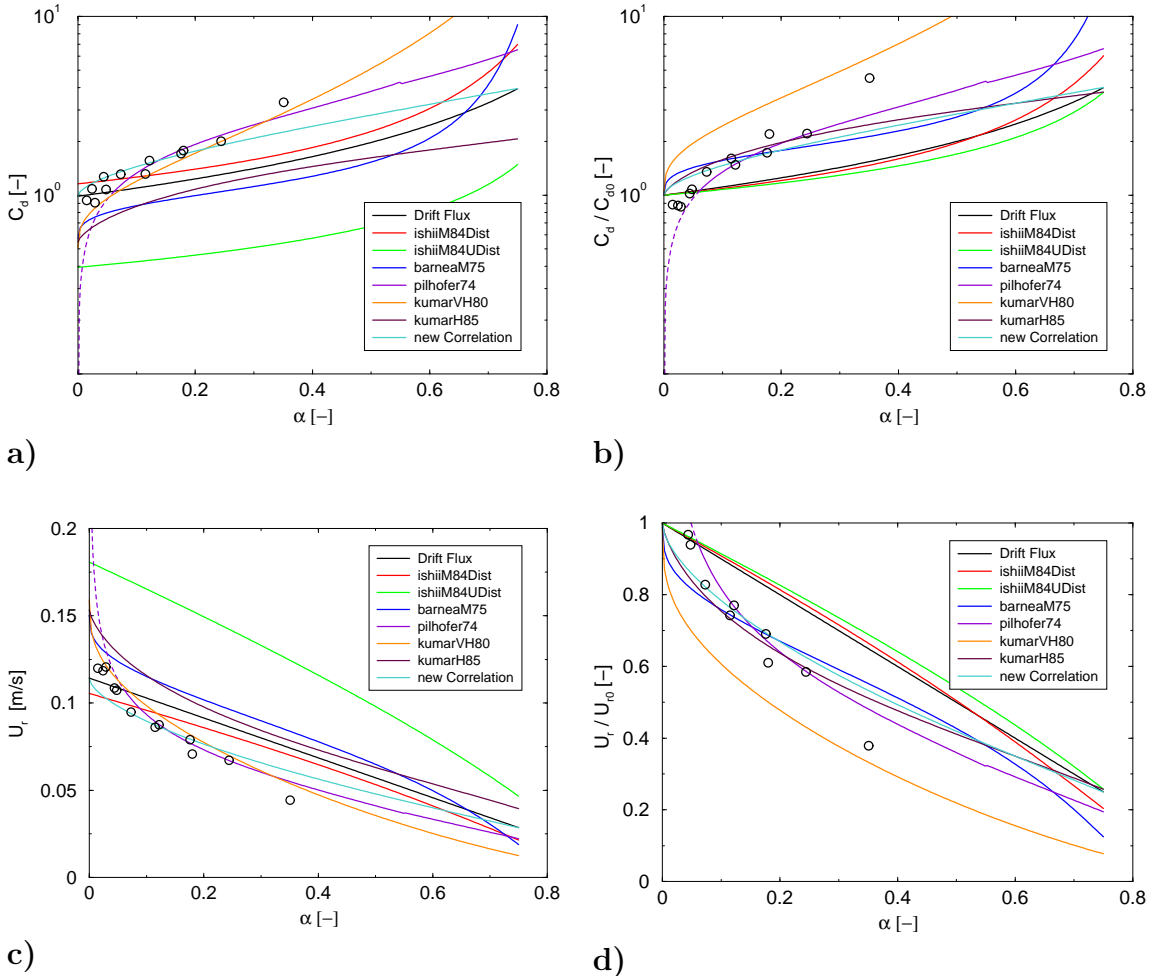


Figure 6.9: Comparison of the predictions of various drag correlations for droplets with data set D3 ($3.5 \times 10^3 < Ar < 1.3 \times 10^4$): **a)** $C_d - \alpha$; **b)** $C_d/C_{d0} - \alpha$; **c)** $U_r - \alpha$; **d)** $U_r/U_{r0} - \alpha$.

The results for data set D5 are depicted in Figure 6.11. The data were collected by Garwin and Smith [111] for benzene droplets rising in water. The Archimedes numbers are between 3.4×10^5 and 1.0×10^6 and the corresponding Reynolds numbers are in the range of 150 to 930. Large discrepancies between the correlations and the experimental data are noticeable for the relative velocity as well as for the drag coefficient. The best fits are with the correlations of Kumar et al. [209], Pilhofer [307] and the new correlation. Again it has to be noted that Kumar et al.'s [209] expression obtains good results only by compensating its errors through its formulation of the single droplet drag law.

It is interesting to note that the correlation of Kumar et al. [209] apparently gives better predictions for the data sets D2, D3 and D5 than its revised version (Kumar

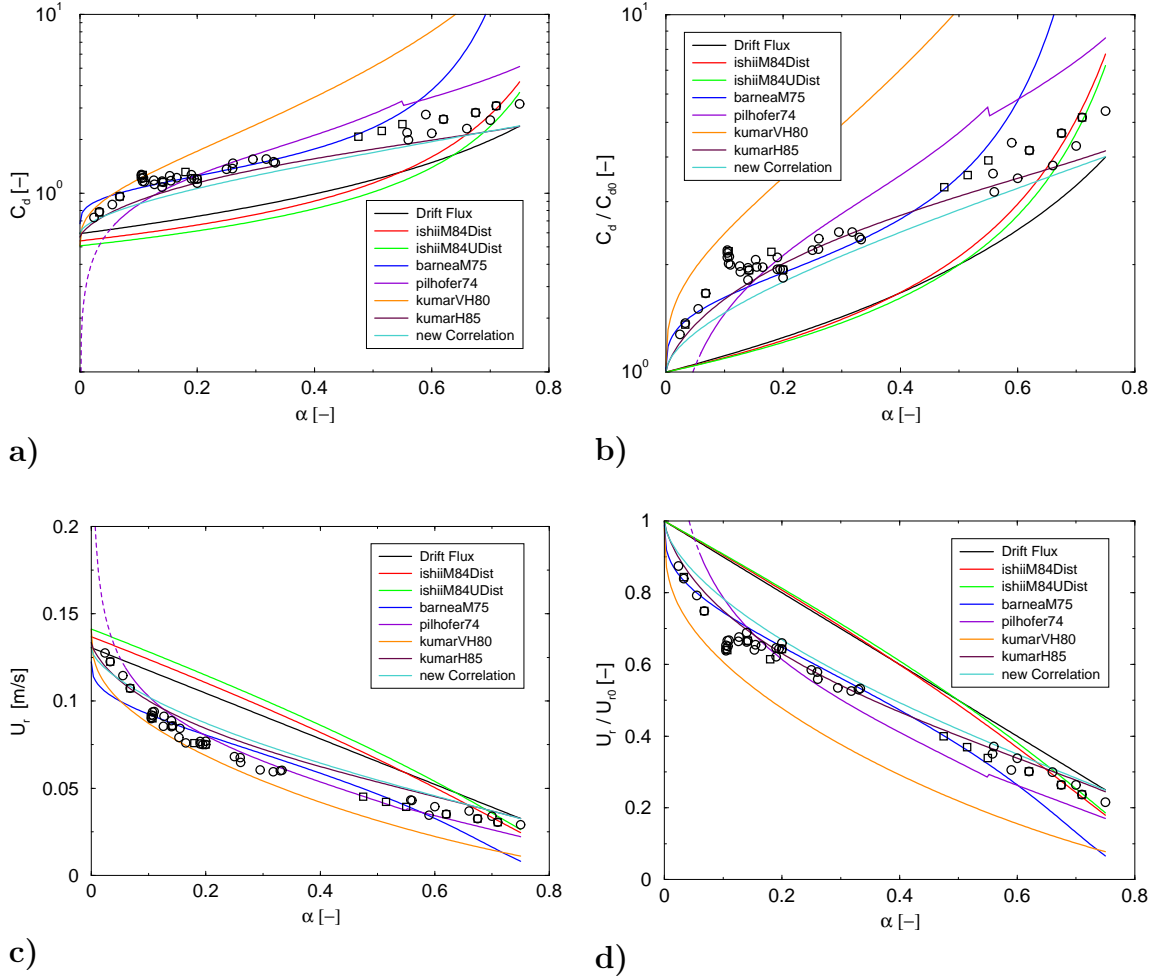


Figure 6.10: Comparison of the predictions of various drag correlations for droplets with data set D4 ($8.6 \times 10^4 < Ar < 3.0 \times 10^5$): **a)** $C_d - \alpha$; **b)** $C_d/C_{d0} - \alpha$; **c)** $U_r - \alpha$; **d)** $U_r/U_{r0} - \alpha$.

and Hartland [208]). Interestingly, Kumar and Hartland [208] derived the coefficients of their revised model from a large collection of experimental results, which does not include the aforementioned data sets. However, they do not give a reason for discarding them.

Some similarities between particle and droplet systems are noticeable from the previous plots. For instance, when comparing the normalised drag coefficient plotted in figures 6.7d and 6.8d, both show that the effect of the phase fraction on the drag coefficient becomes less pronounced with higher Archimedes and Reynolds numbers.

In essence, it is evident from these results that the dynamics of droplets are much more complex than that of particles: firstly the correlations of the various correlations deviate more strongly; and secondly there are larger differences between them and the

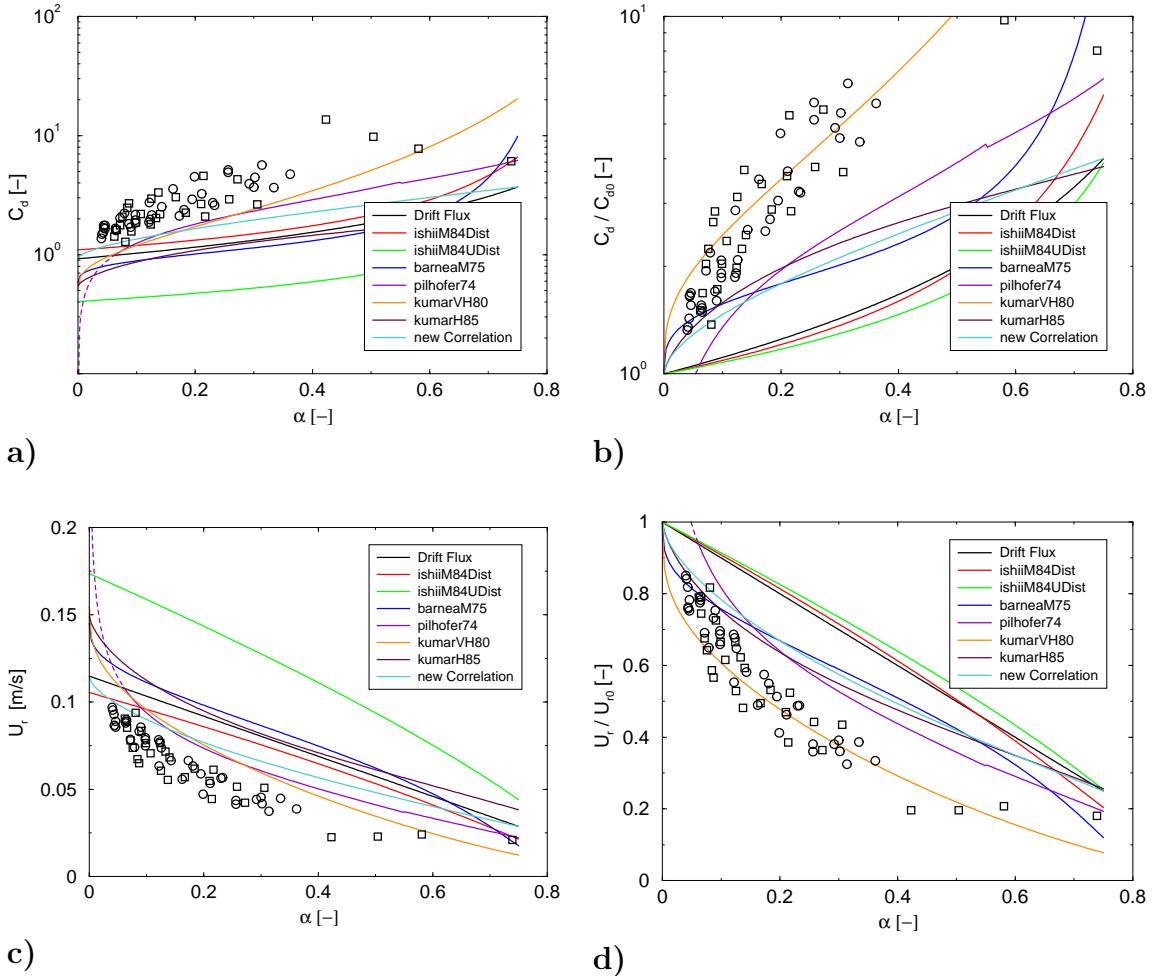


Figure 6.11: Comparison of the predictions of various drag correlations for droplets with data set D5 ($3.4 \times 10^5 < Ar < 1.0 \times 10^6$): **a)** $C_d - \alpha$; **b)** $C_d/C_{d0} - \alpha$; **c)** $U_r - \alpha$; **d)** $U_r/U_{r0} - \alpha$.

experimental results. Overall, the expressions given by Pilhofer [307] and Kumar et al. [209] as well as the new correlation seem to give the best predictions for the terminal velocity of droplets in liquids. As mentioned earlier, Pilhofer's [307] correlation suffers from the deficiency that it cannot be applied to systems at low phase fraction, where the phase fraction is less than 6%. On the other hand, Kumar et al.'s [209] expression is not applicable at low Archimedes and Reynolds numbers. Hence, both correlations lack the generality required for wide use and *it is recommended to use the new correlation*.

6.4.5 Bubbles at High Phase Fraction

Gas-liquid systems are of paramount importance to the chemical process industry and the dynamics of these systems have been researched extensively. However, most of

Data Set	Reference	System	Ar_{min}	Ar_{max}
B1	Liu and Bankoff [249]	air in water	5.4×10^4	1.5×10^5
	Larue de Tournemine [226]	air in water	2.5×10^4	1.5×10^5
B2	Liu and Bankoff [249]	air in water	1.5×10^5	2.5×10^5
	Larue de Tournemine [226]	air in water	1.7×10^5	2.1×10^5
B3	Liu and Bankoff [249]	air in water	2.5×10^5	5.0×10^5
	Larue de Tournemine [226]	air in water	2.9×10^4	4.4×10^5
B4	Liu and Bankoff [249]	air in water	5.0×10^5	1.0×10^6

Table 6.5: Data sets chosen for comparison with drag correlations for bubbles at high phase fraction.

the experimental studies are concerned with bubble columns and it would be difficult to disentangle the various effects, *i.e.* large scale internal circulation, turbulence and phase fraction, on the bubble rise velocity.

In this work, we therefore rely on the data obtained in upward pipe flow. One set was obtained by Liu and Bankoff [249], who measured the phase fraction, bubble diameter, phase velocities and phase r.m.s. velocities in a pipe with a diameter of 38 mm. The second set was recently produced by Larue de Tournemine [226] for bubbles in homogeneous turbulence. The data have been split into five data sets according to the Archimedes number, which is closely related to the bubble size. The resulting conditions for each set are tabulated in Table 6.5.

The data are compared with the following correlations which are described thoroughly in Section 6.3.3: drift flux model (equation (1.12)), Ishii and Zuber [168], Johansen and Boysan [187], Schwarz and Turner [341] as well as the formula developed in the present study which is denoted “new correlation”. Although the expression of Wen and Yu [429] is derived for solid particles, it is included because it has been used by some authors to correlate the rise of systems of bubbles, *e.g.* [27, 293]. Some formulations require an expression for the drag on a single bubble and, as previously, we use the best available to us – in this case the one of Tomiyama et al. [384] (contaminated systems).

Figure 6.12 shows the drag coefficient and the relative velocity as well as their normalised values for data set B1. This is for small bubbles ($1.4 \text{ mm} < d < 2.5 \text{ mm}$) and the Archimedes number is of the order of 2.5×10^4 to 1.5×10^5 . The corresponding

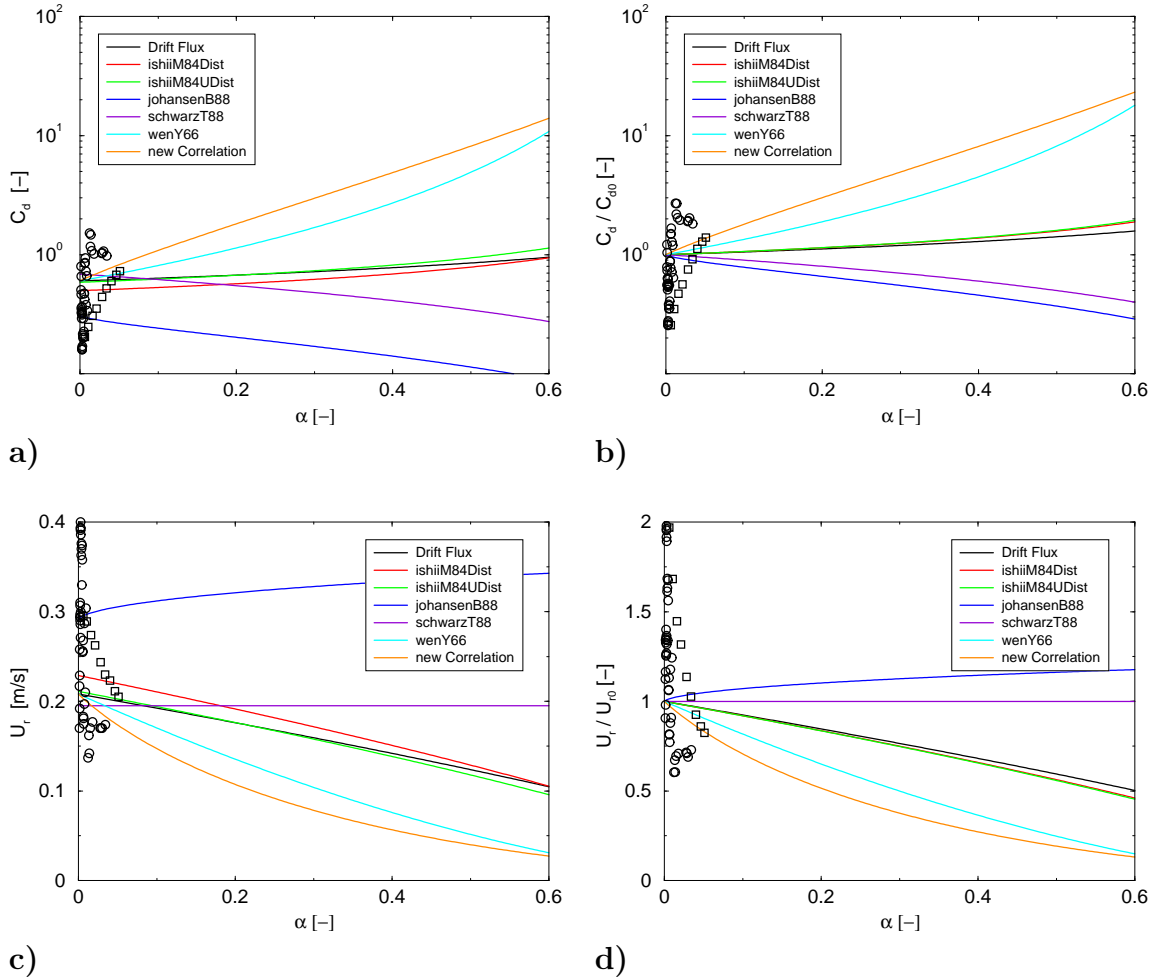


Figure 6.12: Comparison of the predictions of various drag correlations for bubbles with data set B1 ($2.7 \times 10^5 < Ar < 7.8 \times 10^5$). Liu and Bankoff [249] (circles), Larue de Tournemine [226] (squares): **a)** $C_d - \alpha$; **b)** $C_d / C_{d0} - \alpha$; **c)** $U_r - \alpha$; **d)** $U_r / U_{r0} - \alpha$.

Reynolds numbers are between 300 and 820.

The drag coefficient is shown in Figure 6.12a. Large discrepancies between the correlations are noticeable and it is also surprising that they do not even give a consistent trend for the influence of the phase fraction on the drag coefficient. Those of Johansen and Boysan [187] and Schwarz and Turner [341] predict a decrease of the drag coefficient over the whole range of α . The latter assumes a constant slip velocity and the reduction of the drag coefficient is a consequence of this assumption. On the other hand, Johansen and Boysan's [187] model is derived by considering the special case of two particles behind each other, for which experimental results are available. The result is then cast into a relationship for the drag coefficient. As outlined in Section 1.5.4, the drag on a particle in a suspension is always larger than that for a single

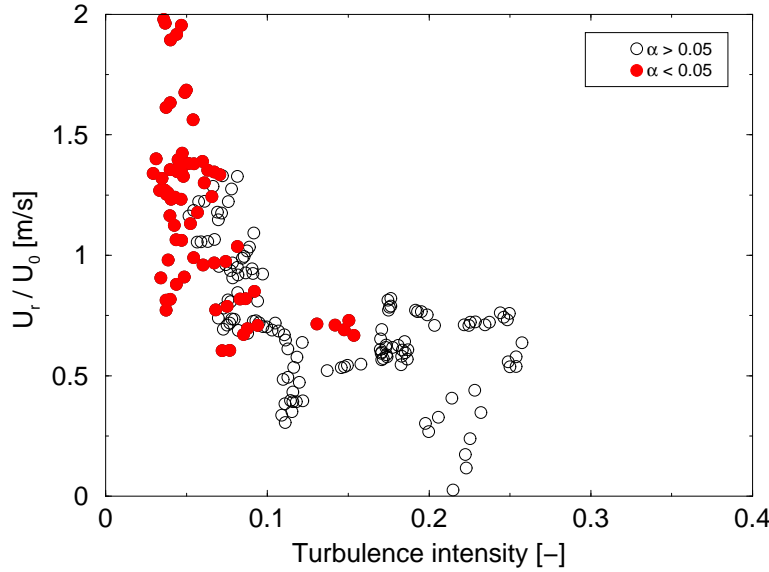


Figure 6.13: Plot of the normalised bubble velocity against turbulence intensity.

particle if α is not too low. This trend is confirmed for bubbles in Figures 6.14, 6.15 and 6.16. Hence, it can be concluded that practices of Johansen and Boysan [187] and Schwarz and Turner [341] are not valid.

Figure 6.12c shows the relative velocity as a function of the phase fraction. A comparison of the correlations reveals that most are in close agreement in the single bubble limit. Only that of Johansen and Boysan predicts larger rise velocities, since it utilises the modified wave analogy model of Clift et al. [56] which is only valid for $Re > 500$.

It is striking that the experimental data exhibit large scatter, especially at low values of the phase fraction. The variations can be quantified with reference to Figure 6.12d. From this plot it is evident that the relative difference can be up to 100% and -50%. This is perhaps not surprising because the rise velocity of single bubbles in the “wobbling” regime is not well understood, as discussed in Section 1.5.3. Furthermore, it has been shown by Eppinger [89] that turbulence has a pronounced effect on the rise velocity of bubbles. He found in his study of bubbles rising in homogeneous turbulence that the rise velocity in the range of 1 to 2 mm diameter decreases by 45% when the turbulence intensity is increased from 3% to 18%. The same trend is evident from Figure 6.13, which shows the normalized bubble velocity plotted against the turbulence intensity for all data points in data sets B1 to B4. The detrimental effect of

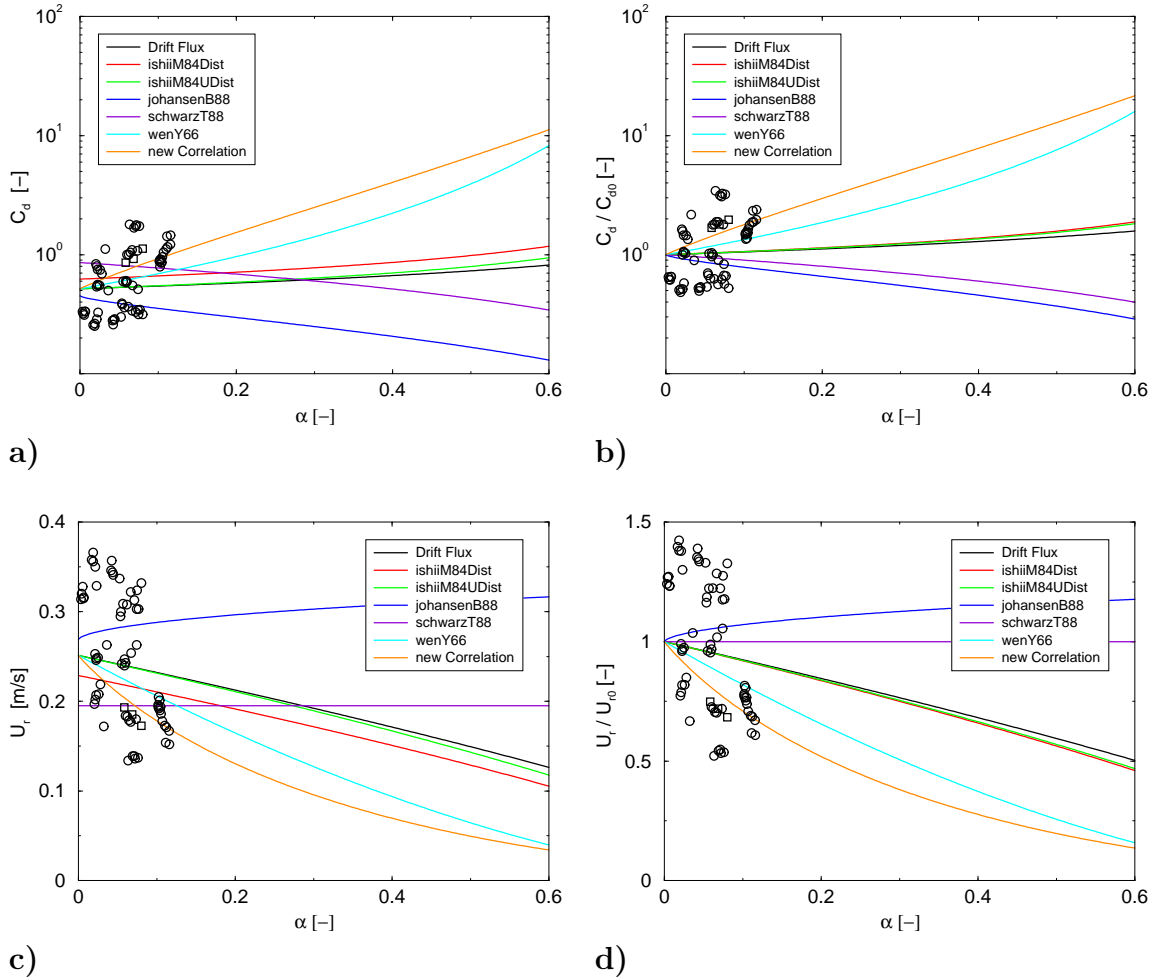


Figure 6.14: Comparison of the predictions of various drag correlations for bubbles with data set B2 ($2.7 \times 10^5 < Ar < 7.8 \times 10^5$). Liu and Bankoff [249] (circles), Larue de Tournemine [226] (squares): **a)** $C_d - \alpha$; **b)** $C_d / C_{d0} - \alpha$; **c)** $U_r - \alpha$; **d)** $U_r / U_{r0} - \alpha$.

the turbulence intensity on the rise velocity is clearly noticeable. However, it has to be noted that bubble size is only approximately constant and the bubble diameter varies in the range 1.8 to 2.8 mm.

The results for data set B2 are given in Figure 6.14. Here, the bubble diameter varies within 2.5 and 2.9 mm, giving Archimedes numbers in the range between 1.5×10^5 and 2.5×10^5 . The corresponding Reynolds numbers are in the range of 350 and 960. It is evident from Figure 6.7a that C_d increases with increasing phase fraction and, correspondingly, the relative velocity shows a decrease. This is in accordance with the results for particles and droplets.

Figures 6.15 and 6.16 show results for data sets B3 and B4. Here, the bubbles have diameters between 3.0 and 3.7 mm and between 3.7 and 4.7 mm, respectively.

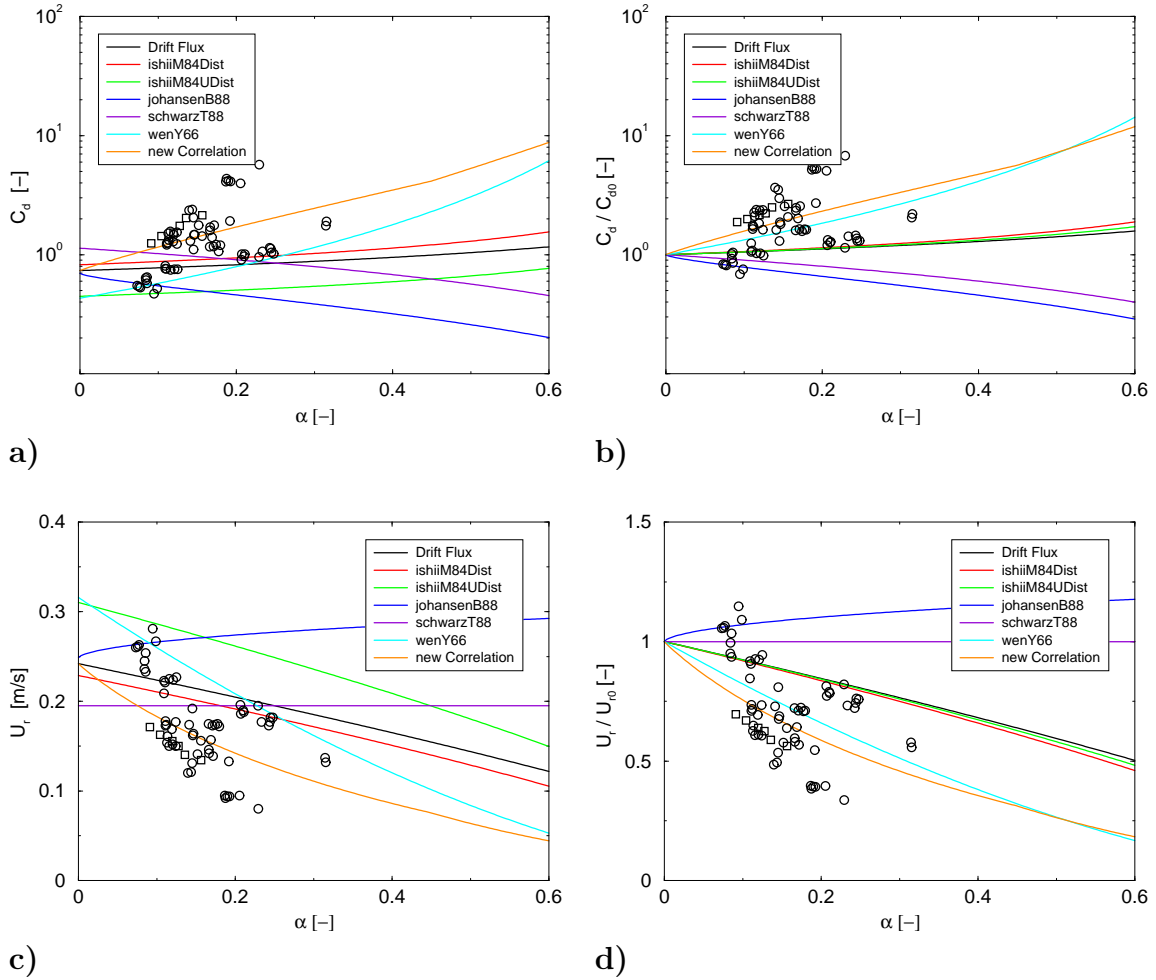


Figure 6.15: Comparison of the predictions of various drag correlations for bubbles with data set B3 ($2.7 \times 10^5 < Ar < 7.8 \times 10^5$). Liu and Bankoff [249] (circles), Larue de Tournemine [226] (squares): **a)** $C_d - \alpha$; **b)** $C_d / C_{d0} - \alpha$; **c)** $U_r - \alpha$; **d)** $U_r / U_{r0} - \alpha$.

The Archimedes numbers are approximately 4×10^5 and 8×10^5 , respectively. Good agreement is obtained for the expression of Wen and Yu [429] as well as the new correlation, whereas the predictions of the drift flux model and the model of Ishii and Zuber [168] (undistorted regime) are less satisfactory.

As mentioned earlier, the relative velocity is a concave function of the phase fraction according to the model of Ishii and Zuber [168]. Consequently, it substantially underpredicts the drag for $\alpha \approx 0.3$ and overestimates the relative velocity by up to 50%. Not surprisingly, large differences between the distorted and the undistorted formulations occur. However, it is interesting to note that the undistorted formulation predicts lower relative velocities and, therefore, agrees better with the experimental data than the distorted formulation. This is surprising, since the Eötvös numbers in

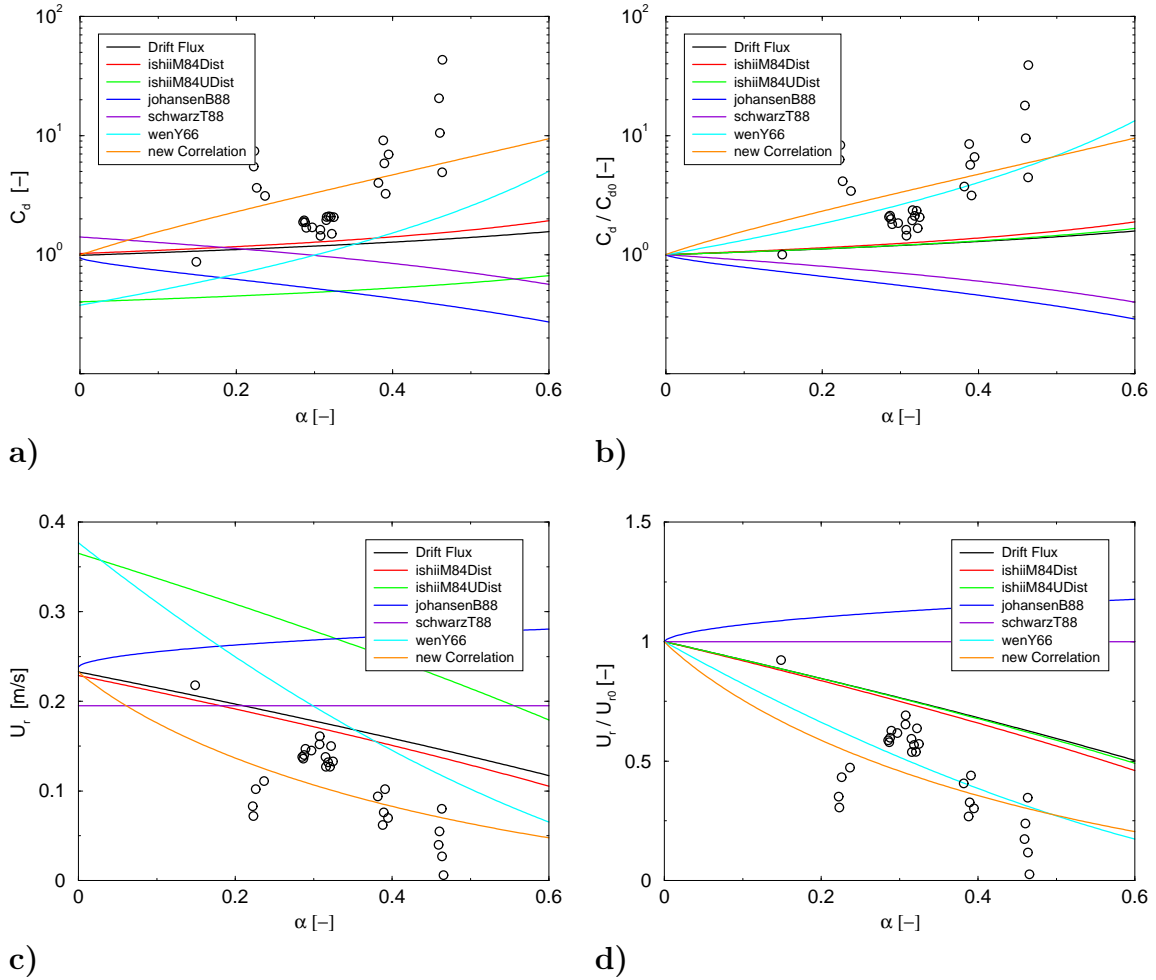


Figure 6.16: Comparison of the predictions of various drag correlations for bubbles with data set B4 ($2.7 \times 10^5 < Ar < 7.8 \times 10^5$). Liu and Bankoff [249] (circles), Larue de Tournemine [226] (squares): **a)** $C_d - \alpha$; **b)** $C_d / C_{d0} - \alpha$; **c)** $U_r - \alpha$; **d)** $U_r / U_{r0} - \alpha$.

this regime are high enough to justify the use of Harmathy's [138] simple drag law.

Unfortunately, the uncertainties in the experimental data, especially related to turbulence effects, make a quantitative assessment very difficult. Nevertheless, *it is evident from the previous results that overall, the correlation developed in the present study seems to give the best predictions for the terminal velocity of bubbles in liquids at high phase fraction*. It is also interesting to note that reasonable predictions can be obtained from the expression put forward by Wen and Yu [429], although it was originally derived for solid particle systems.

It should be mentioned that the expressions presented in this study are for dispersed flows. However, a gas-liquid flow at very high phase fractions ($\alpha > 0.3$) might be "churn turbulent" rather than dispersed, as discussed in Section 1.5.4. In this case,

other correlations must be used.

6.5 Calculations Using the Two-Fluid Methodology

In Chapter 5, two test cases were used to evaluate the different formulations for C_t : the plane mixing layer (at low phase fraction) and the sudden enlargement of a circular pipe (at high phase fraction). The same cases are now employed in order to assess the drag correlations selected in the previous Sections.

Setups

The geometry and setups for the sudden enlargement and the plane mixing layer flows were explained in Sections 3.3.1 and 5.3, respectively. The complete two-fluid methodology was described in detail in Chapter 3 and the version utilised in the present calculations is essentially the same as the one presented in Section 3.3.1. In particular, the standard interface transfer modelling (3.10), including drag, virtual mass and turbulent drag, is employed. The inclusion of the lift term has a detrimental effect on the results for the sudden enlargement flow, but is essential to obtain good predictions for the mixing layer flow, as outlined in Sections 5.2 and 5.3. Hence, the lift term is included in the present calculations for the plane mixing layer, but is neglected in the ones for the sudden enlargement. The issue will be discussed in more detail in Chapter 7. Furthermore, the new expression for C_t is always used. In the following, the drag correlations used in this validation study are outlined.

Even at low phase fractions, there are many uncertainties about the parameters governing the terminal velocity of single bubbles, *e.g.* contamination with surfactants and history effects. Their effects have been discussed in detail in Section 1.5.3, but, up to now, correlations which take them into account have not been presented. However, the majority of measurements for the terminal velocity of single bubbles fall between the existing correlations derived for clean and contaminated systems. These correlations can be regarded as limiting cases and are utilised in this Section for validation. It has been shown in Section 6.4.1 that the more recent correlations give very similar results.

However, overall, the expressions by Tomiyama et al. [384] have been identified as the most suitable for implementation into the two-fluid methodology and are chosen here for the validation work presented in this Section.

At higher phase fractions, several correlations for the calculation of drag in gas-liquid systems at elevated phase fractions have been compared against experimental data in Section 6.4.5. Overall, the correlation of Wen and Yu [429] and that proposed in the present work seem to give the best results and are selected for further testing. In addition, the correlations of Tomiyama et al. [384] for single bubbles in clean and contaminated water are included for reference.

Results for the Plane Mixing Layer

In Figure 5.6, the development of the two-phase flow within the plane mixing layer was discussed giving contour and vector plots of several flow properties. The model used there is very similar to the one used here and the results show no qualitative differences. Hence, the plots are not repeated and the reader may consult Section 5.3 for further details.

Profiles of the measured and calculated gas phase fraction at five cross-sections ($x = -10, 60, 200, 400$ and 600 mm) are shown in Figure 5.7. As mentioned before, the inlet profiles have been prescribed from the measurements and are therefore identical. Around the splitter plate, the aforementioned wall peak is noticeable which is slowly diffused further downstream. The results using the two drag correlations of Tomiyama et al. [384] are very similar. However, the ones for bubbles in contaminated water are slightly larger and this is explained by the lower terminal velocity due to the increased drag on the bubbles. As mentioned before, there are many uncertainties about the influencing factors governing the rise of single bubbles and the correlations used here represent the limiting cases identified in the literature. The differences in the results are small and probably within the uncertainties in the measurements. Therefore, it can be concluded that the formulation of the drag model (within the limiting cases) has only limited effect on the phase fraction distribution in this test case.

Figure 6.18 displays profiles of the axial liquid velocity at five cross-sections within the plane mixing layer. At the first station, the velocity jump between the two inlet

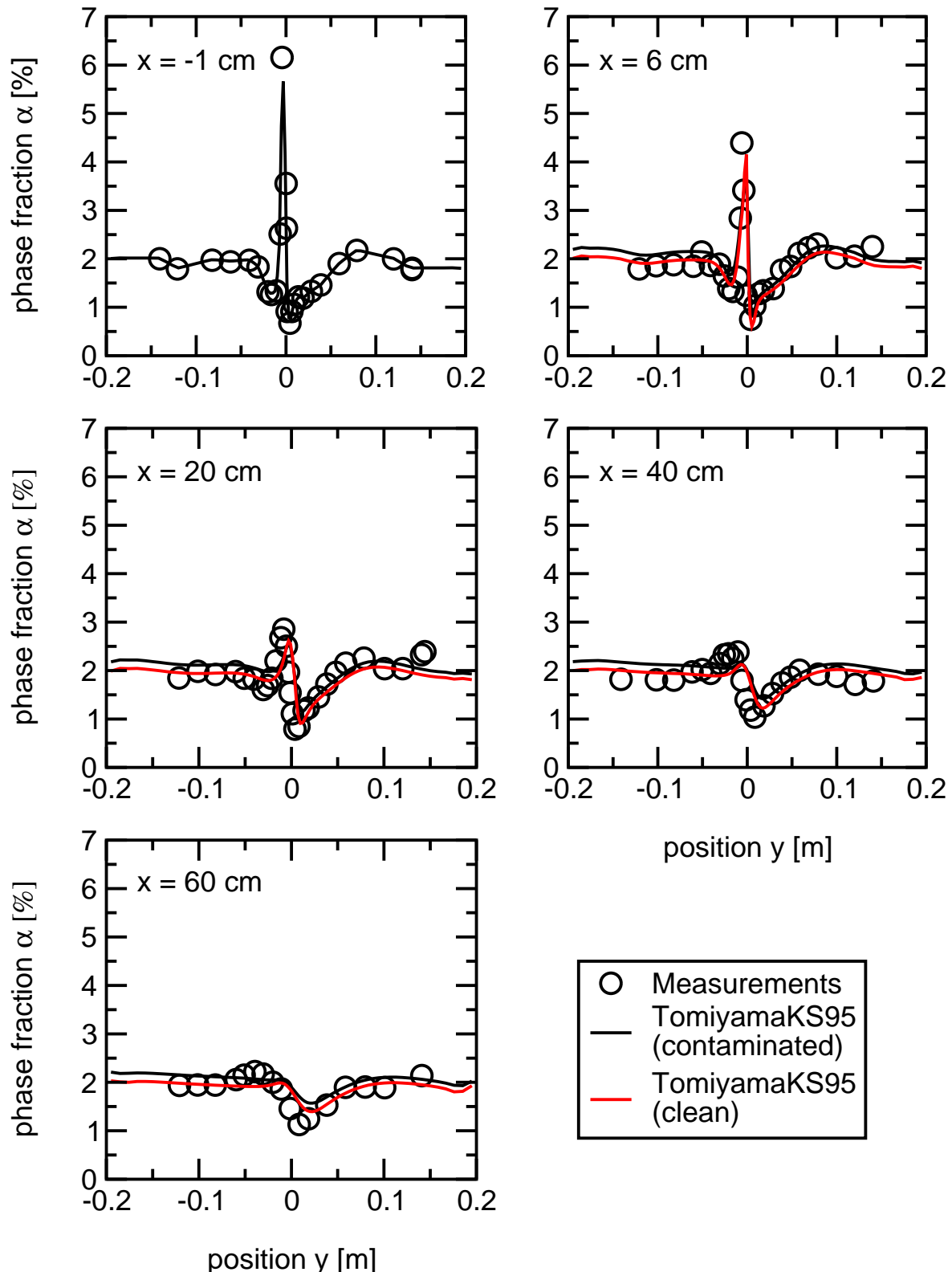


Figure 6.17: Results for the mixing layer test case: predicted phase fraction profiles compared with experimental data (circles). The lines represent predictions with two different drag correlations for bubbles in clean and contaminated water.

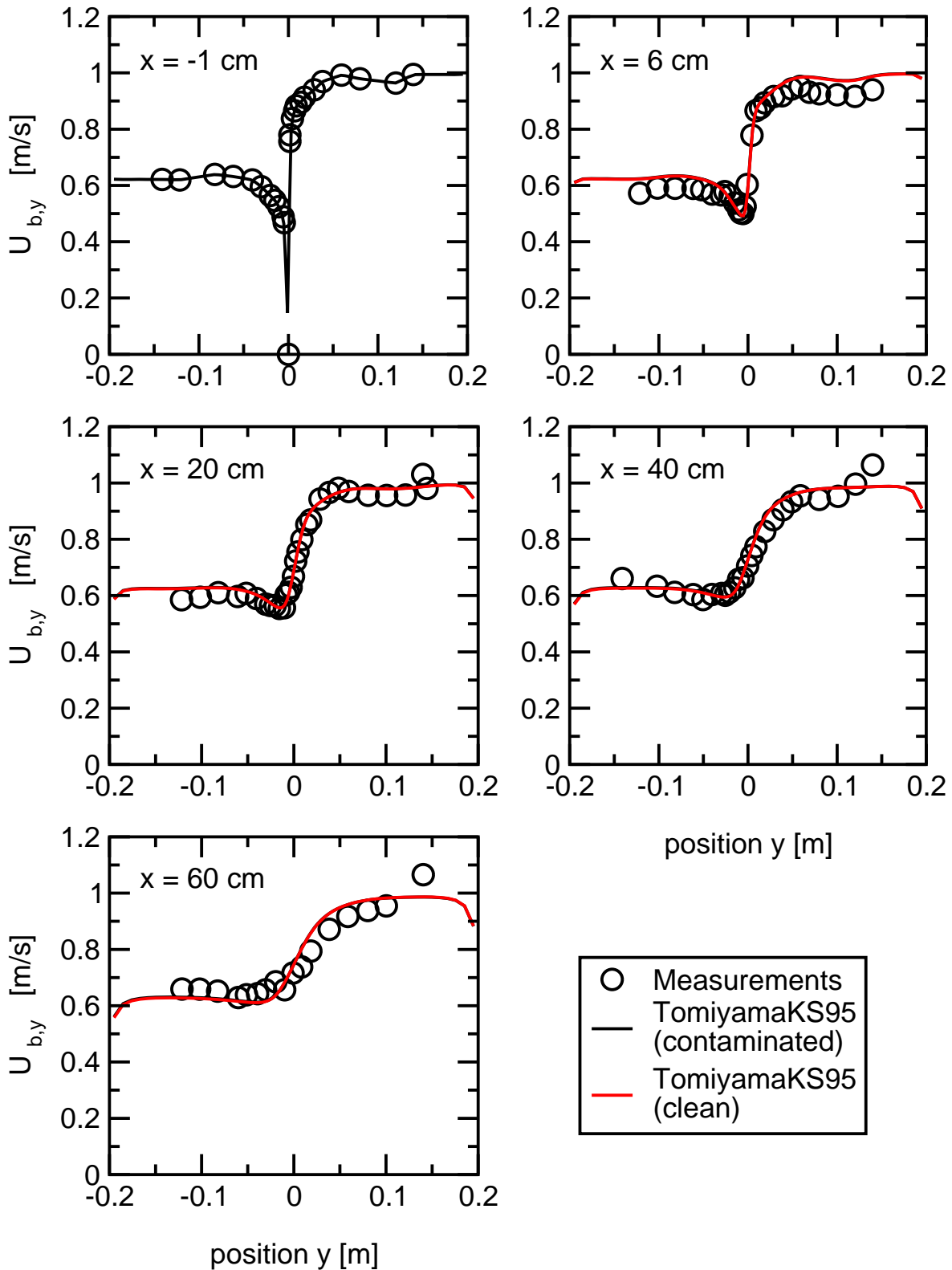


Figure 6.18: Results for the mixing layer test case: predicted profiles of the mean liquid velocity in x -direction compared with experimental data (circles). The lines represent predictions with two different drag correlations for bubbles in clean and contaminated water.

streams as well as the boundary layers on each side of the splitter plate are clearly noticeable. Further downstream, the velocity jump is slowly diffused whereas there is little evidence of the boundary layers at $x = 400$ mm. At every measurement station, the calculations are in good agreement with the experimental data. The predictions for the two drag formulations of Tomiyama are almost identical. This is expected because the dispersed phase has very little influence on the continuous one in this case because the liquid velocity is much larger than the terminal velocity of the bubbles.

Results for the Sudden Enlargement of a Circular Pipe

In Figure 3.3, the development of the two-phase flow behind the sudden enlargement was discussed giving contour and vector plots of several flow properties. The model used there is very similar to the one used here and the results show no qualitative differences. Hence, the plots are not repeated and the reader may consult Section 3.3.1 for further details.

Profiles of the axial liquid velocity at five cross-sections at $x = 70, 130, 180, 250$ and 320 mm downstream of the sudden enlargement are shown in Figure 6.19. The agreement between the calculations and the measurements is excellent at stations close to the enlargement, but the discrepancies increase towards the outlet, *e.g.* the centreline velocity is overpredicted by 31% at the last station. This has to be attributed to deficiencies in the turbulence modelling. Finally, differences between the results for different drag correlations are not noticeable.

The results for the gas phase fraction field are given in Figure 6.20. They agree well with the measurements at stations close to the inlet, but the discrepancies increase towards the outlet. In particular, all correlations overpredict the accumulation of bubbles shortly behind the recirculation zone at $x = 130$ mm and underpredict the development towards fully developed pipe flow. The latter, is apparent from the α value on the centreline. For $x > 130$ mm, the predicted level diminishes whereas the measurements show an earlier replenishment. These deficiencies are somewhat surprising since the liquid velocities are predicted well and at present cannot be explained, but it is possible that the deficiency lies in the lift coefficient correlation. This will be investigated further in Chapter 7.

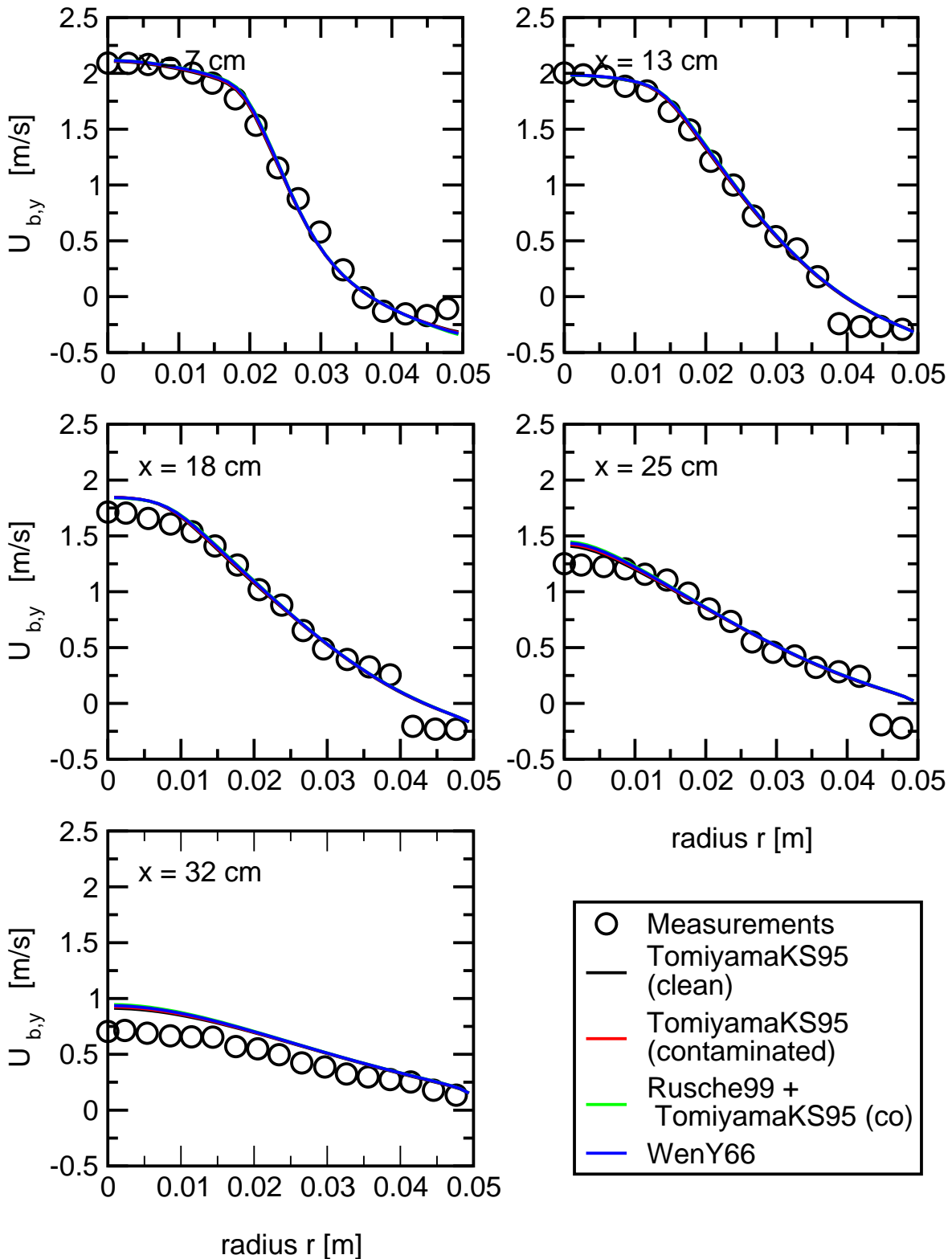


Figure 6.19: Results for the sudden enlargement test case: predicted profiles of the mean axial liquid velocity compared with experimental data (circles). The lines represent predictions with four different drag correlations for bubbles in water at high phase fractions.

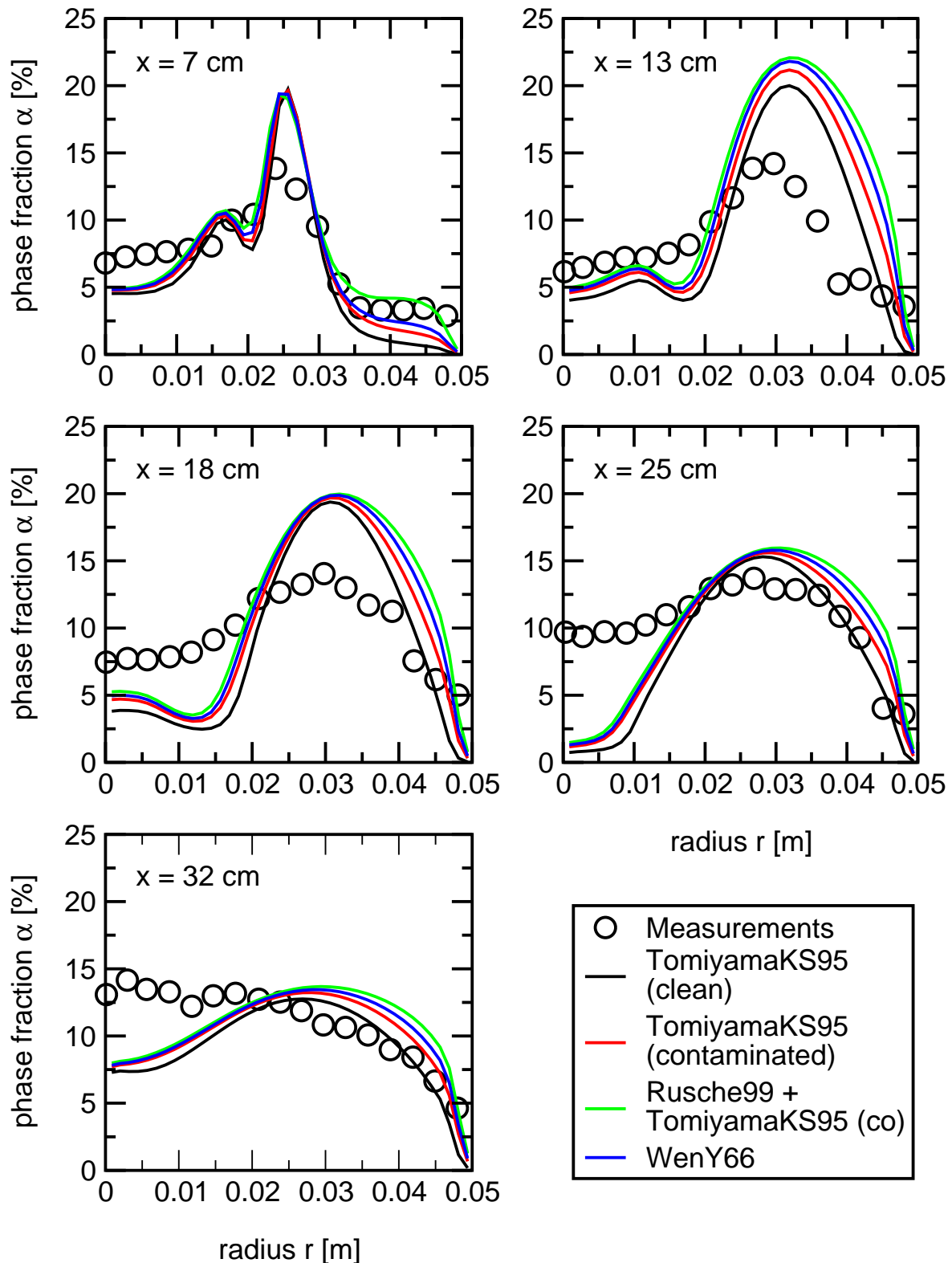


Figure 6.20: Results for the sudden enlargement test case: predicted phase fraction profiles compared with experimental data (circles). The four lines represent predictions with different drag correlations for bubbles in water at high phase fractions.

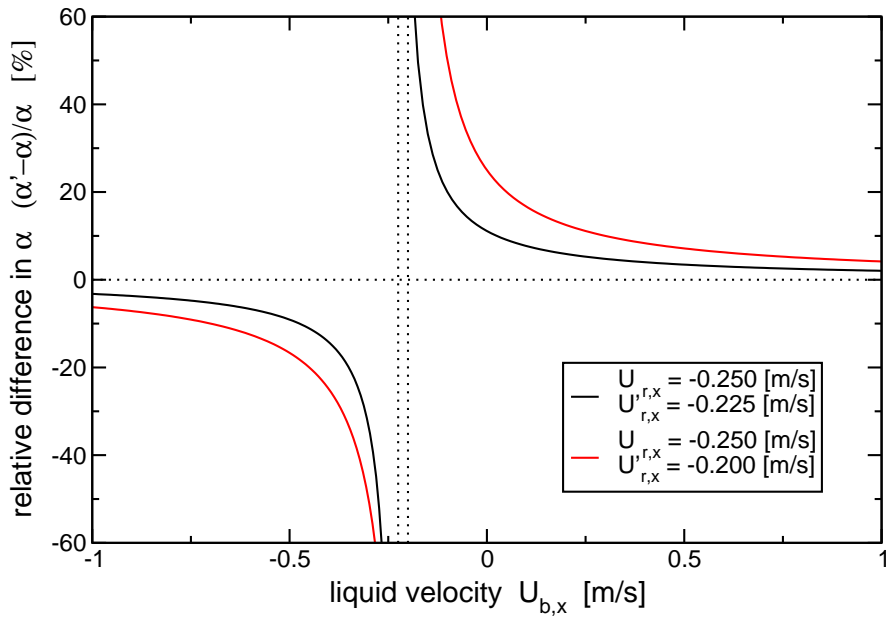


Figure 6.21: Relative difference in α calculated from equation (6.82) as a function of the liquid velocity $U_{b,x}$.

The different drag formulations give similar results. The largest variations occur towards the pipe wall, *i.e.* on the r.h.s., over the whole length of the pipe. This is interesting because the phase fraction is relatively low in this region and one would expect very little difference between the correlations for low and high phase fractions. However, appreciable differences are noticeable in this region and they can be explained by the back-flow within the recirculation zone. Consider the gas flux in axial direction through a control volume which is given by:

$$\dot{V}_a = \alpha A U_{a,x} \quad (6.81)$$

where A is the area of a normal cross-section of the control volume.

Assuming that the gas flux through the control volume as well as the liquid velocity, as shown in Figure 6.19, remain constant when the relative velocity changes, *i.e.* the a different drag correlation is used. With these assumptions, it is easily shown that the relative difference in α in the control volume, *i.e.* $\frac{\alpha' - \alpha}{\alpha}$, changes according to:

$$\frac{\alpha' - \alpha}{\alpha} = \frac{U_{b,x} + U_{r,x}}{U_{b,x} + U'_{r,x}} - 1 \quad (6.82)$$

where the primed quantities denote values after changing the drag correlation.

Equation (6.82) is plotted as a function of the liquid velocity $U_{b,x}$ in Figure 6.21. The black and red line are calculated for reductions of the relative velocity from 0.25

m/s to 0.225 m/s and 0.20 m/s, respectively. These reductions are characteristic if the influence of the phase fraction on the drag coefficient is taken into account, as shown in Figure 6.12c. It is apparent from the plot that the phase fraction in the control volume changes only slightly for extreme values of the liquid velocity. However, the phase fraction changes rapidly if the liquid and relative velocities are similar. This is often referred to as the flood point [273, 308]. In the recirculation zone, areas with appreciable back-flow exist. Hence, the predicted phase fraction is more sensitive to changes of the drag formulation in this region.

6.6 Closure

This Chapter reviewed, formulated and selected correlations to determine the drag force in dispersed two-phase systems at high concentrations of the dispersed phase. First, it presented a comprehensive literature review of the state-of-the art in drag modelling for particles, droplets and bubbles at low and elevated phase fractions. Next, a new correlation at high phase fractions were put forward. The models were then compared against each other as well as experimental data from the literature.

In the case of drag correlations for solid particles at high phase fractions it can be concluded that several give reliable results. Overall, the model by Garside and Al-Dibou [110] meets the requirements in terms of accuracy and generality best. The new correlation proposed in the present study requires some refinement at low Archimedes/Reynolds numbers.

When examining the experimental data and correlations for liquid-liquid and gas-liquid systems, it becomes evident that the dynamics of fluid particles is not as well understood as that of solid particle systems. This is apparent from the deviation between the various correlations as well as the large differences between them and the experimental data. It should also be noted that currently no accurate and reliable model for the drag on single droplets exists. This issue needs to be addressed by future research. Nevertheless, some of the models for elevated phase fractions were able to give reasonable predictions, although some of them lacked generality. It is therefore recommended to use the new correlation.

A large number of models for the drag on single bubbles in an infinite domain have been published. Unfortunately, the effects of surfactant concentration, turbulence and history of the bubble are not well understood. These uncertainties make a quantitative assessment of the individual parameter effects very difficult and limit the quality of the predictions at elevated phase fractions. This should be addressed in future research effort. Nevertheless, it is evident from the results that overall, the new correlation gives the best predictions for the terminal velocity of bubble swarms. It is also interesting to note that reasonable predictions can be obtained from the model put forward by Wen and Yu [429], although it was originally derived for solid particle systems.

Finally, the most promising models were implemented in the two-fluid methodology and validated for two gas-liquid test cases, *i.e.* the plane mixing layer and the sudden enlargement of a circular pipe. In both test cases the influence of the exact drag formulation on the liquid velocity profiles was negligible. However, differences were noticeable in the phase fraction profiles. These were more pronounced in the sudden enlargement test case. Here, the influence of the drag formulation is exaggerated by the back-flow generated behind the enlargement.

In essence, it can be concluded that the exact drag formulation does not have a big effect on the predictions obtained for the two test cases investigated here. In the case of the plane mixing layer, the already excellent predictions did not change. On the other hand, the discrepancies found for the sudden enlargement test case cannot be explained by the influence of the phase fraction on the drag coefficient and a remedy has to be sought elsewhere.

Chapter 7

Lift Modelling

In the modelling of dispersed two-phase flow, closure models to represent the interphase momentum transfer are needed. These are based on the determination of the forces (drag, lift and virtual mass) on a single DPE and are usually in the form of simple expressions obtained either empirically or from simple analysis.

The objective of this Chapter is to provide correlations for the lift force in dispersed two-phase systems. These are intended for the two-fluid methodology presented in Chapter 3, but the same models can be used in other CFD methodologies for the prediction of the dynamics of two-phase flows, *e.g.* the discrete DPE model outlined in Section 1.2.2.

In the introduction to this thesis, several causes for lateral forces on a DPE have been identified (see Section 1.5.5) and some results for bubbles were stated. In this Chapter, the literature related to the modelling of the lateral forces due to the shear of the fluid, wake phenomena and deformation is reviewed more thoroughly and the equations for several models are quoted. These models are of theoretical as well as empirical nature and cover particles as well as bubbles. Specific models for droplets are not reported in the literature.

Very little is known about the influence of the phase fraction on the lift coefficient. The only correlation reported was that by Beyerlein et al. [31] who based it on their own experiments of bubbly air-water flow in a vertical pipe. Their data are utilised here to derive a new, modified correlation which is then assessed using the sudden enlargement and plane mixing layer test cases.

The most promising models are then implemented in the two-fluid methodology and validated for two test cases: the plane mixing layer (at low phase fraction) and the sudden enlargement of a circular pipe (at high phase fraction), as described in the previous chapter. Finally, DNS of an air-water bubble in linear shear flow is carried out to enhance the understanding of the lateral motion of bubbles in this type of flow.

7.1 Definitions

Several expressions have been used to define a dimensionless lift coefficient for a single DPE in an infinite medium. In Section 1.5.5, the one by Auton [10, 9] is given. It reads:

$$C_{l\omega} = \frac{F_l}{\rho_c V |\mathbf{U}_r \times (\nabla \times \mathbf{U}_c)|} \quad (1.15)$$

With this definition, the lift coefficient is a constant ($C_{l\omega} = 0.5$) for the case of a spherical bubble placed in a weak shear flow of an inviscid fluid.

For DPEs in a low Reynolds number flow, a slightly different expression has been proposed by Magnaudet [260]:

$$C_{l\nabla} = \frac{F_l}{\rho_c V |\mathbf{U}_r \cdot (\nabla \mathbf{U}_c)|} \quad (7.1)$$

Note that equations 1.15 and 7.1 lead to identical results for the case of linear shear.

Lateral forces on DPEs are not necessarily caused by shear within the surrounding fluid. Other causes include wake-effects as well as rotation and deformation of the DPE. In these cases, the shear within the fluid might be zero and the expressions stated above are not suitable. Instead, the lift coefficient should be defined by dividing the lift force by the relative dynamic pressure force, so that:

$$C_{lp} = \frac{F_l}{\frac{1}{2} \rho_c A U_r^2} \quad (7.2)$$

The lift force on a DPE is primarily governed by the Reynolds number \mathcal{Re} and the dimensionless shear rate \mathcal{Sr} . In the case of fluid particles, the Eötvös \mathcal{Eo} and Morton \mathcal{Mo} numbers are also important. The definitions of these dimensionless groups have been given in Section 1.5.3 and Section 1.5.5 and are repeated here for convenience:

$$\mathcal{Re} = \frac{\rho_c U_r d}{\mu_c} = \frac{\text{Inertial forces}}{\text{Viscous forces}} \quad (1.5)$$

$$\mathcal{S}_r = \frac{|\nabla \mathbf{U}_c|d}{U_r} \quad (1.16)$$

$$\mathcal{E}_O = \frac{g_{\text{eff}} |\Delta\rho| d^2}{\sigma} = \frac{\text{Gravity}}{\text{Surface Tension}} \quad (1.6)$$

$$\mathcal{M}_O = \frac{g_{\text{eff}} \mu_c^4 |\Delta\rho|}{\rho_c^2 \sigma^3} = \text{Material Group} \quad (1.7)$$

In the definitions given above, μ_c and ρ_c are the dynamic viscosity and density of the continuous phase, respectively. σ is the surface tension and $\Delta\rho$ stands for the density difference between the continuous and dispersed phases, *i.e.* $\Delta\rho = \rho_d - \rho_c$. g_{eff} denotes the magnitude of the effective acceleration given by $g_{\text{eff}} = |\mathbf{g}_{\text{eff}}| = |\mathbf{g} - D\mathbf{U}_c/Dt|$ where $\frac{D\mathbf{U}_c}{Dt}$ is the substantive derivative defined in equation (3.8). F_l and U_r are the magnitudes of the lift force \mathbf{F}_l and the relative velocity \mathbf{U}_r vectors, respectively. The latter is defined as $\mathbf{U}_r = \mathbf{U}_c - \mathbf{U}_d$. A stands for the projected area normal to \mathbf{U}_r , which, for practical reasons outlined in Section 1.5.3, is usually calculated from $A = \pi \frac{d^2}{4}$ where d is the nominal diameter, *i.e.* the diameter of a sphere having the same volume V as the DPE. Hence, the influences of the shape, deformation or orientation on the projected area are neglected.

7.2 Models for Single DPEs

Recent reviews of efforts to model lift on single particles can be found in Moraga et al. [280] for particles as well as Legendre and Magnaudet [237] and Magnaudet and Eames [261] for bubbles. Jakobsen et al. [178, 177] reviewed several models for the lateral migration of particles and bubbles in order to improve the predictions of vertical bubble driven flows, especially bubble columns.

7.2.1 Analytical Results

Analytical solutions for the linear shear flow around bubbles and particles are available in the low Reynolds number and inviscid flow regime. Investigations at finite Reynolds numbers are much more difficult and still in their infancy. The extensive literature available on particles moving in inhomogeneous flows under low Reynolds number conditions has been reviewed by Leal [232].

It is long known that no shear-induced lift force can appear if inertia is neglected, *i.e.* creeping flow [40]. Therefore, the lift force is clearly an effect associated with inertia. Combining several refined techniques with matched asymptotic expansions, Saffman [335] succeeded in obtaining the following expression for the lift force on a small particle in uniform shear:

$$C_{l\nabla} = \frac{3.08}{\sqrt{\mathcal{R}e\mathcal{S}r}} - \frac{33}{32} \quad (7.3)$$

This can be reformulated into an expression for C_{lp} :

$$C_{lp} = 4.11 \sqrt{\frac{\mathcal{S}r}{\mathcal{R}e}} - \frac{11}{8} \mathcal{S}r \quad (7.4)$$

for $\mathcal{R}e \ll \sqrt{\mathcal{R}e\mathcal{S}r} \ll 1$. The product $\mathcal{R}e\mathcal{S}r$ is the shear Reynolds number $\mathcal{R}e_\nabla = \frac{\rho_c |\nabla \mathbf{U}_c| d^2}{\mu_c}$. It should be noted that these conditions, *i.e.* the inequalities given above, have to be satisfied simultaneously. They correspond to very large shear rates in conjunction with to very small relative velocities and are rarely satisfied in real flows. Consequently, McLaughlin [267] extended Saffman's analysis to the more realistic case where $\mathcal{R}e$ and $\sqrt{\mathcal{R}e\mathcal{S}r}$ are independently much smaller than unity. The result can be written as:

$$C_{l\nabla} = \frac{27}{2\pi^2 \sqrt{\mathcal{R}e\mathcal{S}r}} J(\varepsilon) - \frac{33}{32} = \frac{3.08}{\sqrt{\mathcal{R}e\mathcal{S}r}} \frac{J(\varepsilon)}{2.255} - \frac{33}{32} \quad (7.5)$$

or in terms of C_{lp} :

$$C_{lp} = 4.11 \sqrt{\frac{\mathcal{S}r}{\mathcal{R}e}} \frac{J(\varepsilon)}{2.255} - \frac{11}{8} \mathcal{S}r \quad (7.6)$$

where ε denotes the ratio $\sqrt{\mathcal{S}r/\mathcal{R}e}$ and $J(\varepsilon)$ is a monotone function of ε which tends towards zero when $\varepsilon \rightarrow 0$ and to 2.255 when $\varepsilon \rightarrow \infty$, the limit considered by Saffman. McLaughlin [267] tabulated numerical values for $J(\varepsilon)$ which were then fitted by Mei [268] with the following curve:

$$J(\varepsilon) \approx 0.6765 (1 + \tanh(2.5 \log_{10} \varepsilon + 0.478)) (0.667 + \tanh(6\varepsilon - 1.92)) \quad (7.7)$$

where $0.1 < \varepsilon < 20$. There is some confusion due to a missing bracket in the original equation given by Mei [268]. However, of the possible remedies, *i.e.* positions of the missing bracket, the equation above represents the data of McLaughlin [267] best.

It should be noted that the second term on the r.h.s. of equations (7.3), (7.4), (7.5) and (7.6) is a second order correction, which is only effective for large values of $\mathcal{Re}\mathcal{Sr}$, as evident from equation (7.3). This is at odds with the assumptions made in the derivation, *i.e.* $\sqrt{\mathcal{Re}\mathcal{Sr}} \ll 1$, and this term is therefore often neglected. Saffman [335] also gives a third term which accounts for particle rotation.

The case of a clean spherical bubble was first considered by Mei and Klausner [269], but their analysis was incomplete and led them to an erroneous result. The complete analysis was performed by Legendre [234] (see [236]) who showed that in this case the lift force is $(2/3)^2$ times that experienced by a solid sphere, *i.e.* the lift coefficient in equation (7.5) should be multiplied by 0.444. The factor 2/3 corresponds to the ratio of the magnitudes of the vorticities at the surfaces of particles and bubbles. The final equation reads:

$$C_{l\nabla} = \frac{6}{\pi^2 \sqrt{\mathcal{Re}\mathcal{Sr}}} J(\varepsilon) = \frac{0.270}{\sqrt{\mathcal{Re}\mathcal{Sr}}} \frac{J(\varepsilon)}{2.255} \quad (7.8)$$

Equation (7.5) and equation (7.8) imply that $C_{l\nabla}$ decreases very rapidly with \mathcal{Re} , as shown in Figure 1.9.

The determination of the lift force in inviscid shear flow is a difficult problem. The difficulty comes from the fact that, owing to the vortex stretching mechanism, vorticity is distorted during its advection along the particle surface. Therefore solving the Helmholtz equation [19] in order to evaluate the velocity perturbation and then the pressure is not a simple matter. Lighthill [244] derived analytical expressions for the flow generated by a clean spherical bubble in a weak, linear shear flow, for which it could be assumed that the vortical elements are advected passively by the potential flow past the sphere. The distortion of passive vortical elements is clearly related to Darwin's [72] concept of drift and led Lighthill to develop a Lagrangian drift coordinate system to calculate the rotational component of the flow. Important contributions to this problem were given by Lighthill [244] and Cousins [61] until Auton [10, 9] succeeded to obtain the final simple result:

$$C_{l\omega} = 0.5 \quad (7.9)$$

for $\mathcal{Sr} \ll 1$. Later, Naciri [287] extended Auton's [10] result to ellipsoids using a slightly different technique to avoid the calculation of a singular integral.

7.2.2 Computational Results for Particles

Dandy and Dwyer [70] performed the first DNS of a flow around a rigid sphere in a linear shear flow and obtained numerical results for the lift force. $\mathcal{R}e$ ranged between $0.1 < \mathcal{R}e < 100$ and $\mathcal{S}r$ was varied within $0.01 < \mathcal{S}r < 0.8$. Their results were later correlated by Mei [268] using the data within $0.2 < \mathcal{S}r < 0.8$ and $0.1 < \mathcal{R}e < 100$. He gives:

$$\frac{C_{lp}}{C_{lp}^{Sa}} = \begin{cases} \left(1 - 0.2343\sqrt{\mathcal{S}r}\right) \exp(-0.1\mathcal{R}e) + 0.2343\sqrt{\mathcal{S}r} & \text{for } \mathcal{R}e \leq 40 \\ 0.0371\sqrt{\mathcal{S}r\mathcal{R}e} & \text{for } \mathcal{R}e > 40 \end{cases} \quad (7.10)$$

where C_{lp}^{Sa} is given by equation (7.4).

Dandy and Dwyer's [70] predictions displayed some anomalous features for the lowest $\mathcal{R}e$ and lowest $\mathcal{S}r$ considered. Here, McLaughlin's [267] analysis should applies because $\mathcal{R}e \ll 1$ and $\sqrt{\mathcal{R}e\mathcal{S}r} \ll 1$, but Saffman's result does not because $\mathcal{R}e > \sqrt{\mathcal{R}e\mathcal{S}r}$. However, Dandy and Dwyer's [70] results show the opposite behaviour, *i.e.* they agree with Saffman's solution, but differ significantly with McLaughlin's. Later, Legendre and Magnaudet [235] showed that the accuracy of the results of Dandy and Dwyer [70] was compromised by the small size of their computational domain (25 sphere radii). Low Reynolds number flows are dominated by viscous effects and, for the flow around a bluff body, the undisturbed flow field is only recovered far away from the body. If the domain boundaries are placed too close, subtle distortions of the flow field are introduced which have a marked effect on the lift force. This result emphasises the fact that the computation of the lift force is not a trivial matter.

Recently, Cherukat et al. [50] considered the same problem, *i.e.* a rigid sphere in a linear shear flow, at low $\mathcal{R}e$ in the range $0.04 < \mathcal{R}e < 2$ and a wide range of $\mathcal{S}r$ within $0.02 < \mathcal{S}r < 5$. Their results confirm that McLaughlin's [267] approximation apply reasonably well up to $\mathcal{R}e$ of the order of unity. It should be noted that Cherukat et al. also considered rotating spheres.

Komori and Kurose [203, 212, 213] investigated rotating and non-rotating spheres at higher $\mathcal{R}e$ ranging between $1 < \mathcal{R}e < 500$ and with $\mathcal{S}r$ varying within $0.1 < \mathcal{S}r < 0.4$. While the results of Dandy and Dwyer [70] show that C_{lp} tends towards a constant positive value with increasing $\mathcal{R}e$ and a given $\mathcal{S}r$ (see equation (7.10)), those of Komori

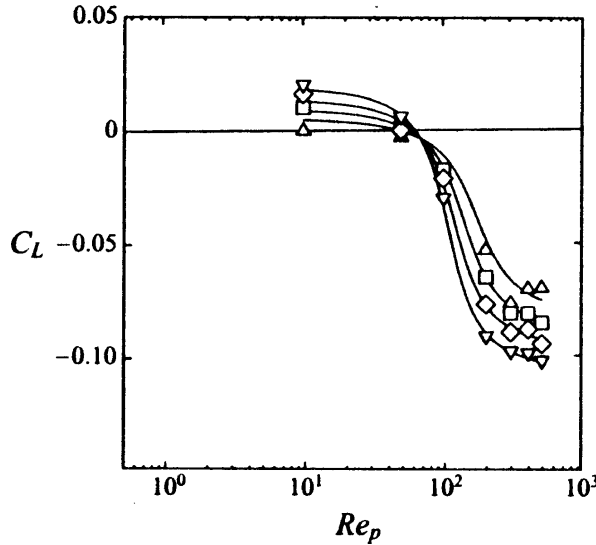


Figure 7.1: Lift coefficient C_{lp} for a sphere in a linear shear flow as a function of the Reynolds number $\mathcal{R}e$. Δ : $Sr = 0.1$; \square : $Sr = 0.2$; \diamond : $Sr = 0.3$; ∇ : $Sr = 0.4$ (from [212]).

and Kurose display a completely different trend: C_{lp} becomes negative for $\mathcal{R}e > 60$ as shown in Figure 7.1. They confirmed this result in an experimental study described in the next Section.

7.2.3 Empirical Correlations for Particles

The first quantitative measurements on particles suspended in shear flow were performed by Eichhorn and Small [85]. In their levitation experiment, the spheres were suspended into a developed Poiseuille flow within an inclined tube. The particle $\mathcal{R}e$ was between $80 < \mathcal{R}e < 247$. However, their technique is limited to moderate Reynolds numbers because an equilibrium position for the particle cannot be established once vortex shedding sets in. They correlated their experimental data in terms of the lift coefficient as a function of $\mathcal{R}e$, Sr and the ratio of the particle and tube diameter and obtained:

$$C_{lp} = 7 \times 10^4 \left(\frac{Sr}{\mathcal{R}e} \frac{d}{D} \right)^2 \quad (7.11)$$

where D stands for the tube diameter. It is evident that their measured lift coefficients were always positive. It has been noted by Eichhorn and Small [85] that another drawback of their technique is the fact that important variables, such as rotation speed of the particle and radial position, are related and cannot be varied independently.

However, it is possible to overcome the problem with eccentrically weighted particles [297].

The first detailed measurements of the lift force on different types of DPEs (solid particles, droplets and bubbles) in linear shear were performed by Kariyasaki [195]. Here, the results for particles are presented, whereas those for fluid particles can be found later in Section 7.2.5. The shear flow was produced in a vertical channel whose side walls consisted of two counter-rotating belts. The continuous fluids were paraffin and glycerine-water solutions. $\mathcal{R}e$ was small ($\mathcal{R}e < 1.4$), but $\mathcal{S}r$ was relatively large ($1.2 < \mathcal{S}r < 28$). They found that their lift coefficient data for particles agreed reasonably well with the expression of Saffman [335] for low values of the shear Reynolds number $\mathcal{R}e_{\nabla} = \mathcal{R}e\mathcal{S}r$ and that of Rubinow and Keller [330] for rotating spheres for large $\mathcal{R}e_{\nabla}$.

Also at low $\mathcal{R}e$, Cherukat et al. [51] measured at the lateral migration velocity of spheres sedimenting in a linear flow field produced in an apparatus in which two rubber timing belts move in opposite directions. The falling particles were followed using two synchronised video cameras positioned such that a sphere passing from the field of view of one camera to the other could migrate a reasonable distance in lateral direction. $\mathcal{R}e$ and $\mathcal{S}r$ varied between $0.20 < \mathcal{R}e < 2.8$ and $0.069 < \mathcal{S}r < 0.48$, respectively. They found that their migration velocities agreed well with McLaughlin's [267] results.

Yamamoto et al. [434, 435] performed pendant as well as tracking experiments on spheres in a square, vertical wind tunnel. The particle $\mathcal{R}e$ and $\mathcal{S}r$ were varied between 4000–36000 and 0.02–0.1, respectively. In the pendant experiment, a rod was used to tether the particle, which was equipped with pressure transducers. This setup avoids the problems associated with particle rotation and repeatability. However, the authors reported that the pendant oscillated due to vortex shedding. The lift force was calculated from the surface pressure distribution as well as the mean inclination of the pendant. Tracking experiments were also carried out using stroboscope photography to verify the results by comparing calculated and recorded trajectories.

In all of their experiments the lift force acted from the higher to the smaller velocity side, *i.e.* producing “negative” lift. They reported that the lift coefficient obtained from the inclination of the pendant scattered broadly and C_{lp} increases as a

function of \mathcal{Sr} . However, the only quantitative result reported from this investigation is that $C_{lp} = -0.02$ for $4000 < \mathcal{Re} < 7000$ and $\mathcal{Sr} = 0.08$. This value of $C_{lp} = -0.02$ was found to give good results when the trajectories of free-falling particles at similar \mathcal{Re} and \mathcal{Sr} were calculated and compared with the measured ones.

The surface pressure distribution was only measured for much larger \mathcal{Re} , namely between 15000–36000. The lift coefficient, obtained by integrating the pressure over the surface of the sphere numerically, was found to vary as:

$$C_{lp} = -\frac{5}{4}\mathcal{Sr} \quad (7.12)$$

This correlation yields a much larger value for C_{lp} than that measured in the pendant experiment. Unfortunately, the authors do not attempt to explain this discrepancy. However, it is likely that this is caused by the uncertainties inherent in the surface pressure measurements and the numerical integration procedure as well as the different parameters used in the different experiments.

In an experimental investigation accompanying their computational study, Kurose and Komori [212] confirmed their predictive result that for high \mathcal{Re} the lift force on a rigid particle acts in the opposite direction to that suggested by the analytical result of Saffman [335]. Their experimental apparatus consisted of a tank filled with a glycerin-water solution in which a linear shear of $Sr \approx 0.013$ was produced by two submerged belts moving in opposite directions. Iron spheres with three different diameters were dropped and their trajectories were recorded using a high speed video system. The particle \mathcal{Re} were 98.8, 167.1 and 276.1 for the three sizes, respectively. Of the 200 spheres dropped of each size, 53.5%, 66% and 76.5%, respectively, migrated towards the lower velocity side, *i.e.* experienced “negative” lift.

Recently, Moraga et al. [280] investigated the lateral force on tethered spheres submerged in a turbulent ($1200 < \mathcal{Re} < 18800$), uniform shear flow ($0.04 < \mathcal{Sr} < 0.2$). Periodic and non-periodic motion of the sphere was observed depending on the flow conditions. The authors adopted a statistical approach to determine the average position of the pendant. Their technique uses two parallel laser beams which are positioned on a traversing table such that they are interrupted by the pendant’s thread. The average position of the pendant can be determined by traversing the laser beams and recording the time sequence of beam interruptions for each position of the beams.

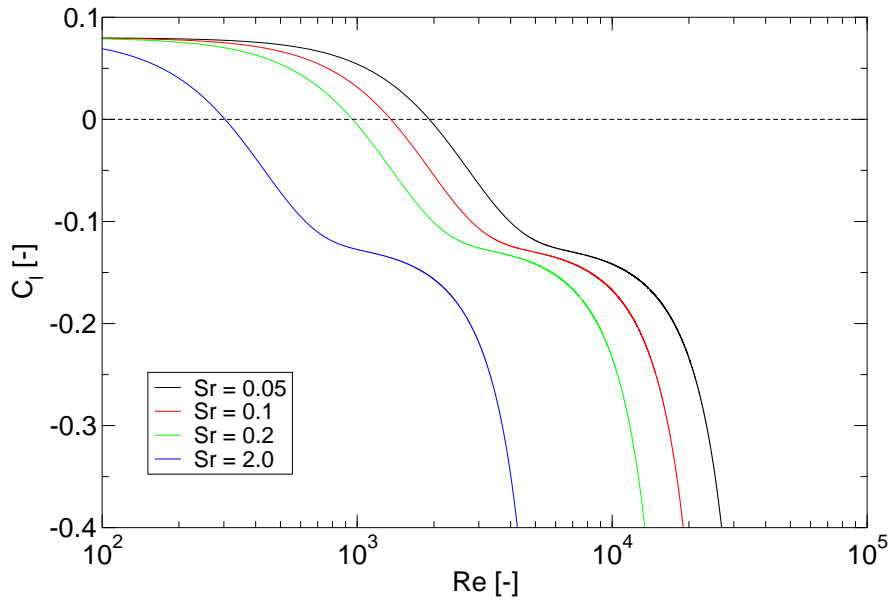


Figure 7.2: Lift coefficient $C_{l\omega}$ calculated from equation (7.13) for a solid sphere in a linear shear flow as a function of the Reynolds number $\mathcal{R}e$ and the dimensionless shear rate $\mathcal{S}r$.

The results of their experiments were found to correlate with the product $\mathcal{R}e^2 \mathcal{S}r$. They give:

$$C_{l\omega} = \left(0.2 \exp \left(-\frac{\mathcal{R}e^2 \mathcal{S}r}{3.6 \times 10^5} \right) - 0.12 \right) \exp \left(\frac{\mathcal{R}e^2 \mathcal{S}r}{3.0 \times 10^7} \right) \quad (7.13)$$

Equation (7.13) is plotted in Figure 7.2 as a function of $\mathcal{R}e$. Note that a sign reversal occurs for $\mathcal{R}e^2 \mathcal{S}r > 18400$. This was explained by assuming that the lateral force on a sphere is the consequence of two forces acting in opposite direction, namely, inviscid and vortex-shedding-induced lateral forces, as explained in Section 1.5.5. The latter are dominant at higher $\mathcal{R}e$ and, therefore, $C_{l\omega}$ becomes negative. It is interesting to note that equation (7.13) yields very large, negative values for large values of the product $\mathcal{R}e^2 \mathcal{S}r$, which seems unphysical.

It is of interest to compare Moraga et al.'s [280] results with those reported earlier. For $\mathcal{R}e = 5500$ and $\mathcal{S}r = 0.08$, Yamamoto et al. [434, 435] gave $C_{lp} = -0.02$, which corresponds to $C_{l\omega} = -0.13$. This compares favourably with Moraga et al.'s [280] correlation, which yields $C_{l\omega} = -0.19$ in the same situation. However, Moraga et al.'s [280] results are at odds with those of Kurose and Komori [212] who did not quantify the lift coefficient, but found that it was clearly negative for $\mathcal{R}e = 276.1$ and $\mathcal{S}r = 0.013$, i.e. $\mathcal{R}e^2 \mathcal{S}r = 991.1$, whereas Moraga et al.'s [280] correlation yields a positive one.

This brief summary of the experimental findings for particles shows that the situation concerning the lift force on a solid sphere is not clear at the present time, except in the low Reynolds number limit for which the asymptotic results of McLaughlin are available and reasonably accurate. At higher $\mathcal{R}e$, there are strong indications that the lift coefficient becomes negative and is dominated by wake rather than inertial effects.

7.2.4 Computational Results for Bubbles

Few experimenters attempted to quantify the lift force on bubbles moving in sheared flows at moderate to high Reynolds numbers due to the difficulties involved. A large part of the present knowledge concerning the alterations of these forces by viscous effects comes from Direct Numerical Simulations (DNS) performed in recent years.

Legendre and Magnaudet [235] used DNS to study the case of a spherical bubble in clean water, *i.e.* a sphere under a shear-free instead of a no-slip surface condition. They used a stationary, body-fitted grid to represent the bubble, *i.e.* deformations of the bubble were not allowed. Of course the assumption of a spherical bubble completely free of surfactants is not valid in most practical situations. However, their results are important in order to examine the range of applicability of the analytical solutions derived by Auton [10, 9] for inviscid flow and by McLaughlin [267] for low $\mathcal{R}e$, as discussed in detail in Section 1.5.5. Legendre and Magnaudet [235] investigated the range $0.01 < \mathcal{R}e < 500$ and $0.01 < \mathcal{S}r < 1$ and give the following curve-fit to their predictions:

$$C_{l\omega} = \sqrt{\left(C_{l\omega}^{low\mathcal{R}e}\right)^2 + \left(C_{l\omega}^{high\mathcal{R}e}\right)^2} \quad (7.14)$$

where $C_{l\omega}$ at low and high $\mathcal{R}e$ are taken as:

$$C_{l\omega}^{low\mathcal{R}e} = \frac{6}{\pi^2 \sqrt{\mathcal{R}e \mathcal{S}r}} J'(\varepsilon) \quad (7.15)$$

$$C_{l\omega}^{high\mathcal{R}e} = \frac{1}{2} \frac{1 + 16\mathcal{R}e^{-1}}{1 + 29\mathcal{R}e^{-1}} \quad (7.16)$$

Equation (7.14) is plotted in Figure 1.9. It should be noted that it corresponds to the result of Auton [10, 9] at large $\mathcal{R}e$. Similarly, equation (7.15) approaches Legendre's

analytical result for low $\mathcal{R}e$ given by equation (7.8), but the tabulated function $J(\varepsilon)$ in the latter is replaced by an analytical expression $J'(\varepsilon) = \frac{J(\infty)=2.255}{(1+0.2\varepsilon^{-2})^{3/2}}$ for $\varepsilon > 0.8$.

As mentioned in Section 1.2.1, the effect of bubble deformation on the lateral force has been investigated numerically by several authors, using different solution procedures [388, 373, 371, 91, 253, 281]. All of this work has been conducted for bubbles in fluids with high liquid viscosities, *i.e.* at high Morton numbers ($\log(\mathcal{M}o) > -5$), in order to keep $\mathcal{R}e$ small ($\mathcal{R}e < 50$). In this way, the computational resources needed are not too large, as compared with high $\mathcal{R}e$. Numerical difficulties also arise when the surface tension force is high, as explained in Section 1.5.1. Surface tension is important when the bubbles are nearly spherical or ellipsoidal which is the case for diameters smaller than approximately 5 mm.

In a series of investigations, Taeibi-Rahni *et al.* [372, 371, 253] simulated two-dimensional single bubbles in a free shear layer using a front-tracking technique. The time and length scales of the bubble and the shear layer were comparable, therefore, strong interactions between them were observed. The hydrodynamic forces were inferred from the trajectory using the equation of motion given by Auton *et al.* [11]. The surface tension coefficient was parametrically varied in order to explore the effect of the bubble's deformation on its dynamics. Concerning the lift force, they found that its time-averaged value is close to Auton's value of $C_{lw} = 0.5$ if the bubble shape is close to spherical. However, large transient fluctuations were observed. For smaller surface tension, the deformation of the bubble resulted in negative lift.

Figure 7.3 shows the predicted trajectories and the evolutions of the shape for bubbles at different $\mathcal{E}o$ and fixed $\mathcal{M}o$ rising in linear shear flows of various strengths. It is apparent from Figure 7.3a that the direction of the lateral force alters when the shear rate is increased. On the other hand, when $\mathcal{E}o$ is increased, very deformed airfoil-shaped bubbles result which always migrate towards the centre of the duct, as shown in Figure 7.3b. The explanation is that the vortex behind a deformed bubble becomes slanted and, consequently, the bubble migrates towards the pipe centre. This implies another kind of lift force, which is caused by the interaction between the bubble wake and the external shear field. Although these results were for hypothetical two-dimensional bubbles, similar three-dimensional calculations are reported by [373,

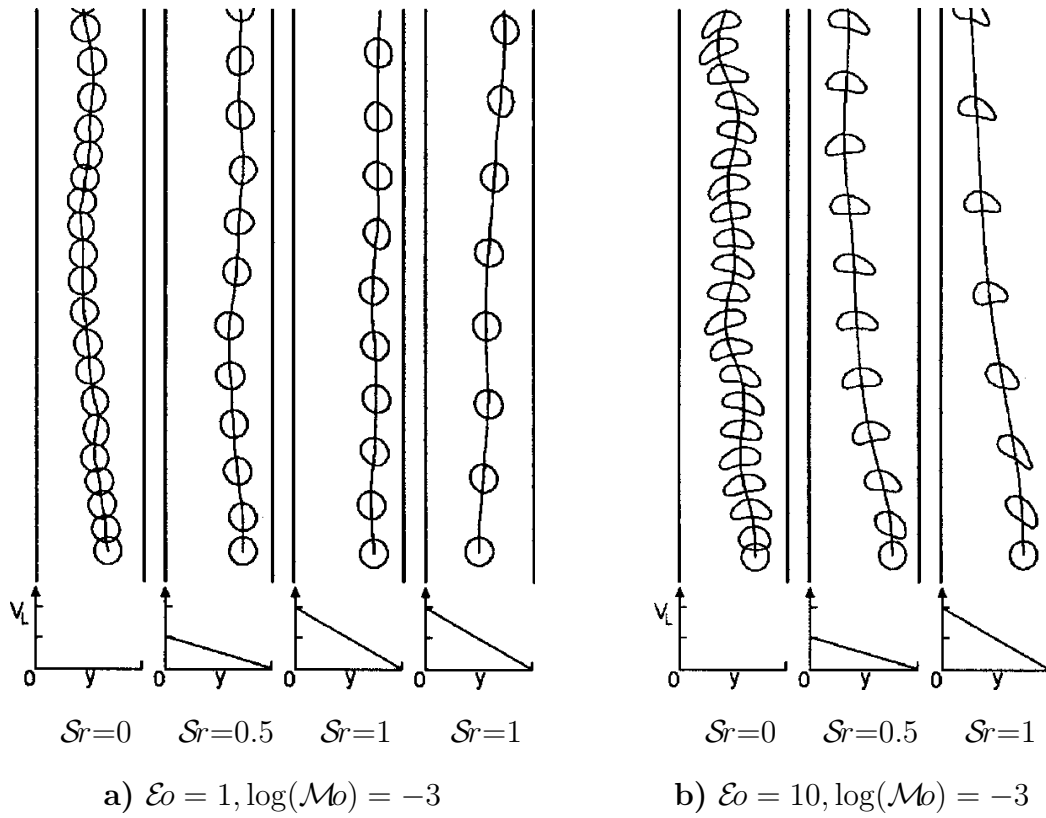


Figure 7.3: Bubble trajectories in linear shear flows (from [388]).

91] and show qualitatively similar behaviour. However, sufficient data to derive a correlation for C_l has not yet been gathered, due to the enormous computational effort required.

7.2.5 Empirical Correlations for Bubbles

It has been pointed out in Section 1.5.5 that lift coefficient data have often been derived from measured phase fraction distributions in vertical pipes. These results are not repeated here and the reader is referred there for details on how this can be done as well as the results obtained by various researchers.

Kariyasaki [195] conducted detailed measurements of the lift force on different types of DPEs (solid particles, droplets and bubbles) in linear shear. The results for solid particles as well as a discussion of the experimental setup can be found in Section 7.2.3. The results for fluid particles are presented below.

The most striking finding of Kariyasaki's [195] study was that the lift force on bubbles (and droplets) can act in the opposite direction to that described by low $\mathcal{R}e$

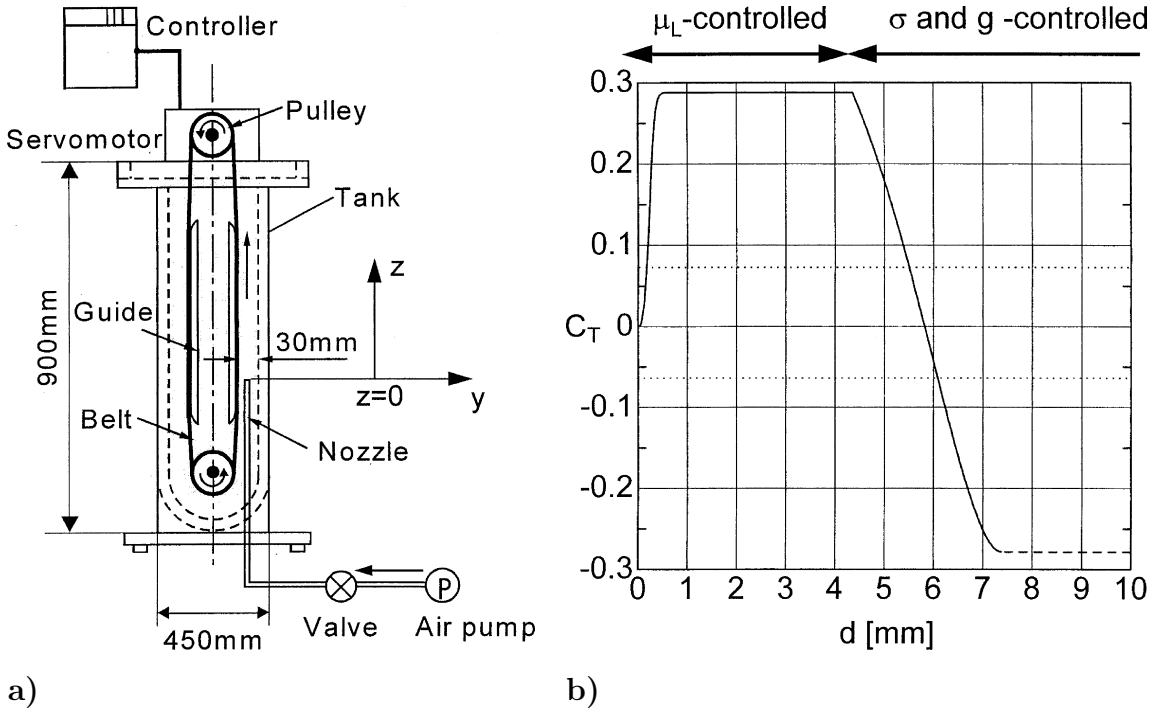


Figure 7.4: a) Sketch of the experimental apparatus; b) Lift coefficient as a function of the bubble diameter (from [389]).

analysis given in Section 7.2.1. He also derived a model for the lift force on highly deformed fluid particles by considering an analogy with a flat, two-dimensional plate suspended in a linear shear flow and determined the model coefficients using his experimental data. He obtained:

$$C_{l\omega} = -40.9 \mathcal{D}e^2 \quad (7.17)$$

Here, $\mathcal{D}e = \frac{a-b}{a+b}$ is the deformation factor where a and b are the major and minor half axes of the fluid particle, respectively. He also deduced the following correlation from his experiments:

$$\mathcal{D}e \approx 0.43 (\mathcal{S}r \mathcal{W}e \mathcal{R}e)^{0.6} = 0.43 \mathcal{S}r^{0.6} \mathcal{M}o^{0.3} \mathcal{E}o^{-0.3} \mathcal{R}e^{1.8} \quad (7.18)$$

Unfortunately, Kariyasaki [195] does not report the parameters of the experimental setup for fluid particles in sufficient detail to allow deduction of the parameter space investigated by him. However, from the limited data given in his paper, it can be concluded that $\mathcal{M}o$ is large and the range of $\mathcal{S}r$ is similar to the values reported by him for particles.

Recently, Tomiyama et al. [389] investigated bubbles using a similar apparatus, which was driven by a single belt as depicted in Figure 7.4a. The bubble trajectories

and shapes were measured using a high speed video camera and are shown in Figure 7.5. Different glycerol-water solutions were selected for the continuous phase giving viscosities between 18 to 80 times that of water, in order to suppress the oscillating motion frequently encountered for bubbles in low viscosity fluids. Consequently, $\mathcal{R}e$ was moderate ($3.7 < \mathcal{R}e < 210$). The other parameter ranges were $-5.5 < \log(\mathcal{M}o) < -2.8$, $1.39 < \mathcal{E}o < 5.74$ and $0.036 < \mathcal{S}r < 0.27$. They found that the lift coefficient is a strong function of $\mathcal{E}o$ and almost independent of the shear rate. The latter finding is in contrast to some of the direct numerical simulations discussed in the previous Section. However, this might be due to the limited parameter range, especially in $\mathcal{S}r$, investigated by Tomiyama et al. [389]. They then utilised collected data to derive the following empirical correlation for the combined effects of shear-induced and wake-induced lift on a single bubble:

$$C_{lw} = \begin{cases} \min [0.288 \tanh(0.121\mathcal{R}e), f(\mathcal{E}o_h)] & \text{for } \mathcal{E}o_h < 4 \\ f(\mathcal{E}o_h) & \text{for } 4 \leq \mathcal{E}o_h \leq 10 \\ -0.29 & \text{for } \mathcal{E}o_h > 10 \end{cases} \quad (7.19)$$

where $f(\mathcal{E}o_h) = 0.00105\mathcal{E}o_h^3 - 0.0159\mathcal{E}o_h^2 - 0.0204\mathcal{E}o_h + 0.474$ and $\mathcal{E}o_h$ is based on the projected diameter (as defined in Appendix A) of the bubble.

Tomiyama et al. [389] used their correlation to extrapolate to the case of an air-water system with a Morton number of $\log(Mo) = -11$. The resulting predicted variation of the lift coefficient as a function of the bubble diameter is shown in Figure 7.4b. C_l changes sign at 5.6 mm, so that, for example, in vertical, bubbly pipe flow, bubbles larger than 5.6 mm will migrate towards the pipe centre and smaller ones to the pipe wall. This is consistent with the observations reported by several authors and reviewed in Section 1.5.5. It has to be noted, however, that an extrapolation over several orders of magnitude to an extremely low $\mathcal{M}o$ is rarely valid because low $\mathcal{M}o$ bubbles frequently exhibit unsteady trajectories and this instability is damped by the high viscosity of the continuous phase used in Tomiyama et al.'s [389] experiment. An example of the unsteady motion of the bubbles is pictured in the lower right corner in Figure 7.5, which relates to the lowest $\mathcal{M}o$ and largest $\mathcal{E}o$ considered by them. $\mathcal{R}e$ was approximately 210. A direct consequence of unsteady motion is that more data have to be acquired before an average lift coefficient can be calculated with reasonable

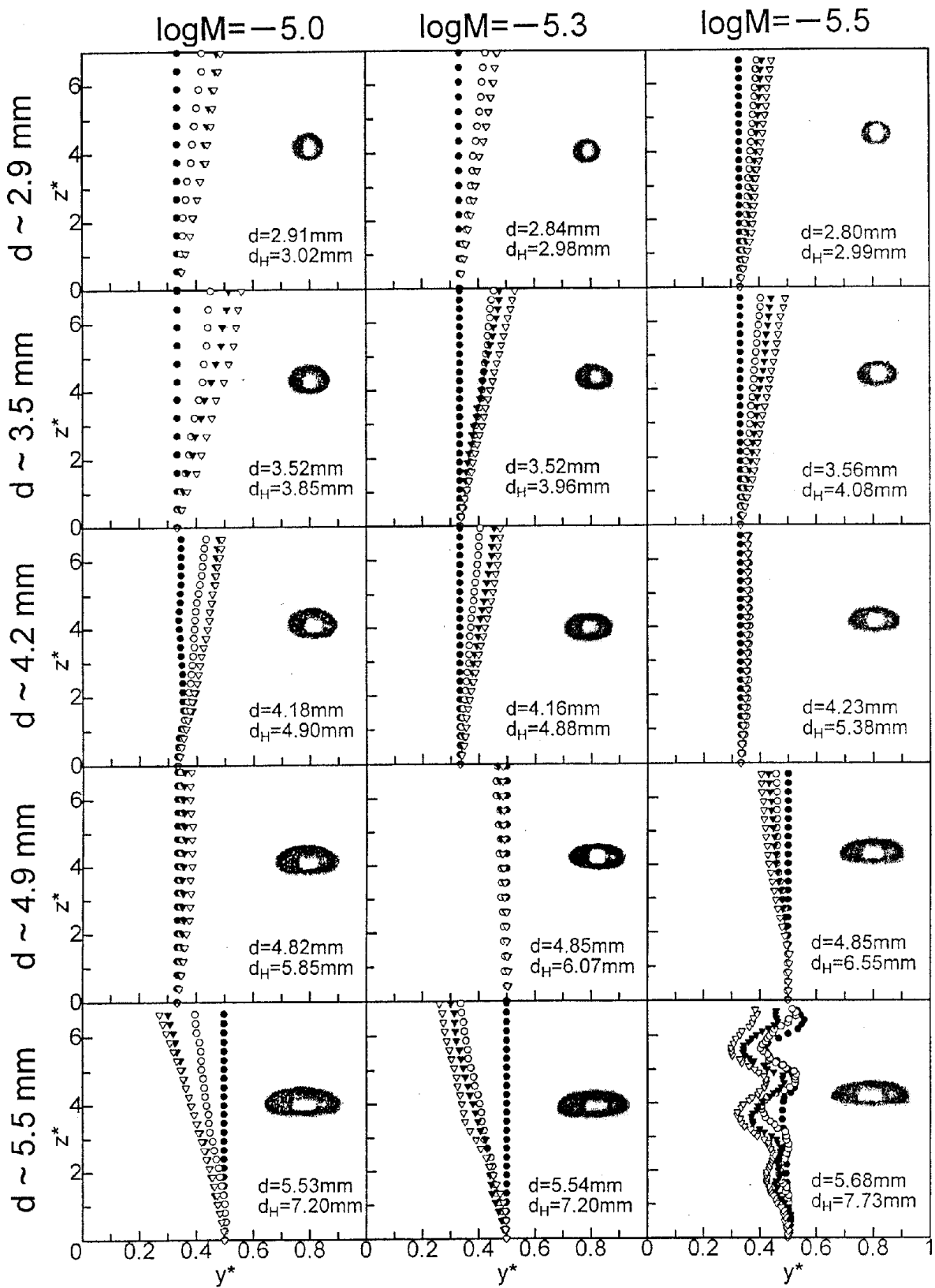


Figure 7.5: Trajectories and characteristic shapes of bubbles of five size classes in three glycerol-water solutions. The symbols denote the trajectories for different shear rates ranging between 0 and 6.4 1/s. y^* and z^* stand for the y - and z -coordinates normalised by the bubble diameter (from [389]).

accuracy. This was probably the reason why they could not conduct experiments for fluids with much lower viscosity.

The lift force on stationary bubbles within a rotating cylinder was measured by Naciri [287] using a levitation experiment, in which the equilibrium position of the bubble within the cylinder was determined and the lift force was inferred from the balance of drag, buoyancy and lift forces. Unfortunately, this technique requires a stable equilibrium point and, therefore, it is impossible to use it for high $\mathcal{R}e$ flows. Hence, they investigated air bubbles between $0.8 < d < 12$ mm in glycerol-water solutions, for which $10 < \mathcal{R}e < 100$. For $\mathcal{S}r = 0.1$, C_{lp} was found to increase moderately with $\mathcal{R}e$ from 0.2 to 0.3 – a trend opposite to the numerical results of Dandy and Dwyer [70] which showed a strong, decreasing influence of the $\mathcal{R}e$, giving a C_{lp} value lower by almost an order of magnitude for $\mathcal{R}e = 100$. However, it has to be noted that Dandy and Dwyer's [70] results are obtained for particles, so this difference is not surprising, but it indicates that one should be extremely cautious when applying particle lift models to deformable DPEs.

Particle Image Velocimetry (PIV) is a promising technique for the measurement of lateral forces, since it allows the simultaneous determination of the instantaneous velocity field and the bubble position. In this way, complicated flows, usually unknown a-priori, can be examined and the validity of the models can be checked for these flows. Sridhar and Katz [359] successfully employed PIV to measure the lift force on small bubbles ($500 < d < 800$ μm) entrained in a laminar ring vortex generated by moving a piston immersed in a tank of water. Their experiments were for moderate $\mathcal{R}e$ ($20 < \mathcal{R}e < 80$) and low $\mathcal{S}r$ ($0.01 < \mathcal{S}r < 0.1$). They found that C_{lp} is independent of the Reynolds number in the considered range. A curve-fit to their data is:

$$C_{lp} = 0.50\mathcal{S}r^{0.25} \quad (7.20)$$

This expression can be reformulated to give an expression for $C_{l\omega}$:

$$C_{l\omega} = 0.38\mathcal{S}r^{-0.75} \quad (7.21)$$

They then compared their data with published measurements for spinning spheres and found large quantitative and qualitative differences which has to be expected because of the different physical nature of the two situations. However, good agreement

d [mm]	1.5	2.5	3.5	4.5
$C_{l\omega}[-]$	0.04	-0.09	-0.06	-0.7

Table 7.1: Experimental results obtained by Ford and Loth [104].

was found with Naciri's [287] data.

Ford and Loth [104] employed PIV to gain fundamental knowledge about the drag and lift forces exerted on single, ellipsoidal bubbles ($1.5 < d < 4.5$ mm) in a turbulent shear layer, with $150 < \mathcal{Re} < 2050$ and $\mathcal{Sr} < 1$. They found that the instantaneous lift forces varied similar to a sin-function in time, but were generally out of phase with the predictions of the theoretical model of Auton [10, 9]. They then calculated time-average values of $C_{l\omega}$, which are given in Table 7.1. For bubbles with diameters between $1.5 < d < 3.5$ mm, $C_{l\omega}$ is almost constant and varies only slightly between 0.04 and -0.09. However, for the largest bubble ($d = 4.5$ mm) investigated, the time-averaged $C_{l\omega}$ drops to -0.7.

7.3 The Influence of Phase Fraction on the Lift Coefficient

Given the limited understanding of the lift force on a single DPE, it is not surprising that studies on the influence of the phase fraction on the lift force are extremely rare. To the author's knowledge, this effect has only been investigated in the two studies of Wang et al. [419, 215] and Beyerlein et al. [31]. In both, the lift correlation and other coefficients in simplified two-fluid models are adjusted so that best agreement is obtained for the phase fraction distribution in co-current bubbly flow in pipes, as outlined in Section 1.5.5. Unfortunately, a measurement technique allowing direct determination of the lift force on an individual DPE in a dense two-phase flow does exist.

Wang et al. [419, 215] deduced lift coefficients in the manner described above for a range of conditions and correlated the data as a function of the local phase fraction, the ratio of the bubble diameter and the pipe diameter as well as several other parameters. They found that the lift coefficient diminished exponentially with the local

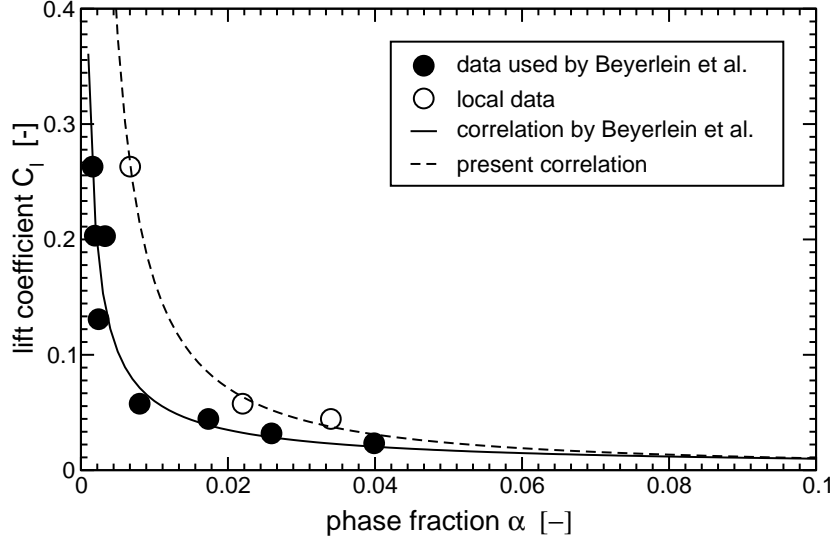


Figure 7.6: Lift coefficient as a function of the phase fraction. Original correlation by Beyerlein et al. [31] and the model developed in the present work.

phase fraction and ranged between 0.01 and 0.1. Unfortunately, their correlation can only be applied to flows in pipes because it depends on the pipe diameter.

A reduction of the lift coefficient with increasing phase fraction may be expected, since the vorticity around a bubble will become increasingly dominated by that contained in the wakes of the bubbles in front of it. In this case, the lift force depends only weakly on the mean flow, but strongly on the position of the surrounding bubbles. Hence, the effective lift coefficient diminishes for increasing phase fractions.

Beyerlein et al. [31] utilised a simplified two-fluid model, in which the liquid velocity was assumed to be undisturbed by the bubbles to derive a correlation for the lift coefficient. Hence, their study is limited to very low phase fractions. They found that $C_{l\omega}$ could not be independent of the phase fraction if the profiles of the latter were to be predicted accurately. They correlated $C_{l\omega}$ as a function of the mean phase fraction $\bar{\alpha}$, as follows:

$$C_{l\omega} = 1.65 \times 10^{-3} \bar{\alpha}^{-0.78} \quad (7.22)$$

Equation (7.22) is plotted in Figure 7.6 and it is evident that it decays rapidly with increasing $\bar{\alpha}$. $C_{l\omega}$ tends to zero even at moderate phase fractions. Unfortunately, this correlation is suspect and of limited utility, since $C_{l\omega}$ must clearly depend on the local phase fraction. The validity is particularly suspect near the wall of a pipe flow where

the peak phase fraction can be several times larger than the mean value and where the vorticity and, hence, lift force are strongest.

This problem has been addressed in the present study fitting the data using the peak phase fraction value α instead of the mean one. Unfortunately, the peak values could only be extracted for three of the eight cases investigated by Beyerlein et al.. However, this is sufficient if one retains the functional form of equation (7.22). The modified correlation is shown in Figure 7.6 and given by:

$$C_{l\omega} = 6.51 \times 10^{-4} \alpha^{-1.2} \quad (7.23)$$

7.4 Calculations Using the Two-Fluid Methodology

In the Chapters 5 and 6, two test cases were used to evaluate the different correlations for drag and the turbulence response function C_t : the plane mixing layer (at low phase fraction) and the sudden enlargement of a circular pipe (at high phase fraction). The same cases are now employed in order to assess some of the lift correlations presented in this Chapter.

As shown in Figure 6.17, good results for the plane mixing layer are obtained using a constant lift coefficient of $C_{l\omega} = 0.25$. On the other hand, the same value for the lift coefficient yields unsatisfactory results for the sudden enlargement, as reported by many authors, *e.g.* [27, 25, 228, 418, 393]. Hence, the calculations presented in Sections 6.5 and 3.3.1 were obtained for $C_{l\omega} = 0$. However, a general lift correlation should be able to predict both cases reasonably well because they share many similarities.

In both cases, the fluid flow is in vertical, upward direction. Furthermore, both flows are turbulent with Reynolds numbers based on the mean liquid velocity and the characteristic length scales of the devices of 78500 and 160000 for the sudden enlargement and the plane mixing layer, respectively. In addition, the mean bubble diameter is identical with $d = 2$ mm. It therefore follows that the bubble dynamics and in particular the relative velocity between the phases are very similar. Finally, both flows are mainly driven by the liquid and not the bubbles, as evident by comparison of the liquid and relative velocities. Hence, the bubbles have a relatively small influence

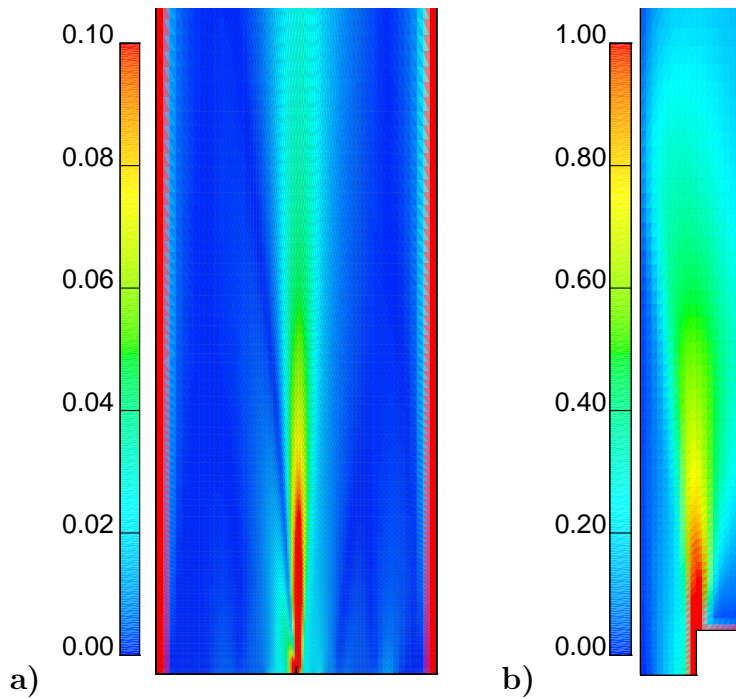


Figure 7.7: Contour plot of the dimensionless shear rate Sr : **a)** mixing layer and **b)** sudden enlargement test case.

on the flow field of the liquid.

However, two significant differences between the test cases can be identified. Firstly, the mean as well as peak phase fraction are much higher for the sudden enlargement, as evident from Figures 6.17 and 6.20. As discussed in Section 7.3, the presence of other DPEs seems to cause a reduction of the lift force. Secondly, the magnitude of the dimensionless shear rate Sr is larger for the sudden enlargement, as shown in Figure 7.7, and varies by almost an order magnitude between the two cases. Note that the scales for the two contour plots in this figure are different.

In the following discussion, correlations are selected and tested which predict a reduction of the lift coefficient under conditions similar to those found in the sudden enlargement. It is hoped that these models will also give reasonable results for plane mixing layer. These models are then implemented into the two-fluid methodology and validated against the two cases.

Setups

The geometry and setups for the sudden enlargement and the plane mixing layer were explained in Sections 3.3.1 and 5.3, respectively. The complete two-fluid methodology

was described in detail in Chapter 3 and the version utilised in the present calculations is essentially the same as the one presented in Section 6.5. In particular, the expressions for C_t and drag developed in this study are employed. In the following, only the lift correlations used in the validation study are outlined.

Four lift correlations have been selected for assessment: the first one is that of Moraga et al. [280] and is given by equation (7.13). It takes into account the influence of \mathcal{Re} and \mathcal{Sr} on the lift coefficient, as shown in Figure 7.2. It is evident from this plot that $C_{l\omega}$ decreases as \mathcal{Sr} and \mathcal{Re} increase. This trend is consistent with the requirements outlined above. The second model is that of Beyerlein et al. [31], which is given by equation (7.22). It centres on the effect of increasing phase fraction and has been modified in the present study to give $C_{l\omega}$ in terms of the local phase fraction rather than the mean one. This variant is given by equation (7.23). Finally, results for conventional lift modelling, *i.e.* a constant lift coefficient of $C_{l\omega} = 0.25$, are included.

Some of the correlations presented earlier are based on very interesting experimental results, but have not been included in this study because they would not improve the predictions. For example, the correlation of Tomiyama et al. [389] yields a constant $C_{l\omega}$ for a given bubble diameter and therefore does not vary between the two test cases. On the other hand, Sridhar and Katz's [359] expression predicts a reduction of $C_{l\omega}$ with \mathcal{Sr} , but yields rather large $C_{l\omega}$ of 5.6 and 0.38 for $\mathcal{Sr} = 0.1$ and 1, respectively, which is inappropriate for the sudden enlargement test case.

Results for the Sudden Enlargement of a Circular Pipe

Plots of the local variation of the lift coefficients calculated with the different correlations are given in Figure 7.8. It is evident that the correlation of Moraga et al. [280] produces negative $C_{l\omega}$ in regions of high shear immediately after the enlargement. However, the values are very close to zero elsewhere. On the other hand, the correlation of Beyerlein et al. [31] gives non-zero $C_{l\omega}$ only in regions within the recirculation zone where the phase fraction is low. The differences between the results with the original and modified version are very small.

The predicted phase fraction profiles obtained with the different lift correlations are given in Figure 7.9. They are all in reasonable agreement with the measurements,

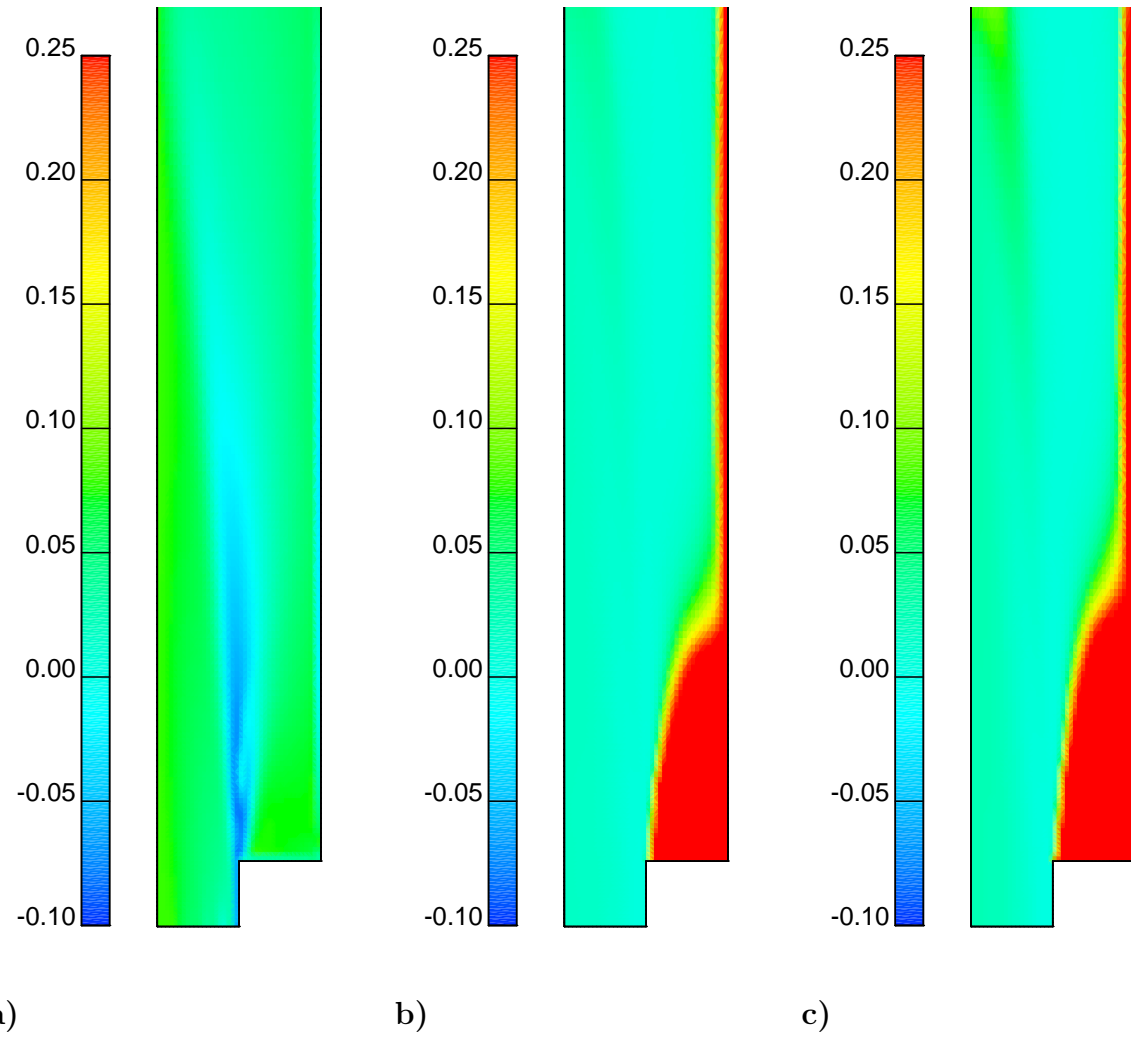


Figure 7.8: Contour plots of the lift coefficient for the sudden enlargement test case: **a)** Moraga et al. [280] **b)** Beyerlein et al. [31] **c)** present correlation.

except the results with $C_{l\omega} = 0.25$, for which it is apparent that an unphysical accumulation of the bubbles within the recirculation zone at $x = 130$ mm is produced. This limitation is well known and has been reported by several authors, as discussed earlier. The results for the other models are very similar and capture the phase fraction distribution at the first three stations better, but there is still room for further improvements. Further downstream at $x = 180, 250$ and 320 mm, some discrepancies with the measurements are noticeable especially on the centreline. Here, the presence of the dispersed phase is underestimated in the calculation in all cases. However, inspection of a profile further downstream (not shown) revealed that the experimental behaviour is eventually recovered. The redistribution of bubbles towards the centreline is governed by bubble diffusion and remedy has to be sought in the modelling of the

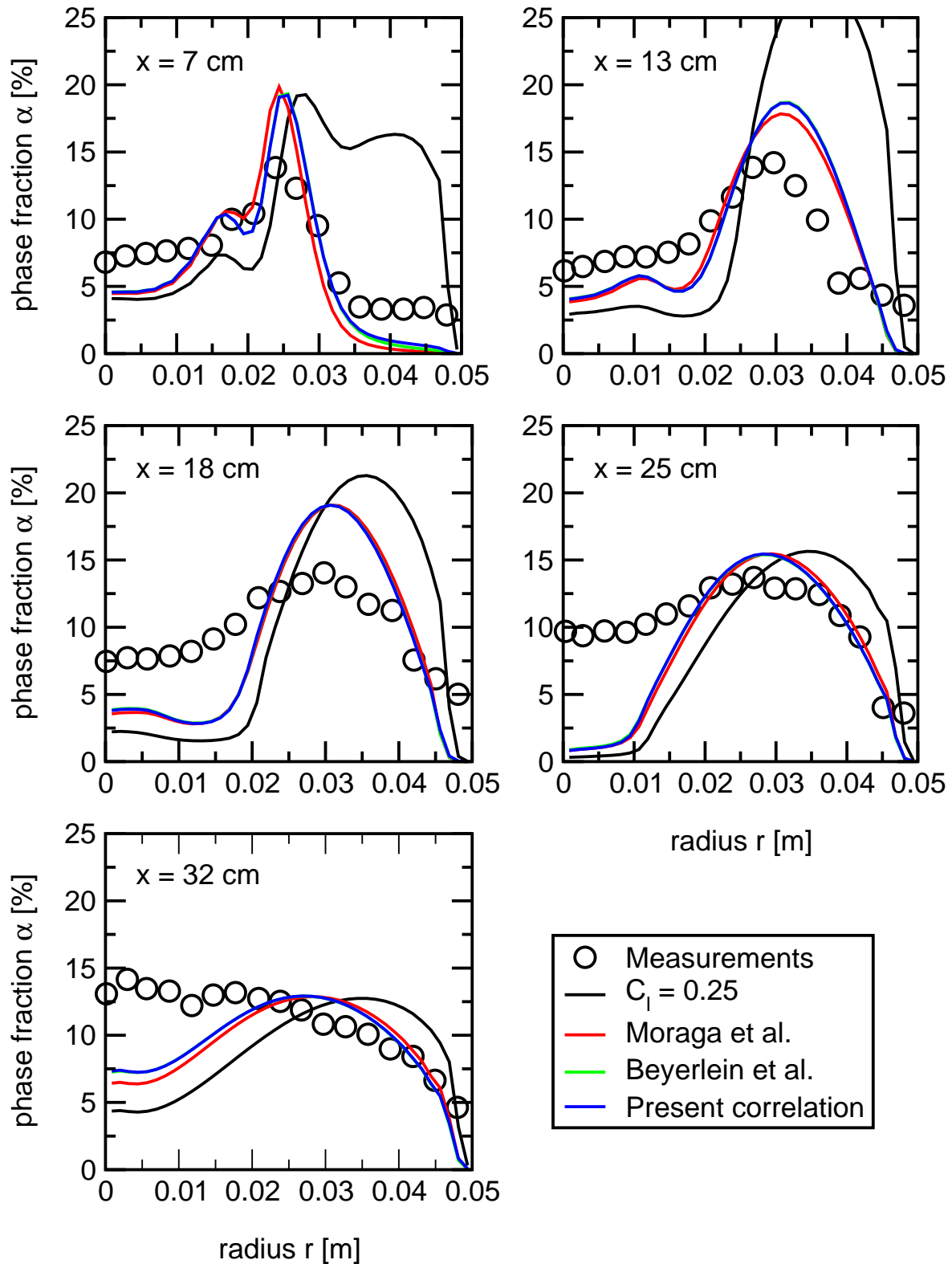


Figure 7.9: Results for the sudden enlargement test case: predicted phase fraction profiles compared with experimental data (circles). The four lines represent predictions with different lift correlations.

turbulent drag term.

Figure 7.10 shows profiles of the axial liquid velocity. There is only very little difference between the predictions using the various lift correlations, except for those with $C_{l\omega} = 0.25$, which are slightly smaller on the centreline. In general, the agreement is excellent up to $x \approx 180$ mm. However, the velocity on the centreline is overpredicted further downstream, as noted previously in Section 6.5.

Results for the Plane Mixing Layer

The spatial variations of the lift coefficients for the plane mixing layer are shown in Figure 7.11. The variations are confined to the region downstream of the splitter plate and are small for all correlation, except for the present one. On average, the lift coefficient given by the latter is very small even for the relatively low phase fractions found in the plane mixing layer and is even smaller for the original version. The Moraga et al. [280] model predicts that $C_{l\omega}$ reaches its maximum value of 0.08 (according to this correlation) everywhere in the field.

The experimental comparison for the phase fraction distribution is plotted in Figure 7.12 and it is evident that the extrema, which originate from those prescribed at the inlet, are slowly diffused. This is captured well in the calculations with $C_{l\omega} = 0.25$, but all other models overpredict the redistribution of bubbles. In the case of Beyerlein et al.'s [31] model, it must be concluded that the proposed formulation approaches zero too rapidly as the phase fraction increases. The present correlation performs slightly better, but the diffusion of the phase fraction extrema is still overpredicted.

As mentioned earlier, the correlation of Moraga et al. [280] yields its maximum value of 0.08 everywhere in the field, which is too low to obtain reasonable predictions. However, the expression was originally derived for particles and it therefore seems appropriate to change the first constant in equation (7.13) from 0.2 to 0.37 for the purpose of this study. Using this variant, the result for the plane mixing layer (not shown) is similar to that obtained with $C_{l\omega} = 0.25$, but that for the sudden enlargement (not shown) deteriorates and the bubbles accumulate in the recirculation zone.

Profiles of the x -component of the liquid velocity are shown in Figure 7.13 and it is evident that the lift correlations have negligible effect on this quantity.

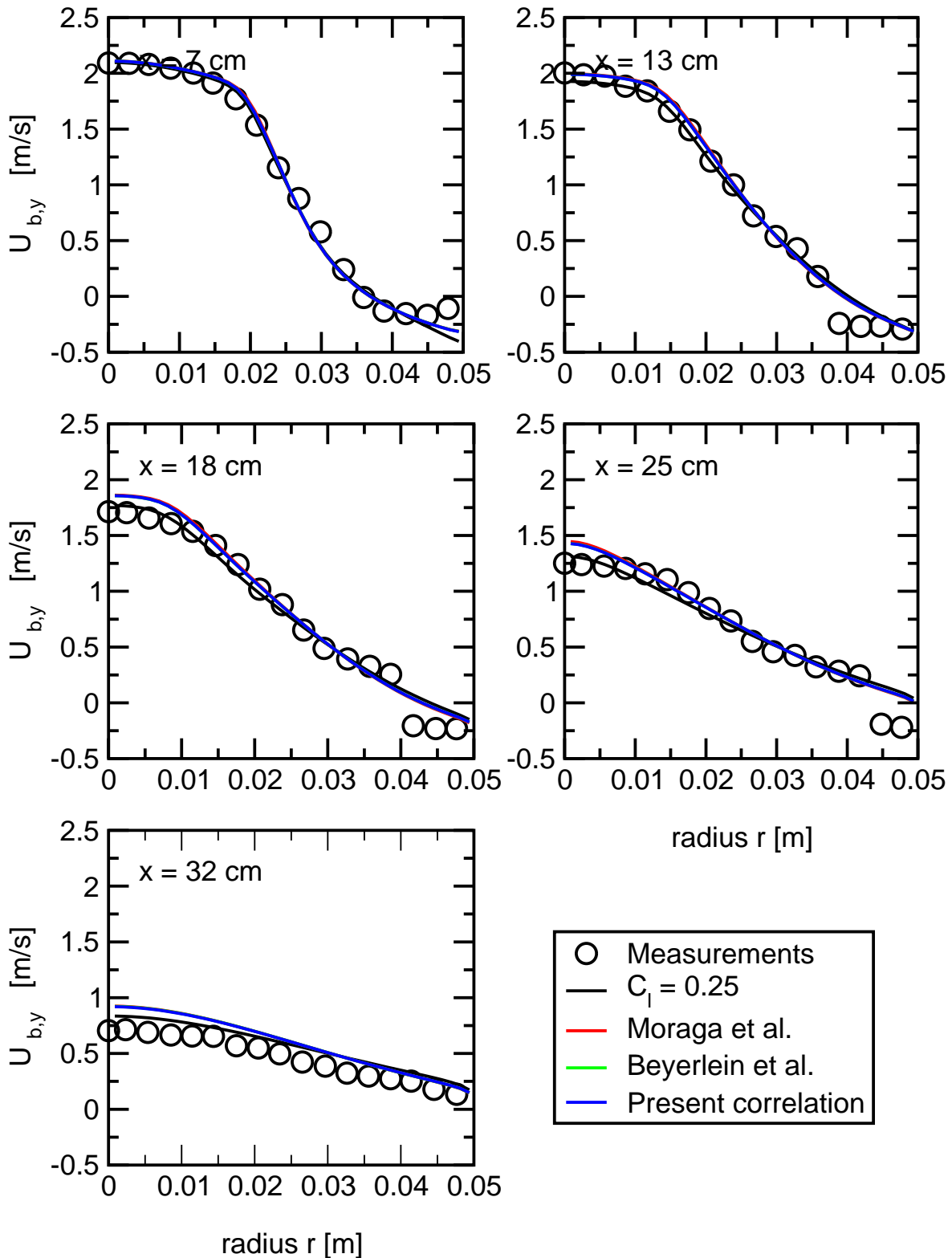


Figure 7.10: Results for the sudden enlargement test case: predicted profiles of the mean axial liquid velocity compared with experimental data (circles). The four lines represent predictions with different lift correlations.

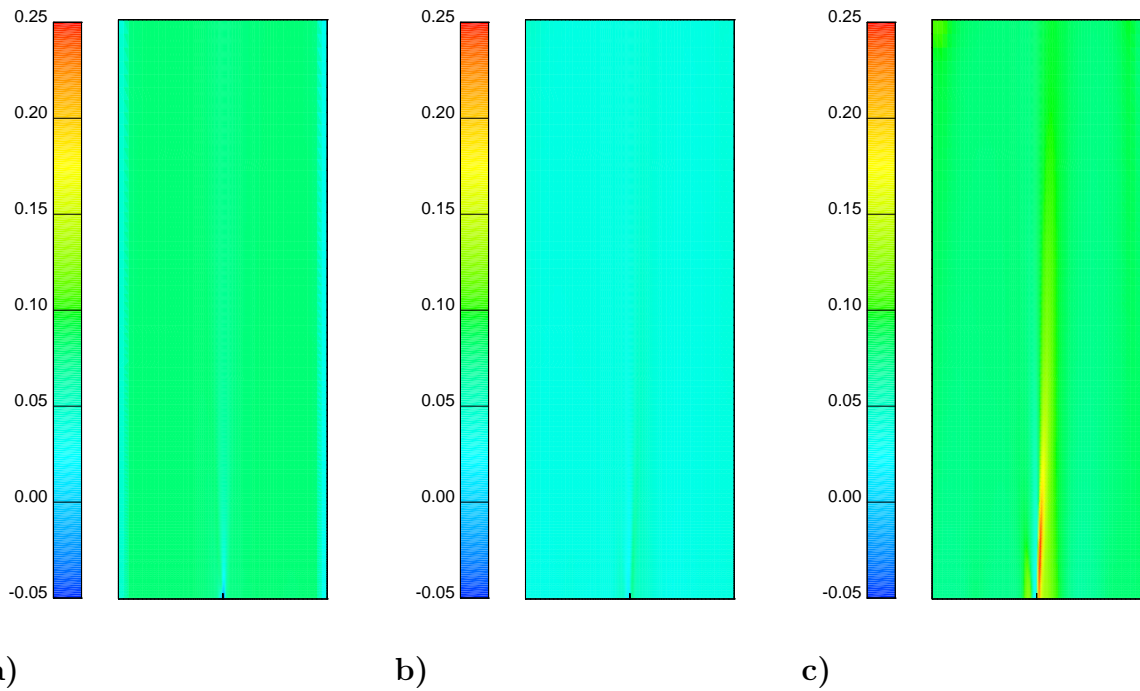


Figure 7.11: Contour plots of the lift coefficient for the mixing layer test case: **a)** Moraga et al. [280]; **b)** Beyerlein et al. [31]; **c)** present correlation.

It can be concluded from these two cases that the new lift models identified in the literature yield better results for the sudden enlargement, but poorer ones for the plane mixing layer. In particular, the unphysical accumulation of bubbles within the recirculation zone behind the sudden enlargement, which is obtained with $C_{l\omega} = 0.25$, is greatly reduced and the predictions are in better agreement with the experimental findings. However, the results for the mixing layer are less favourable since the magnitudes of the local phase fraction extrema are reduced noticeably. None of the lift models tested yields reasonable results for both flows, which suggests that lift modelling by itself is not responsible for the errors.

7.5 Interface Capturing Methodology: Rising Bubble in Shear Flow

In this Section, the dynamics of single air bubbles in water are investigated using DNS. The motivation for this work stems from the results of the validation work presented in the previous Section which showed that none of the lift models tested yields rea-

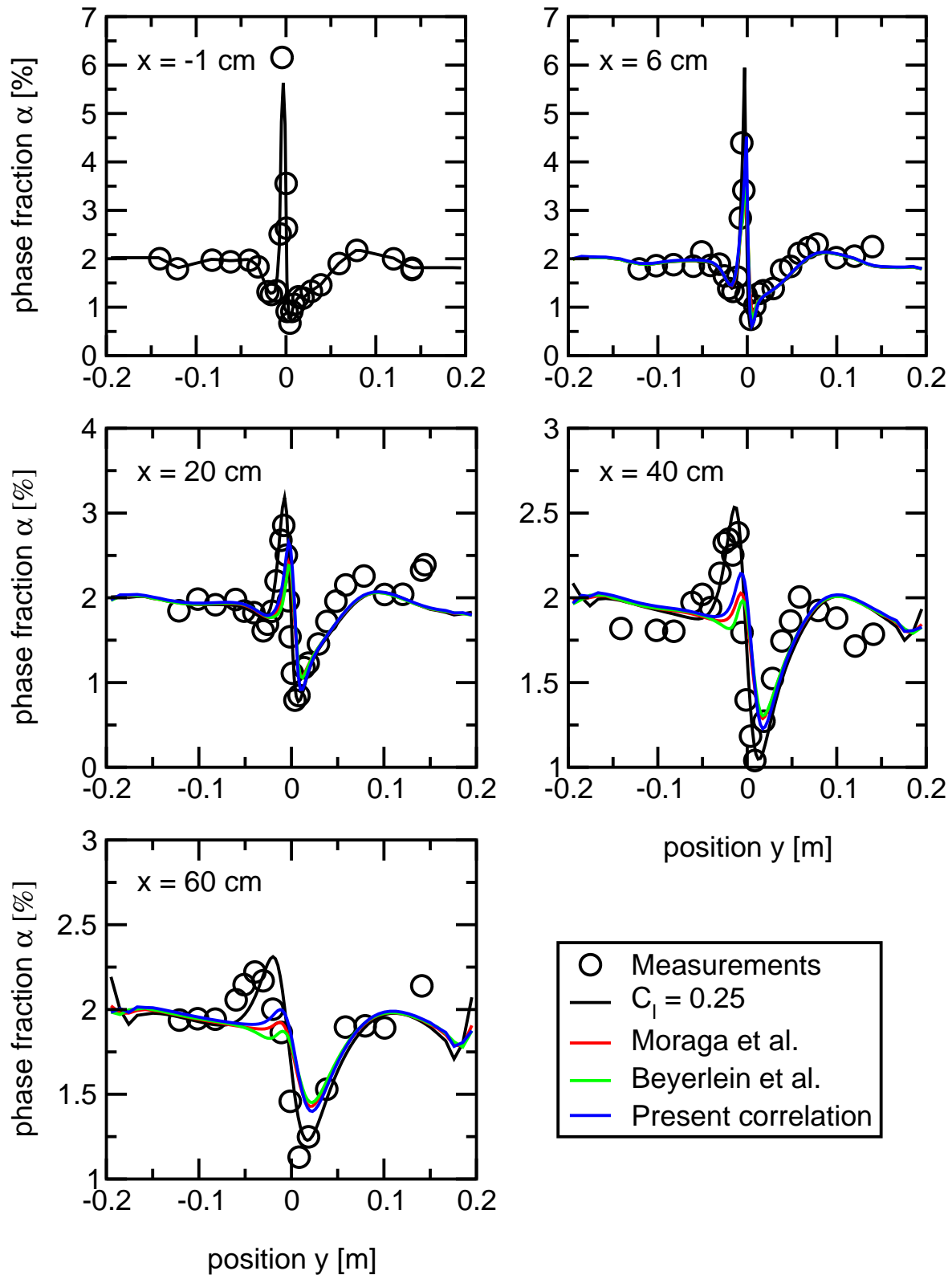


Figure 7.12: Results for the mixing layer test case: predicted phase fraction profiles compared with experimental data (circles). The lines represent predictions with four different lift correlations.

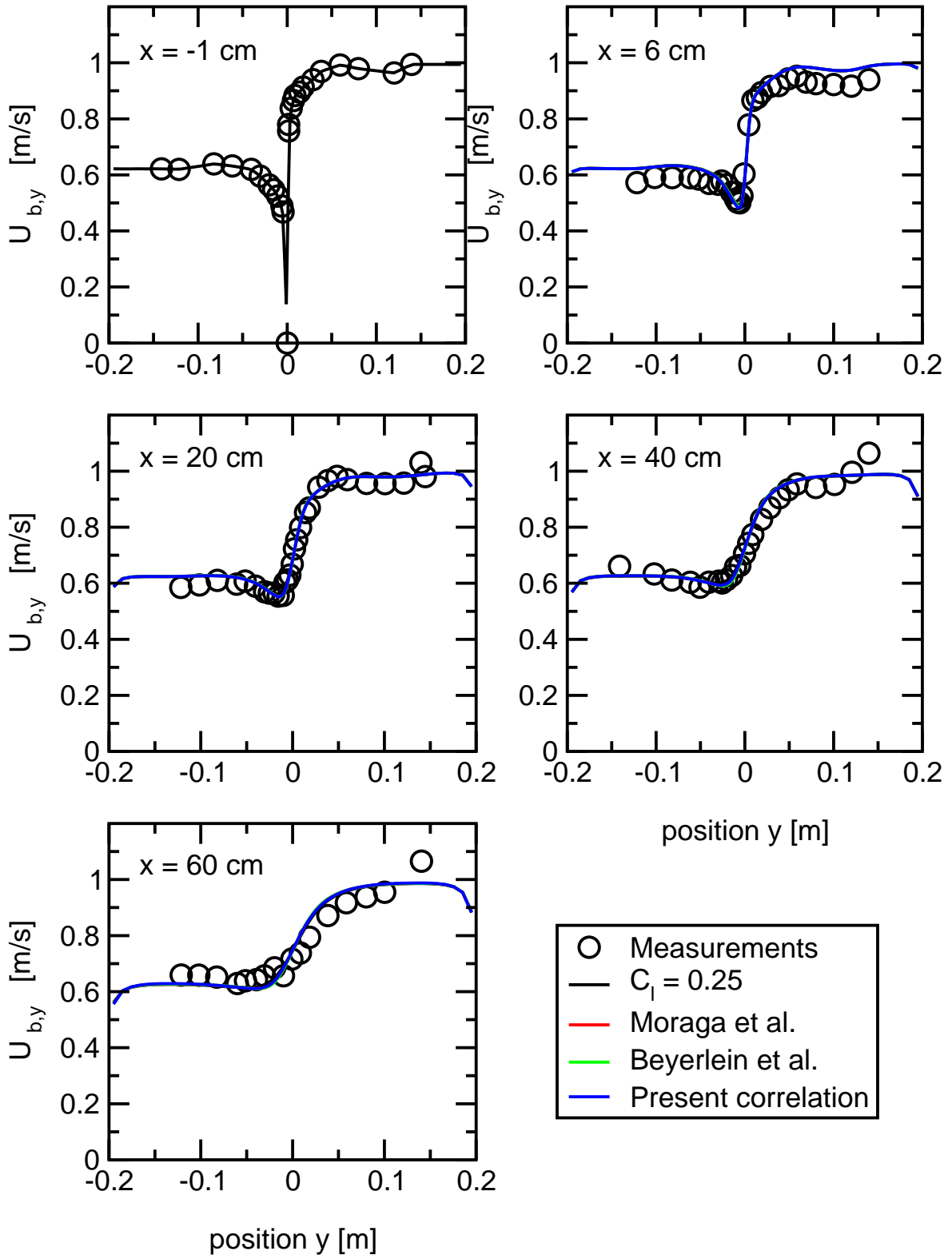


Figure 7.13: Results for the mixing layer test case: predicted profiles of the mean liquid velocity in x -direction compared with experimental data (circles). The lines represent predictions with four different lift correlations.

d [mm]	$\mathcal{E}\sigma$ [-]	ω [1/s]	$\mathcal{R}e_s$ [-]	$\mathcal{S}r$ [-]	\overline{U}_r [m/s]	$\mathcal{R}e$ [-]	$\overline{C}_{l\omega}$ [-]
1.0	0.14	-10	640	0.0337	0.230	296.5	0.618
1.0	0.14	-50	3200	0.467	0.107	107.1	1.12
2.5	0.88	-10	4000	0.0874	0.286	715.4	-0.234
2.5	0.88	-20	8000	0.175	0.286	715.8	-0.128
2.5	0.88	-50	20000	0.708	0.177	441.5	0.809
2.5	0.88	-100	40000	1.82	0.138	344.0	0.619
5.0	3.5	-10	16000	0.224	0.223	1116	-0.127
5.0	3.5	-20	32000	0.448	0.223	1115	-0.399
5.0	3.5	-30	48000	0.839	0.179	894.3	-0.281

Table 7.2: Parameters of the calculations and time-averaged results for the relative velocity and lift coefficient.

sonable results for both the plane mixing layer and the sudden enlargement test cases. Therefore, a more fundamental study is carried out to enhance the understanding of the lateral forces acting on bubbles under conditions similar to those generated in the two test cases under investigation.

Previous research into the dynamics of deformable bubbles in shear flows using numerical techniques was presented in Section 7.2.4. Nearly all of this work has been conducted for bubbles in high $\mathcal{M}o$ fluids and/or in two spatial dimensions to save computational resources. As outlined in Section 1.5.1, additional numerical difficulties arise when the surface tension force is high. This is the case for air-water bubbles with diameters smaller than approximately 5 mm, which are found in many industrial applications.

Setup

In the calculations presented below, the interface-capturing methodology of Weller [424] presented in Chapter 4 has been used. It has been validated for the case of single free rising air bubbles in quiescent water (high $\mathcal{M}o$) as well as free rising air bubbles subjected to a linear shear flow in glycerol-water solution (low $\mathcal{M}o$). This work was presented in Sections 4.3.1 and 4.3.2, respectively.

Here, three-dimensional air bubbles rising in water are subjected to a linear shear

flow. The setup is essentially the same, as outlined Section 4.3.2, except for the fluid properties. The Mo for this system is $\log(Mo) = -11$. Nine calculations were performed for different bubble sizes and shear rates. The conditions for each calculation are summarised in Table 7.2. The bubbles have nominal¹ diameters between 1 and 5 mm and \mathcal{E}_o is between 0.14 and 3.5. The resulting bubble Re lie between 107 and 1120. The shear rate ω is varied between -10 and -100 1/s which yields $0.03 < Sr < 1.82$. These values have been selected such that they are similar to those found in the plane mixing layer and sudden enlargement (see Figure 7.7).

A Reynolds number characterising the shear flow Re_s can be determined based on the width w of the computational domain and velocity difference ΔU_c across it, thus:

$$Re_s = \frac{\rho_c \Delta U_c w}{\mu_c} = \frac{\rho_c \omega w^2}{\mu_c} \quad (7.24)$$

where w is given by $w = 8d$, as evident in Figure 4.12.

The Re_s for the calculations performed in this study are given in Table 7.2. It is apparent that Re_s becomes quite large, especially for larger bubble diameters, since it is proportional to the square of the bubble diameter. A fully developed flow of this kind would certainly be turbulent. However, in the calculations no attempt is made to resolve the turbulent fluctuations accurately and although the instantaneous Navier-Stokes equations are employed in the calculations, it should be noted that the spatial and temporal resolutions are not adequate to resolve the turbulent scales. This problem should be addressed in future research and some suggestions can be found in Section 8.2.

Results

Figure 7.14 shows the velocity fields and the bubble shapes for two calculations at different shear rates ($\omega = -10$ and -100 1/s). The nominal diameter is constant with $d = 2.5$ mm. From the plot, the imposed shear flow is clearly noticeable; the y -component of the velocity decreases in the \hat{x} -direction. Animations of these results have been produced and are included on the CD-ROM accompanying this thesis.

¹The definition of the nominal diameter is given in Appendix A.

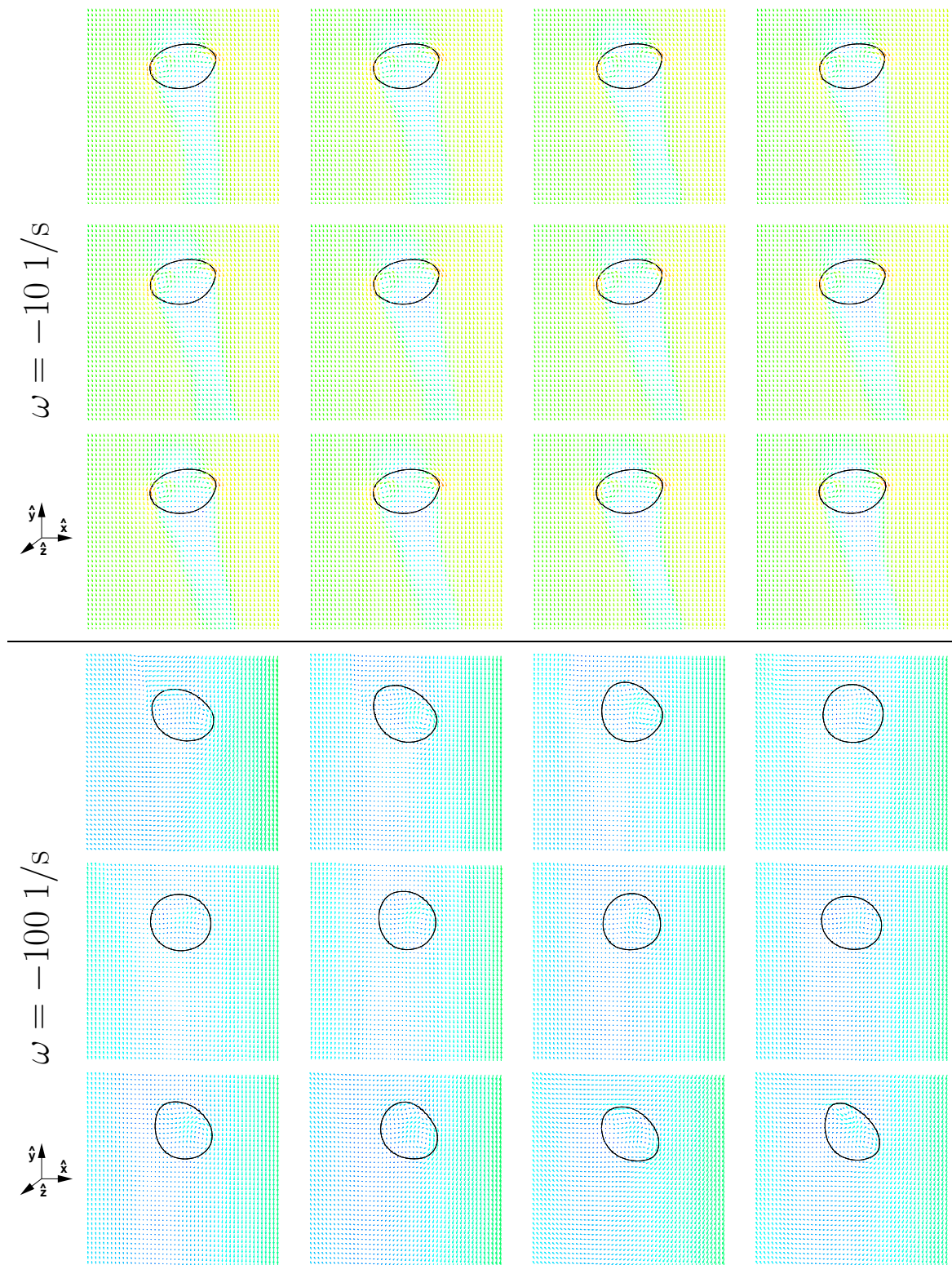


Figure 7.14: Time sequence of the velocity fields around free rising air-water bubbles ($\log(Mo) = -11$) in linear shear flows with two different shear rates ($\omega = -10$ and -100 1/s). The nominal diameter is $d = 2.5 \text{ mm}$ in both calculations and the time difference between each picture is $\Delta t = 18 \text{ ms}$.

The results for $\omega = -10 \text{ 1/s}$ are given in the first three rows of Figure 7.14. The deformation of the bubble shape and the wake of the bubbles are clearly noticeable. Some unsteadiness in the bubble wake was noticeable, but no oscillating motion, as observed for a bubble rising in quiescent water and shown in Figure 4.8, occurred. Hence, this relatively low shear has a stabilising effect on the wake dynamics. The shape of the bubble is similar to that found in absence of shear, but its orientation is now constant. The last three rows of pictures show the results for $\omega = -100 \text{ 1/s}$. As the magnitude of the shear increases, two marked changes are evident: firstly, the bubble shape appears to be less deformed and some of the pictures show almost circular cross-sections. However, it is evident that the shape of the bubble is not constant. Secondly, no wake can be seen behind the bubble.

Figure 7.15 shows the projections of the trajectories to the horizontal $x-z$ plane (l.h.s.) and the vertical $x-y$ plane (r.h.s.). Each row of graphs in the figure corresponds to a nominal diameter, $d = 1.0, 2.5$ and 5.0 mm , respectively. Two shear rates ($\omega = -10$ and -50) have been investigated for the smallest $d = 1 \text{ mm}$ bubble. It is evident from the $x-z$ plot that the bubbles move in a straight lines, which are almost parallel to the x -coordinate, towards the higher velocity side. Hence, they experience “positive” lift. Furthermore, their motion is steady – oscillations are not noticeable. The bubble subjected to the weaker shear (black line) drifts slowly in the z -direction. It should be noted that the magnitude of the relative velocity in the z - direction, *i.e.* the drift velocity, is only 1.4% and 7.4% of that in the y - and the x -direction, respectively. However, this is a deficiency of the numerical solution procedure and similar drift velocities have been reported in Section 4.3.1 for bubbles of the same size rising in quiescent water. The deficiency stems from the fact that the discretisation of the surface tension term does not guarantee that its surface integral over a closed surface equals zero. This has been explained in Section 4.2.2.

The graphs on the r.h.s. of Figure 7.15 show the bubble’s motion in the vertical $x-z$ plane. Most of the bubbles prescribe parabolic trajectories. This is explained as follows: consider a bubble migrating with a constant relative velocity in x -direction due to the lift force acting on it. Since the bubble moves within a linear shear flow, the liquid velocity in the z -direction decreases proportionally to the distance travelled

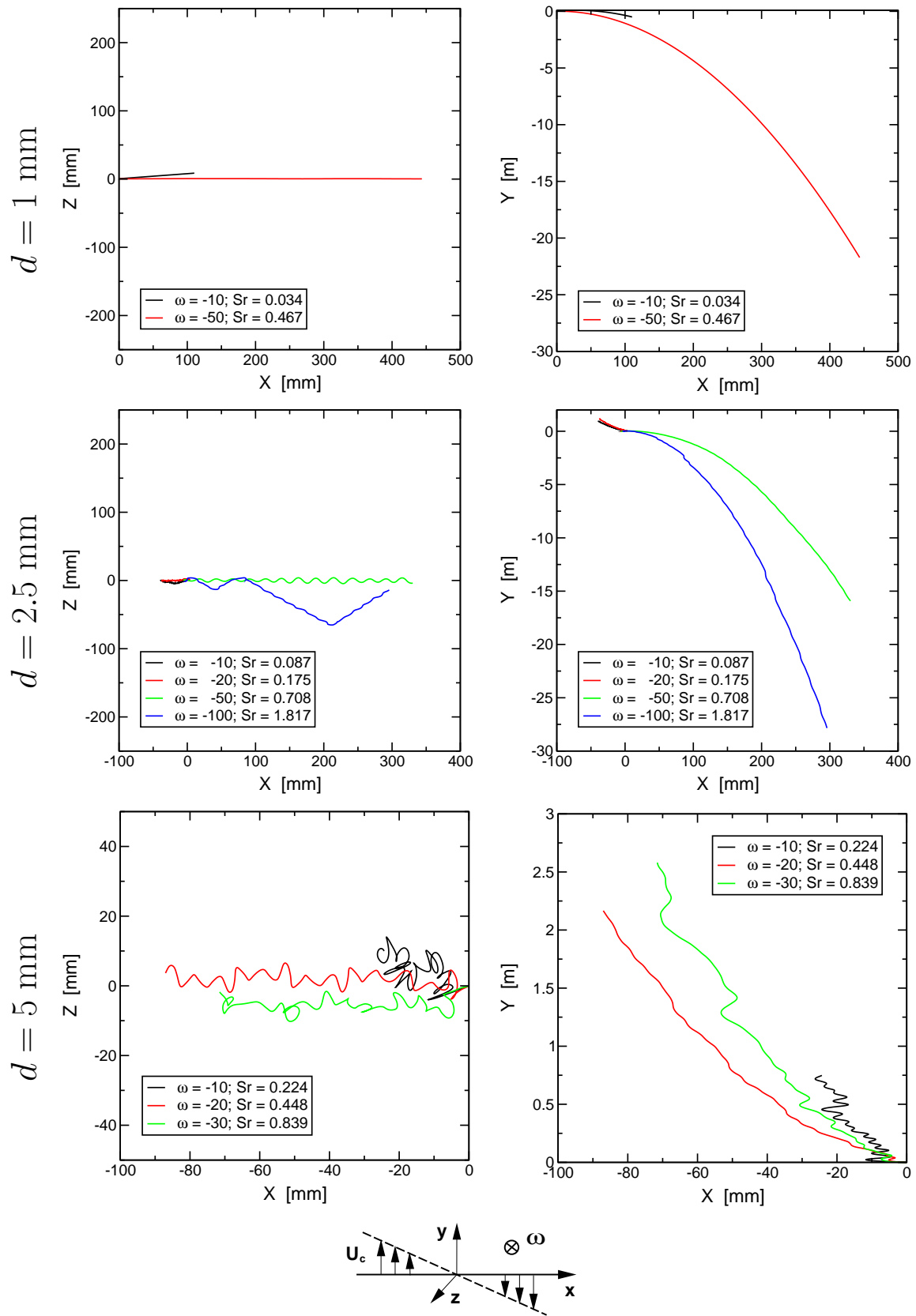


Figure 7.15: Bubble trajectories in a horizontal $x - z$ plane (l.h.s.) and vertical $x - y$ plane (r.h.s.) ($\log(Mo) = -11$).

in the x -direction. The bubble is advected with this flow and, hence, its trajectory is similar to a parabola. It should be noted that the scales in the x - and the z -direction are very different. For example, a bubble with a nominal diameter of $d = 2.5$ mm in a shear flow with $\omega = -50$ 1/s travels 15 m in vertical direction, but only 0.3 m in horizontal direction. This is, of course, an extreme example, but the corresponding dimensionless shear rate of $Sr = 0.7$ is easily obtained (at least locally) in the sudden enlargement, as shown in Figure 7.7.

The trajectories of bubbles with $d = 2.5$ mm and -100 1/s $< \omega < -10$ 1/s are given in the middle row of graphs in Figure 7.15. It is striking that the direction of the lift force changes when the shear acting on the bubble is increased. The lift coefficient is positive for strong shear ($-100 < \omega < -50$ 1/s) and negative for weak shear ($-20 < \omega < -10$ 1/s). For the strongest shear ($\omega = -100$ 1/s), appreciable drift in the z -direction is noticeable. It is, however, unlikely that the drift is caused by the numerical deficiency mentioned above, for two reasons: firstly, appreciable drift is only obtained for the largest shear rate, whereas in the results presented for the smaller bubbles with $d = 1$ mm the drift was only apparent for low and zero shear rates. Secondly, the drift velocity is much larger than the one found for $d = 1$ mm. However, further investigations are needed to clarify these results.

In the bottom row of the Figure 7.16, the results for $d = 5$ mm and -30 1/s $< \omega < -10$ 1/s are shown. It is apparent that the motion of these bubbles is oscillatory. The trajectory in the horizontal $x - z$ plane is a superposition of a helical motion and a translation due to lift. It should be noted that helical bubble motion was previously found for bubbles of the same size rising in a quiescent liquid, as evident in Figure 4.4. However, it is interesting that this kind of motion is not noticeable for bubbles with nominal diameters of $d = 2.5$ mm because the wake dynamics is altered by the shear, as shown in Figure 7.14. In the $x - y$ plane, the parabolic trajectories found for smaller bubbles are superimposed with a sinusoidal motion in x -direction.

In Figure 7.16, the magnitude of the relative velocity U_r (r.h.s.) and $C_{l\omega}$ (l.h.s.) are plotted as functions of time for the fore-mentioned bubbles. For the smallest bubble with $d = 1$ mm, it is evident from the relative velocity plot that the motion is steady. This is also true if the bubble is subjected to relatively strong shear flow ($\omega = -50$ 1/s,

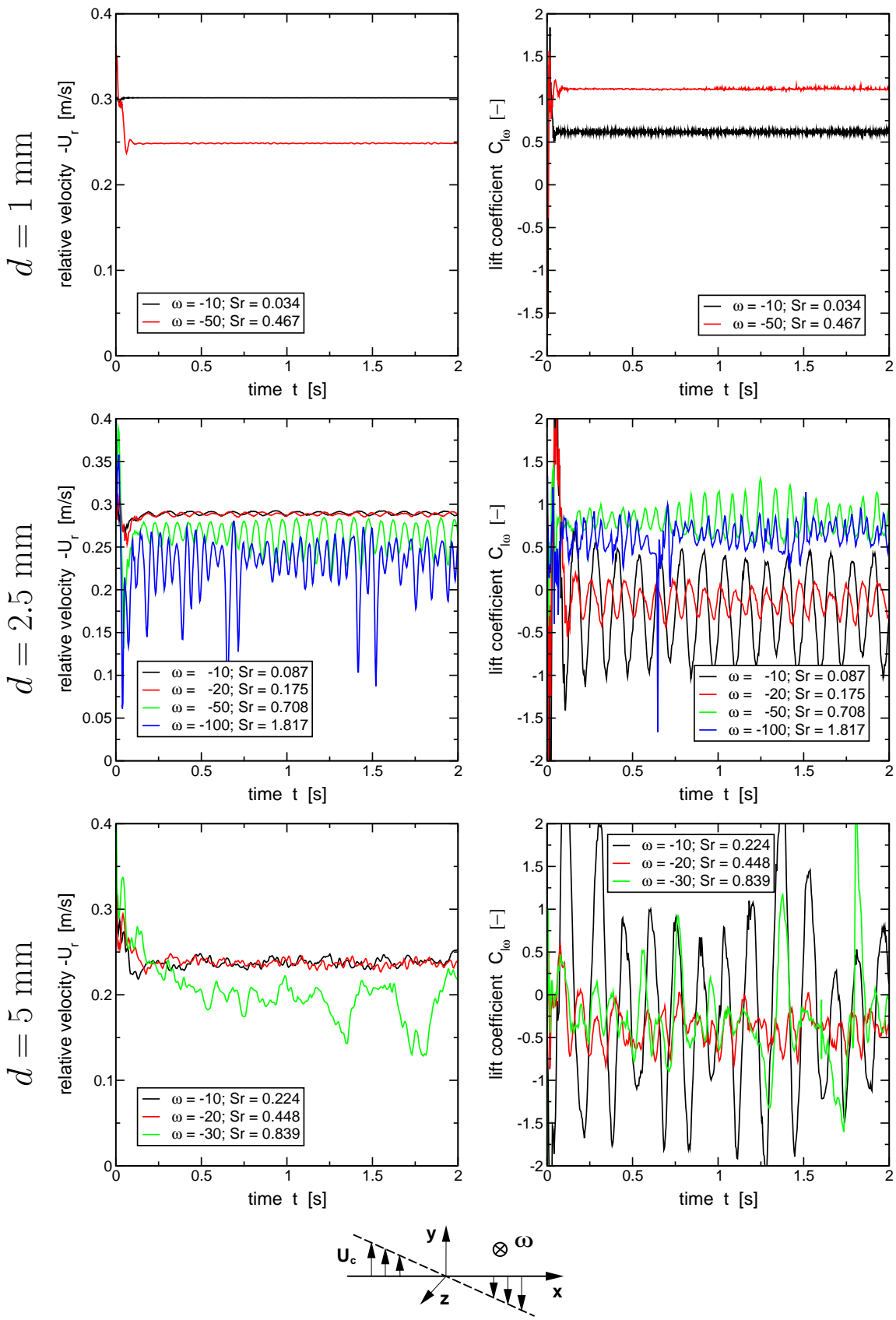


Figure 7.16: Magnitude of the relative velocity $-U_r$ (l.h.s.) and lift coefficient (r.h.s.) as functions of time ($\log(Mo) = -11$).

$\mathcal{S}r=0.467$). However, a reduction of U_r is evident in this case. On the right hand side, plots of $C_{l\omega}$ as a function of time are shown. Some numerical noise can also be seen in these results. It originates from the evaluation of the bubble acceleration which is needed in the calculation of the virtual mass term as outlined in Appendix B.

The predictions for bubbles with $d = 2.5$ mm and $-100 \text{ 1/s} < \omega < -10 \text{ 1/s}$ are given in the middle row of graphs in Figure 7.16. For weak shear rates, U_r is similar to that of a bubble in quiescent water, as shown in Figure 4.9. However, a reduction in U_r occurs as ω increases. Furthermore, it is evident that the bubble motion is almost steady for small ω and oscillating for large ones.

The results for the lift coefficient $C_{l\omega}$ for this bubble size are discussed next. It is striking that $C_{l\omega}$ oscillates for all ω considered. In fact, the fluctuations in $C_{l\omega}$ are largest for $\omega = -10 \text{ 1/s}$ and are reduced for $\omega = -20 \text{ 1/s}$. The time average of $C_{l\omega}$ is given in Table 7.2. For weak shear, the time-averaged lift coefficient is negative. However, it is interesting to note that it changes sign and becomes positive at extreme shear rates. This phenomenon, which has never been reported before, is probably due to the marked effects that the shear flow exerts on the bubble shape as well as its wake, as shown in Figure 7.14. In fact, the present study is the first of air-water bubbles at $\mathcal{S}r > 1$.

In the bottom row of the Figure 7.16 the results for $d = 5$ mm and $-30 \text{ 1/s} < \omega < -10 \text{ 1/s}$ are shown. They are very similar to those for $d = 2.5$ mm. Again, for weak shear rates, the magnitude of the relative velocity is similar to that of a bubble in quiescent water, as shown in Figure 4.3. However, an appreciable reduction of U_r and larger velocity fluctuations are evident for the strongest shear rates investigated ($\omega = -30 \text{ 1/s}$). It is also interesting to note that, in contrast to the results for $d = 2.5$ mm, $C_{l\omega}$ is always negative and does not change its sign for strong shear although $\mathcal{S}r$ for $d = 5$ mm, $\omega = -30 \text{ 1/s}$ and $d = 2.5$ mm, $\omega = -50 \text{ 1/s}$ are very similar.

Next, the time-averaged values for $C_{l\omega}$ (see Table 7.2) are compared with results given by other authors. For $d = 1$ mm and $\omega = -10 \text{ 1/s}$, the present result agree quite well with Auton's [10, 9] analysis for inviscid flow, *i.e.* $C_{l\omega}=0.5$. This is encouraging because his theory should apply when the bubble is almost spherical, *i.e.* when $\mathcal{R}e$ is large and $\mathcal{S}r$ is small. However, at $\omega = -50 \text{ 1/s}$ the results deviate significantly from

this value because $\mathcal{S}r$ is no longer small in this case.

It has been mentioned that Tomiyama et al. [389] extrapolated their experimental results obtained for air bubbles in glycerol-water solution to an air-water system. As shown in Figure 7.4b, their correlation predicts that the lift coefficient changes sign at $d = 5.6$ mm and is positive for smaller bubbles. For bubbles with $d < 4.3$ mm, it takes a constant value of 0.288, unless $\mathcal{R}e < 2.5$. This finding is contradictory to the results presented in this study. However, this has to be expected and supports the view that extrapolation over several orders of magnitude to an extremely low $\mathcal{M}o$ is of dubious validity because the unsteady motion and wake effects do not occur at high $\mathcal{M}o$.

The only experiments conducted at conditions similar to the ones considered in this study are those of Sridhar and Katz [359] and Ford and Loth [104]. Details of these are given in Section 7.2.5. Ford and Loth [104] reported lift coefficients measured in a turbulent shear layer for four bubbles sizes, which are given in Table 7.1. Unfortunately, they only give an upper bound to the dimensionless shear rate ($\mathcal{S}r < 1$), which complicates the comparison with the numerical results. For the smallest bubble ($d = 1.5$ mm) investigated by them, the value given by them ($C_{l\omega} = 0.04$) falls between those obtained in this study for weak flow, *i.e.* $\overline{C_{l\omega}} = 0.618$ and -0.234 for $d = 1.0$ and 2.5 mm, respectively. For the larger bubbles with $d = 2.5$ and 3.5 mm, they measured $C_{l\omega} = -0.09$ and -0.06, respectively. These values are slightly larger than those determined for weak shear in the present study, *i.e.* $\overline{C_{l\omega}} = -0.234$ and -0.128. However, larger discrepancies are apparent for the largest bubble ($d = 4.5$ mm) considered by Ford and Loth [104]. Here, their value of $C_{l\omega} = -0.7$ is much smaller than that calculated for $d = 5$ mm.

The results reported by Sridhar and Katz [359] are for relatively small, almost spherical bubbles ($0.5 < d < 0.8$ mm) entrained in a laminar ring vortex. They investigated moderate $\mathcal{R}e$ ($20 < \mathcal{R}e < 80$) and low $\mathcal{S}r$ ($0.01 < \mathcal{S}r < 0.1$). For the smallest bubble and the weakest shear rate considered in the present study, *i.e.* $d = 1$ mm and $\mathcal{S}r = 0.03$, their correlation (7.21) yields $C_{l\omega} = 4.8$, which is almost an order of magnitude larger than the value found in this work. However, Sridhar and Katz's [359] result is also at odds with the DNS performed by Legendre and Magnaudet [235] who give values of around $C_{l\omega} = 0.35$ for similar $\mathcal{R}e$, as shown in Figure 1.9.

7.6 Closure

This Chapter reviewed and formulated correlations to determine the lift force in dispersed two-phase systems. First, a comprehensive literature review of the state-of-the art in lift modelling for particles, droplets and bubbles, including the influence of elevated phase fractions, was presented

Next, the most promising models were implemented in the two-fluid methodology and validated for two gas-liquid test cases, *i.e.* the plane mixing layer and the sudden enlargement of a circular pipe. The importance of having a correct model for lift has been demonstrated by many authors, *e.g.* Lathouwers [228, p. 139] and Bel F'dhila [25], in that they could not obtain reasonable predictions of the phase fraction for the sudden enlargement test case when using $C_{l\omega} = 0.25$. However, the same model yields excellent results for the plane mixing layer, as shown by Hill et al. [148, 147]. These observations were confirmed in this study.

The lift models identified in the literature yield better results for the sudden enlargement. In particular, the unphysical accumulation of bubbles within the recirculation zone, which would be obtained with $C_{l\omega} = 0.25$, is greatly reduced and the predictions are in better agreement with the experimental findings. However, the results for the mixing layer were shown to be less favourable because the local extrema in the phase fraction profiles are reduced noticeably. In essence, it can be concluded that none of the lift models tested yields reasonable results for both the plane mixing layer and the sudden enlargement test cases.

As a step towards finding a general lift correlation, DNS calculations of single air bubbles in water were carried out to investigated their dynamics under conditions similar to those found in the two test cases. The results of this fundamental work stressed the marked influence of the wake dynamics. For example, for bubbles with $d = 2.5$ mm, weak shear has a stabilising effect on the wake dynamics and the lift coefficient takes negative values, whereas when the bubbles are subjected to stronger shear, their wake is suppressed and the lift coefficient becomes positive.

Some of DNS results agree favourable with the experimental data, whereas others clash considerably. However, it should be noted that the experimental findings are often contradictory amongst themselves because of the difficulties and uncertainties inherent

in the experimental techniques. Hence, it was impossible within this study to collect enough numerical and/or experimental data to derive a reliable lift model.

Chapter 8

Closure

This research work has been concerned with the development and validation of CFD methodology for simulating dispersed two-phase flows at high phase fractions. In this study, two-fluid and interface-capturing methodologies have been developed further, validated and utilised. Contributions have been made towards improved numerical techniques as well as mathematical models of key physical phenomena.

This last Chapter concludes the thesis and is divided in two Sections. The first Section summarises the conclusions acquired from this work and the second one makes suggestions for future work.

8.1 Conclusions

The results of the present study have been extensively assessed and discussed in the previous Chapters. In the following, the most important conclusions are summarised.

- Our current understanding of lateral forces on DPEs is far from complete. For high Reynolds numbers and/or high shear rates, the direction, let alone the magnitude, of the lift force is often unknown. Furthermore, deformations of fluid particles can produce negative lift and there is strong evidence, that the lift force is strongly affected by the dynamics of the wakes. Given this limited insight at low phase fraction, it is not surprising that very little is known about the influence of neighbouring DPEs on the lift force. However, there is evidence that the lift force diminishes rapidly as the phase fraction increases.

- The importance of having a correct model for lift was demonstrated in that reasonable predictions for the phase fraction profiles in a gas-liquid sudden enlargement flow cannot be obtained using the conventional lift model with $C_{l\omega} = 0.25$. However, this model yields excellent results for a gas-liquid plane mixing layer flow. These findings are in good agreement with previous calculations performed by Lathouwers [228], Bel F'dhila [25] and Hill et al. [148, 147]
- The lift models identified in the literature yield better results for the sudden enlargement flow than those obtained with conventional lift modelling. In particular, the unphysical accumulation of bubbles within the recirculation zone is greatly reduced. However, the previously excellent results for the mixing layer deteriorate when the new models are used. In particular, the magnitudes of the local maxima and minima of the volume fraction profiles are reduced noticeably. Therefore, it must be concluded that none of the lift models tested can yield reasonable results for both flows.
- The new interface-capturing methodology of Weller [424] is suitable for the DNS of millimeter-size air bubbles in water if the Morton number is sufficiently small ($\log(\mathcal{M}_o) \leq -4.2$). In particular, the findings using this method are:
 - The computational results for air bubbles rising in quiescent water showed many features previously described by experimentalists, *e.g.* path instabilities and the shedding of wakes. Two types of trajectories were observed depending on the bubble size: bubbles with nominal diameters larger than 2 mm prescribe a helical trajectory, whereas smaller bubbles exhibit zigzag motion.
 - The predicted terminal velocities of air bubbles in water with nominal diameters between 1 and 5 mm agree well with the empirical correlation of Tomiyama et al. [384, 383].
 - The velocity fluctuations of a 2.5 mm-bubble were compared with recent measurements by Ellingsen and Risso [88, 87]. The velocity in the horizontal direction are reasonably predicted, but the results for the vertical fluctuations are less favourable.

- For air bubbles in shear flow generated in a viscous liquid, the key experimental findings of Tomiyama et al. [389] were confirmed numerically, namely that the lift coefficient is independent of the shear rate in the parameter space investigated and that it changes sign for large Eötvös numbers. The results for the lift coefficient are in reasonable agreement with the measured ones if \mathcal{M}_0 is small. However, for larger \mathcal{M}_0 , large discrepancies are noticeable. These are probably due to the relatively coarse mesh, which should be refined in future studies.
- DNS calculations of single air bubbles in water were carried out to investigate the dynamics of the bubbles under conditions similar to those found in the mixing layer and sudden enlargement flow. The results of this work stress the marked influence of the wake on the bubble motion. For example, for bubbles with $d = 2.5$ mm, weak shear has a stabilising effect on the wake dynamics and the lift coefficient takes negative values. On the other hand, when the bubble is subjected to stronger shear, its wake is suppressed and the lift coefficient becomes positive. Unfortunately, it was not possible during this study to generate enough data with the given resources to derive a lift model based on the numerical results.
- Recent experimental data suggest that the turbulence response function is a strong function of the phase fraction and approaches unity as the phase fraction increases beyond a certain limit, which could be as small as 6%. A modified expression for C_t was proposed based on these data sets and has then been validated for the plane mixing layer and the sudden enlargement flows.

For the sudden enlargement flow, the previous C_t -model of Issa [171] overpredicts the turbulence kinetic energy of the continuous phase, with the consequence that the liquid velocity profiles are too diffused. However, the level of continuous phase turbulence obtained with the new model, is in much better agreement with the experimental data and it follows that the liquid velocity profiles are also greatly improved. The phase fraction field is much better predicted at stations close to the inlet and within the recirculation zone, but discrepancies with the experiments increase towards the outlet. Here, the redistribution of the bubbles towards the

centreline and, hence, the development towards fully developed two-phase pipe flow is underpredicted.

For the plane mixing layer flow, excellent predictions are obtained with the previous model, which are largely unchanged with the new formulation, except for the continuous phase kinetic energy, whose level is lower and in better agreement with the measurements.

- At low phase fractions, the drag on particles has been researched extensively and many correlations are available. They are believed to be accurate, although this has not been checked in this study. For single bubbles, a large number of models have been published in the literature and the recent models in particular yield very similar results. However, the effects of the surfactant concentration, the turbulence within the surrounding fluid and the history of the bubble are not well understood and not taken into account in the correlations. For single droplets, no accurate and reliable model is currently available.
- At elevated phase fractions, a comparison of particle drag models against experimental data showed that a number of correlations give reliable results. However, for fluid particles, large deviations exist not only between the models and the experimental evidence, but they are often contradictory amongst themselves. This is partly due to the fact that the dynamics of fluid particles at low phase fractions is not as well understood. Nevertheless, some of the correlations for elevated phase fractions are able to give reasonable predictions, although some of them lack generality.
- New drag correlations applicable to particles, droplets and bubbles at high phase fractions were put forward, which agree with the experimental data reasonably well. However, the correlations for particles could be improved at low Archimedes numbers by including the influence of the latter.
- Assessment of the drag models has also been carried out through application of two-fluid methodology to two test cases. The results for the plane mixing layer and sudden enlargement flows showed that the influence of the drag correlations on the liquid velocity profiles is negligible for both test cases. However, differences

are noticeable in the phase fraction profiles, which are most pronounced in the sudden enlargement flow. Here, the influence of the drag formulation is amplified by the back-flow generated behind the enlargement. However, the discrepancies between the measured and calculated phase fraction profiles for this flow cannot be explained by the dependence of the drag on the phase fraction.

- The standard solution procedure for the two-fluid methodology based on those outlined in [426, 295, 147] employs phase-intensive momentum equations. It is stable in situations where the phase fraction vanishes gradually and the convergence problems reported in earlier studies are avoided by preventing the phase momentum equations from becoming singular when the phase fraction approaches zero. However, the turbulent drag term compromises convergence if the related diffusion term in the phase fraction equation is discretised explicitly.
- The standard solution procedure is not sufficiently stable in cases where the phases separate and a decoupling of the pressure and the velocity field occurs. This can be prevented by using the solution procedure of Weller [423], which is stable even for high density ratios.

The advantages of the Weller [423] solution procedure were shown in two calculations: firstly, the separation of a gas-liquid mixture in a tank; and secondly, the transient motion of a bubble plume. In both cases, the calculation includes the region above the liquid, with the position of the free-surface being determined as part of the calculation wherever necessary. For the bubble plume, a preliminary comparison with experimental data was carried out, which showed that the motion of the plume is captured well.

8.2 Suggestions for Future Work

Before we proceed with recommendations for the future work, the important role of measurements has to be emphasised. Many sub-models in the two-fluid model rely on the availability and accuracy of measurements. Therefore, only more extensive experimental data will reduce the uncertainty inherent in some of the models and/or will give evidence of phenomena currently unaccounted for.

The author is not an expert in the experimental methods. Therefore, the suggestions which follow will be mainly directed towards researchers in the field of modelling and numerics. Tasks which are, arguably, of the most priority are as follows:

- Derivation of accurate and reliable correlations for the drag on fluid particles.
In particular, no accurate and reliable model currently exists for droplets. For bubbles, the effects of surfactant concentration, turbulence and the history of the bubble should be taken into account in the correlations.
- Performance of DNS of single bubbles in shear flow to gain better insight into the nature of the bubble wake and its effect on the bubble dynamics. Eventually, the data collected from these simulations should be used together with the available experimental data to derive a lift model for low \mathcal{M}_o . Such two-phase DNS can also provide valuable insight into many complex phenomena involving two-phase flow, *e.g.* turbulence, heat and mass transfer and phase change.
- Inclusion of Large Eddy Simulation (LES) turbulence models in the interface-capturing calculations. The shear flows investigated in this study had relatively high shear Reynolds numbers (7.24). However, in order to accurately represent the turbulence in these flows, very high resolution would be required. The main idea of LES is to filter the small scales out of the Navier-Stokes equations and resolve the larger ones. The smaller scales are represented using a so-called sub-grid model by relating the sub-grid Reynolds stress tensor to the sub-grid fluctuations.
- Validation of the current two-fluid methodology against a more complete set of experimental data. Several test cases were presented in Section 1.5.7. Of the cases listed there, the following ones could yield new insights:
 - Bubbly jets exhibit regions of high shear within the liquid phase and the accurate prediction of bubble distribution has been shown to depend on the lift modelling [439];
 - Bubble-driven flows where liquid velocity is smaller than or similar to the terminal velocity. In such cases, bubble-induced turbulence and large scale instabilities cause additional difficulties [227, 8].

Depending on the operating conditions, both types of flow can also exhibit regions where the phase fraction is high.

- Improvements in the turbulence modelling for the two-fluid methodology. Although the influence of turbulence modelling has not been investigated extensively, it is very likely that some of the discrepancies discovered in this study are due to deficiencies in the models used. For example, it is very difficult to incorporate the effects of large scale eddies, so-called coherent structures, on the averaged inter-phase momentum transfer.

However, the behaviour of bubbles within these coherent structures is described reasonably well by the equation of motion and the instantaneous forces therein, in particular the lift force. Therefore, a possible route is to derive a two-phase LES model, in which the coherent structures are not averaged, but fully resolved and an expression for the averaged inter-phase momentum transfer is not needed. However, the effects of the bubbles on the sub-grid Reynolds stress and the sub-grid inter-phase momentum transfer now require modelling. Initial LES calculations for gas-liquid flows are presented in [393].

The present study should be regarded as a further step towards the accurate simulation of dispersed two-phase flows. The two-fluid model presented in here has not addressed many important phenomena, such as heat- and mass transfer, size distribution effects as well as phase change. The inclusion of these into the framework of the two-fluid model is by no means uncharted territory and many researchers have made contributions towards it. However, it is unlikely that a single model will emerge eventually because of the many ways these phenomena interact with each other. More likely, several two-fluid methodologies will co-exist, each specialising in the aspects most relevant to the particular industrial application in mind. In this respect, it is the hope of the author that this study might serve as a tool-box to other modellers and engineers in industry who attempt the prediction of two-phase flows.

Appendix A

Determination of the Projected Diameter from Interface-Capturing Calculations

The characteristic diameter of a deformed bubble can be defined in many ways. Two definitions are in common use:

nominal diameter is defined as the diameter of a sphere having the same volume V as the Dispersed Phase Element (DPE);

projected diameter is defined as the diameter of a circle with the same area as the projection of the DPE normal to the relative velocity.

In principle, the projected diameter should be used to calculate the projected area used in the expression for the drag force. However, in most engineering calculations the projected diameter is unknown and difficult to obtain. Therefore, the nominal diameter is used instead.

Tomiyama et al. [389] choose the projected diameter to correlate their experimental data for the lift coefficient. They obtained it from high speed camera pictures taken during the experiments. In order to be able to compare their results with the interface tracking calculations, the projected diameter has to be determined from the calculations. This is, however, complicated by the fact that an exact full 3D description of the surface is not available.

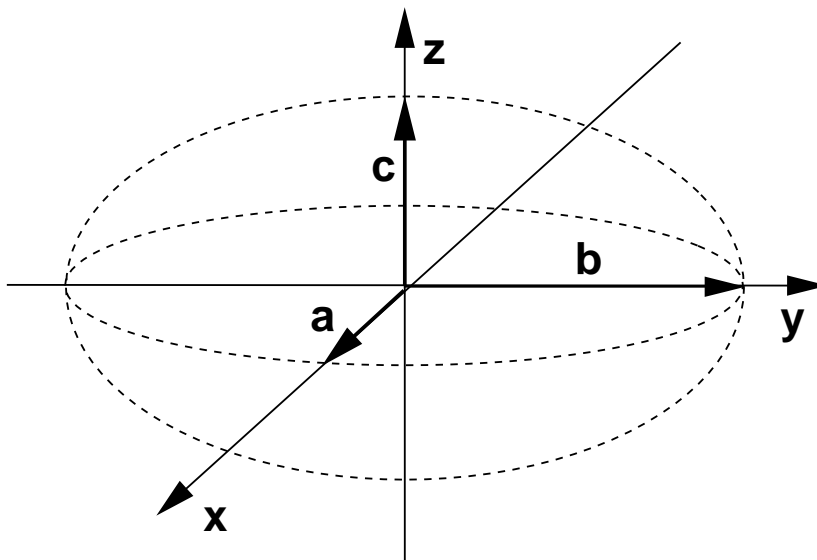


Figure A.1: Sketch of an ellipsoid.

An approximate solution to this problem is outlined next. Ellingsen and Risso [88, 87] investigated the shape and orientation of bubbles rising in still liquids. They found in their experiments that the bubble shape is an oblate ellipsoid of constant shape; and secondly, that the axis of symmetry of rising bubbles is parallel to the velocity of the bubble.

In following, it is therefore assumed that an ellipsoid, as shown in Figure A.1, is a good approximation for a DPE. The lengths of its half axes a, b and c can be determined by comparing the principal moments of inertia of the distribution of the indicator function with the analytical results for an ellipsoid. In order to simplify the analysis, we require that the DPE is spherical or flat as well as axisymmetric with respect to the z -axis of the local coordinate system of the ellipsoid, *i.e.* $a, b < c$ and $a = b$. It is also assumed that the relative velocity is parallel to the z -axis. These assumptions hold for the high \mathcal{M}_o bubbles investigated in Section 4.3.2, as evident from Figure 4.13. However, none of these restrictions are strictly necessary and the analysis could be refined further in future.

In the general, the moment inertia of an arbitrary body is given by the following symmetric second rank tensor [422]:

$$\Theta = \int_V \rho (|\mathbf{r}|^2 \mathbf{I} - \mathbf{r}\mathbf{r}) dV \quad (\text{A.1})$$

where Θ is the moment of inertia. ρ and \mathbf{I} denote the density and the identity tensor, respectively. \mathbf{r} stands for the vector between dV and a reference point, usually the centre of mass. The principle moments of inertia are obtained by taking the eigenvalues of Θ .

First, we obtain the moment of inertia of a DPE from the results of the interface-capturing calculations. The moment of inertia tensor is approximated by:

$$\Theta^C = \rho_a \sum_{P=all} \gamma_P (|\hat{\mathbf{x}}_P - \hat{\mathbf{x}}_d|^2 \mathbf{I} - (\hat{\mathbf{x}}_P - \hat{\mathbf{x}}_d)^2) V_P \quad (\text{A.2})$$

where ρ_a is the fluid density. Here, V stands for the volumes of the computational cells and $\hat{\mathbf{x}}$ is the position vector. The subscript P denotes the value for the cell P and the indicator function γ is defined in Section 4.1.1. $\hat{\mathbf{x}}_d$ is the centre of mass of the DPE, which is calculated from:

$$\hat{\mathbf{x}}_d = \frac{\sum_{P=all} \gamma_P \hat{\mathbf{x}}_P V_P}{\sum_{P=all} \gamma_P V_P} \quad (\text{A.3})$$

The orientation of the DPE is unknown in the calculations and the principal moments of inertia are therefore obtained by calculating the eigenvalues of Θ^C which are denoted by Θ_{xx}^C , Θ_{yy}^C and Θ_{zz}^C .

This numerical result is then compared with the analytical result for an ellipsoid, as depicted in Figure A.1. With respect to the three local coordinate axes, the principal moments of inertia are given by Merziger and Wirth [272, p. 495] as:

$$\Theta_{xx}^E = \rho \frac{4}{15} \pi abc (b^2 + c^2) \quad (\text{A.4})$$

$$\Theta_{yy}^E = \rho \frac{4}{15} \pi abc (a^2 + c^2) \quad (\text{A.5})$$

$$\Theta_{zz}^E = \rho \frac{4}{15} \pi abc (a^2 + b^2) \quad (\text{A.6})$$

In our case, we assume that the ellipsoid is symmetric with respect to z -axis, i.e. $a = b$, and the result can be further simplified:

$$\Theta_{zz}^E = \rho \frac{8}{15} \pi (l^4 m) \quad (\text{A.7})$$

$$\Theta_{xx}^E = \Theta_{yy}^E = \rho \frac{4}{15} \pi (l^4 m + l^2 m^3) \quad (\text{A.8})$$

where $l = a = b$ is the major axis and $m = c$ is the minor axis of the ellipsoid.

The minor and major axes of the DPE are obtained by replacing the analytical results for the principal moments of inertia by the numerical ones. Finally, after substitution of equation (A.7) into equation (A.8), algebraic expressions for l and m are obtained:

$$l = \sqrt[10]{\frac{15^2}{8^2\pi^2\rho^2} \frac{(\Theta_{zz}^C)^3}{2\Theta_{yy}^C - \Theta_{zz}^C}} \quad (\text{A.9})$$

$$m = \frac{15\Theta_{zz}^C}{8\pi\rho l^4} \quad (\text{A.10})$$

Appendix B

Determination of the Lift Coefficient from Interface-Capturing Calculations

The lift coefficient is not an immediate result of the interface-capturing calculations and some post-processing is required to obtain its value. In this study, a procedure is utilised similar to that employed by Sridhar and Katz [359] who determined the lift coefficient from bubble trajectories. Here, it is adapted to obtain the lift coefficient from interface-capturing calculations.

Consider the equation of motion for a Dispersed Phase Element (DPE) given by:

$$-\rho_d V \frac{d\mathbf{V}_d}{dt} = \mathbf{F}_b + \mathbf{F}_p + \mathbf{F}_{vm} + \mathbf{F}_b + \mathbf{F}_d + \mathbf{F}_l + \mathbf{F}_b \quad (\text{B.1})$$

where the terms on the r.h.s. are, in order, buoyancy, pressure, virtual mass, drag, lift and Basset forces. Sridhar and Katz [359] showed that for small bubbles in a shear flow the Basset force only accounts for up to 6% of the buoyancy force and it is therefore neglected.

The functional forms for these forces have been subject to intensive research [274, 260, 11, 264]. In this study, we follow Sridhar and Katz [359] and use:

$$\mathbf{F}_b = V (\rho_d - \rho_c) \mathbf{g} \quad (\text{B.2})$$

$$\mathbf{F}_p = \rho_c V \frac{D_c \mathbf{V}_c}{Dt} \quad (\text{B.3})$$

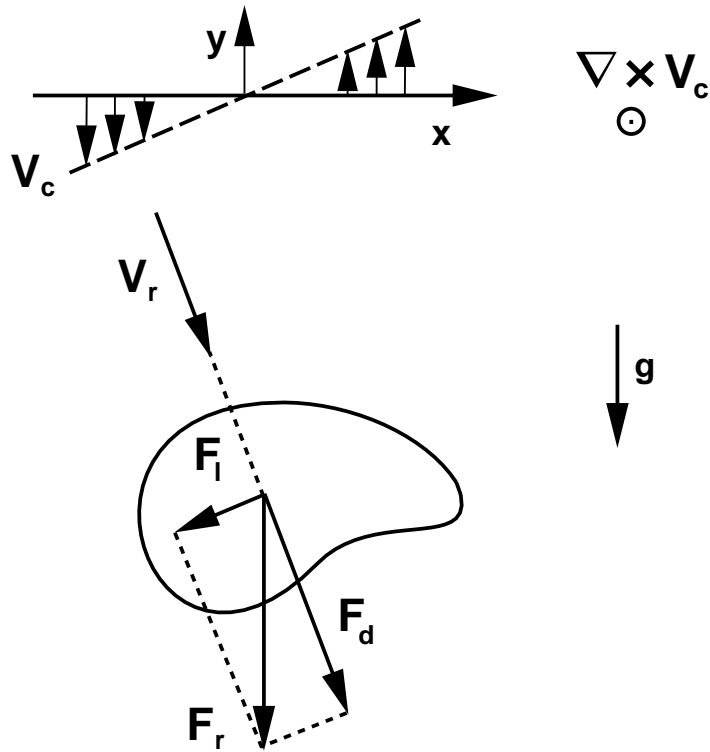


Figure B.1: Forces on a dispersed phase element in a simple shear flow.

$$\mathbf{F}_{vm} = \rho_c V C_{vm} \left(\frac{d\mathbf{V}_d}{dt} - \frac{D_c \mathbf{V}_c}{Dt} \right) \quad (\text{B.4})$$

$$\mathbf{F}_d = \frac{1}{2} \rho_c A C_d |\mathbf{V}_r| \mathbf{V}_r \quad (\text{B.5})$$

$$\mathbf{F}_c = \rho_c V C_l \mathbf{V}_r \times (\nabla \times \mathbf{V}_c) \quad (\text{B.6})$$

Here, ρ and \mathbf{V} stand for the density and velocity, respectively, and the subscripts c and d for the properties of the continuous and dispersed material. \mathbf{V}_r is the relative velocity defined as $\mathbf{V}_r = \mathbf{V}_c - \mathbf{V}_d$. The volume of the DPE and its projected area normal to \mathbf{V}_r are denoted by V and A . C_d , C_l and C_{vm} are the coefficients in the drag, lift and virtual mass models.

The velocity of the continuous fluid \mathbf{V}_c at the centre of the DPE, its substantive derivative $\frac{D_c \mathbf{V}_c}{Dt}$ and its vorticity $\nabla \times \mathbf{V}_c$ appear in the above equations. These quantities have to be evaluated in absence of the DPE, *i.e.* \mathbf{V}_c is the so-called unperturbed velocity [260]. In this study, the motion of a single DPE in simple shear flow is investigated. Such a flow is depicted in Figure B.1 and is defined by:

$$\mathbf{V}_c = \begin{pmatrix} 0 \\ -\omega x \\ 0 \end{pmatrix} \quad (4.37)$$

where ω and x denote the shear rate and x -coordinate, respectively. The vorticity

of this flow is given by $\nabla \times \mathbf{V}_c = \begin{pmatrix} 0 \\ 0 \\ \omega \end{pmatrix}$ and it can further be shown that $\frac{D_c \mathbf{V}_c}{Dt} = 0$. This simplifies the analysis substantially and the following expression for the sum of the drag and lift forces \mathbf{F}_r is obtained after substitution of equations (B.2) and (B.4) into equation (B.1):

$$\mathbf{F}_r = V (\rho_c - \rho_d) \mathbf{g} - V (\rho_d + C_{vm} \rho_c) \frac{d\mathbf{V}_d}{dt} \quad (\text{B.7})$$

Finally, \mathbf{F}_r is decomposed into its components, *i.e.* drag and lift, using:

$$\mathbf{F}_d = \frac{\mathbf{F}_r \cdot \mathbf{V}_r}{|\mathbf{V}_r|} \quad (\text{B.8})$$

$$\mathbf{F}_l = \mathbf{F}_r - \mathbf{F}_d \quad (\text{B.9})$$

and the associated coefficients are then easily calculated from:

$$C_d = \frac{2|\mathbf{F}_d|}{\rho_c A \mathbf{V}_r^2} \quad (\text{B.10})$$

$$C_l = \frac{2|\mathbf{F}_l|}{\rho_c V |\mathbf{V}_r \times (\nabla \times \mathbf{V}_c)|} \quad (\text{B.11})$$

What remains is to give details of the determination of the bubble velocity \mathbf{V}_d , its acceleration $\frac{d\mathbf{V}_d}{dt}$ and the position of the bubble \mathbf{x}_d , which is needed to calculate the velocity of the continuous fluid from equation (4.37). These quantities are needed relative to the inertial reference frame and are not directly available from the interface-capturing calculations, which are performed relative to a moving reference frame, as outlined in Section 4.1.3. However, they can be determined from the velocity of the reference frame \mathbf{V}_F and the bubble position relative to the frame $\hat{\mathbf{x}}_d$, which are determined from equations (A.3) and (4.33), respectively, and recorded for each time step. The analysis requires numerical differentiation and integration and is performed a-posteriori, *i.e.* after the CFD calculations. In this way, the values for the next time step are available and the derivatives can be evaluated more accurately using central differences. The numerical schemes are second order accurate and given by:

$$\mathbf{V}_d^i = \mathbf{V}_F^i + \frac{\hat{\mathbf{x}}_d^{i+1} - \hat{\mathbf{x}}_d^{i-1}}{t^{i+1} - t^{i-1}} \quad (\text{B.12})$$

$$\left(\frac{d\mathbf{V}_d}{dt} \right)^i = \frac{\mathbf{V}_d^{i+1} - \mathbf{V}_d^{i-1}}{t^{i+1} - t^{i-1}} \quad (\text{B.13})$$

$$\mathbf{x}_d^i = \hat{\mathbf{x}}_d^i + \sum_{j=2 \dots i} \frac{\mathbf{V}_F^j + \mathbf{V}_F^{j+1}}{2} (t^j - t^{j-1}) \quad (\text{B.14})$$

Here, the superscript denotes values at specific time steps.

Bibliography

- [1] E. Achenbach. Vortex shedding from spheres. *J. Fluid Mech.*, 62:209–211, 1974.
- [2] H. S. Allen. The motion of a sphere in a viscous fluid. *Phil. Mag.*, page 519, 1900.
- [3] F. Aloui and M. Souhar. Experimental study of a two-phase bubbly flow in a flat duct symmetric sudden expansion – I: Visualization, pressure and void fraction. *Int. J. Multiphase Flow*, 22(4):651–665, 1996.
- [4] F. Aloui and M. Souhar. Experimental study of a two-phase bubbly flow in a flat duct symmetric sudden expansion – II: Liquid and bubble velocities, bubble sizes. *Int. J. Multiphase Flow*, 22(5):849–861, 1996.
- [5] K. E. B. Andersson. Pressure drop in ideal fluidization. *Chem. Eng. Sci.*, 15: 276–297, 1960.
- [6] N. Ashgriz and J. Y. Poo. FLAIR: flux line-segment model for advection and interface reconstruction. *J. Comp. Phys.*, 93:449–468, 1991.
- [7] F. Augier. *Structure locale du champ hydrodynamique dans les écoulements dispersés liquide-liquide concentrés*. PhD thesis, Institut National Polytechnique de Toulouse, 2001.
- [8] F. Augier, P. Guiraud, and O. Masbernat. Volume fraction gradient induced flow patterns in a two-liquid phase mixing layer. In Michaelides et al. [275].
- [9] T. R. Auton. The lift on a spherical body in a rotational flow. *J. Fluid Mech.*, 183:199–218, 1987.
- [10] T. R. Auton. *The Dynamics of Bubbles, Drops and Particles in Motion in Liquids*. PhD thesis, University of Cambridge, 1988.
- [11] T. R. Auton, J. C. R. Hunt, and M. Prud’homme. The force exerted on a body in inviscid unsteady non-uniform rotational flow. *J. Fluid Mech.*, 197:241–257, 1988.
- [12] N. M. Aybers and A. Tapucu. The motion of gas bubbles rising through a stagnant liquid. *Wärme- und Stoffübertragung*, 2:118–128, 1969.
- [13] A. Bakker and H. E. A. van den Akker. A computational model for the gas-liquid flow in stirred reactors. *Chem. Eng. Res. Des., Part A: Trans. IChemE*, 72:594–606, 1994.

- [14] H. Z. Barakat and J. A. Clark. Analytical and experimental study of transient laminar natural convection flows in partially filled containers. In *Third Int. Heat Transfer Conf.*, volume II, 1966. paper 57.
- [15] E. Barnea and J. Mizrahi. A generalised approach to the fluid-dynamics of particulate systems – I. General correlation for fluidization and sedimentation. *Chem. Eng. J.*, 5:171–189, 1973.
- [16] E. Barnea and J. Mizrahi. A generalised approach to the fluid-dynamics of particulate systems: II: Sedimentation and fluidisation of clouds of spherical liquid drops. *Canadian J. Chem. Eng.*, 53:461–468, 1975.
- [17] B. Basara, A. Alajbegović, F. J. Moraga, and F. J. Bonetto. The lift force on a cylinder in a high Reynolds number shear flow. In ICMF98 [161].
- [18] A. B. Basset. *A Treatise on Hydrodynamics*. Cambridge Univ. Press, 1888.
- [19] G. K. Batchelor. *An Introduction to Fluid Dynamics*. Cambridge Univ. Press, 1967.
- [20] S. Becker. *Experimentelle Untersuchungen von Blasensäulen als Basis für detallierte Modellrechnungen*. PhD thesis, Universität Stuttgart, 1997. see also Fortschritt-Berichte VDI : Reihe 3, Volume 467.
- [21] S. Becker, A. Sokolichin, and G. Eigenberger. Gas-liquid flow in bubble columns and loop reactors – II. Comparison of detailed experiments and flow simulations. *Chem. Eng. Sci.*, 49:5747–5762, 1994.
- [22] C. Beckermann, H.-J. Diepers, I. Steinbach, A. Karma, and X. Tong. Modeling melt convection in phase-field simulations of solidification. *J. Comp. Phys.*, 154: 468, 1999.
- [23] A. Behzadi, R. I. Issa, and H. Rusche. Effects of turbulence on inter-phase forces in dispersed flow. In Michaelides et al. [275].
- [24] A. Behzadi, R. I. Issa, and H. Rusche. Modelling of dispersed bubble flow at high phase fractions. submitted to *Chem. Eng. Sci.*, 2002.
- [25] R. Bel F'dhila. *Analyse expérimentale et modélisation d'un écoulement vertical à bulles dans un élargissement brusque*. PhD thesis, Institut National Polytechnique de Toulouse, 1991.
- [26] R. Bel F'dhila, L. Masbernat, and C. Suzanne. Measurements in two-phase bubbly flows in complex geometries. In G. F. Hewitt, F. Mayinger, and J. R. Riznic, editors, *Phase-Interface Phenomena in Multiphase Flow*, pages 245–257. Hemisphere Publ. Corp., Washington, 1991.
- [27] R. Bel F'dhila and O. Simonin. Eulerian prediction of a turbulent bubbly flow downstream of a sudden pipe expansion. In Sommerfeld [354], pages 141–148.
- [28] R. Bel F'dhila, C. Suzanne, and L. Masbernat. Two-phase bubbly flow measurements in a vertical sudden pipe expansion. In Sommerfeld [354], pages 1392–1401.

- [29] A. E. Bergles, J. G. Collier, J. M. Delhaye, G. F. Hewitt, and F. Mayinger, editors. *Two-phase Flow and Heat Transfer in the Power and Process Industries*. Hemisphere Publ. Corp., Washington, 1981.
- [30] A. Berlemon, P. Desjonquieres, and G. Gouesbet. Particle Lagrangian simulation in turbulent flows. *Int. J. Multiphase Flow*, 16(1):19–34, 1990.
- [31] S. W. Beyerlein, R. K. Cossmann, and H. Richter. Prediction of bubble concentration profiles in vertical turbulent two-phase flow. *Int. J. Multiphase Flow*, 11:629–641, 1985.
- [32] N. Boisson and M. R. Malin. Numerical prediction of two-phase flow in bubble columns. *Int. J. Num. Meth. Fluids*, 23:1289–1310, 1996.
- [33] W. N. Bond and D. A. Newton. Bubbles, drops and Stokes' law (paper 2). *Phil. Mag. J. Sci.*, 5(31):794–800, 1928.
- [34] Boulange. *Parties de pression dans un tube parcouru par un écoulement diphasique à bulles*. PhD thesis, Ecole Centrale de Paris, 1991.
- [35] J. Boussinesq. Théorie de l'écoulement tourbillant. *Mem. par. div. Sav., Paris*, 23:46, 1877.
- [36] L. A. Bozzi, J. Q. Feng, T. C. Scott, and A. J. Pearlstein. Steady axisymmetric motion of deformable drops falling or rising through a homoviscous fluid in a tube at intermediate Reynolds number. *J. Fluid Mech.*, 336:1–32, 1997.
- [37] J. U. Brackbill, D. B. Kothe, and C. Zemach. A continuum method for modelling surface tension. *J. Comp. Phys.*, 100:335–354, 1992.
- [38] H. Brauer. Impuls-, Stoff und Wärmetransport durch die Grenzfläche kugelförmiger Partikeln. *Chem. Ing. Tech.*, 45:1099–1103, 1973.
- [39] D. Brennan. *The Numerical Simulation of Two-Phase Flows in Settling Tanks*. PhD thesis, Imperial College, University of London, 2001.
- [40] F. P. Bretherton. The motion of rigid particles in a shear flow at low Reynolds number. *J. Fluid Mech.*, 14:284–304, 1962.
- [41] S. Bröring, J. Fischer, T. Korte, S. Sollinger, and A. Lübbert. Flow structure of the dispersed gas phase in real multiphase chemical reactors investigated by a new ultrasound-doppler technique. *Can. J. Chem. Eng.*, 69:1247–1256, 1991.
- [42] B. Bunner and G. Tryggvason. Direct numerical simulation of three-dimensional bubbly flow. *Phys. Fluids*, 11:1967, 1999.
- [43] M. B. Carver. A method of limiting intermediate values of volume fraction in iterative two-fluid computations. *J. Mech. Eng. Sci.*, 24(4):221–224, 1982.
- [44] M. B. Carver. Numerical computation of phase separation in two fluid flow. *J. Fluids Eng., Trans. ASME*, 106:147–153, 1984.

- [45] M. B. Carver and M. Salcudean. Three-dimensional numerical modeling of phase distribution of two-fluid flow in elbows and return bends. *Num. Heat. Trans.*, 10: 229–251, 1986.
- [46] M. Casey, E. Lang, R. Mack, R. Schlegel, and M. Wehrli. Applications of computational fluid dynamics for process engineering at Sulzer. *Speedup J.*, 12(1): 43–51, 1988.
- [47] G. P. Celata et al., editors. *Proc. 2nd Symp. on Two-Phase Flow Modelling and Experimentation, Rome, Italy*, May 23–26, 1999. Edizioni ETS, Italy.
- [48] L. Chen, S. V. Garimella, J. A. Reizes, and E. Leonardi. Motion of interacting gas bubbles in a viscous liquid including wall effects and evaporation. *Num. Heat. Transfer A*, 31:629–654, 1997.
- [49] L. Chen, S. V. Garimella, J. A. Reizes, and E. Leonardi. The development of a bubble rising in a viscous liquid. *J. Fluid Mech.*, 387:61–96, 1999.
- [50] P. Cherukat, J. B. McLaughlin, and D. S. Dandy. A computational study of the inertial lift on a sphere in a linear shear flow field. *Int. J. Multiphase Flow*, 25: 15–33, 1999.
- [51] P. Cherukat, J. B. McLaughlin, and A. L. Graham. The inertial lift on a rigid sphere translating in a linear shear flow field. *Int. J. Multiphase Flow*, 20(2): 339–353, 1994.
- [52] A. K. Chesters. An approximate bubble-eddy interaction model. In *Symp. Int. Union Th. Appl. Mech., Birmingham, UK*, 1993. see [89].
- [53] C. I. Christov and P. K. Volkov. Numerical investigation of the steady viscous flow past a stationary deformable bubble. *J. Fluid Mech.*, 158:341–364, 1985.
- [54] R. Clift and W. H. Gauvin. The motion of particle in turbulent gas streams. In *Proc. Chemeca '70*, volume 33 of *IChemE Symp. Ser.*, pages 14–28, Melbourne, Aug 19–26, 1970. Butterworths of Australia.
- [55] R. Clift and W. H. Gauvin. Motion of entrained particles in gas streams. *Canadian J. Chem. Eng.*, 49:439, 1971.
- [56] R. Clift, J. R. Grace, and M. E. Weber. *Bubbles, Drops and Particles*. Academic Press, London, 1st edition, 1978.
- [57] P. Colella and P. Woodward. The piecewise parabolic method (PPM) for gas-dynamics simulations. *J. Comp. Phys.*, 54:174–201, 1984.
- [58] H. W. Coleman, editor. *Proc. 1996 ASME Fluids Engineering Division Summer Meeting, San Diego, CA, USA*, Jul 7–11, 1996.
- [59] C. Colin and D. Legendre. Bubble distribution in turbulent shear flows: Experiments and numerical simulations on single bubbles. In Michaelides et al. [275].

- [60] R. Courant, E. Isaacson, and M. Rees. On the solution of non-linear hyperbolic differential equations by finite differences. *Comm. Pure Appl. Math.*, 5:243, 1952.
- [61] R. R. Cousins. A note on the shear flow past a sphere. *J. Fluid Mech.*, 40:543–547, 1970.
- [62] R. G. Cox and S. G. Mason. Suspended particles in fluid flow through tubes. *Ann. Rev. Fluid Mech.*, 3:291–316, 1971.
- [63] C. T. Crowe. Review – numerical models for dilute gas-particle flows. *J. Fluids Eng., Trans. ASME*, 104:297–303, 1982.
- [64] C. T. Crowe et al., editors. *Numerical methods in multiphase flows: presented at the 1994 ASME Fluids Engineering Division Summer Meeting, Lake Tahoe, NV, USA*, volume 185, Jun 19-23, 1994.
- [65] C. T. Crowe, M. Sommerfeld, and Y. Tsuji. *Multiphase Flow with Droplets and Particles*. CRC Press, 1998.
- [66] C. T. Crowe, T. R. Troutt, and J. N. Chung. Numerical models for two-phase turbulence. *Ann. Rev. Fluid Mech.*, 28:11–43, 1996.
- [67] B. Cuenot, J. Magnaudet, and B. Spennato. Effects of slightly soluble surfactants on the flow around a spherical bubble. *J. Fluid Mech.*, 339:25–53, 1997.
- [68] B. J. Daly. Numerical study of two fluid Raleigh-Taylor instability. *Phys. Fluids*, 10(2):297–307, 1967.
- [69] B. J. Daly. A technique for including surface tension effects in hydrodynamic calculations. *J. Comp. Phys.*, 4:97–117, 1969.
- [70] D. S. Dandy and H. A. Dwyer. Sphere in shear flow at finite Reynolds number. effect of shear on particle lift, drag, and heat transfer. *J. Fluid Mech.*, 216:381–410, 1990.
- [71] D. S. Dandy and Leal. Buoyancy-driven motion of a deformable drop through a quiescent liquid at intermediate Reynolds numbers. *J. Fluid Mech.*, 208:161–192, 1988.
- [72] C. Darwin. Note on hydrodynamics. *Proc. Camb. Phil. Soc.*, 49:342–354, 1953.
- [73] R. M. Davies and G. I. Taylor. The mechanics of large bubbles rising through extended liquids and through liquids in tubes. *Proc. R. Soc. London, Ser. A*, 200:375–390, 1950.
- [74] S. F. Davis. Flux difference splittings and limiters for the resolution of contact discontinuities. *Appl. Math. Comp.*, 65:3–18, 1994.
- [75] S. Decker and M. Sommerfeld. Numerical calculations of two-phase flows in agitated vessels using the Euler/Lagrange approach. In D. E. Stock, editor, *Proc. 2000 ASME Fluids Engineering Division Summer Meeting, Boston, MA USA*, Jun 11-15, 2000.

- [76] E. Delnoij. *Fluid Dynamics of Gas-Liquid Bubble Columns*. PhD thesis, Universiteit Twente, 1999.
- [77] E. Delnoij, F. A. Lammers, J. A. M. Kuipers, and W. P. M. van Swaaij. Dynamic simulation of dispersed gas-liquid two-phase flow using a discrete bubble model. *Chem. Eng. Sci.*, 52(9):1429–1458, 1997.
- [78] R. Djebbar, M. Roustan, and A. Line. Numerical computation of turbulent gas-liquid dispersion mechanically agitated vessels. *Chem. Eng. Res. Des., Part A: Trans. IChemE*, 74:492–498, 1996.
- [79] C. Dopazo. On conditional averages for intermittent turbulent flows. *J. Fluid Mech.*, 81(3):433–438, 1977.
- [80] J. K. Dukowicz. A particle-fluid numerical model for liquid sprays. *J. Comp. Phys.*, 155:229–253, 1980.
- [81] F. Durst, D. Milojevic, and B. Schönung. Eulerian and Lagrangian predictions of particulate two-phase flows: A numerical study. *Appl. Math. Modelling*, 8:101–115, 1984.
- [82] F. Durst, A. M. K. P. Taylor, and J. F. Whitelaw. Experimental and numerical investigation of bubble-driven laminar flow in an axisymmetric vessel. *Int. J. Multiphase Flow*, 5:557–569, 1984.
- [83] R. M. Edge and C. D. Grant. The terminal velocity and frequency of oscillation of drops in pure systems. *Chem. Eng. Sci.*, 26:1001–1012, 1971.
- [84] D. A. Edwards, H. Brenner, and D. T. Wasan. *Interfacial Transport Processes and Rheology*. Butterworth-Heinemann, Boston, 1991.
- [85] R. Eichhorn and S. Small. Experiments on the lift and drag on spheres suspended in Poiseuille flows. *J. Fluid Mech.*, 20:513–527, 1964.
- [86] S. Elgobashi. On predicting particle-laden turbulent flows. *Appl. Sci. Res.*, 52:309–329, 1994.
- [87] K. Ellingsen and F. Risso. Measurements of the flow field induced by the motion of a single bubble. In ICMF98 [161].
- [88] K. Ellingsen and F. Risso. On the rise of an ellipsoidal bubble in water : oscillatory paths and liquid induced velocity. *J. Fluid Mech.*, 2001.
- [89] K. Eppinger. *Étude du mouvement des bulles dans une turbulence homogène isotrope*. PhD thesis, Institut National Polytechnique de Toulouse, 1995.
- [90] S. Ergun. Fluid flow through packed columns. *Chem. Eng. Progr.*, 48:89, 1952.
- [91] E. A. Ervin and G. Tryggvason. Rise of bubbles in a vertical shear flow. *J. Fluids Eng., Trans. ASME*, 119:443–449, 1997.
- [92] A. Esmaeeli and G. Tryggvason. An inverse energy cascade in two-dimensional low reynolds number bubbly flows. *J. Fluid Mech.*, 314:315–330, 1996.

- [93] A. Esmaeeli and G. Tryggvason. Direct numerical simulation of bubbly flows – I. Low reynolds number arrays. *J. Fluid Mech.*, 377:313, 1998.
- [94] A. Esmaeeli and G. Tryggvason. Direct numerical simulation of bubbly flows – II. Moderate reynolds number arrays. *J. Fluid Mech.*, 385:325, 1999.
- [95] L. S. Fan and K. Tsuchiya. *Bubble Wake Dynamics in Liquids and Liquid-Solid Suspensions*. Butterworth-Heinemann, Boston, 1st edition, 1990.
- [96] J. H. Farmer, L. Martinelli, and A. Jameson. Fast multigrid method for solving incompressible hydrodynamic problems with free surfaces. *AIAA J.*, 32:1175–1182, 1994.
- [97] B. Farrar and H. H. Bruun. Computer based hot-film technique used for flow measurements in a vertical kerosene-water pipe flow. *Int. J. Multiphase Flow*, 22:733–751, 1996.
- [98] FEDSM97, editor. *Proc. 1997 ASME Fluids Engineering Division Summer Meeting, Vancouver, Can*, Jun 22-26, 1997.
- [99] J. H. Ferziger and M. Perić. *Computational Methods for Fluid Dynamics*. Springer-Verlag, Berlin, 1996.
- [100] J. Fischer, S. Bröring, and A. Lübbert. Gas-phase properties in stirred tank bioreactors. *Chem. Eng. Tech.*, 15:390–394, 1992.
- [101] R. L. C. Flemmer and C. L. Banks. On the drag coefficient of a sphere. *Powder Tech.*, 48:217–221, 1986.
- [102] J. M. Floryan and H. Rasmussen. Numerical methods for viscous flow with moving boundaries. *Appl. Mech. Rev.*, 42:323–340, 1989.
- [103] H. Fogt. *Die Anwendung des Zwei-Fluid Modelles auf die numerische Berechnung der Strömung von Gas-Flüssigkeitsgemischen mit hohem Gasphasenanteil*. PhD thesis, Universität Erlangen-Nürnberg, 1993. see also Fortschritt-Berichte VDI : Reihe 7, Volume 232.
- [104] B. Ford and E. Loth. Forces on ellipsoidal bubbles in a turbulent shear layer. *Phys. Fluids*, 10(1):178–188, 1998.
- [105] B. Fornberg. Steady viscous flow past a sphere at high Reynolds numbers. *J. Fluid Mech.*, 190:471–489, 1988.
- [106] M. J. Fritts and J. P. Boris. The Lagrangian solution of transient problems in hydrodynamics using a triangular mesh. *J. Comp. Phys.*, 31:173–215, 1979.
- [107] Y. C. Fung. *Classical and computational solid mechanics*. World Scientific, Singapore, 2001.
- [108] D. E. Fyfe, E. S. Oran, and M. J. Fritts. Surface tension and viscosity with Langrangian hydrodynamics on a triangular mesh. *J. Comp. Phys.*, 76:349–384, 1988.

- [109] C. Garnier, M. Lance, and J. L. Marié. Measurements of local flow characteristics in buoyancy-driven bubbly flow at high void fraction. In Michaelides et al. [275].
- [110] J. Garside and M. R. Al-Diboui. Velocity-voidage relationships for fluidization and sedimentation in solid-liquid systems. *Ind. Eng. Chem., Proc. Des. Dev.*, 16: 206–214, 1977.
- [111] L. Garwin and D. Smith. Liquid-liquid spray-tower operation in heat transfer. *Chem. Eng. Prog.*, 49(11):591–602, 1961.
- [112] R. A. Gentry, R. E. Martin, and B. J. Daly. An Eulerian differencing method for unsteady compressible flow problems. *J. Comp. Phys.*, 5:243, 1952.
- [113] H. Glaeser and H. Brauer. *Berechnung des Impuls- und Stofftransports durch die Grenzfläche einer formveränderlichen Blase*. Number 581 in VDI-Forschungsheft. VDI Verlag, 1977.
- [114] J. Glimm, J. Grove, B. Lindquist, O. A. Mc Bryan, and G. Tryggvason. The bifurcation of tracked scalar waves. *SIAM J. Sci. Stat. Comp.*, 9(1):61–79, 1988.
- [115] J. Glimm, O. A. McBryan, R. Menikoff, and D. H. Sharp. Front tracking applied to Rayleigh-Taylor instability. *SIAM J. Sci. Stat. Comp.*, 7(1):230–251, 1986.
- [116] A. J. Goldsmith and S. G. Mason. The microrheology of dispersions. In F. R. Eirich, editor, *Rheology Theory and Applications*, pages 85–250. Academic Press, London, 1967.
- [117] G. H. Golub and C. van Loan. *Matrix Computations*. John Hopkins Press, Baltimore, 1990.
- [118] S. Gomes, N. Gilbert, D. Pfleger, and H.-G. Wagner. Experimental investigation of two-phase gas-liquid flows in bubble column reactors. In *Proc. of Meßtechnik für instationäre und transiente Mehrphasenströmungen*, volume FZR 241, pages 75–82. FZR Rosendorf, Germany, 1998.
- [119] A. D. Gosman. Developments in industrial computational fluid dynamics. *Chem. Eng. Res. Des.*, 76(A2):153–161, 1998.
- [120] A. D. Gosman and E. Ioannides. Aspects of computer simulation of liquid-fueled combustors. *AIAA J. Energy*, 7(6):482–490, 1983.
- [121] A. D. Gosman, R. I. Issa, C. Lekakou, M. K. Looney, and S. Politis. Multidimensional modelling of turbulent two-phase flows in stirred vessels. *AICHE J.*, 38(12):1946–1956, 1992.
- [122] G. Gouesbet and A. Berlemont. Eulerian and Lagrangian approaches for predicting the behaviour of discrete particles in turbulent flows. *Prog. Energy Combustion Sci.*, 25:133–159, 1999.
- [123] J. R. Grace. Shapes and velocities of bubbles rising in infinite liquids. *Trans. IChemE*, 51:116–120, 1973.

- [124] J. R. Grace, T. Wairegi, and T. H. Nguyen. Shapes and velocities of single drops and bubbles moving freely through immiscible liquids. *Trans. IChemE*, 54: 167–173, 1976.
- [125] Grace Team. Grace – The free 2d plotting tool for scientific data. Available from <http://www.grace.com/>.
- [126] J. Grienberger. *Untersuchung und Modellierung von Blasensäulen*. PhD thesis, Universität Erlangen-Nürnberg, 1992.
- [127] J. Grienberger and H. Hofmann. Investigations and modelling of bubble columns. *Chem. Eng. Sci.*, 47:2215–2220, 1992.
- [128] R. M. Griffith. The effect of surfactants on the terminal rise velocity of drops and bubbles. *Chem. Eng. Sci.*, 17:1057–1070, 1962.
- [129] C. Grossetete. Experimental investigation of void profile development in a vertical cylindrical pipe. *Adv. Multiphase Flow*, page 333, 1995.
- [130] W. L. Haberman and R. K. Morton. An experimental investigation of the drag and shape of air bubbles rising in various liquids. In *Trans. Amer. Soc. Civ. Eng.*, volume 121, pages 227–252, 1956.
- [131] J. Hadamard. Mouvement permanent lent d'une sphère liquide et visqueuse dans un liquide visqueux. *Compt. Rend. Acad. Sci. Paris*, 152:1735–1738, 1911.
- [132] J. Han and G. Tryggvason. Secondary breakup of liquid drops in axisymmetric geometry – I. Constant acceleration. *Phys. Fluids*, 11:3650, 1999.
- [133] T. J. Hanratty and A. Bandukwala. Fluidization and sedimentation of spherical particles. *AICHE J.*, 3:293–296, 1957.
- [134] F. H. Harlow and A. A. Amsden. Flow of inter-penetrating material phases. *J. Comp. Phys.*, 18:440–464, 1975.
- [135] F. H. Harlow and A. A. Amsden. Numerical calculation of multiphase fluid flow. *J. Comp. Phys.*, 17:19–52, 1975.
- [136] F. H. Harlow, A. A. Amsden, and J. R. Nix. Relativistic fluid dynamics calculations with the particle-in-cell technique. *J. Comp. Phys.*, 20:119–129, 1976.
- [137] F. H. Harlow and J. E. Welch. Numerical calculation of time dependant viscous incompressible flow with a free surface. *Phys. Fluids*, 8(12):2182–2189, 1965.
- [138] T. Z. Harmathy. Velocity of large drops and bubbles in media of infinite or restricted extent. *AICHE J.*, 6:281–288, 1960.
- [139] N. Harnby, M. F. Edwards, and A. W. Nienow, editors. *Mixing in the Process Industries*. Butterworth-Heinemann, Boston, 1992.
- [140] J. F. Harper. The motion of bubbles and drops through liquids. *Adv. Appl. Mech.*, 12:59–129, 1972.

- [141] R. A. Herringe and M. R. Davies. Structural development of gas-liquid mixture flow. *J. Fluid Mech.*, 73:97–123, 1976.
- [142] E. Hervieu. *Écoulement monophasique et diphasique à bulles dans un branchemen-t en te : Étude theorique et expérimentale*. PhD thesis, Ecole Centrale de Paris, 1988.
- [143] M. R. Hestenes and E. L. Stiefel. Methods of conjugate gradients for solving linear systems. *NBS J. Res.*, 29:409–436, 1952.
- [144] G. Hetsroni, editor. *Handbook of Multiphase Systems*. Hemisphere Publ. Corp., Washington, 1982.
- [145] D. P. Hill. Inertial break-up model validation. Technical report, BRITE/EURAM II (BE 4098), II-17, 1993.
- [146] D. P. Hill. Bubble dispersion in a plane shear layer. Technical report, BRITE/EURAM II (BE 4098), II-35, 1994.
- [147] D. P. Hill. *The Computer Simulation of Dispersed Two-Phase Flows*. PhD thesis, Imperial College, University of London, 1998.
- [148] D. P. Hill, D. M. Wang, A. D. Gosman, and R. I. Issa. Numerical prediction of bubble dispersion in shear layers. In *Third Int. Symp. on Multiphase Flow and Heat Transfer, Xian, China*, pages 110–117, 1994.
- [149] G. Hillmer, L. Weismantel, and H. Hofmann. Investigations and modelling of slurry bubble columns. *Chem. Eng. Sci.*, 49:837–843, 1994.
- [150] J. H. Hills. Radial non-uniformity of velocity and voidage in a bubble column. *Trans. IChemE*, 52:1–9, 1974.
- [151] J. O. Hinze. *Turbulence*. McGraw-Hill, New York, 1975.
- [152] M. Hirano and A. Tomiyama. Numerical method for a two-fluid model based on the modified SOLA method. In Crowe et al. [64], pages 125–129.
- [153] C. Hirsch. *Numerical Computation of Internal and External Flows*, volume I & II. John Wiley & Sons, 1991.
- [154] C. W. Hirt, A. A. Amsden, and J. L. Cook. An arbitrary Lagrangian-Eulerian computing method for all flow speeds. *J. Comp. Phys.*, 14:227, 1974.
- [155] C. W. Hirt and B. D. Nicols. Volume of fluid (VOF) method for the dynamics of free boundaries. *J. Comp. Phys.*, 39:201–225, 1981.
- [156] B. H. Hjertager. Computational fluid dynamics (CFD) analysis of multiphase chemical reactors. *Trends Chem. Eng.*, 4:45–92, 1998.
- [157] H. H. Hu. Direct simulation of flows of solid-liquid mixtures. *Int. J. Multiphase Flow*, 22:335, 1996.

- [158] H. H. Hu, N. A. Patankar, and M. Y. Zhu. Direct numerical simulation of fluid-solid systems using the arbitrary Lagrangian-Eulerian technique. *J. Comp. Phys.*, 169:427, 2001.
- [159] S. Hu and R. C. Kinter. The fall of single liquid drops through water. *AICHE J.*, 1:42–50, 1955.
- [160] J. P. Hulin, C. Fierfort, and R. Coudol. Experimental study of vortex emission behind bluff obstacles in a gas liquid vertical two-phase flow. *Int. J. Multiphase Flow*, 8(5):475–490, 1982.
- [161] ICMF98, editor. *Proc. 3rd Int. Conf. on Multiphase Flow, Lyon, France (CDROM)*, June 8-12, 1998.
- [162] M. Iguchi, K. Okita, T. Nakatani, and N. Kasai. Structure of turbulent round bubbling jet generated by premixed gas and liquid injection. *Int. J. Multiphase Flow*, 23(2):249–262, 1997.
- [163] M. Iguchi, H. Ueda, and T. Uemura. Bubble and liquid flow characteristics in a vertical bubbling jet. *Int. J. Multiphase Flow*, 21(5):861–873, 1995.
- [164] F. Ihme, H. Schmidt-Traub, and H. Brauer. Theoretische Untersuchung über die Umströmung und den Stoffübergang an Kugeln. *Chem. Ing. Tech.*, 44(5):306–316, 1972.
- [165] M. Ishii. *Thermo-Fluid Dynamic Theory of Two-Phase Flow*. Eyrolles, Paris, 1975.
- [166] M. Ishii and T. C. Chawla. Local drag laws in dispersed two-phase flow. Technical Report ANL-79-105, Argonne National Laboratory, Illinois, 1979.
- [167] M. Ishii and K. Mishima. Two-fluid model and hydrodynamic constitutive relations. *Nuc. Eng. Des.*, 82:107–126, 1984.
- [168] M. Ishii and N. Zuber. Drag coefficient and relative velocity in bubbly, droplet or particulate flows. *AICHE J.*, 25(5):843–855, 1979.
- [169] M. Islam. *Numerical and Experimental Investigations of High-Pressure Diesel Sprays*. PhD thesis, Imperial College, University of London, 2002.
- [170] R. I. Issa. Solution of the implicitly discretised fluid flow equations by operator-splitting. *J. Comp. Phys.*, 62(1):40–65, January 1986.
- [171] R. I. Issa. A simple model for C_t . private Communication, see [147], 1992.
- [172] R. I. Issa and P. J. Oliveira. Modelling of turbulent dispersion in two phase flow jets. In *Turbulence Modelling and Experiment 2*, pages 947–957. Elsevier, 1993.
- [173] R. I. Issa and P. J. Oliveira. Validation of two-fluid model in shearfree mixing layers. In Coleman [58], pages 113–120.
- [174] R. I. Issa and P. J. Oliveira. Numerical prediction of turbulence dispersion in two-phase jet flow. In Celata et al. [47], pages 421–428.

- [175] D. A. H. Jacobs. Preconditioned conjugate gradient methods for solving systems of algebraic equations. Technical Report RD/L/N 193/80, Central Electricity Research Laboratories, Leatherhead, Surrey, England, 1980.
- [176] D. Jacquim. Calculation of two-phase Navier-Stokes flows using phase-field modeling. *J. Comp. Phys.*, 155:96–127, 1999.
- [177] H. A. Jakobsen. *On the Modelling and Simulation of Bubble Column Reactors Using a Two-Fluid Model*. PhD thesis, Norwegian University of Science and Technology, Trondheim, 1993.
- [178] H. A. Jakobsen, B. H. Sannæs, S. Grevskott, and H. F. Svendsen. Modeling of vertical bubble-driven flows. *Ind. Eng. Chem. Res.*, 36(10):4052–4074, 1997.
- [179] H. A. Jakobsen, H. F. Svendsen, and K. W. Hjarbo. On the prediction of local flow structures in internal loop and bubble column reactors using a two-fluid model. *Comp. Chem. Eng.*, 17:S531–536, 1993.
- [180] Y.-J. Jan. *Computational Studies of Bubble Dynamics*. PhD thesis, University of Michigan, 1994.
- [181] Y.-J. Jan and G. Tryggvason. Computational studies of contaminated bubbles. In I. Sahin and G. Tryggvason, editors, *Symp. on Bubble Dynamics and Vortices near a Free Surface*, pages 535–540. ASME, New York, 1991.
- [182] J. J. M. Janssen, A. Boon, and W. G. M. Agterof. Emulsification in a pipe mixer – III. Modified set-up and LDA analysis of flow condition. Technical report, BRITE/EURAM II (BE 4098), II-38, 1994.
- [183] J. J. M. Janssen, A. Boon, and W. G. M. Agterof. Emulsification in a pipe mixer – IV. Local mean drop size and local volume fraction. Technical report, BRITE/EURAM II (BE 4098), II-48, 1994.
- [184] J. J. M. Janssen, A. Boon, and W. G. M. Agterof. Emulsification in a pipe mixer – V. Additional evaluation of lda measurements. Technical report, BRITE/EURAM II (BE 4098), II-52, 1995.
- [185] H. Jasak. *Error Analysis and Estimation for Finite Volume Method with Applications to Fluid Flow*. PhD thesis, Imperial College, University of London, 1996.
- [186] H. Jasak, H. G. Weller, and A. D. Gosman. High resolution NVD differencing scheme for arbitrarily unstructured meshes. *Int. J. Num. Meth. Fluids*, 31:431–449, 1999.
- [187] S. T. Johansen and F. Boysan. Fluid dynamics in bubble stirred ladles - II. Mathematical modelling. *Metallurg. Trans. B*, 19B:755–764, 1988.
- [188] A. A. Johnson and T. E. Tezduyar. 3d simulation of fluid-particle interactions with the number of particles reaching 100. *Comp. Meth. Appl. Mech. Eng.*, 145:301–321, 1997.

- [189] A. I. Johnson and L. Braida. The velocity of fall of circulating and oscillating liquid drops through quiscent liquid phases. *Canadian J. Chem. Eng.*, 35:165–172, 1957.
- [190] Y. Joo and V. K. Dhir. An experimental study of drag on a single tube and on a tube in an array under two-phase cross flow. *Int. J. Multiphase Flow*, 20:1009–1019, 1994.
- [191] S. K. Jordan and J. E. Fromm. Fundamentals concerning wave loading on offshore structures. *Phys. Fluids*, 15(6):972–976, 1972.
- [192] D. Juric and G. Tryggvason. A front tracking method for dendritic solidification. *J. Comp. Phys.*, 123:127, 1996.
- [193] D. Juric and G. Tryggvason. Computations of boiling flows. *Int. J. Multiphase Flow*, 24:387, 1998.
- [194] D. G. Karamanov and L. N. Nikolov. Free rising spheres do not obey Newton's law for free settling. *AICHE J.*, 38(11):1843–1846, 1992.
- [195] A. Kariyasaki. Behaviour of a gas bubble in a linear velocity profile. *Nippon Kikai Gakkai Ronbunshu, B Hen/Trans. JSME, Part B*, 53:533, 1987.
- [196] B. A. Kashiwa, N. T. Padial, R. M. Rauenzahn, and W. B. Van der Heyden. Cell-centered ICE method for multiphase flow simulations. In Crowe et al. [64], pages 159–167.
- [197] A. Kaskas. *Schwarmgeschwingigkeiten in Mehrphasensuspensionen am Beispiel der Sedimentation*. PhD thesis, Technische Universität Berlin, 1970.
- [198] F. Keil, W. Mackens, H. Voß, and J. Werther. *Scientific Computing in Chemical Engineering II – Computational Fluid Dynamics, Reaction Engineering and Molecular Properties*. Springer-Verlag, Berlin, 1999.
- [199] J. K. Klahn, W. J. Tiaberinga, and A. Boon. Emulsification in a pipe mixer – II. Experiments on droplet break-up and coalescence comparison to computational fluid dynamics results. Technical report, BRITE/EURAM II (BE 4098), II-24, 1993.
- [200] A. J. Klee and R. E. Treybal. Rate of rise or fall of liquid drops. *AICHE J.*, 2:444–447, 1956.
- [201] M. Kleiber, editor. *Handbook of computational solid mechanics: survey and comparison of contemporary methods*. Springer-Verlag, Berlin, 1998.
- [202] B. Koglin. Experimentelle Untersuchung zur Sedimentation von Teilchenkomplexen in Suspensionen. *Chem. Ing. Tech.*, 44(8):515–521, 1972.
- [203] S. Komori and R. Kurose. Drag and lift forces acting on a rotating sphere in a linear shear flow. In L. Gavrilakis, L. Machiels, and P. Monkewitz, editors, *Advances in Turbulence VI*, pages 551–554. Kluwer, 1996.

- [204] S. Koshizuka, H. Tamako, and Y. Oka. A particle method for incompressible viscous flow with fluid fragmentation. *Comp. Fluid Dyn. J.*, 4(1):29–46, 1995.
- [205] Č. Kralj. *Numerical Simulation of Diesel Spray*. PhD thesis, Imperial College, University of London, 1993.
- [206] V. Kroll. Sub-task 2.3 – Industrial experiments. Technical report, BRITE/EURAM III (BE 4322), III-27, 2001.
- [207] J. A. M. Kuipers and W. P. M. van Swaaij. Computational fluid dynamics applied to chemical reaction engineering. *Adv. Chem. Eng.*, 24:227–328, 1998.
- [208] A. Kumar and S. Hartland. Gravity settling in liquid/liquid dispersions. *Canadian J. Chem. Eng.*, 63:368–376, 1985.
- [209] A. Kumar, D. K. Vohra, and S. Hartland. Sedimentation of droplet dispersions in counter-current spray columns. *Canadian J. Chem. Eng.*, 58:154–159, 1980.
- [210] S. Kumar, W. B. Vanderheyden, N. Devanathan, N. T. Padial, M. P. Duduković, and B. A. Kashiwa. Numerical simulation and experimental verification of the gas-liquid flow in bubble columns. In *Industrial Mixing Fundamentals with Applications*, volume 91 of *AICHE Symp. Ser.*, pages 11–19, 1995.
- [211] J. T. Kuo and G. B. Wallis. Flow of bubbles through nozzles. *Int. J. Multiphase Flow*, 14:547, 1988.
- [212] R. Kurose and S. Komori. Drag and lift forces acting on a rotating sphere in a linear shear flow. *J. Fluid Mech.*, 384:183–206, 1999.
- [213] R. Kurose, R. Misumi, and S. Komori. Drag and lift forces acting on a spherical bubble in a linear shear flow. *Int. J. Multiphase Flow*, 27:1247–1258, 2001.
- [214] B. Lafaurie, C. Nardonne, R. Scardovelli, S. Zaleski, and G. Zanetti. Modelling merging and fragmentation in multiphase flows with SURFER. *J. Comp. Phys.*, 113:134–147, 1994.
- [215] R. T. Lahey, Jr. The analysis of phase separation and phase distribution phenomena using two-fluid models. *Nuc. Eng. Des.*, 122:17–40, 1990.
- [216] R. T. Lahey, Jr., M. Lopez de Bertodano, and O. C. Jones. Phase distribution phenomena in complex geometry conduits. *Nuc. Eng. Des.*, 141:177–201, 1993.
- [217] R. T. Lahey, Jr., S. Sim, and D. A. Drew. An evaluation of interfacial drag models for bubbly two-phase flow. In J. C. Chen and S. G. Bankoff, editors, *ASME 18th Nat. Heat Transfer Conf., New York, USA*, pages 11–17, 1979.
- [218] S. Lain, D. Bröder, and M. Sommerfeld. Numerical studies of hydrodynamics in a bubble column using the Euler-Lagrange approach. In M. Sommerfeld, editor, *Proc. 9th Workshop on Two-Phase Flow Predictions, Merseburg, Germany*, Apr 13-16, 1999.

- [219] M. Lance and J. Bataille. Turbulence in the liquid phase of a uniform bubbly air-water flow. *J. Fluids Mech.*, 222:95–118, 1991.
- [220] M. Lance and M. Lopez de Bertodano. Phase distribution phenomena and wall effects in bubbly two-phase flows. In G. F. Hewitt et al., editors, *Multiphase Science and Technology*, volume 8, pages 69–123. Hemisphere Publ. Corp., Washington, 1994.
- [221] M. Lance, J. L. Marié, and J. Bataille. Homogeneous turbulence in bubbly flows. *J. Fluids Eng., Trans. ASME*, 113:295–300, 1991.
- [222] M. Lance, J. L. Marié, E. Moursali, J. Bataille, C. Suzanne, V. Roig, R. Bel Fd-hila, and L. Masbernat. Experimental study of turbulent bubbly shear flows. *Chem. Eng. Comm.*, 141-142:51–70, 1996.
- [223] A. Lapin and A. Lübbert. Dynamic simulation of the two-phase flow mixing in bubble columns. volume 136 of *IChemE Symp. Ser.*, pages 365–373, 1994.
- [224] A. Lapin and A. Lübbert. Numerical simulation of the dynamics of two-phase gas-liquid flows in bubble columns. *Chem. Eng. Sci.*, 49(21):3661–3674, 1994.
- [225] C. E. Lapple and C. B. Shepherd. Calculation of particle trajectories. *Ind. Eng. Chem., Sep. Oper.*, 77(12):318–320, 1933.
- [226] A. Larue de Tournemine. Bubble rise velocities. Private Communication, 2000.
- [227] A. Larue de Tournemine, V. Roig, and C. Suzanne. Experimental study of the turbulence in bubbly flows at high void fraction. In Michaelides et al. [275].
- [228] D. Lathouwers. *Modelling and Simulation of Turbulent Bubbly Flow*. PhD thesis, Technische Universiteit Delft, 1999.
- [229] D. Lathouwers and H. E. A. Van Den Akker. Numerical method for the solution of two-fluid model equations. In Coleman [58], pages 121–126.
- [230] B. E. Launder and D. B. Spalding. The numerical computation of turbulent flows. *Comp. Meth. Appl. Mech. Eng.*, 3:269–289, 1974.
- [231] H. Laux. *Modelling of Dilute and Dense Dispersed Fluid-Particle Two-Phase Flows*. PhD thesis, Norwegian University of Science and Technology, Trondheim, 1998.
- [232] L. G. Leal. Particle motion in a viscous fluid. *Ann. Rev. Fluid Mech.*, 12:435–476, 1980.
- [233] S.-J. Lee, R. T. Lahey, Jr., and O. C. Jones, Jr. The prediction of two-phase turbulence and phase distribution using a $k - \varepsilon$ model. *Jap. J. Multiphase Flow*, 3(4):335–368, 1989.
- [234] D. Legendre. *Quelques aspects des forces hydrodynamiques et de la chaleur sur une bulle sphérique*. PhD thesis, Institut National Polytechnique de Toulouse, 1996.

- [235] D. Legendre and J. Magnaudet. The lift force on a spherical bubble in a linear shear flow. *J. Fluid Mech.*, 368:81–126, 1998.
- [236] D. Legendre and J. J. M. Magnaudet. A note on the lift force on a bubble or a drop in a low-reynolds number shear flow. *Phys. Fluids*, 9:3572–3574, 1997.
- [237] D. Legendre and J. J. M. Magnaudet. Some aspects of the lift force on a spherical bubble. *App. Sci. Res.*, 58:441–461, 1998.
- [238] F. Lehr, M. Millies, and D. Mewes. Berücksichtigung von blasengrößenverteilungen beim berechnen von strömungsfeldern in blasensäulen. *Chem. Ing. Tech.*, 73:1245–1259, 2001.
- [239] I. H. Lehrer. A rational terminal velocity equation for bubbles and drops at intermediate and high reynolds numbers. *J. Chem. Eng. Japan*, 9:237–240, 1976.
- [240] R. Letan. *Chem. Eng. Sci.*, 29:621, 1974.
- [241] V. G. Levich. *Physicochemical Hydrodynamics*. Prentice-Hall, Englewood Cliffs, 1962.
- [242] A. Leviton and A. Leighton. *J. Phys. Chem.*, 40:71, 1936.
- [243] Y. S. Li and J. M. Zhan. An efficient three-dimensional semi-implicit finite element scheme for simulation of free surface flows. *Int. J. Num. Meth. Fluids*, 16:187–198, 1993.
- [244] J. Lighthill. Drift. *J. Fluid Mech.*, 1:31–53, 1956. Corrigendum: Lighthill [245].
- [245] J. Lighthill. Corrigendum – Drift. *J. Fluid Mech.*, 2:311, 1957.
- [246] J. Lighthill. Fundamentals concerning wave loading on offshore structures. *J. Fluid Mech.*, 173:667–681, 1986.
- [247] J. Lighthill. *An Informal Introduction to Theoretical Fluid Dynamics*. Oxford Univ. Press, 1986.
- [248] T. J. Liu. Bubble size and entrance length effects on void development in a vertical channel. *Int. J. Multiphase Flow*, 19:99–113, 1993.
- [249] T. J. Liu and S. G. Bankoff. Structure of air-water bubbly flow in a vertical pipe – I. Liquid mean velocity and turbulence measurements; II. Void fraction, bubble velocity and bubble size distribution. *Int. J. Heat Mass Transfer*, 36(4):1049–1072, 1993.
- [250] S. Lo. Applications of population balance to CFD modelling of gas-liquid reactors. In *Trends in Numerical and Physical Modelling for Industrial Multiphase Flows, Corse*, September 27-29, 2000.
- [251] M. Lopez de Bertodano, R. T. Lahey, Jr., and O. C. Jones. Development of a $k - \varepsilon$ model for bubbly two-phase flow. *J. Fluids Eng., Trans. ASME*, 116(1):128–134, 1994.

- [252] M. Lopez de Bertodano, S.-J. Lee, R. T. Lahey, Jr., and D. A. Drew. The prediction of two-phase turbulence and phase distribution phenomena using a Reynolds stress model. *J. Fluids Eng., Trans. ASME*, 112:107–113, 1990.
- [253] E. Loth, M. Taeibi Rahni, and G. Tryggvason. Deformable bubbles in a free shear layer. *Int. J. Multiphase Flow*, 23(5):977–1001, 1997.
- [254] R. Loutaty, A. Vignes, and P. Le Goff. Transfert de chaleur et dispersion axiale dans une colonne à pulvérisation liquide-liquide en lit lâche et en lit dense. *Chem. Eng. Sci.*, 24:1795–1811, 1969.
- [255] Nabla Ltd. *FOAM – The Complete Guide*. Nabla Ltd., 2001. Available from <http://www.nabla.co.uk/>.
- [256] A. Lübbert and A. Lapin. Dynamic numerical experiments with 3d-bubble columns. analysis of some key mixing mechanisms. *Revue de L’Institut Français du Pétrole*, 51(2):269–277, 1996.
- [257] Lunde and Perkins. Observations on wakes behind spheroidal bubbles and particles. In FEDSM97 [98].
- [258] K. Lunde and R. Perkins. Shape oscillations of rising bubbles. *Appl. Sci. Res.*, 58:387–408, 1998.
- [259] Kamp A. M., A. K. Chesters, C. Colin, and J. Fabre. Bubble coalescence in turbulent flows: A mechanistic model for turbulence-induced coalescence applied to microgravity bubbly pipe flow. *Int.J. Multiphase Flow*, 27:1363–1396, 2001.
- [260] J. J. M. Magnaudet. Forces acting on bubbles and rigid particles. In FEDSM97 [98].
- [261] J. J. M. Magnaudet and I. Eames. The motion of high Reynolds-number bubbles in homogeneous flow. *Ann. Rev. Fluid Mech.*, 32:659–708, 2000.
- [262] G. Magnus. A note on the rotary motion of the liquid jet. *Annalen der Physik und Chemie*, 63:363–365, 1861.
- [263] G. Marruci, G. Apuzzo, and G. Astarita. Motion of liquid drops in non-newtonian systems. *AICHE J.*, 16:538, 1970.
- [264] M. R. Maxey and J. J. Riley. Equation of motion for a small rigid sphere in a non-uniform flow. *Phys. Fluids*, 26:883–889, 1983.
- [265] D. Mazumdar and R. I. L. Guthrie. The physical and mathematical modelling of gas stirred ladle systems. *ISIJ Int.*, 35(20):1–20, 1995.
- [266] J. McHyman. Numerical methods for tracking interfaces. *Physica D*, 12:396–407, 1984.
- [267] J. B. McLaughlin. Inertial migration of a small sphere in linear shear flow. *J. Fluid Mech.*, 224:261–274, 1991.

- [268] R. Mei. An approximate expression for the shear lift force on spherical particle at finite Reynolds number. *Int. J. Multiphase Flow*, 18:145–147, 1992.
- [269] R. Mei and J. F. Klausner. Shear lift on a small sphere in a slow shear flow. *Int. J. Heat Fluid Flow*, 15:62–65, 1994.
- [270] H. D. Mendelson. The prediction of bubble terminal velocity from wave theory. *AIChe J.*, 13:250–252, 1967.
- [271] T. Menzel. *Die Reynolds-Schubspannungen als wesentlicher Parameter zur Modellierung der Strömungsstruktur in Blasensäulen und Airlift-Schlaufenreaktoren*. PhD thesis, Universität Dortmund, 1989. see also Fortschritt-Berichte VDI : Reihe 3, Volume 198.
- [272] G. Merziger and T. Wirth. *Repetitorium der höheren Mathematik*. Feldmann Verlag, Springe, 1st edition, 1991.
- [273] D. Mewes. Manuskript zur Vorlesung: "Mehrphasenströmungen – Feststoffe, Fluide". Technical report, Universitat Hannover, 1989.
- [274] E. E. Michaelides. Review – the transient equation of motion for particles, bubbles and droplets. *J. Fluids Eng.*, 119:233–247, 1997.
- [275] E. E. Michaelides et al., editors. *Proc. 4th Int. Conf. on Multiphase Flow, New Orleans, LA, USA*, May 27-June 1, 2001.
- [276] K. Minemura and M. Murakami. Distributions of velocity and void fractions in a radial-flow pump impeller handling air-water mixtures. In *cavitation forum, Atlanta, USA*, 1986.
- [277] K. Minemura, T. Uchiyama, and T. Ishikawa. Experimental investigations on bubbly flows in a straight channel rotated around an axis perpendicular to the channel. *Int. J. Multiphase Flow*, 19:439–450, 1993.
- [278] D. W. Moore. The boundary layer on spherical gas bubble. *J. Fluid Mech.*, 16: 161–176, 1963.
- [279] D. W. Moore. The velocity of rise of distorted gas bubbles in a liquid of small viscosity. *J. Fluid Mech.*, 23:749–766, 1965.
- [280] F. J. Moraga, F. J. Bonetto, and R. T. Lahey. Lateral forces on spheres in turbulent uniform shear flow. *Int. J. Multiphase Flow*, 25:1321–1372, 1999.
- [281] S. Mortazavi and G. Tryggvason. A numerical study of the motion of drops in poseuille flow – I. Lateral migration of one drop. *J. Fluid Mech.*, 411:325, 2000.
- [282] K. E. Morud and B. H. Hjertager. LDA measurements and CFD modelling of gas-liquid flow in a stirred vessel. *Chem. Eng. Sci.*, 51:233–249, 1996.
- [283] E. Moursali, J. L. Mari , and J. Bataille. Upward turbulent bubbly boundary layer along a vertical flat plate. *Int. J. Multiphase Flow*, 21:107–117, 1995.

- [284] R. F. Mudde and O. Simonin. Two- and three dimensional simulations of a bubble plume using a two-fluid model. *Chem. Eng. Sci.*, 54:5061–5069, 1999.
- [285] Y. Murai and Y. Matsumoto. Numerical simulation of turbulent bubble plumes using Eulerian-Lagrangian bubbly flow model equations. In Coleman [58], pages 67–74.
- [286] S. Muzaferija. *Adaptive Finite Volume Method for Flow Prediction Using Unstructured Meshes and Multigrid Approach*. PhD thesis, Imperial College, University of London, 1994.
- [287] M. A. Naciri. *Contribution à l'étude des forces exercées par un liquide sur une bulle de gaz: Portance, masse ajoutée, interactions hydrodynamiques*. PhD thesis, Ecole Centrale de Lyon, 1992.
- [288] B. T. Nadiga and S. Zaleski. Investigations of a two-phase fluid model. *European J. Mech., B/Fluids*, 15:885–896, 1996.
- [289] V. E. Nakoryakov, O. N. Kashinsky, V. V. Randin, and L. S. Timkin. Gas-liquid bubbly flow in vertical pipes. *J. Fluids Eng., Trans. ASME*, 118:377–382, 1996.
- [290] S. Nas. *Computational Investigation of Therocapillary Migration of Bubbles and Drops in Zero Gravity*. PhD thesis, University of Michigan, 1995.
- [291] I. Newton. *Philosophiae Naturalis: Principia Mathematica*. Colloniae Allobrocum, Sumptibus Cl. & Ant. Philibert Bibliop., Roma, 1760.
- [292] B. D. Nicols and C. W. Hirt. Calculating three-dimensional free surface flows in the vicinity of submerged and exposed structured. *J. Comp. Phys.*, 12:234–246, 1973.
- [293] R. S. Oey, R. F. Mudde, L. M. Portela, and H. E. A. Van Den Akker. Simulation of a slurry airlift using a two-fluid model. *Chem. Eng. Sci.*, 56:673–681, 2001.
- [294] P. J. Oliveira. *Computer Modelling of Multidimensional Multiphase Flow and Application to T-Junctions*. PhD thesis, Imperial College, University of London, 1992.
- [295] P. J. Oliveira. Numerical aspects of the two-phase flow algorithm. Technical report, BRITE/EURAM III (BE 4322), III-12, 1999.
- [296] P. J. Oliveira and R. I. Issa. Numerical treatment of interphase forces in two-phase flow. In Crowe et al. [64], pages 131–140.
- [297] Oliver. The influence of particle rotation on radial migration in the Poiseuille flow of suspensions. *Nature*, 194:1269–1271, 1962.
- [298] P. J. O'Rourke. Statistical properties and numerical implementation of a model for droplet dispersion in a turbulent gas. *J. Comp. Phys.*, 83:345–360, 1989.
- [299] C. W. Oseen. *Hydrodynamik*. Akademische Verlagsgesellschaft Leipzig, 1927.

- [300] S. Osher and J. A. Sethian. Fronts propagating with curvature-dependant speed: algorithmns based on Hamilton-Jacobi formulations. *J. Comp. Phys.*, 79:12–49, 1988.
- [301] S. V. Patankar. *Numerical Heat and Mass Transfer*. Hemisphere Publ. Corp., Washington, 1980.
- [302] S. V. Patankar and D. B. Spalding. A calculation procedure for heat, mass and momentum transfer in 3-d parabolic flow. *Int. J. Heat Mass Transfer*, 15:1787, 1972.
- [303] F. N. Peebles and H. J. Garber. Studies on the motion of gas bubbles in liquids. *Chem. Eng. Progr.*, 49(2):88–97, 1953.
- [304] M. Perić. *A Finite Volume Method for the Prediction of Three-Dimensional Fluid Flow in Complex Ducts*. PhD thesis, Imperial College, University of London, 1985.
- [305] M. Perić, R. Kessler, and G. Scheuerer. Comparison of finite-volume numerical methods with staggered and colocated grids. *Comp. Fluids*, 16(4):389–403, 1988.
- [306] D. Pfleger, S. Gomes, N. Gilbert, and H.-G. Wagner. Hydrodynamic simulations of laboratory scale bubble colums fundamental studies of the Eulerian-Eulerian modelling approach. *Chem. Eng. Sci.*, 54:5091–5099, 1999.
- [307] T. Pilhofer. Hydrodynamik von Tropfenschwärm en in flüssig/flüssig-Sprühkolonnen. *Chem. Ing. Tech.*, 46:783, MS 133/74, 1974.
- [308] T. Pilhofer and D. Mewes. *Siebboden-Extraktionskolonnen: Vorausberechnung unpulsierter Kolonnen*. Verlag Chemie, Weinheim, 1979.
- [309] J. L. M. Poiseuille. Recherches sur le mouvement du sang dans les vein capillaires. *Mem. de l'Academie des Sciences*, 7:105–175, 1841.
- [310] S. Politis. *Prediction of Two-Phase Solid-Liquid Turbulent Flow Stirred Vessels*. PhD thesis, Imperial College, University of London, 1989.
- [311] S. Popinet and S. Zaleski. A front-tracking algorithm for accurate representation of surface tension. *Int. J. Num. Meth. Fluids*, 30:775–793, 1999.
- [312] M. Popp and D. W. Sallet. Experimental investigation of one- and two-phase flow through a tee-junction. In *Int. Conf. Physical Modelling of Multiphase Flow, Coventry, UK*, 1983.
- [313] L. Råde and B. Westergren. *Mathematics Handbook*. Springer-Verlag, Berlin, 4th edition, 1999.
- [314] V. V. Ranade. Modelling of turbulent flow in a bubble column reactor. *Chem. Eng. Res. Des., Part A: Trans. IChemE*, 75:14–23, 1997.
- [315] V. V. Ranade and V. R. Deshpande. Gas-liquid flow in stirred reactors: Trailing vortices and gas accumulation behind impeller blades. *Chem. Eng. Sci.*, 54:2305–2315, 1999.

- [316] V. V. Ranade and S. M. S. Dommeti. Computational snapshot of flow generated by axial impellers in baffled stirred vessels. *Chem. Eng. Res. Des., Part A: Trans. IChemE*, 74:476–484, 1999.
- [317] J. Rensen and Roig. Experimental study of the unsteady structure of a confined bubble plume. *Int. J. Multiphase Flow*, 27:1431–1449, 2001.
- [318] C. M. Rhie and W. L. Chow. A numerical study of the turbulent flow past an isolated airfoil with trailing edge separation. *AIAA J.*, 21(11):1525–1532, 1983.
- [319] J. F. Richardson and W. N. Zaki. Sedimentation and fluidisation : Part 1. *Trans. IChemE*, 32:35–53, 1954.
- [320] W. J. Rider and D. B. Kothe. Reconstructing volume tracking. *J. Comp. Phys.*, 141:112–152, 1998.
- [321] W. J. Rider and D. B. Kothe. Stretching and tearing interface tracking methods. Technical Report LA-UR-98-1145 and AIAA Paper 95-1717, Los Alamos National Laboratory, 1998. Available from <http://www.math.ucdavis.edu/~egp/>.
- [322] K. Rietema and S. P. P. Ottengraf. Laminar liquid circulation and bubble street formation in a gas-liquid system. *Trans. IChemE*, 48:T54–T62, 1970.
- [323] G. D. Rigby and G. M. Evans. CFD simulation of gas dispersion dynamics in liquid cross-flows. *App. Math. Modelling*, 22:799–810, 1998.
- [324] G. D. Rigby, G. M. Evans, and Jameson. G. L. Bubble breakup from ventilated cavities in multiphase reactors. *Chem. Eng. Sci.*, 52:3677–3684, 1997.
- [325] Y. Rimon and S. I. Cheng. Numerical solution of a uniform flow over a sphere at intermediate Reynolds numbers. *Phys. Fluids*, 12:949–959, 1969.
- [326] A. Rinne and R. Loth. Axial and radial development of local two-phase flow parameters for vertical bubbly flow in a pipe with sudden expansion. In G. P. Celata and R. K. Shah, editors, *Proc. 1st Symp. on Two-Phase Flow Modelling and Experimentation*. Edizioni ETS, Italy, Oct 9-11, 1995.
- [327] A. Rinne and R. Loth. Development of local two-phase flow parameters for vertical bubbly flow in a pipe with sudden expansion. *Exp. Thermal Fluid Sci.*, 13:152–166, 1996.
- [328] V. Roig. *Zone de mélange d'écoulements diphasiques à bulles*. PhD thesis, Institut National Polytechnique de Toulouse, 1993.
- [329] V. Roig, C. Suzanne, and L. Masbernat. Experimental investigation of a turbulent mixing layer. *Int. J. Multiphase Flow*, 24(1):35–54, 1998.
- [330] S. I. Rubinow and J. B. Keller. The transverse force on a spinning sphere moving in a viscous fluid. *J. Fluid Mech.*, 11:447–459, 1961.
- [331] M. Rudman. Volume-tracking methods for interfacial flow calculations. *Int. J. Num. Meth. Fluids*, 24:671–691, 1997.

- [332] W. Rybczynski. Über die fortschreitende Bewegung einer flüssigen Kugel in einem zähen Medium. *Bull. Int. Acad. Sci. Cracovie A*, 40:40–46, 1911.
- [333] G. Ryskin and L. G. Leal. Numerical solution of free-boundary problems in fluid mechanics. – I. The finite-difference technique; II. Bouyancy-driven motion of a gas bubble through a quiescent liquid; III. Bubble deformation in an axissymmetric straining flow. *J. Fluid Mech.*, 148:1–43, 1984.
- [334] P. G. Saffman. On the rise of small air bubbles in water. *J. Fluid Mech.*, 1: 249–275, 1956.
- [335] P. G. Saffman. The lift on a small sphere in a slow shear flow. *J. Fluid Mech.*, 22(2):385–400, 1965. Corrigendum: Saffman [336].
- [336] P. G. Saffman. Corrigendum – The lift on a small sphere in a slow shear flow. *J. Fluid Mech.*, 31:624, 1968.
- [337] H. Sakamoto and H. Haniu. The formation mechanism and shedding frequency of vortices from a sphere in uniform shear flow. *J. Fluid Mech.*, 287:151–171, 1995.
- [338] T. Sarpkaya. Vortex-induced oscillations. *J. Appl. Mech., Trans. ASME*, 46: 241–258, 1979.
- [339] R. Scardovelli and S. Zaleski. Direct numerical simulation of free-surface and interfacial flow. *Ann. Rev. Fluid Mech.*, 31:567–603, 1999.
- [340] L. Schiller and A. Naumann. Über die grundlegenden Berechnungen bei der Schwerkraftaufbereitung. *Z. Vereins deutscher Ing.*, 77(12):318–320, 1933.
- [341] M. P. Schwarz and W. J. Turner. Applicability of the standard $k-\varepsilon$ turbulence model to gas-stirred baths. *Appl. Math. Modelling*, 12:273, 1988.
- [342] G. Segré and A. Silberberg. Radial particle displacement in Poiseuille flow of suspensions. *Nature*, 189:209–210, 1961.
- [343] G. Segré and A. Silberberg. Behavior of macroscopic rigid spheres in Poiseuille flow. *J. Fluid Mech.*, 14:115–157, 1962.
- [344] A. Serizawa et al., editors. *Proc. 2nd Int. Conf. on Multiphase Flow, Kyoto, Japan*, Apr 3-7, 1995.
- [345] A. Serizawa and I. Kataoka. Phase distribution in two-phase flow. In N. H. Afghan, editor, *Transient Phenomena in Multiphase Flow*, pages 179–225, Washington, 1988. Hemisphere Publ. Corp.
- [346] A. Serizawa, I. Kataoka, and I. Michiyoshi. Turbulence structure of air-water bubbly flow – I. Measuring techniques; II. Local properties; III. Transport properties. *Int. J. Multiphase Flow*, 2:221–259, 1974.
- [347] J. A. Sethian. *Level Set Methods: Evolving Interfaces in Geometry, Fluid Mechanics, Computer Vision and Material Sciences*. Cambridge Univ. Press, 1996.

- [348] Y. Y. Sheng and G. A. Irons. The impact of bubble dynamics on the flow in plumes of laddle water models. *Appl. Math. Modelling*, 26B:625–635, 1995.
- [349] W. Shyy, H. Udaykumar, M. M. Rao, and Smith R. W. *Computational Fluid Dynamics with Moving Boundaries*. Taylor & Francis, London, 1996.
- [350] O. Simonin. Combustion and turbulence in two-phase flows. In *Lecture Ser. - continuum modelling of dispersed phase flows*. Von Karman Institute for Fluid Dynamics, 1996.
- [351] B. L. Smith. On the modelling of bubble plumes in a liquid pool. *Appl. Math. Modelling*, 22:773–797, 1998.
- [352] A. Sokolichin and G. Eigenberger. Gas-liquid flow in bubble columns and loop reactors – I. Detailed modelling and numerical simulation. *Chem. Eng. Sci.*, 49: 5735–5746, 1994.
- [353] A. Sokolichin, G. Eigenberger, A. Lapin, and A. Lübbert. Dynamic numerical simulation of gas-liquid two-phase flows. Euler/Euler versus Euler/Lagrange. *Chem. Eng. Sci.*, 52(4):611–626, 1997.
- [354] M. Sommerfeld, editor. *Proc. 6th Workshop on Two-Phase Flow Predictions, Erlangen, Germany*, Mar 30-Apr 2, 1992.
- [355] M. Sommerfeld. Modellierung und numerische Berechnung von partikelbeladenen Strömungen mit Hilfe des Euler/Lagrange Verfahrens. Habilitationsschrift, University of Erlangen-Nürnberg, 1995.
- [356] D. B. Spalding. Numerical computations of multiphase flow and heat transfer. In C. Taylor and K. Morgan, editors, *Recent advances in numerical methods in fluids*, volume 1. Pineridge Press, 1981.
- [357] D. B. Spalding. Developments in the IPSA procedure for numerical computation of multiphase-flow phenomena with interphase slip, unequal temperatures, etc. In T. M. Shih, editor, *Numerical Properties and Methodologies in Heat Transfer: presented at the 2nd National Symp., Univ. Maryland, USA*, pages 421–436, Washington, Sep 28-30, 1983. Hemisphere Publ. Corp.
- [358] D. B. Spalding. The numerical computation of multi-phase flows. Technical report, CFDU, Imperial College, London, Report CFD/85/7, 1985.
- [359] G. Sridhar and J. Katz. Drag and lift forces on microscopic bubbles entrained by a vortex. *Phys. Fluids*, 7(2):389–399, 1995.
- [360] H. Städtker, G. Franchello, and B. Worth. Towards a high resolution numerical simulation of transient two-phase flow. In ICMF98 [161].
- [361] L. Steiner and S. Hartland. Hudrodynamics of liquid-liquid spray columns. In N. P. Cheremisinoff and R. Gupta, editors, *Handbook of Fluids in Motion*, chapter 40, pages 1049–1092. Ann Arbor Science, 1983.

- [362] H. H. Steinour. Rate of sedimentation: Nonflocculated suspensions of uniform spheres. *Ind. Eng. Chem.*, 36(7):618–624, 1944.
- [363] G. G. Stokes. On the effect of the internal friction of fluids on the motion of pendulums. *Trans. Camb. Phil. Soc.*, 9:8–27, 1851.
- [364] K. Sugiyama and Y. Matsumoto. Numerical study of bubbly flow around a circular cylinder. In FEDSM98, editor, *Proc. 1998 ASME Fluids Engineering Division Summer Meeting, Washington, DC, USA*, Nov 15-20, 1998.
- [365] K. X. Sun, Y. Xiang, M. Y. Zhang, and X. J. Chen. Measurements of physical characteristics of bubbles in gas-liquid plumes. In ICMF98 [161].
- [366] T. Y. Sun and G. M. Faeth. Structure of turbulent bubbly jets - I. Methods and centerline properties; II. Phase property profiles. *Int. J. Multiphase Flow*, 12(1):99–126, 1986.
- [367] M. Sussman, P. Smereka, and S. Osher. A level set approach for computing solutions to incompressible two-phase flow. *J. Comp. Phys.*, 114:146–159, 1994.
- [368] H. F. Svendsen, H. A. Jakobsen, and R. Torvik. Local flow structures in internal loop and bubble column reactors. *Chem. Eng. Sci.*, 47(13-14):3299–3304, 1992.
- [369] G. Tabor. An analytical method for determining C_d at high phase fraction. Technical report, BRITE/EURAM III (BE 4322), III-13, 1999.
- [370] G. Tabor. Turbulence modelling at high phase fraction. Technical report, BRITE/EURAM III (BE 4322), III-14, 1999.
- [371] M. Taeibi Rahni and E. Loth. Forces on a large cylindrical bubble in an unsteady rotational flow. *AIChE J.*, 42:638–648, 1996.
- [372] M. Taeibi Rahni, E. Loth, and G. Tryggvason. Flow modulation of a planar free shear layer with large bubbles – direct numerical simulations. *Int. J. Multiphase Flow*, 20(6):1109–1128, 1994.
- [373] S. Takagi and Y. Matsumoto. Three dimensional calculation of a rising bubble. In Serizawa et al. [344], pages PD2.9–16.
- [374] A. Takizawa, S. Koshizuka, and S. Kondo. Generalization of physical component boundary fitted (PCBFC) method for the analysis of free-surface flow. *Int. J. Num. Meth. Fluids*, 15:1213–1237, 1992.
- [375] W. Tauber and G. Tryggvason. Direct numerical simulation of primary breakup. *Comp. Fluid Dyn. J.*, 9, 2000.
- [376] D. Thai Van, J. P. Minier, O. Simonin, P. Freydier, and J. Olive. Multidimensional two-fluid model computation of turbulent dispersed two-phase flows. In Crowe et al. [64], pages 277–291.
- [377] N. T. Thang and M. R. Davis. The structure of bubbly flow in venturies. *Int. J. Multiphase Flow*, 5:17–37, 1979.

- [378] J. L. Thé, G. D. Raithby, and G. D. Stuble. Surface-adaptive finite-volume method for solving free-surface flows. *Num. Heat Transfer, Part B: Fundamentals*, 26:367–380, 1994.
- [379] T. Theodoropoulos. *Prediction of Three-Dimensional Engine Flow on Unstructured Meshes*. PhD thesis, Imperial College, University of London, 1990.
- [380] W. J. Tiaberinga, A. Boon, and J. K. Klahn. Emulsification in a pipe mixer – I. Flow characterisation: Laser Doppler anemometry and fluid flow simulation with DUCTFLOW. Technical report, BRITE/EURAM II (BE 4098), II-16, 1992.
- [381] A. Tomiyama. Struggle with computational bubble dynamics. In ICMF98 [161].
- [382] A. Tomiyama, I. Kataoka, T. Fukuda, and T. Sakaguchi. Drag coefficients of bubbles (2nd report, drag coefficient for a swarm of bubbles and its applicability to transient flow). *Nippon Kikai Gakkai Ronbunshu, B Hen/Trans. JSME, Part B*, 61:2810–2817, 1995.
- [383] A. Tomiyama, I. Kataoka, and T. Sakaguchi. Drag coefficients of bubbles (1st report, drag coefficients of a single bubble in a stagnant liquid). *Nippon Kikai Gakkai Ronbunshu, B Hen/Trans. JSME, Part B*, 61:2357–2364, 1995.
- [384] A. Tomiyama, I. Kataoka, I. Žun, and T. Sakaguchi. Drag coefficients of single bubbles under normal and microgravity conditions. *JSME Int. J., Ser. B: Fluids Thermal Eng.*, 41:472–479, 1998.
- [385] A. Tomiyama, A. Sou, H. Minagawa, and T. Sakaguchi. Numerical analysis of a single bubble by VOF method. *JSME Int. J., Ser. B: Fluids Thermal Eng.*, 36: 51–56, 1993.
- [386] A. Tomiyama, A. Sou, I. Žun, N. Kanami, and T. Sakaguchi. Effects of Eötvös number and dimensionless liquid volumetric flux on lateral motion of a bubble in a laminar duct. In Serizawa et al. [344], pages PD1.11–18.
- [387] A. Tomiyama, S. Yoshida, and S. Hosokawa. Surface tension force dominated regime of single bubbles rising through stagnant liquids. In *UK-Japan Seminar on Multiphase Flow, Keio House, Bury St. Edmunds, UK*, 2001.
- [388] A. Tomiyama, I. Žun, A. Sou, and T. Sakaguchi. Numerical analysis of bubble motion with the VOF method. *Nuc. Eng. Des.*, 141:69–82, 1993.
- [389] A. Tomiyama, I. Žun, H. Tamai, S. Hosokawa, and T. Okuda. Measurements of traverse migration of single bubbles in a couette flow. In Celata et al. [47], pages 941–948.
- [390] R. Tonhardt and G. Amberg. Phase-field simulations od dendritic growth in a shear flow. *J. Cryst. Growth*, 194:406, 1998.
- [391] R. Torvik and H. F. Svendsen. Modelling of slurry reactors. A fundamental approach. *Chem. Eng. Sci.*, 45:2325–2332, 1990.

- [392] P. Trambouze. CFD applied to process engineering – An introduction. *Revue de L'Institut Français du Pétrole*, 51(2):199–203, 1996.
- [393] M. L. Tran. *Modélisation instationnaire de la distribution spatiale des phases dans les écoulement diphasique en régime à bulles*. PhD thesis, L'Université Claude Bernard – Lyon I, 1997.
- [394] G. Tryggvason, B. Bunner, J. Che, O. Ebrat, A. Esmaeeli, J. Han, S. Homma, D. Juric, S. Mortazavi, S. Nas, M. R. H. Nobari, and W. Tauber. Computations of multiphase flows by a finite difference/front tracking method – I. Multi-fluid flows; II. Applications; III. Variable surface tension and phase change. In *29th Comp. Fluid Dyn. Lecture Ser.* Von Karman Institute for Fluid Dynamics, 1998.
- [395] G. Tryggvason, B. Bunner, A. Esmaeeli, D. Juric, N. Al-Rawahi, W. Tauber, J. Han, S. Nas, and Y.-J. Jan. A front-tracking method for the computations of multiphase flow. *Int. J. Multiphase Flow*, 169:708–759, 2001.
- [396] K. Tsuchiya and L.-S. Fan. Near-wake structure of a single gas bubble in a two-dimensional liquid-solid fluidized bed: Vortex shedding and wake size variation. *Chem. Eng. Sci.*, 43:1167–1181, 1988.
- [397] H. Tsuge. The behaviour of single bubbles. *Adv. Chem. Eng.*, 16:1–26, 1982.
- [398] H. Tsuge and S. Hibino. The motion of single gas bubbles rising in various liquids. *Kagaku Kogaku*, 35:65–71, 1971.
- [399] H. Tsuge and S. Hibino. The onset conditions of oscillatory motion of single gas bubbles rising in various liquids. *J. Chem. Eng. Japan*, 10:66–68, 1977.
- [400] Y. Tsuji, Y. Morikawa, and H. Shinomi. LDV measurements of air-solid two phase flow in a vertical pipe. *J. Fluid Mech.*, 139:417–434, 1984.
- [401] Y. Tsuji, Y. Morikawa, and K. Terashima. Fluid-dynamic interaction between two spheres. *Int. J. Multiphase Flow*, 8:71–82, 1982.
- [402] R. Turton and O. Levenspiel. Short note on the drag correlation for spheres. *Powder Tech.*, 47:83–86, 1986.
- [403] O. Ubbink. *Numerical Prediction of Two Fluid Systems with Sharp Interfaces*. PhD thesis, Imperial College, University of London, 1997.
- [404] O. Ubbink and R. I. Issa. A method for capturing fluid interfaces on arbitrary meshes. *J. Comp. Phys.*, 153(1):26–50, 1999.
- [405] T. Uchiyama and K. Minemura. Numerical analysis of incompressible two-fluid model by finite element method (numerical method and calculation of flow around a circular cylinder). *Nippon Kikai Gakkai Ronbunshu, B Hen/Trans. JSME, Part B*, 62:977–984, 1996.
- [406] S. O. Univerdi and G. Tryggvason. A front-tracking method for viscous, incompressible, multi-fluid flows. *J. Comp. Phys.*, 100:25–37, 1992.

- [407] G. E. V. Vaessen. Unilever experiments on pin stirrers. Technical report, BRITE/EURAM III (BE 4322), III-7, 2000.
- [408] N. Vaidya, P. J. Dionne, and A. K. Singhal. Two-fluid model finite volume formulation for computing two-phase flows in complex geometries. In *Proc. ASME/JSM Fluids Engineering and Laser Anemometry Conf. and Exhibition, Hilton Head, SC, USA*, volume 225, pages 179–191, Aug 13–18, 1995.
- [409] H. A. Van Der Vorst. Bi-CGSTAB: A fast and smoothly converging variant of Bi-CG for the solution of nonsymmetric linear systems. *SIAM J. Sci. Stat. Comp.*, 13(2):631–644, 1992.
- [410] R. van der Welle. Void fraction, bubble velocity and bubble size in two-phase flow. *Int. J. Multiphase Flow*, 11:317–345, 1985.
- [411] K. van't Riet and J. M. Smith. The behaviour of gas-liquid mixtures near rushton turbin blades. *Chem. Eng. Sci.*, 28:1031–1037, 1973.
- [412] S. Vedaiyan, T. E. Degaleesan, and G. S. Laddha. Mean dropsize and characteristic velocity of droplet swarms in spray columns. *Ind. J. Tech.*, 12:135–142, 1973.
- [413] H. K. Versteeg and W. Malalasekera. *Computational Fluid Dynamics*. Longman Scientific & Technical, 1995.
- [414] G. B. Wallis. *One-dimensional Two-Phase flow*. McGraw Hill, New York, 1969.
- [415] D. M. Wang. A curve-fitted drag coefficient model. Private communication, 1994. see Hill [147].
- [416] D. M. Wang. Modelling of bubbly flow in a sudden pipe expansion. Technical report, BRITE/EURAM II (BE 4098), II-34, 1994.
- [417] D. M. Wang and R. Issa. Two-phase turbulence modelling. a review. Technical report, BRITE/EURAM II (BE 4098), II-14, 1992.
- [418] D. M. Wang, R. I. Issa, and A. D. Gosman. Numerical prediction of dispersed bubbly flow in a sudden enlargement. In Crowe et al. [64], pages 141–148.
- [419] S. K. Wang, S.-J. Lee, O. C. Jones, Jr., and R. T. Lahey, Jr. 3-d turbulence structure and phase distribution measurements in bubbly two-phase flows. *Int. J. Multiphase Flow*, 13(3):327–343, 1987.
- [420] C. Webb, F. Que, and P. R. Senior. Dynamic simulation of gas-liquid dispersion behaviour in a 2-d bubble column using a graphics mini-supercomputer. *Chem. Eng. Sci.*, 47:3305–3312, 1992.
- [421] P. P. Wegner and J. Y. Parlange. Spherical-cap bubbles. *Ann. Rev. Fluid Mech.*, 5:79–100, 1973.
- [422] E. W. Weisstein. Eric Weissteins's world of physics: Moment of inertia. Available from <http://www.scienceworld.wolfram.com/physics/MomentofInertia.html>.

- [423] H. G. Weller. Alternative pressure-velocity algorithmn. Private communication, 1999.
- [424] H. G. Weller. Interface capturing methodology. Private Communication, 1999.
- [425] H. G. Weller. A code independant notation for finite volume algoritmns. Technical Report TR/HGW/01, Nabla Ltd., 2002.
- [426] H. G. Weller. Derivation, modelling and solution of the conditionally averaged two-phase flow equations. Technical Report TR/HGW/02, Nabla Ltd., 2002.
- [427] H. G. Weller, G. Tabor, H. Jasak, and C. Fureby. A tensorial approach to computational continuum mechanics using object orientated techniques. *Comp. in Phys.*, 12(6):620–630, 1998.
- [428] C. Y. Wen and L. S. Fan. *Ind. Eng. Chem., Proc. Des. Dev.*, 13:194, 1974.
- [429] C. Y. Wen and Y. H. Yu. Mechanics of fluidization. volume 62 of *Chem. Eng. Prog. Symp. Ser.*, pages 100–111, 1966.
- [430] R. H. Wilhelm and M. Kwauk. Fluidization of solid particles. *Chem. Eng. Prog.*, 44(3):201–218, 1948.
- [431] M. W. Williams, D. B. Kothe, and E. G. Puckett. Accuracy and convergence of continuum surface tension models. Technical Report LA-UR-98-2268, Los Alamos National Laboratory, 1998. Available from <http://www.math.ucdavis.edu/~egp/>.
- [432] P. Woodward and P. Colella. The numericall simulation of two-dimensional fluid flow with strong shocks. *J. Comp. Phys.*, 54:115–173, 1984.
- [433] W.-X. Xu, G. D. Raithby, and G. D. Stuble. Application of a novel algorithm for moving surface flows. *J. Hydrodynamics*, 9(1):87–95, 1997.
- [434] F. Yamamoto, M. Koukawa, H. Monya, A. Teranishi, and H. Miyanoto. An experimental study for simulation of pneumatic conveying (lift and drag applied to a sphere in high Reynolds-number linear shear flows). *JSME Int. J., Ser. B: Fluids Thermal Eng.*, 41(2):294–299, 1993.
- [435] F. Yamamoto, L. Ohta, M. Iguchi, and T. Kawamoto. Experiments and numerical simulation on particle motion in the linear shear flow. In Serizawa et al. [344], pages PD1.11–18.
- [436] M. Yokosawa, Y. Kozawa, A. Inoue, and S. Aoki. Studies on two-phase cross flow – I. Flow characteristics around a cylinder; II. Transition Reynolds number and drag coefficient; III. Characteristics of unsteady flow behavior. *Int. J. Multiphase Flow*, 12:149–202, 1986.
- [437] D. L. Youngs. Time-dependent multi-material flow with large fluid distortion. In K. W. Morton and M. J. Baines, editors, *Numerical Methods for Fluid Dynamics*, pages 273–285. Academic Press, London, 1982.

- [438] S. Zaleski, J. Li, and S. Succi. 2-dimensional Navier-Stokes simulation of deformation and breakup of liquid patches. *Phys. Rev. Lett.*, 75:244, 1995.
- [439] L. Zhang. Mathematical simulation of fluid flow in gas-stirred liquid systems. *Mod. Sim. Mat. Sci. Eng.*, 8:463–476, 2000.
- [440] Q. Zhou and M. A. Leschziner. A Lagrangian particle dispersion model based on a time-correlated approach. In *Gas-Solid Flows*, volume 121, pages 225–260. ASME, 1991.
- [441] H. Zuber. On the dispersed two-phase flow in the laminar regime. *Chem. Eng. Sci.*, 19:897–917, 1964.
- [442] H. Zuber and J. Hench. Steady state and transient void fraction of bubbling systems and their operating limits. Technical Report 62GL100, General Electric Company, Scenectady, N. Y., 1962. see Wallis [414].
- [443] I. Žun. Transverse migration of bubbles influenced by walls in vertical bubbly flow. *Int. J. Multiphase Flow*, 6:583–588, 1980.
- [444] I. Žun. The mechanism of bubble non-homogeneous distribution in two-phase shear flow. *Nuc. Eng. Des.*, 118:155–162, 1990.